University of Rhode Island

DigitalCommons@URI

2014

ELASTIC BENDING MOMENT AND SHEAR FORCE LIMIT STATES OF STEEL BRIDGE PLATE GIRDERS CONSIDERING FATIGUE CRACK GROWTH

Sebastian B. Mendes
University of Rhode Island, sebastian.b.mendes@gmail.com

ELASTIC BENDING MOMENT AND SHEAR FORCE LIMIT STATES OF STEEL

BRIDGE PLATE GIRDERS CONSIDERING FATIGUE CRACK GROWTH

BY

SEBASTIAN B. MENDES

A DISSERTATION SUBMITTED IN PARTIAL FULFILLMENT OF THE

REQUIREMENTS FOR THE DEGREE OF

DOCTOR OF PHILOSOPHY

IN

CIVIL AND ENVIRONMENTAL ENGINEERING

UNIVERSITY OF RHODE ISLAND

2014

DOCTOR OF PHILOSOPHY DISSERTATION

OF

SEBASTIAN B. MENDES

APPROVED:

Dissertation Committee:

Major Professor: George Tsiatas

Co-Major Professor: David G. Taggart

Martin H. Sadd

Nasser H. Zawia
DEAN OF THE GRADUATE SCHOOL

UNIVERSITY OF RHODE ISLAND

2014

Abstract

The passage of vehicular traffic over short-span steel highway bridges generates cumulative fatigue damage within the supporting plate girders. Over time, fatigue crack growth may lead to the untimely occurrence of elastic limit states which may cause a bridge to become structurally deficient or even collapse. It may be useful for structural engineers to be able to design or otherwise modify plate girders for presumed through-thickness fatigue crack configurations so that the premature occurrence of elastic limit states may be averted. The objective of this research was to develop theoretical expressions for the residual bending moment and shear force strengths of I-shaped, transversely stiffened, steel plate girders corresponding to various elastic limit states. Several through-thickness fatigue crack configurations were considered. The formulation of the expressions employed various theories from solid mechanics including elasticity theory, linear elastic fracture mechanics, classical plate theory, and the principle of stationary potential energy. Finite element analyses were then conducted to validate the formulated expressions. The correspondence between the analytical and numerical results was generally in good agreement. Plots of the formulated and validated expressions as functions of crack length and load cycle demonstrated that various elastic limit states influence the overall residual strength of a fatigue-cracked plate girder at varying scales; certain limit states may be neglected in favor of more detrimental limit states. A design procedure for modifying the initial design of a plate girder for prescribed fatigue crack configurations was finally developed and demonstrated by employing the newly formulated and validated expressions.

Acknowledgements

My foremost gratitude goes to my co-Major advisers, Professor Tsiatas and Professor Taggart. Their strategic guidance and technical expertise was essential throughout the course of this research project. I am also grateful to Professor Sadd for serving as a member of my doctoral committee. Professor Sadd's knowledge and advice was fundamental in helping me understand the theory behind much of this research. Much appreciation also goes to Professor Thiem and Professor Brown for taking the time to be members of my comprehensive exam and defense committees. I am also thankful for the support of the faculty and staff of the Civil and Environmental Engineering Department. Last but not least, I am thankful for the unending support of my family and friends.

Table of Contents

List of Tables

List of Figures

xiii

1   Introduction

The short-span slab-girder steel bridge is the most common highway bridge type in the United States (see Figure 1.1) (Barker & Puckett, 1997, sec. 6.3.1). The growth of fatigue cracks in the plate girders of these bridges has previously caused many to become structurally deficient or even collapse (Bowman, 2002, 2004; Chajes, Mertz, Quiel, Roecker, & Milnius, 2005; Kirke & Al-Jamel, 2004; Lichtenstein, 1990; Minor & Woodward, 1996; Stockfish, 2011; Wardhana & Hadipriono, 2003; Zhou & Biegalski, 2010). The ageing of bridge infrastructure in the U.S. is only exacerbating the problem of potential structural deficiencies and collapses of these bridges. A recent study by Wardhana & Hadipriono (2003) analyzed over *500* bridge failures (structural deficiencies and collapses) in the U.S. between 1989 and 2000 and found that almost *30%* involved slab-girder steel bridges Approximately *5%* of all the failures were caused by steel deterioration, corrosion, or fatigue cracks.

Figure 1.1: Typical short-span slab-girder steel highway bridge (Ryan, Mann, Chill, & Ott, 2012).

I-shaped transversely stiffened steel plate girders constitute an integral component of short-span slab-girder steel highway bridge superstructures (see Figure 1.2) (Taly, 1998, sec. 1.3.3.1). The code-based procedure for bridge design in the U.S. requires engineers to design these plate girders for various limit states assuming that a girder will always remain uncracked (AASHTO, 2010). Furthermore, the state departments of transportation are required by the Federal Highway Administration (FHWA) National Bridge Inspection Program (NBIP) to conduct inspections of all public highway bridges at a maximum of every two years (CRS, 2007). In the time period between bridge inspections, fatigue crack growth may lead to untimely plate girder failure which may cause a bridge to become structurally deficient or even collapse.

Figure 1.2: Typical I-shaped transversely stiffened steel plate girders (MRC, 2013).

The passage of vehicular traffic over these superstructures produces sub-critical quasi-static stress fluctuations in the plate girders which generate cumulative fatigue damage. Specifically, high concentrations of stresses form at locations of discontinuity such as at flaws in the welds connecting the web plate to the flange or stiffener plates, or

at the ends of weld lines (Crocetti, 2003; Davies, Roberts, Evans, & Bennett, 1994; Goodpasture & Stallmeyer, 1967; Hall & Stallmeyer, 1964; Kouba & Stallmeyer, 1959; Marek, Perlman, Pense, & Tall, 1970; Meguid, 1989; Mueller & Yen, 1967; Roberts, Davies, & Bennett, 1995; Yen, 1963; Yen & Mueller, 1966). These stress concentrations may cause pre-existing microscopic flaws to develop into through-thickness macrocracks (see Figure 1.3) (Lawn, 1993; Osman & Roberts, 1999; Rolfe & Barsom, 1977).
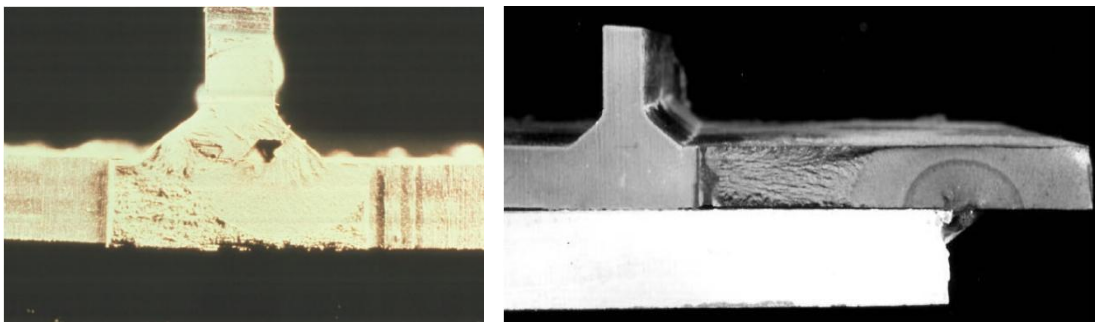
Figure 1.3: Cross-sections of through-thickness fatigue cracks in I-shaped plate girders. The cracks have propagated through the flange and web plates (Mertz, 2012; Ryan, Mann, Chill, & Ott, 2012).

The stress fluctuations may then cause a crack to propagate along the weld line or through the flange or web plates (see Figure 1.4) (Crocetti, 2003; Davies et al., 1994; Goodpasture & Stallmeyer, 1967; Hall & Stallmeyer, 1964; Kouba & Stallmeyer, 1959; Marek et al., 1970; Meguid, 1989; Mueller & Yen, 1967; Roberts et al., 1995; Yen, 1963; Yen & Mueller, 1966). The resulting loss of gross cross-sectional area may hasten the advent of various elastic limit states such as flange local yielding, section yielding, elastic flange local buckling, and elastic web local buckling due to bending moment or shear force effects (Brighenti, 2009). Furthermore, the crack may attain a critical length such that the stress intensity at the crack tip equals or exceeds the fracture toughness of the girder steel resulting in brittle fracture (Meguid, 1989, sec. 3.3). Alternatively, the plastic

region at the crack tip may grow to a critical size indicating impending ductile failure (Meguid, 1989, sec. 5.4. Overall, the growth of a fatigue crack may serve to initiate the premature occurrence of elastic limit states in a plate girder under sub-critical loading conditions.

Figure 1.4: Fatigue-cracked steel plate girders (Kirke & Al-Jamel, 2004; Stockfish, 2011; Zhou & Biegalski, 2010).

Herein are described some specific instances of bridge deficiencies and collapses caused directly by the formation and growth of fatigue cracks. The King's Street Bridge in Melbourne, Australia collapsed in 1962 due to the brittle fracture limit state (Kirke & Al-Jamel, 2004, sec. 2.3.3). Inherent discontinuities and flaws in the welds holding together the supporting plate girders induced high concentrations of local stresses within the loaded girders. The high stress concentrations, combined with the low ambient temperatures and the low fracture toughness of the girder steel, led to the sudden fracture and collapse of the supporting girders.

More recently in 1994, one of the supporting I-shaped girders of the Blue River Bridge carrying I-64 in southern Indiana experienced the formation of a long, vertical, through-thickness crack within the web plate (Bowman, 2002, 2004). It was concluded

that the low temperatures during the winter of 1994 around the location of the bridge served to greatly reduce the fracture toughness of the girder steel. Inherent flaws within the plate girder welds initiated the propagation of a fatigue crack. The fatigue crack eventually propagated to a critical size causing the loaded web plate to fracture in a brittle manner.

In 2003, a fascia steel plate girder supporting the I-95 Bridge over the Brandywine River in Delaware experienced the formation of a long, vertical, through-thickness crack (Chajes et al., 2005). The crack was concluded to be caused primarily by the brittle fracture limit state. Although the bridge did not experience collapse, it had to be partially closed to traffic for over two months for repairs. Also in 2003, two plate girders supporting the I-895 Bridge over U.S. Route 1 and the Patapsco River in Maryland experienced the formation of two long through-thickness cracks (Zhou & Biegalski, 2010). As with the I-95 Bridge over the Brandywine River, the crack was deemed to be caused primarily by the brittle fracture limit state.

Minor & Woodward (1996) described the buckling of a cracked web panel located within an I-shaped transversely stiffened steel plate girder supporting the I-40 Bridge over the Rio Grande in New Mexico. The girder did not collapse and therefore retained a certain quantity of residual strength. However, the presence of the long, vertical, through-thickness crack in the web panel led directly to the buckling of the web panel. The buckled region of the web panel was limited to the local region adjacent to the crack.

2 Objective

It may be useful for structural engineers to be able to design or otherwise modify the elastic capacities and fatigue lives of plate girders for presumed through-thickness fatigue crack configurations. In this way, the premature occurrence of elastic limit states may be averted in between bridge inspection periods. The objective of this research was to develop theoretical expressions for the bending moment and shear force capacities of I-shaped transversely stiffened steel plate girders corresponding to the limit states of flange local yielding, section yielding, elastic flange local buckling, elastic web local buckling, brittle fracture, and impending ductile failure while considering the presence of various through-thickness fatigue crack configurations. These elastic limit states generally do not correspond to ultimate failure modes and may therefore be viewed as initial limit states which are to be conservatively avoided.

The capacity expressions considered non-composite girder configurations in which the girder cross-section considered was exclusively that of the steel plate girder. Theoretical expressions were also developed for the incremental decay of the bending moment and shear force capacities per cycle of stress application by considering the growth of the through-thickness fatigue crack configurations. The general finite element (FE) software ABAQUS/CAE 6.11 was employed to model and perform analyses on a series of full-scale trial plate girders for the purpose of validating the capacity expressions.

A procedure for designing or otherwise modifying the elastic capacities and fatigue lives of plate girders for prescribed through-thickness fatigue crack configurations was finally demonstrated. Constant-amplitude load functions were developed from the

American Association of State Highway and Transportation Officials (AASHTO) bridge design specifications (AASHTO, 2010). The load functions were used in conjunction with the capacity and decay expressions to investigate the capacities, limit states, critical crack lengths, and fatigue lives of a trial plate girder considering different prescribed fatigue crack configurations. The AASHTO *LRFD Bridge Design Specifications* (2010) was employed to perform the initial design of the trial girder. The trial girder design was then modified to have prescribed fatigue lives and sufficient capacities for the prescribed crack configurations. The modified trial girder design was then compared and contrasted to the initial design.

In summary, the following tasks were accomplished:

- Formulation of theoretical expressions for the elastic bending moment and shear force capacities of I-shaped transversely stiffened non-composite steel plate girders considering various through-thickness fatigue crack configurations

- Development of theoretical expressions for the incremental decay of the elastic bending moment and shear force capacities per cycle of stress application as affected by fatigue crack growth

- Development and demonstration of a procedure for designing new plate girders or modifying existing girders for prescribed through-thickness crack configurations and fatigue lives

3 Background

3.1 Overview

A comprehensive background is presented to give a solid theory base relating to the effects of fatigue crack growth on the elastic bending moment and shear force limit states of short-span steel highway bridge plate girders. A summary of the broader context within which steel highway bridges belong to is first given by assessing the current state of the highway system in the United States. The typical structural configurations and general statistics of steel highway bridges are then evaluated. Much attention is given to the geometrical and material properties of steel plate girders and their associated elements. Fatigue load models derived from vehicular traffic traveling over highway bridges are then briefly overviewed. Finally, an overview of various analytical and numerical methods for analyzing the effects of fatigue crack growth on the elastic bending moment and shear force capacities of steel plate girders is presented.

3.2 Steel Plate Girders

3.2.1 Highways in the United States

Highways in the U.S. are categorized into two broad types of systems: the National Highway System (NHS) and state highway systems (Oglesby & Hicks, 1982, pp. 13-19). These two systems are not mutually exclusive in that a road belonging to the NHS may also belong to the state highway system. Also, these two systems generally do not include the networks of local roads and streets, which are administered by appropriate county, city, or town agencies.

The NHS was approved by Congress in 1995 and incorporated mostly preexisting primary and secondary roads deemed essential for the economic strength and defense of the U.S. (Slater, 1996). Importantly, the NHS incorporated the nationwide network of highways known as the Dwight D. Eisenhower National System of Interstate and Defense Highways (henceforth referred to as the Interstate Highway System or IHS) which in 2008 consisted of *47,000* miles of limited-access highways (see Figure 3.2.1) (USDOT, 2011). More than *40%* of all highway traffic and *75%* of heavy truck traffic utilize the almost *160,000* miles of NHS roads (Slater, 1996). This is despite the fact that the NHS constitutes only about *4%* of the total road mileage in the U.S.
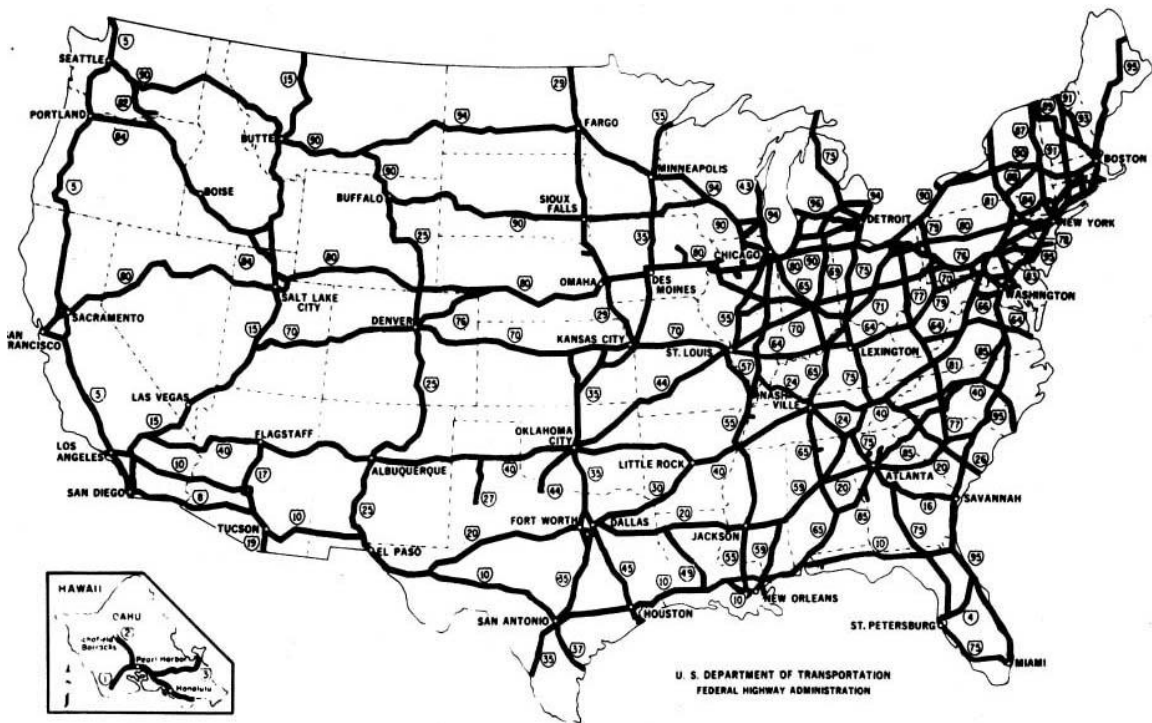
Figure 3.2.1: Nationwide extent of the IHS (FHWA, 2012a).

Approximately *95%* of the roads belonging to the NHS are owned and maintained by the state governments with the rest owned by the federal government or local

governments (USDOT, 2010). A substantial portion of funding for the construction and maintenance of the NHS is provided by the federal government. Federal funding for roads that would later become part of the NHS was first made possible by a series of acts beginning with the Federal-Aid Highway Act of 1921 (Oglesby & Hicks, 1982, p. 13). The development of the IHS was later initiated with the Federal-Aid Highway Act of 1956 (USDOT, 2010). The Federal Highway Administration (FHWA), which itself is a division of the United States Department of Transportation (USDOT), monitors the allocation of Federal-Aid funds to the state departments of transportation.

Similar to the NHS, the state highway systems primarily consist of primary and secondary roads (OLA, 2008). The state highway systems are owned and maintained by the state governments (Oglesby & Hicks, 1982). State highways generally receive a mix of Federal-Aid and state funds for their construction and maintenance (USDOT, 2010). Overall, approximately *20%* of the *4.1* million miles of public roads in the U.S. belong to either the NHS, state highway systems, or both (USDOT, 2010).

Another lesser known designated highway system is the National Network. The National Network is concerned with the regulation of truck traffic traveling on the NHS and state highway systems. The National Network was designated under the Surface Transportation Assistance Act of 1982 and incorporated approximately *200,000* miles of roads belonging to the state highway systems and roads that would later become part of the NHS (USDOT, 2010). The 1982 act essentially requires individual states to allow trucks with conventional combinations to travel on the highways designated as being part of the National Network. The FHWA (2012b) defines conventional combinations as

"tractors with one semitrailer up to *48* ft. in length or with one *28* ft. semitrailer and one *28* ft. trailer, and can be up to *102* in. wide".

In 2008, Americans accumulated almost *3.0* trillion vehicle miles traveled (VMT) on all public roads. A little over *60%* of VMT were on either the NHS, state highway systems, or both (USDOT, 2010). Furthermore, the USDOT (2011) reports that over *12* billion tons of freight was shipped using trucks in 2010 alone, and this amount is expected to double by 2040. As previously mentioned, approximately three quarters of all heavy truck traffic utilizes roads that are part of the NHS (Slater, 1996). In 2009, 288 billion VMT were accumulated for combination trucks and single-unit trucks on all public roads with approximately *37%* of VMT on the IHS (USDOT, 2011). This data implies that the NHS and state highway systems constitute an indispensible mode of transportation for moving people and freight.

Overall, the NHS and state highway systems form an essential component of the transportation infrastructure in the U.S. Together, they greatly facilitate interstate commerce by allowing for the passage of people and freight throughout the country. Additionally, they help provide for national defense by allowing for the rapid mobilization of military forces and their support systems (USDOT, 2010).

3.2.2   Steel Highway Bridges

3.2.2.1 Design and Maintenance

Highway bridges are an integral part of both the NHS and state highway systems. They provide essential access across various natural obstacles such as rivers, streams, and gullies, as well as over man-made obstacles such as railroads and other roads (Tonias,

1995, p. 3). Highway bridge design is performed in accordance with the AASHTO *LRFD Bridge Design Specifications* (see Appendix A: AASHTO LRFD Bridge Design Specifications). The overwhelming majority of highway bridges belonging to the NHS are owned and maintained by various state agencies, such as state highway departments, under the umbrella of the state departments of transportation (FHWA, 2011). These bridges are largely financed by Federal-Aid funds through the Highway Bridge Program (HBP) (Oglesby & Hicks, 1982, p. 13; CALTRANS, 2008, p. 2-3). Highway bridges belonging to the state highway systems are also owned and maintained by various state agencies and are financed by a mix of HBP and state funds.

The state departments of transportation are required by the FHWA to periodically inspect and report the properties and conditions of all public vehicular bridges in their respective states (see Appendix B: Bridge Inspection and Evaluation) (FHWA, 2011). Bridges included in this requirement are those belonging to the NHS, state highway systems, and networks of local roads and streets (CRS, 2007). The FHWA uses this information to maintain a record called the National Bridge Inventory (NBI) which lists the various properties and conditions of all public vehicular bridges in the U.S. having spans greater than *20* ft. (OLA, 2008, p. 30). As of 2011, the NBI listed over *600,000* bridges in its inventory (FHWA, 2011). Approximately half of these bridges are part of the NHS, state highway systems, or both, while the rest belong mostly to networks of local roads and streets (CRS, 2007).

3.2.2.2 Classification

Bridges listed in the NBI are organized by various criteria such as bridge owner, location by state and county, year built, unit cost, structure type, wearing surface type, deck type, span length, construction material, and condition (FHWA, 2011). In terms of structural properties, bridges may generally be classified based only upon span length, structure type, and material of construction (Taly, 1998, pp. 47-50). Short-span bridges typically have spans of *20* to *125* ft., medium-span bridges have spans of *125* to *400* ft., and long-span bridges have spans exceeding *400* ft. Spans of these lengths may be part of single-span or multi-span bridges (Taly, 1998, p. 50).

Structure type refers to the physical configuration of a bridge and is directly related to the manner by which the superstructure transfers load to the substructure. According to Tonias (1995), the superstructure "comprises all the components above the supports" while the substructure "consists of all elements required to support the superstructure" (pp. 4, 6). There are many classifications of structure type including slab-girder bridges, orthotropic bridges, truss bridges, arch bridges, cantilever bridges, cable-stayed bridges, and suspension bridges (Taly, 1998, pp. 50-80). The material of construction refers to the type of material used in the construction of the superstructure and may include structural steel, concrete, timber, or advanced composite materials (Taly, 1998, pp. 47-49). This research focuses upon short-span, slab-girder, steel highway bridges (henceforth referred to simply as steel highway bridges), as shown in Figure 3.2.2.

The slab-girder configuration is the most common bridge structure type in the U.S. (Barker & Puckett, 1997, p. 276). At the end of 2011, approximately *255,000*

bridges listed in the NBI were classified as slab-girder bridges (FHWA, 2011). This amounts to nearly *50%* of the total number of bridges listed in the NBI. Furthermore, approximately *15%* of the slab-girder bridges, or about *38,000* slab-girder bridges, were classified as structurally deficient (see Appendix B: Bridge Inspection and Evaluation) (FHWA, 2011). Further analysis of the study by Wardhana & Hadipriono (2003) suggests that approximately *25%* of the structurally deficient slab-girder bridges, or about *9,000* bridges, were made structurally deficient by steel deterioration, corrosion, or fatigue cracks.

Figure 3.2.2: Typical short-span slab-girder steel highway bridge (Ryan et al., 2012).

3.2.2.3 Superstructure and Substructure

Typical of most bridge types, steel highway bridges consist of a superstructure and substructure (see Figure 3.2.3). The primary function of the superstructure is to transfer vehicular traffic load, along with any other type of load, from the bridge deck to the substructure, which provides support for the superstructure (Tonias, 1995, pp. 4, 6).

Slab-girder superstructures essentially consist of a concrete deck supported by a series of girders. The girders are in turn supported by components of the substructure (Taly, 1998, sec. 1.3.3.1).

The components of the substructure typically include bearings, piers, and abutments (Tonias, 1995, p. 353). Piers serve to provide intermediate support of the superstructure between the end supports of the bridge. Although piers are constructed in a variety of different shapes and forms, their ultimate function is to transfer load from the superstructure to the foundations (Tonias, 1995, p. 384). Similarly, abutments serve to provide end support of the superstructure (Barker & Puckett, 1997, p. 1107). In addition to transmitting load from the superstructure to the foundations, abutments may act as retaining walls to resist horizontal earth pressure from soil supporting the approach highways (Tonias, 1995, p. 355). Piers and abutments are generally constructed of reinforced concrete, but may also be constructed of steel or timber (Tonias, 1995, pp. 355, 384). Bearings serve to directly transmit load from the superstructure to supporting piers and abutments by providing translational and rotational support. Cylindrical bearings, rocker bearings, and pot bearings provide translational restraint while allowing rotational movement. Roller bearings and sliding bearings allow for both translational and rotational movement (Barker & Puckett, 1997, pp. 1091-1094).
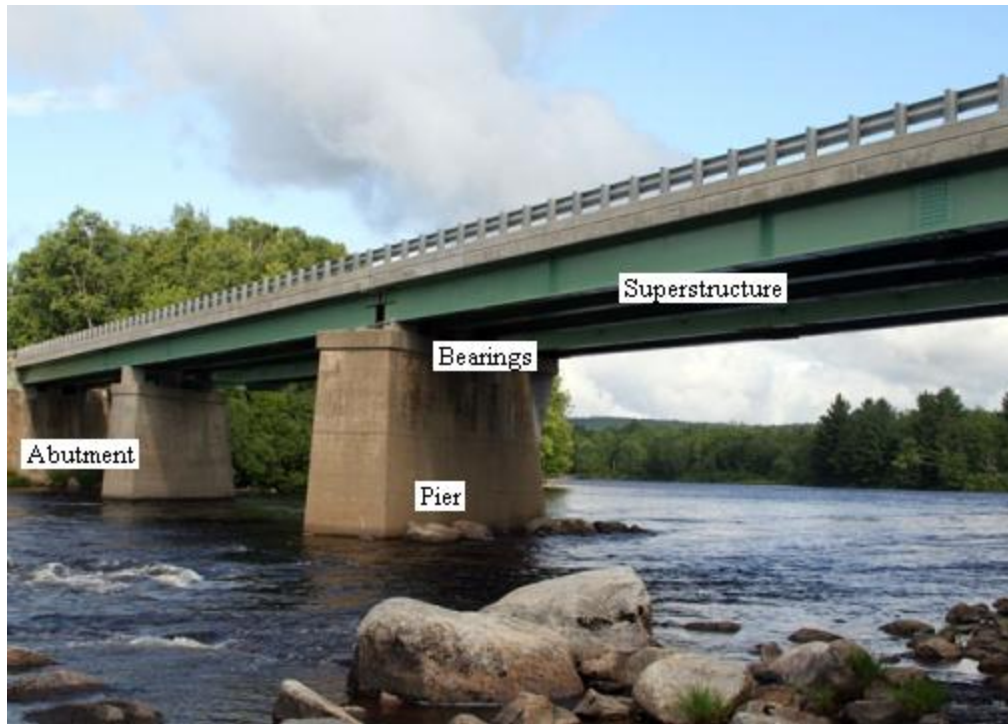
Figure 3.2.3: Superstructure and substructure of a slab-girder bridge (About Bridges).

3.2.3   Superstructure

Steel highway bridge superstructures generally consist of a deck, girders, and secondary members (see Figure 3.2.4) (Tonias, 1995, p. 5). The deck is commonly a cast-in-place or precast reinforced concrete slab with a wearing surface to resist deterioration from vehicular traffic (Barker & Puckett, 1997, p. 276). Various other components such as traffic barriers, parapets, and sidewalks are monolithically attached to or otherwise situated upon the slab (Tonias, 1995, pp. 5, 141). Generally, the slab is directly or indirectly supported by girders. Cast-in-place concrete slabs cast upon cold-formed steel decking are indirectly supported by the girders in that the decking serves as an intermediate component in the transfer of load from the slab to the girders (Salmon,

Johnson, & Malhas, 2009, ch. 16). Conventional cast-in-place concrete slabs do not utilize steel decking and are thus directly supported by the girders.
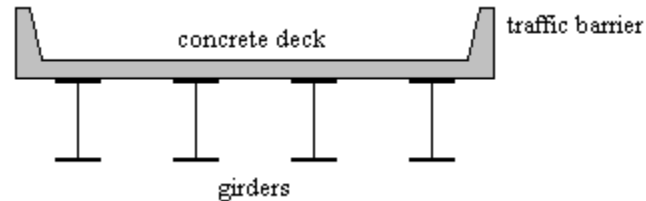
Figure 3.2.4: Cross-section of highway bridge superstructure with concrete deck, traffic barriers, and supporting girders.

The primary function of the slab is to distribute and transfer vehicular live loads to the girders (Tonias, 1995, p. 5). Additional types of load such as dead loads, vehicular dynamic loads, wind loads, and earthquake loads are also transferred from the slab to the girders (AASHTO, 2010). The slab behaves as a plate-like structure and thus carries load primarily by flexure (MacGregor & Wight, 2005, pp. 610-611). Design standards such as the American Concrete Institute (ACI) *Standard 318* (2005) and the AASHTO *LRFD Bridge Design Specification*s (2010) provide codified procedures for the analysis and design of concrete bridge slabs.

The supporting girders are oriented longitudinally to the direction of traffic and are generally spaced at a constant distance across the bottom width of the slab in order to efficiently support the deck (Barker & Puckett, 1997, p. 278). The primary function of the steel girders is to transfer load from the slab to supporting bearings, piers, and abutments (Tonias, 1995, p. 6-7). Lateral bracing is usually required along the length of the girders to prevent lateral-torsional buckling (Salmon et al., 2009, ch. 9). Therefore, secondary members are attached to and oriented perpendicular to the girders in order to provide lateral bracing (Tonias, 1995, p. 6).

Elements of the steel girders, referred to as details, include such components as welded stiffener plates, welded cover plates, welded shear stud connectors, welded connections, and bolted connections (Massarelli & Baber, 2001). Steel details perform various roles such as holding the components of the girder together, attaching the girder to other components, and providing additional stiffness to the girder to prevent local buckling (Salmon et al., 2009, ch. 11).

3.2.4   Steel Plate Girders

3.2.4.1 Geometrical Properties

Commonly used steel girder types used in steel highway bridge superstructures include rolled beams, plate girders, and box girders (Tonias, 1995, p. 73). Rolled beams are members that have been hot-rolled to form an I-shaped cross-section (see Figure 3.2.5a). Plate girders are generally fabricated from two flange plates and a single web plate which are welded together to form an I-shaped cross-section (see Figure 3.2.5b) (Blodgett, 1966, p. 4.3-1). Box girders are similar to plate girders except that they are generally fabricated from two flange plates and two web plates to form a box shaped cross-section (see Figure 3.2.5c).
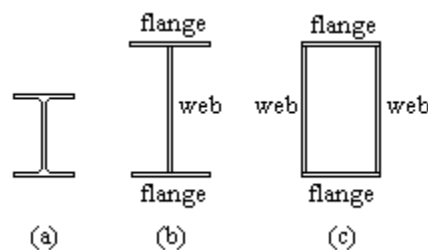
Figure 3.2.5: (a) Hot-rolled I-shaped beam, (b) I-shaped plate girder, and (c) box girder.

Plate girders may be configured to form a wide range of I-shaped section types possessing different section properties. This is because the flanges and webs may be proportioned to achieve various I-shaped cross-sections. In this way, the most efficient plate girder design may be attained in terms of weight and material savings (Salmon et al., 2009, sec. 11.1). Dimensions which may be modified include the flange width, flange thickness, web depth, and web thickness. Changing these dimensions modifies various section properties including the neutral axis, cross-sectional area, moment of inertia, elastic section modulus, plastic section modulus, radius of gyration, and polar moment of inertia. In contrast, a limited range of standard rolled beam section types are available and may not allow for the most efficient design (Salmon et al., 2009, sec. 1.5). The American Society for Testing and Materials (ASTM) and AASHTO publish standard specifications (ASTM A709 and AASHTO M270, respectively) by which structural steel shapes used for bridges conform to (AASHTO, 2010).

I-shaped plate girders (henceforth referred to simply as plate girders or girders) are designed to resist many loading effects including bending, torsional, shearing, and axial stresses. The flange plates nominally act to resist most of the internal bending moment effects (see Figure 3.2.6a). The web plate nominally acts to resist most of the internal shear force effects (see Figure 3.2.6b) (Chen & Duan, 1999, p. 12-5).
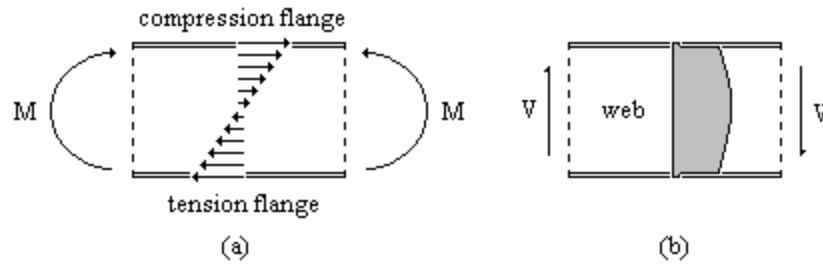
Figure 3.2.6: Profile views of I-shaped girder with (a) flange plates resisting the bending stress distribution and (b) web plate resisting the shear stress distribution.

A major consideration in the design of a girder is the avoidance of shear-based limit states including shear yielding of the web and web local buckling (Salmon et al., 2009, sec. 11.7). The shear force capacity of a girder corresponding to shear yielding may be increased by enlarging the gross cross-sectional area of the web. Similarly, the shear strength of a girder corresponding to web local buckling may be increased by modifying the dimensions of the web as well as adjusting additional parameters. It can be deduced from classical plate theory that the elastic buckling strength of a plate loaded under pure shear is maximized if the length-to-width ratio of the plate approaches unity (Ugural, 1999, ch. 3). For this reason, transverse stiffener plates are generally welded to the web and flanges at varying intervals along the length of the girder, effectively subdividing the web into individual panels bounded by the flanges and stiffener plates (see Figure 3.2.7) (Salmon et al., 2009, sec. 11.7). In regions of the girder loaded under predominantly shear, the web panels are effectively loaded under pure shear (Salmon et al., 2009, sec. 11.7). Hence, the modification of the spacings between the stiffener plates directly influences the buckling strengths of the web panels.
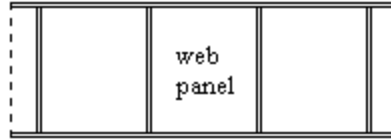
Figure 3.2.7: Profile view of I-shaped girder with transverse stiffener plates subdividing the web into individual web panels.

3.2.4.2 Material Properties

Plate girders are typically constructed of structural steel. Structural steel is essentially an alloy composed primarily of iron and carbon (see Appendix C: Structural Steel). Small amounts of additional alloying elements include manganese, phosphorus, sulfur, silicon, aluminum, vanadium, columbium, nickel, copper, chromium, nitrogen, and boron (Taly, 1998, p. 118). Various proportions of these alloying elements serve to modify the material properties of steel such as the yield strength, ultimate tensile strength, ductility, hardness, toughness, and corrosion resistance (Blodgett, 1966, p. 2.1-1; Barker & Puckett, 1997, p. 702). Carbon is by far the most important alloying element and helps to modify the strength of steel (Barker & Puckett, 1997, p. 703). Increasing the amount of carbon serves to increase the resulting steel strength while at the same time reducing its ductility, toughness, and weldability (Salmon et al., 2009, sec. 2.1). The ASTM A709 and AASHTO M270 specifications provide equivalent standards by which the material properties of structural steels used for bridges must conform to (AASHTO, 2010, p. 6-24). For the purpose of this research, the girders are implied to be constructed of standard high-strength low-alloy structural steel.

3.2.4.3 Non-composite and Composite Configurations

Steel highway bridge superstructures may be constructed in non-composite or composite configurations (Barker & Puckett, 1997). In non-composite configurations, the plate girders carry load independently of the reinforced concrete slab (see Figure 3.2.8a). The girders may thus be analyzed and designed considering only the girder cross-sections and neglecting the influence of the concrete slab.

In composite configurations, the plate girders act compositely with a portion of the concrete slab to carry load (see Figure 3.2.8b) (Taly, 1998, p. 726). The geometrical and material properties of the concrete slab affect the overall section properties and therefore influence the stress and strain bending distributions (Salmon et al., 2009, ch. 16). Full composite action is developed when there is continuous compatibility at the interface between the slab and the girder, and the strain distribution across the slab-girder interface remains uniform under load (Salmon et al., 2009, sec. 16.2).
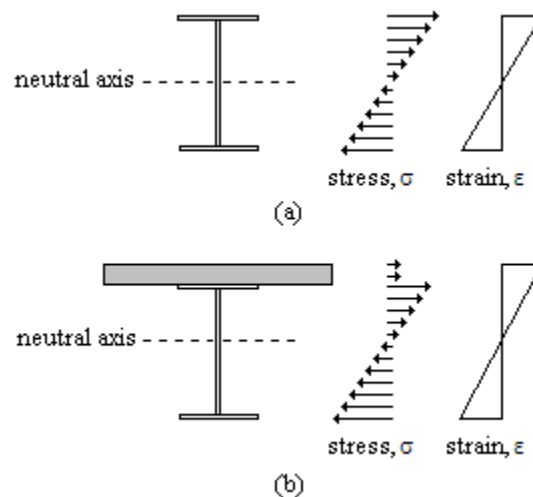
Figure 3.2.8: (a) Non-composite and (b) composite girder sections with corresponding stress and strain bending distributions.

Shear stud connectors are generally employed to resist the horizontal shear stresses and to maintain uniform strain distribution across the interface (Barker & Puckett, 1997, sec. 8.9). These connectors are typically welded along the top flanges of the girders before the slab is poured such that they become embedded within the slab after the concrete hardens (Salmon et al., 2009, sec. 16.1). In positive bending moment regions, the slab essentially behaves as a concrete cover plate attached to the compression flange (Taly, 1998, p. 728). In negative bending moment regions, the tensile resistance of the slab is not relied upon and only the longitudinal reinforcing steel is considered (Taly, 1998, p. 735). Overall, the steel-concrete composite action allows for increased span lengths, increased deck stiffness, and shallower plate girder depths (Salmon et al., 2009, sec. 16.3). This translates into material and cost savings, and an overall efficient design.

3.2.5 Fatigue Loading

Vehicular traffic passing over a steel highway bridge induces fluctuating sub-critical bending moments and shear forces within the superstructure girders. These cyclic bending moments and shear forces are directly coupled to fluctuating stresses within the structural members and elements of the superstructure. The magnitudes of the stresses depend upon a number of factors originating from the spectrum of loading and the configuration of the superstructure (Taly, 1998, p. 181). Vehicular traffic load, termed as vehicular live load, varies depending upon such parameters as the gross vehicle weights, axle loads, axle configurations, the longitudinal and transverse positions of vehicles, multipresence of vehicles, and vehicle speeds (Nowak, 1993). As such, the magnitude of vehicular live load at any one location along the superstructure changes over time and is

thus classified as transient load (Barker & Puckett, 1997, p. 139). These load fluctuations may be approximately described by constant-amplitude trigonometric load functions (see Figure 3.2.9). It follows that the corresponding magnitudes of stresses within the superstructure also changes over time. Hence, the continuous passage of vehicular traffic across a bridge induces repeated stress cycles in the steel plate girders of the superstructure (Barker & Puckett, 1997, p. 106).
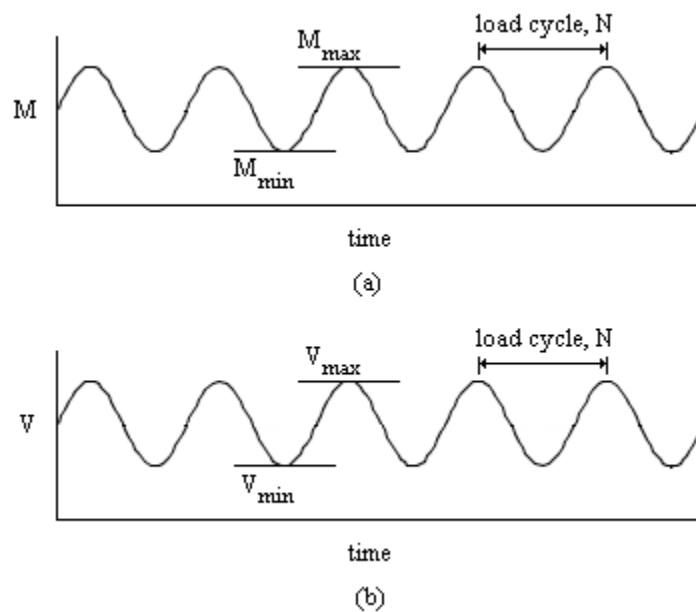
Figure 3.2.9: Constant-amplitude trigonometric load functions for (a) bending moment and (b) shear force.

The live load due to car traffic is negligible when compared to the live load due to truck traffic, namely because of the much greater weight of trucks (Barker & Puckett, 1997, p. 142). Therefore, truck traffic produces the critical load effects in steel highway bridge superstructures (Nowak et al., 1993). The stress cycles due to the vehicular live load (henceforth implied to mean the truck live load) generates cumulative damage in the steel plate girders, which may lead to the initiation of fatigue cracks (Barker & Puckett, 1997, p. 106). The newly formed fatigue cracks may continue to propagate through the

24

girders under the fluctuating stress, and may eventually lead to the untimely occurrence of elastic limit states or ultimate failure modes.

Vehicular live loads generally act concurrently with additional types of load such as dead loads, vehicular dynamic loads, wind loads, and earthquake loads. Dead loads are generally permanent and include loads due to structural components, nonstructural attachments, wearing surfaces, and utilities (Barker & Puckett, 1997, p. 140). Vehicular dynamic loads act together with the static aspect of vehicular live loads, and occur due to the dynamic force effects from vehicles traveling over discontinuities in the wearing surface such as deck joints, cracks, potholes, and delaminations (AASHTO, 2010, p. 3-30). The possible load combinations acting upon a highway bridge are numerous and result in a potentially complex loading spectrum (Taly, 1998, p. 181). The AASHTO *LRFD Bridge Design Specifications* (AASHTO, 2010) provides a code-based procedure for determining load types and load combinations specific to fatigue loading (see Appendix A: AASHTO LRFD Bridge Design Specifications).

3.3   Structural Analysis and Design

3.3.1   Analytical Analysis

The bending moment and shear force capacities of I-shaped transversely stiffened steel plate girders are adversely influenced by fatigue crack growth. As previously mentioned, the propagation of a fatigue crack through a girder may induce the premature occurrence of various elastic limit states. The influence of fatigue crack growth on the elastic strength and fatigue life of steel plate girders may be analyzed with various theories from solid mechanics including beam theory, the theory of elasticity, classical

plate theory, the principle of stationary potential energy, and linear elastic fracture mechanics (LEFM).

3.3.1.1 Fatigue Crack Growth

Every structure contains microscopic flaws which can develop into macrocracks as discussed by Lawn (1993, ch. 9) and Rolfe & Barsom (1977, ch. 7). As previously mentioned, the ongoing passage of vehicular traffic over steel highway bridge induces sub-critical cyclic bending moments and shear forces within the supporting girders (Barker & Puckett, 1997). These forces are directly coupled to fluctuating bending and shear stresses acting throughout the supporting steel plate girders. High concentrations of fluctuating stress may form at inherent discontinuities in a girder (Crocetti, 2003; Davies et al., 1994; Goodpasture & Stallmeyer, 1967; Hall & Stallmeyer, 1964; Kouba & Stallmeyer, 1959; Marek et al., 1970; Meguid, 1989; Mueller & Yen, 1967; Roberts et al., 1995; Yen, 1963; Yen & Mueller, 1966). These discontinuities are generally attributable to flaws in the fillet welds connecting the web to the flanges and stiffener plates, and may include incomplete fusion, porosity, undercutting, and partial penetration (Crocetti, 2003). The fluctuating stress concentrations may in time cause a pre-existing microcrack to grow into a through-thickness macrocrack (Lawn, 1993; Osman & Roberts, 1999; Rolfe & Barsom, 1977) (see Figure 3.3.1).
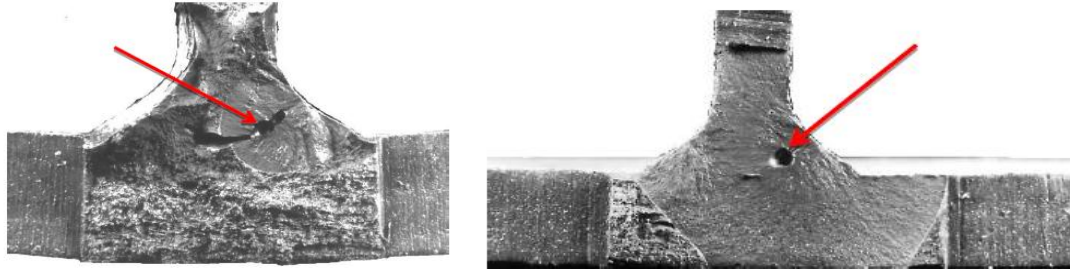
Figure 3.3.1: Cross-sections of through-thickness fatigue cracks in the flange-to-web connections of I-shaped plate girders. The arrows indicate the locations of the crack initiations (Mertz, 2012).

The fatigue crack may then continue to propagate through the girder to form one of several fatigue crack configurations (Crocetti, 2003; Davies et al., 1994; Goodpasture & Stallmeyer, 1967; Hall & Stallmeyer, 1964; Kouba & Stallmeyer, 1959; Marek et al., 1970; Meguid, 1989; Mueller & Yen, 1967; Roberts et al., 1995; Yen, 1963; Yen & Mueller, 1966). In regions of a girder loaded under predominantly bending, some crack configurations include but are not limited to vertical edge-cracks extending from the tension flange through the web plate, cracks extending through one or both sides of the tension flange, and three-ended cracks extending through the web plate and both sides of the tension flange (see Figure 3.3.2a, b, c, d). In regions of a girder loaded under predominantly shear, a fatigue crack may initiate in a corner of a web panel at the junction of a flange and transverse stiffener plate and propagate diagonally through the web plate (see Figure 3.3.2e).
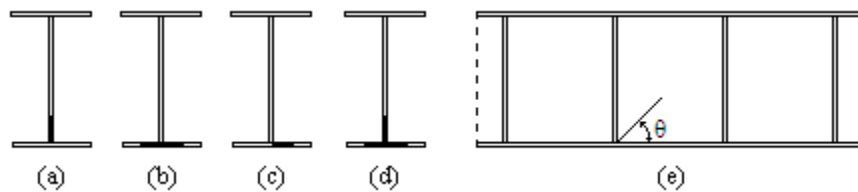
Figure 3.3.2: (a) Vertical edge-crack in web plate, (b) crack extended through both sides of tension flange, (c) crack extending through one side of tension flange, (d) three-ended crack, and (e) diagonal fatigue crack originating at a corner of a web panel.

The presence of macrocracks, as well as intentional discontinuities such as holes and notches, produces stress concentrations in the local vicinity of the discontinuities (Meguid, 1989, sec. 1.17). Inglis (1913) was one of the first to investigate the concentration of stresses around an elliptical hole in a stressed plate. The shape of an elliptical hole can be modified to represent a wide array of flaw shapes ranging from round holes to straight cracks (see Figure 3.3.3). In general, it was found that the concentration of stresses about the corners of a flaw is dependent upon the radius of curvature of the elliptical hole.
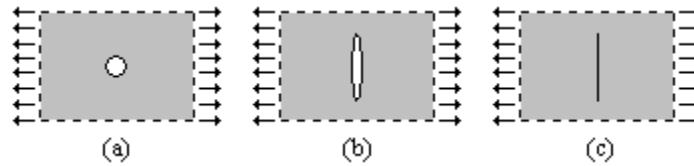
Figure 3.3.3: Infinite plates loaded under uniaxial tensile stress containing (a) a round hole, (b) a narrow elliptical hole, and (c) a straight through-thickness crack.

Using an energy approach, Griffith (1921) theorized that the formation and growth of a crack in a stressed body serves to release the elastic strain energy in the body (Rolfe & Barsom, 1977, ch. 2). The total energy change, dU_T, of a stressed body due to crack growth is thus equal to the energy change, dU_E, from the work performed by external loads, and the energy change, dU_A, from the release of elastic strain energy from the crack growth. This is expressed by (Lawn, 1993, p. 21)

$$dU_T = dU_E + dU_A \tag{3.3.1}$$

The total energy change per unit area of potential crack surface, dA, at the crack tip is called the energy release rate, G, given by (Meguid, 1989, pp. 113-114)

$$G = -\frac{dU_T}{dA} \tag{3.3.2}$$

The concept of the energy release rate remains valid only if the plastic work at the crack tip is small, as is the case for brittle materials and ductile materials under low levels of stress (Meguid, 1989, sec. 3.5.2). A crack will propagate if the energy release rate exceeds a critical value, G_c. In other words, a crack will propagate if the energy at the crack tip equals or exceeds the amount of energy necessary to extend the crack (Shukla, 2005, p. 33).

3.3.1.2 Elastic Limit States of Fatigue-Cracked Plate Girder

There exist several elastic limit states and corresponding plate girder capacities associated with the propagation of a fatigue crack in a loaded girder. These limit states generally include flange local yielding, section yielding, elastic flange local buckling, elastic web local buckling, brittle fracture, and impending ductile failure (Salmon et al., 2009, ch. 11; Sun & Jin, 2012, ch. 3). Each limit state is associated with a critical magnitude of bending moment or shear force, which is equivalent to the elastic capacity or elastic strength of the girder (Beer, Johnston, & DeWolf, 2006, chs. 4, 6). The limit states of flange local yielding, section yielding, elastic flange local buckling, and elastic web local buckling concerning a cracked girder are essentially modified limit states of an uncracked girder. Conversely, the limit states of brittle fracture and impending ductile failure are limit states uniquely associated with a fatigue-cracked girder.

It is noted that elastic limit states generally do not correspond to ultimate failure modes. The occurrence of an elastic limit state within an uncracked girder does not necessarily result in the immediate or complete collapse of the girder. Elastic limit states pertaining to yielding are concerned with the stress within a local region of the girder

29

initially exceeding the yield strength of the girder steel, such as at the yield moment, M_y

(see Figure 3.3.4a). Elastic limit states pertaining to buckling are concerned with local or

global buckling of the girder when the stresses remain below the yield strength of the

girder steel. Conversely, ultimate failure modes pertain to the complete exhaustion of

strength of the girder which may lead directly to collapse, such as at the plastic moment,

M_p, in which a plastic hinge is formed (see Figure 3.3.4b). Elastic limit states are

nevertheless important because their occurrence may eventually lead to the onset of an

ultimate failure mode (Bowman, 2002, 2004; Chajes et al., 2005; Kirke & Al-Jamel,

2004; Lichtenstein, 1990; Minor & Woodward, 1996; Stockfish, 2011; Wardhana &

Hadipriono, 2003; Zhou & Biegalski, 2010).
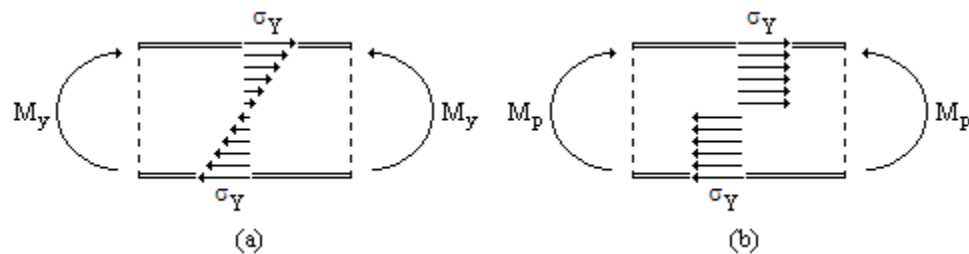
Figure 3.3.4: (a) Uncracked girder showing bending stress distribution at the yield moment, M_y, with the extreme outer fibers of the girder reaching the yield strength, and (b) uncracked girder showing bending stress distribution at the plastic moment, M_p, with the entire cross-section reaching the yield strength.

3.3.1.3 Flange Local Yielding

The elastic limit state of flange local yielding as influenced by fatigue cracks is

related to plate girders loaded under predominantly bending. The presence of a vertical

crack in the web plate may serve to locally increase the bending stress in the compression

flange, thereby precipitating premature yielding of the compression flange in the region

directly above the crack (see Figure 3.3.5). The normal bending stress field within the

girder as influenced by the crack, and the flange local yielding capacity, may be analyzed using the theory of elasticity (see Appendix D: Theory of Elasticity).
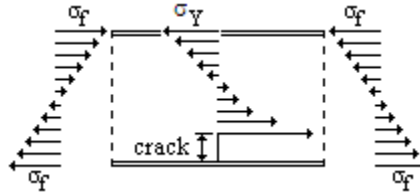
Figure 3.3.5: Local increase of bending stress in compression flange directly above the crack in the web.

3.3.1.4 Section Yielding

The limit state of section yielding as affected by fatigue cracks is concerned with plate girders loaded under predominantly shear. In an uncracked girder, the limit state of section yielding occurs when the shear stresses acting throughout the gross cross-section of the web plate exceed the shear yield strength nearly simultaneously, resulting in yielding of the entire cross-section (see Figure 3.3.6a). The shear force corresponding to yielding of the cross-section is the beam action shear strength. The presence of a diagonal or vertical crack in the web plate serves to reduce the gross cross-sectional area of the web plate. The shear stress field along the cross-section above the crack exceeds the shear yield strength at lower magnitudes of external shear force, thus serving to reduce the beam action shear strength of the girder (see Figure 3.3.6b). The shear stress field within the girder as affected by the crack, and the section yielding capacity, may be analyzed using the theory of elasticity (see Appendix D: Theory of Elasticity).

31
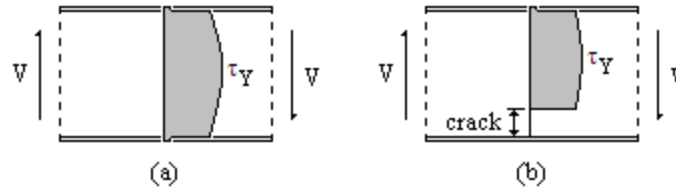
Figure 3.3.6: (a) Uncracked girder displaying the shear stress distribution in a state of shear yielding, and (b) vertically-cracked girder displaying the shear stress distribution above the crack in a state of shear yielding.

3.3.1.5 Elastic Flange Local Buckling

The limit state of elastic flange local buckling as influenced by fatigue cracks pertains to plate girders loaded under predominantly bending. Elastic buckling refers to the advent of buckling in the flange with the stresses within the flange remaining below the steel yield strength. The presence of a crack in the tension flange may induce local transverse compressive stresses adjacent to the crack which may in turn lead to so-called tension buckling (see Figure 3.3.7a). Tension buckling results in the wrinkling of the flange steel in the immediate region around the crack. The local transverse compressive stresses in the tension flange stems as influenced by the crack may be analyzed using the theory of elasticity (see Appendix D: Theory of Elasticity). The associated tension buckling capacity may be approximately analyzed using the Rayleigh-Ritz energy method (see Appendix E: Principle of Stationary Potential Energy).

Alternatively, the presence of a vertical crack in the web plate may serve to locally increase the bending stress in the compression flange, thereby leading to premature elastic buckling of the compression flange stems (see Figure 3.3.7b). The bending stress in the compression flange as influenced by the vertical crack in the web plate may be analyzed using the theory of elasticity (see Appendix D: Theory of

32

Elasticity). The associated elastic flange local buckling capacity may be analyzed using classical plate theory (see Appendix F: Classical Plate Theory).
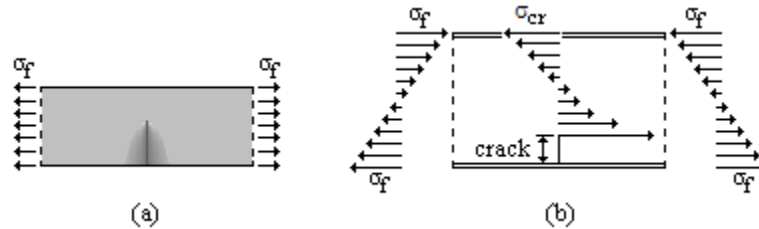
Figure 3.3.7: (a) Plan view of a single tension flange containing an edge-crack with transverse compressive stresses adjacent to the crack, and (b) vertically-cracked girder showing the local increase of bending stress in the compression flange directly above the crack in the web.

3.3.1.6 Elastic Web Local Buckling

The limit state of elastic web local buckling as influenced by fatigue cracks is related to plate girders loaded under predominantly bending or shear. For a plate girder loaded under predominantly bending, the presence of a vertical crack in the tensile region of the web plate may induce local compressive stresses near the crack (see Appendix D: Theory of Elasticity) which may in turn induce tension buckling (see Appendix E: Principle of Stationary Potential Energy) (see Figure 3.3.8). Alternatively, the presence of the vertical crack may locally increase the stress distribution in the compressive region of the web (see Appendix D: Theory of Elasticity), thereby influencing the web local buckling capacity (see Appendix E: Principle of Stationary Potential Energy).
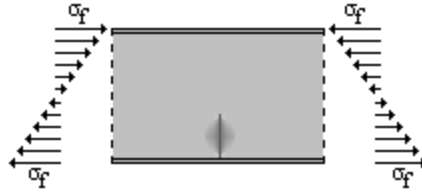
Figure 3.3.8: Profile view of a girder containing an edge-crack in the web with transverse compressive stresses adjacent to the crack.

For a plate girder loaded under predominantly shear, the presence of a diagonal or vertical crack may adversely influence the shear stress field within a web panel (see Appendix D: Theory of Elasticity), thereby precipitating premature buckling of the web panel (see Appendix E: Principle of Stationary Potential Energy).

3.3.1.7 Brittle Fracture

The limit state of brittle fracture concerns plate girders loaded under predominantly bending or shear. For a plate girder loaded under predominantly bending, the growth of a fatigue crack in the web plate or tension flange is driven by opening-mode loading (Mode I). For a plate girder loaded under predominantly shear, the growth of a diagonal crack in the web plate is driven by a combination of Mode I loading and sliding-mode loading (Mode II). The stress intensity factors for both of these cases are inherently coupled to the far-field stress driving the crack growth. Brittle fracture occurs when the stress intensity factor at the crack tip equals or exceeds the fracture toughness of the girder steel. The stress intensity factor and the brittle fracture capacity may be analyzed using LEFM (see Appendix G: Linear Elastic Fracture Mechanics).

3.3.1.8 Impending Ductile Failure

The limit state of impending ductile failure is related to plate girders loaded under predominantly bending or shear. The fracture toughness characterization holds true as long as the plastic region at the crack tip remains small, as is the case for brittle materials and ductile materials under low levels of stress (see Figure 3.3.9) (Meguid, 1989, sec. 3.5.2). Brittle materials have low fracture toughness and thus the plastic region always remains small up until fracture. Conversely, ductile materials have high fracture toughness and the plastic region may become quite large prior failure. The presence of a large plastic region invalidates the fracture toughness characterization for ductile materials, and the impending ductile failure must be described using elasto-plastic fracture mechanics (EPFM) (Meguid, 1989, ch. 6; Rolf & Barsom, 1977, ch. 16).
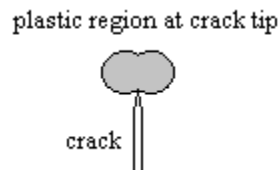
Figure 3.3.9: Plastic region at crack tip.

The impending ductile failure limit state may be postulated to correspond to a critical plastic region size indicating the approximate transition to a ductile failure mode (i.e., the transition from LEFM to EPFM). Converting the Westergaard stress function given by (G.2.1) to polar coordinates and substituting the result into (G.1.3) results in the stress field near the crack tip expressed in terms of K_I (Sun & Jin, 2012, sec. 3.4)

$$\sigma_x = \frac{K_I}{\sqrt{2\pi r}} \cos\frac{\theta}{2} \left(1 - \sin\frac{\theta}{2}\sin\frac{3\theta}{2}\right)$$

$$\sigma_y = \frac{K_I}{\sqrt{2\pi r}} \cos\frac{\theta}{2} \left(1 + \sin\frac{\theta}{2}\sin\frac{3\theta}{2}\right) \qquad (3.3.3)$$

$$\tau_{xy} = \frac{K_I}{\sqrt{2\pi r}} \sin\frac{\theta}{2} \cos\frac{\theta}{2}\cos\frac{3\theta}{2}$$

where r is the radius with respect to the crack tip and θ is the angle of the radius with respect to the longitudinal direction of the crack. The size and shape of the plastic region at the crack tip may be predicted using (3.3.3) in conjunction with the Mises yield criterion (Meguid, 1989, sec. 5.4).

3.3.1.9 Fatigue Life

The plate girder fatigue life is defined as the number of load cycles that a girder is capable of resisting prior to the occurrence of a governing limit state. The elastic capacity of a fatigue-cracked girder is in part directly dependent upon the crack length. The incremental extension of the crack length with each load cycle implies that a governing limit state may occur when the crack length achieves a critical value. Similarly, a governing limit may occur when the number of load cycles achieves a critical value, which is the fatigue life. The propagation of the crack with each load cycle may be predicted using an empirical crack growth law (see Appendix H: Empirical Crack Growth Law).

3.3.2 Numerical Analysis

The influence of fatigue crack growth on the elastic strength and fatigue life of steel plate girders may alternatively be analyzed with the finite element method (FEM, or

FEA for finite element analysis). In FEM, a structure is discretized into individual elements and the equilibrium equations are subsequently derived. The approximate stress, strain, and displacement fields are therein solved for using the constitutive equations, compatibility equations, and strain-displacement relations. FEM is in contrast to analytical methods in which the stress, strain, and displacement fields are directly derived considering the structure as a continuum (see Appendix D: Theory of Elasticity).

In FEM, the equilibrium equations may be formulated either directly or with energy methods. There are two methods for directly deriving the equilibrium equations including the direct stiffness method (DSM) and the force method (Hibbeler, 2006, sec. 10.1; McGuire, Gallagher, & Ziemian, 2000). In these two methods, matrix structural analysis is employed to assemble local stiffness or flexibility matrices considering the local geometric and material properties of each individual element. Global stiffness or flexibility matrices are then assembled and the equilibrium equations are therein formulated. The approximate displacement field or force field is finally formulated considering the external boundary conditions. DSM and the force method are typically used for analyzing indeterminate lattice-like structures such as building frames or trusses, in which the elements are the individual beams or truss members (McGuire et al., 2000).

Alternatively, the equilibrium equations may be derived using the Rayleigh-Ritz energy method (see Appendix E: Principle of Stationary Potential Energy), which is essentially identical to the principle of virtual work. The internal virtual strain energy, or variation of internal strain energy, of a structure is set equal to the external virtual work, or variation of external work. The displacements within each element (beam, plate, etc.) are therein described by a shape function subject to variation. The variation of potential

energy of the entire system of elements is then minimized, therein forming the equilibrium equations and allowing for the approximate displacement field to be solved for. The stress and strain fields are finally solved for using the constitutive equations, compatibility equations, and strain-displacement relations.

3.3.3   Code-based Design

I-shaped transversely stiffened steel plate girders are designed in accordance with the AASHTO *LRFD Bridge Design Specifications* (2010). As previously mentioned, highway bridge girders are designed for various limit states assuming that they will always remain uncracked. The procedure for obtaining load cases and combinations, and designing for the strength limit state and the fatigue and fracture limit state, is briefly outlined in Appendix A: AASHTO LRFD Bridge Design Specifications.

4   Literature Review

4.1   Overview

A comprehensive literature review is presented to give an overall view of former research relating to the effects of fatigue crack growth on the elastic bending moment and shear force limit states of steel highway bridge plate girders. Former research works concerning the static and fatigue testing of full-scale and small-scale plate girders are first reviewed. Next, research works regarding the residual strength and stability of cracked plate-like structures are reviewed. Also, research investigations pertaining to the residual strength and stability of beam-like structures containing cracks and intentional discontinuities are reviewed. Finally, a synopsis of the literature review is given.

4.2   Research Works

4.2.1   Static Testing of Plate Girders

The theoretical mechanisms by which uncracked plate girders and beam-like structures carry load had been understood ever since the developments of beam theory, elasticity theory, and classical plate theory in the 17th, 18th, and 19th centuries (Love, 1892; Timoshenko, 1983; Timoshenko & Woinowsky-Krieger, 1959; Todhunter, 1886, 1893; Ventsel & Krauthammer, 2001). Numerous experimental and analytical studies initiated in the early to mid 20th century investigated the load carrying behavior of plate girders including the post-buckling behavior and the influence of stiffener plates (Basler, 1961; Basler, Bung-Tseng, Mueller, & Thurlimann, 1960a, b, c, d; Basler & Thurlimann, 1960a, b; D'Apice & Cooper, 1965; Fujii, 1968; Herzog, 1974; Kuhn, 1940; Lee & Yoo,

1998; Moore, 1942; Rockey, 1956; Salmon et al., 2009, ch. 11; Smith, Bradford, & Oehlers, 1999; Sparkes, 1947; Wagner, 1931), the interaction between bending moment and shear force effects (Basler, 1961; Basler et al., 1960d; Herzog, 1974; Liang, Uy, Bradford, & Ronagh, 2005; Salmon et al., 2009, sec. 11.9), and composite action (Baskar, Shanmugam, & Thevendran, 2002; Brendel, 1964; Chen, Aref, Ahn, Chiewanichakorn, Carpenter, Nottis, & Kalpakidis, 2005; Grant, Fisher, & Slutter, 1977; Heins & Fan, 1976; Liang, Uy, Bradford, & Ronagh, 2005; Nassif & Salama, 2011; Salmon et al., 2009, ch. 16; Slutter & Dricoll, 1963; Viest, 1960, 1974). The general experimental setups of the tests involved statically loading small-scale or full-scale plate girders under three-point or four-point loading. Wheatstone strain gauges and vertically aligned dial gauges were then employed to measure the strains and displacements, respectively. The findings of some of these studies were later adopted by the AASHTO bridge design specifications (AASHTO, 2010; Liang et al., 2005).

For experimental tests of girders loaded under predominantly bending, the resulting normal bending stress distributions along the depth of the girder sections were found to generally comply with the linearly varying triangular bending stress distribution derived from beam theory (Basler et al., 1960b; Basler & Thurlimann, 1960a; Salmon et al., 2009, sec. 11.4). For tests of girders loaded under predominantly shear, the web plate was found to resist most of the shear stresses as predicted from beam theory (Basler et al., 1960c; Basler & Thurlimann, 1960b; Salmon et al., 2009, sec. 11.7). Transverse stiffener plates were found to contribute additional shear strength by way of so-called tension field action (Fujii, 1968; Lee & Yoo, 1998; Salmon et al., 2009, sec. 11.8; Wagner, 1931). Tension field action was determined to predominate especially upon buckling or yielding

40

of the web plate, thereby greatly contributing to the post-buckling shear strength of transversely stiffened plate girders. For tests of girders loaded under combined bending and shear, it was found that the interaction between the bending moment and shear force is generally minimal (Basler et al., 1960c; Basler & Thurlimann, 1960b, Salmon et al., 2009, sec. 11.9). Nonetheless, interaction expressions have been devised (Basler, 1961; Basler et al., 1960d; Herzog, 1974).

4.2.1.1 Research Works

A major step toward a theory describing the post-buckling behavior of stiffened plate girders was made by Wagner (1931) in which a theory of a thin web plate resisting shear by pure diagonal tension field action was put forth. The theory postulated that the stresses within a thin web plate under shear loading transform into a state of pure diagonal tension, and that the flange plate rigidities have an effect on the magnitude of the tension field. Specifically, an increase in the flange rigidities results in a decrease in the tension field magnitude. The theory necessarily neglected the beam action shear resistance and in-plane bending resistance of the web plate. Kuhn (1940) suggested that the theory by Wagner (1931) was too conservative in that a state of pure diagonal tension field action is never truly achieved due to the persistent effects of beam action shear resistance. A semi empirical theory was hence put forth describing a so-called incomplete diagonal tension field (Kuhn, 1940).

Experimental tests such as those carried out by Moore (1942), Rockey (1956), and Sparkes (1947) investigated the effects of stiffener plates on the static load carrying behavior of plate girders (Hall & Stallmeyer, 1964). Specifically, the effects of the

41

spacings and rigidities of transverse stiffener plates on the buckling behavior of web panels were analyzed. The tests collectively demonstrated that transverse stiffener plates, which were presumed to effectively divide the web plate into distinct panels, serve to increase the local buckling capacity of the web. It was also confirmed that stiffener plates perform an important role in the distribution of stresses in the web plate, especially in the formation of diagonal tension fields.

Comprehensive experimental tests on full-scale transversely stiffened plate girders were carried out at Lehigh University from 1957 to 1961 by Basler et al. (1960a, 1960b, 1960c, 1960d) for the purpose of investigating the ultimate strength of plate girders. The theoretical aspects of the tests were put forth by Basler & Thurlimann (1960a, 1960b) and Basler (1961), and an overall summary of the experimental and theoretical results were presented by Yen & Basler (1962). Ultimate load tests were conducted on a total of thirteen full-scale girders of which five were tested under bending, two under shear, and six under combined bending and shear (Basler et al., 1960a). The girders tested under bending and under shear utilized cover plates to thicken the cross-sections along the end regions of their lengths for the purpose of concentrating the stresses in the test sections at mid-span. The girders tested under combined bending and shear had prismatic cross-sections. All of the girders were fabricated from mild steel. Tension test coupons were obtained from the flange and web plates, of which the tested yield strength was found to range from *33 ksi* to *45.7 ksi*.

For the girders subjected to bending, it was found that the compression stresses in the flange were slightly greater than the stresses predicted from beam theory (Basler et al., 1960b). Furthermore, the compression stresses in the web were slightly different from

the stresses predicted from beam theory. These phenomena were attributed to a redistribution of stresses from the web plate to the compression flange, and suggested that the flange plates are primarily responsible for the bending resistance of girders. It was shown that flange local yielding or flange local buckling may occur due to the stress redistribution. Overall, it was concluded that the compression flange fails by way of local buckling in most cases, thus controlling the overall bending moment capacity. A limiting width-to-thickness ratio for the flange plate and a limiting depth-to-thickness ratio for the web plate were derived to prevent vertical buckling of the compression flange (Basler & Thurlimann, 1960a). Additionally, allowable stress formulas were derived to prevent lateral and torsional buckling of the compression flange while taking into account the stress redistribution from the web to the flange.

The girders subjected to shear demonstrated that tension field action in the web plate and presumed compression in the transverse stiffener plates only occurs after the advent of web local buckling (Basler et al., 1960c). This phenomenon was shown to be analogous to the load distribution in a loaded Pratt truss in which the diagonal struts are in tension and the vertical struts are in compression. In the case of the girders, the transverse stiffener plates act as the vertical compression struts and the diagonal tension fields in the web plate act as the diagonal tension struts. As previously implied by Kuhn (1940), it was concluded that the total shear capacity of a web panel is derived from both beam action and tension field action. The post-buckling behavior of plate girders was hence understood to adhere by the following process: a girder initially resists shear primarily through beam action until the advent of web local buckling, at which point the girder transitions to resist shear primarily through tension field action. The girder then

fails by way of the diagonal tension fields causing yielding in the web panel. The tension field action was thus shown to be the post-buckling shear resistance of girders. It was found, however, that if the depth-to-thickness ratio of the web plate is low enough, the beam action shear resistance is sustained until web local yielding, and the tension field action shear resistance does not occur. Ultimate shear load and allowable shear stress formulas were derived which took into account both the beam action shear strength and tension field action shear strength. In contrast to the method of Wagner (1931), the contribution of flange plate rigidity to the tension field action shear strength was neglected. Formulas were also developed for the sizing and spacing of transverse stiffeners. In general, it was confirmed that the shear capacity of a girder is dependent upon the web plate and transverse stiffener plates.

The girders subjected to combined bending and shear demonstrated a redistribution of compression stresses from the web to the compression flange, presumed compression stresses in the transverse stiffener plates, and beam action and tension field action in the web (Basler et al., 1960d). Interaction formulas and corresponding interaction curves were developed for combined bending and shear (Basler, 1961). A limit was established such that the interaction of the bending stresses and shear stresses may be neglected so long as the bending stresses and shear stresses do not exceed *75%* and *60%* of the their allowable values, respectively.

Fujii (1968) later recognized some errors in the post-buckling shear strength theory put forth by Basler & Thurlimann (1960b). First, it was shown that the contribution of flange plate rigidity should in fact be considered in the calculation of tension field action shear resistance as originally postulated by Wagner (1931). Tension

field action evidently induces additional compressive stresses in the compression flange which has an effect on the angle of the diagonal tension fields. Secondly, it was shown that the shear resistance of the transverse stiffener plates should also be taken into account in the calculation of tension field action shear resistance. Lastly, it was shown that the interaction curves for combined bending and shear should take into account the compressive stresses in the compression flange from tension field action, in addition to the compressive stresses from bending. Modified formulas for the ultimate shear capacity of plate girders were developed by taking into account the aforesaid corrections. Results from the modified formulas were shown to be in good agreement with the experimental results from the shear capacity tests by Basler et al. (1960c).

Most of the test girders used in previous research investigated the effects of transverse stiffener plates. D'Apice & Cooper (1965) investigated the effects of longitudinal stiffener plates on the static bending capacity of full-scale plate girders. Specifically, the effects of longitudinal stiffener plates on web local buckling, the post-buckling strength of web panels, and the out-of-plane deflection of web panels were scrutinized. Four girders were fabricated with both longitudinal and transverse stiffener plates, and one girder was fabricated with only transverse stiffener plates. Each girder was subjected to four-point loading using Amsler hydraulic jacks. The strain distribution in the web was obtained from a vertical series of strain gauges located along the center line of the test web panel at mid-span. The out-of-plane web deflection was measured using a series of vertically aligned dial gauges positioned along the test panel. Results from the tests indicated that the longitudinal stiffener plates had no apparent effect in increasing the ultimate load capacity of the girders. The redistribution of compression

stresses from the web plate to the compression flange as observed in the tests on transversely stiffened girders by Basler et al. (1960b) did not occur until after the longitudinal stiffener plate buckled. Instead, the longitudinal stiffener plate assisted in maintaining a linear strain distribution as predicted from beam theory. The longitudinal stiffener plates also served to greatly reduce out-of-plane web deflections and assisted in limiting the occurrence of vertical flange buckling, such that the ultimate load of each longitudinally stiffened girder was achieved by way of the compression flange yielding. These results were in contrast to the conclusions made by Basler & Thurlimann (1960a) in which the compression flanges in transversely stiffened girders were predicted to fail primarily by way of buckling. This suggests that the geometrical requirements for the compression flange and web plate put forth by Basler & Thurlimann (1960a) may be relaxed with the presence of longitudinal stiffener plates.

Herzog (1974) derived simplified formulas for the ultimate static strength of symmetrical and unsymmetrical, homogeneous and hybrid, unstiffened and stiffened plate girders in shear, bending, and combined shear and bending. Formulas were also introduced for calculating the flange yield moment and the web yield shear force, and correction factors were introduced for the prevention of local buckling. It was shown that the shear strength of plate girders is essentially unaffected by simultaneous bending as long as the bending moment is lower than that to cause flange local yielding. Similarly, it was shown that the bending capacity of plate girders is essentially unaffected by simultaneous shear as long as the shear force is lower than that to cause web local yielding. Results from the formulas were compared to several hundred tests conducted throughout the world and were deemed to be adequate for general design purposes.

The previously discussed studies had focused purely on the static load carrying behavior of plate girders without considering the effects of composite action with a concrete slab. Composite steel-concrete construction was first employed in the early 1900s in the form of concrete-encased steel beams (Taly, 1998, sec. 8.5.2). This form of composite action is developed purely by the natural bond and friction between the steel and concrete. However, these early designs did not necessarily take into account the effects of composite action and may have resulted in overly conservative designs (Salmon et al., 2009, sec. 16.1). In the 1930s, the development and use of shear stud connectors in composite construction became widespread, culminating in the approval of composite steel-concrete construction in highway bridge design in the 1944 AASHO *Standard Specifications* (Taly, 1998, p. 728).

Numerous texts provide a historical background and detailed discussion on the load carrying behavior of composite steel-concrete construction, such as by Barker & Puckett (1997, sec. 8.9), Salmon et al. (2009, ch. 16), and Taly (1998, sec. 8.5). A comprehensive review of research relating to composite steel-concrete construction is provided by Viest (1974, 1960) (Salmon et al., 2009, pp. 805-806). The analysis of the effective slab width has especially been the subject of many studies. This concept originated with theoretical work by von Karman in 1923 with later analytical and experimental developments by many others such as Metzer in 1929 and Timoshenko & Goodier (1951) (Nassif & Salama, 2011; Taly, 1998, p. 729). Brendel (1964) reported comparisons between theoretical formulas for determining the effective slab width with test results on T-beams and various code-based requirements. Heins & Fan (1976) later developed two empirical equations for calculating the effective slab width by using finite

difference methods to approximate the deformations of numerous composite slab-girder bridges.

A recent report for the National Cooperative Highway Research Program by Chen et al. (2005) provides recommendations for the determination of the effective slab width based on a comprehensive review of research findings. These recommendations were incorporated into the *LRFD Specifications* (2010, sec. 4.6.2.6). Nassif & Salama (2011) further investigated this matter by comparing experimental results from tests on *8* composite steel-concrete beam specimens with results from finite element models of composite steel-concrete beams. The results were also compared to code-based requirements. The finite element results correlated well with the experimental results, and it was found that the number of shear stud connectors is directly related to the effective slab width. Namely, the effective slab width increases with the number of connectors. Furthermore, it was concluded that the code-based provisions are generally overly conservative.

Many static loading tests on composite steel-concrete girders have been conducted, such as the tests by Slutter & Dricoll (1963) on twelve full-scale composite beams. Most of the beams utilized mechanical shear connectors to induce composite action. Two beams were fabricated without shear connectors and relied upon the natural bond between the steel top flange and concrete for composite action. Additionally, a series of pushout tests were conducted on nine slab-beam specimens in which the connectors were directly tested under shear by pulling the slab and beam in opposite directions. The tests confirmed that the use of an adequate number of shear connectors allow composite beams to attain the theoretical ultimate bending moment capacity

regardless of connector spacing. Grant, Fisher, & Slutter (1977) later summarized results from numerous tests on composite beams utilizing lightweight concrete cast upon cold-formed ribbed steel decking. It was found that the rib depth has much more influence than the rib slope on the ultimate bending moment capacity. An empirical expression was developed for the strength of shear stud connectors in the ribs of steel decking. Expressions were also developed for the effective moment of inertia and section modulus for use in calculating deflections and stresses.

More recently, Baskar et al. (2002) developed a finite element model of a composite steel-concrete girder which produced comparable results to experimental tests in the elastic and plastic region. Liang et al. (2005) also conducted numerical analyses of composite beams and developed an expression for the shear strength as well as an interaction formula for combined bending and shear. These two expressions consider the shear strength of the overall composite section.

By the mid 1970s, knowledge concerning the post-buckling behavior of stiffened plate girders had advanced to the point where a complete set of theories describing the mechanisms by which plate girders carry load had largely been achieved. The research by Basler et al. (1960a, 1960b, 1960c, 1960d), Basler & Thurlimann (1960a, 1960b), Basler (1961), Fujii (1968), and many others concerning the post-buckling strength, interaction between bending and shear, and composite action of stiffened plate girders, led to provisions which were adopted by the AISC and AASHTO specifications (Cooper & Roychowdhury, 1990).

4.2.2 Fatigue Testing of Plate Girders

Fatigue loading tests on small-scale and full-scale plate girders have been conducted at the University of Illinois (Goodpasture & Stallmeyer, 1967; Hall & Stallmeyer, 1964; Kouba & Stallmeyer, 1959), Lehigh University (Marek et al., 1970; Mueller & Yen, 1967; Yen, 1963; Yen & Mueller, 1966), and elsewhere (Crocetti, 2003; Davies et al., 1994; Roberts et al., 1995). In general, small-scale or full-scale plate girders were arranged under three-point or four-point loading configurations and cyclically loaded using electro-hydraulic fatigue testing machines. These studies found that fatigue cracks in stiffened plate girders subjected to sub-critical cyclic loading initiate at the base of the fillet welds connecting the web plate to the flange or transverse stiffener plates. Specifically, the cracks form at locations of discontinuity such as at the ends of weld lines, and at imperfections due to porosity and incomplete fusion.

The cracks may propagate along the weld boundaries (Crocetti, 2003; Davies et al., 1994; Goodpasture & Stallmeyer, 1967; Hall & Stallmeyer, 1964; Mueller & Yen, 1967; Roberts et al., 1995; Yen, 1963; Yen & Mueller, 1966), through the web panels (Crocetti, 2003; Hall & Stallmeyer, 1964; Kouba & Stallmeyer, 1959; Yen, 1963), and through the flange plates (Kouba & Stallmeyer, 1959; Marek et al., 1970), in areas under both tension and compression stresses. The cracks initiate as surface cracks and propagate short distances before becoming through-thickness cracks (Osman & Roberts, 1999). It was generally concluded that the cracks are initiated by a combination of residual stresses, in-plane tensile membrane stresses, and out-of-plane bending stresses due to so-called plate breathing. More recent studies have investigated the influence of plate breathing on the fatigue behavior of plate girders (Davies & Roberts, 1996; Davies

et al., 1994; Roberts et al., 1995). Some fatigue crack classification schemes have been devised (Maeda & Okura, 1983; Roberts & Davies, 2002).

4.2.2.1 Research Works

Early testing of girders under fatigue loading was conducted by Kouba & Stallmeyer (1959) at the University of Illinois. A series of small-scale plate girders were tested using various arrangements of transverse stiffeners and weld patterns. A Wilson lever-type fatigue machine was used to produce two concentrated fatigue loads at the mid-span of each test girder. Through-thickness fatigue cracks were observed to initiate in both the web plate and the flange plates, and in areas of the girder under tension stresses and compression stresses. It was concluded that the configuration of transverse stiffener plates did not have any apparent effect on where the fatigue cracks initiated. In general, the fatigue cracks were observed to initiate along the web panel boundaries at locations of discontinuity such as at the toe of the fillet welds connecting the web plate to the flange or stiffener plates, or at the end of a weld line. Fatigue cracks in the flange generally propagated in a straight line perpendicular to the web, and cracks in the web propagated diagonally towards the centerline of the girder.

Whereas the tests by Kouba & Stallmeyer (1959) were somewhat general, fatigue loading tests conducted at Lehigh University by Yen (1963) on two full-scale stiffened plate girders sought to investigate the actual sources of fatigue crack initiation and growth. The girders were tested under predominantly shear loading at *250* cycles per minute and endured hundreds of thousands of load cycles before any fatigue cracks were

observed. The web panels were observed to laterally deflect under repeated loading which produced out-of-plane plate bending stresses, also known as secondary stresses.

The fatigue cracks generally initiated as surface cracks on the tension side of the web panel boundaries, and slowly propagated along the weld boundaries or into the web plate before becoming through-thickness cracks. Overall, it was concluded that the combination of residual stresses, membrane stresses, and out-of-plane bending stresses in the web plate are responsible for the formation and propagation of fatigue cracks. The bending resistance of plate girders is presumably unaffected by the growth of fatigue cracks in the web panels since the flanges are primarily responsible for this task. The shear resistance may ultimately be affected if the length of the crack becomes long enough as to affect beam action or tension field action shear resistance. However, it was found that the formation of fatigue cracks did not result in the immediate loss of girder strength. The reason given was that the cracks were mainly formed due to secondary stresses and not primary stresses. It was thus concluded that plate girders have a significant post-cracking fatigue life.

Further fatigue loading tests at the University of Illinois were conducted by Hall & Stallmeyer (1964) on small-scale thin-web plate girders. The focus of the tests was to investigate the fatigue behavior of the web panels. Specifically, the effects of flange rigidity, transverse stiffener plate rigidity, and load type were investigated. The test girders were subjected to two different loading schemes including pure shear and a combination of shear and bending. As with the tests by Kouba & Stallmeyer (1959), fatigue loading was applied with a Wilson lever-type fatigue machine. The resulting stresses were measured with strain gauge rosettes and the out-of-plane deflections of the

web panels were measured with a series of dial gauges. Fatigue failure was assumed to occur when observed through-thickness fatigue cracks attained a length of approximately *3* in.

The fatigue cracks were observed to initiate on the tension side of the web panel boundaries undergoing plate bending, and propagate along the weld boundary or into the web itself. The fatigue cracks initiated as surface cracks and propagated short distances before become through-thickness cracks. For the case of the test girders loaded under combined shear and bending, the fatigue cracks generally propagated approximately 1 in. before becoming through-thickness cracks. The propagation of fatigue cracks through the thickness of the web plate was not discussed in detail. The fatigue cracks were concluded to have been caused by a combination of residual stresses, membrane stresses, and out-of-plane bending stresses in the web panels. These conclusions were generally in agreement with earlier observations made by Yen (1963). Furthermore, it was concluded that the rigidities of the flange and transverse stiffener plates, as well as the initial deflection pattern of the web plate, greatly influence the fatigue behavior of the web panels. Specifically, an increase in flange rigidity was correlated with an increase in fatigue life. A correlation between increased transverse stiffener plate rigidity and an increase in fatigue life was less complete, although this trend was generally accepted to be true. The initial web plate deflections, or web distortions, were concluded to have both beneficial and detrimental effects on the fatigue life. Namely, it was thought to be possible for the initial web distortions to either decrease the out-of-plane web panel stresses or to increase the web panel membrane stresses at the web panel boundaries.

Goodpasture & Stallmeyer (1967) conducted fatigue loading tests on small-scale girders for the purpose of investigating the effects of longitudinal stiffener plates and initial web distortions on the fatigue behavior of the web panels. The tests were performed in the same manner as the tests by Hall & Stallmeyer (1964). Static loading tests were also performed on the same girders. The longitudinal stiffener plates were proportioned according to requirements by Massonnet (1948) to be rigid enough in order to prevent buckling with the web plate (Goodpasture & Stallmeyer, 1967, sec. 2.3). As with the tests by Hall & Stallmeyer (1964), fatigue failure was assumed to occur when observed through-thickness fatigue cracks attained a length of approximately 3 in. It was found that the longitudinal stiffener plates served to effectively divide the web panels into smaller sub panels which had the effect of nearly eliminating out-of-plane deflections of the overall web panel. Additionally, it was concluded that the longitudinal stiffener plates did not increase the static load carrying capacity unless the stiffeners were uneconomically rigid, which confirmed the findings by D'Apice & Cooper (1965).

The girders fabricated with initial web distortions behaved as if web local buckling had already occurred. The post-buckling theory by Basler & Thurlimann (1960b) and Fujii (1968) would suggest that the shear strength was carried primarily by tension field action in these girders, which would affect the membrane stresses at the web panel boundaries. Indeed, all of the fatigue cracks were observed to form and propagate along the web panel boundaries, and was attributed to a combination of residual stresses, membrane stresses, and out-of-plane stresses, which further confirmed the conclusions of Hall & Stallmeyer (1964) and Yen (1963). The formation of fatigue cracks in the web panels had no apparent effect on the static girder strength unless the cracks had formed in

the tension flange, which was in agreement with the conclusion by Yen (1963). It was generally concluded that an increase in the magnitude of initial web distortions results in a decrease of the fatigue life of plate girders. This was in contrast to the conclusion by Hall & Stallmeyer (1964) that initial web distortions could also have a beneficial effect on the fatigue life.

Around the same time, fatigue loading tests on full-scale thin-web plate girders were conducted by Yen & Mueller (1966) and further analyzed by Mueller & Yen (1967). The test girders were subjected to shear effects and combined shear and bending effects. The relation between stresses in the web panels and the initiation and growth of fatigue cracks was investigated. A correlation was found between out-of-plane plate bending stresses along the web panel boundaries and observed fatigue behavior. Specifically, it was concluded that out-of-plane plate bending stresses are primarily responsible for the initiation of fatigue cracks, as previously suggested by Goodpasture & Stallmeyer (1967), Hall & Stallmeyer (1964), and Yen (1963). Importantly, it was confirmed that normal membrane tensile stresses in the web panels also have a role in the formation of fatigue cracks. The fatigue cracks were presumed to initiate where the plate bending stresses were maximum along the web panel boundaries. In web panels subjected to primarily shear stresses, fatigue cracks were observed to form in the tension diagonal corners. In web panels subjected to primarily bending stresses, fatigue cracks were observed to form along the web plate boundaries under plate bending tensile stresses. In all cases, the fatigue cracks initiated and propagated along the web panel boundary.

Only a few of the fatigue cracks in the previously discussed studies propagated into the flange plates, such as in the tests by Kouba & Stallmeyer (1959). During the first phase of an experimental program by Marek et al. (1970), three-ended through-thickness cracks were generated by fatigue loading. The cracks formed at the boundary between the web plate and tension flange and propagated through both sides of the flange plate and up through the web plate.

Maeda & Okura (1984) derived a relation between out-of-plane bending stresses and in-plane bending stresses in a thin-walled web plate. The strength of fatigue cracks was then expressed in terms of the in-plane plane bending stresses. Soon after, Okura & Maeda (1985) examined the relation between of out-of-plane bending stresses and in-plane shear stresses through a finite element analysis. Analyses by Okura, Yen, & Fisher (1993) further examined the effects of out-of-plane bending stresses on the fatigue behavior of thin-walled plate girders.

More recently, Davies et al. (1994) and Roberts et al. (1995) further investigated the effects of out-of-plane bending stresses on the fatigue behavior of web plates. Each set of fatigue loading tests were conducted on fourteen small-scale plate girders. For each test, the plate girders were simply supported and a concentrated fatigue load was applied at mid-span by a servo-controlled dynamic testing machine. Each test girder had double stiffener plates located at mid-span and at each end over the supports. A transducer bar was used to measure out-of-plane displacements of the web. Pairs of strain gauges were placed near the outer boundary of one of the two web panels and used to determine the membrane and out-of-plane stresses.

The strain gauges revealed a complex state of stress near the weld boundaries of the web plate which were generally in agreement with the results by Mueller & Yen (1967). The formation of fatigue cracks occurred in these boundary areas and were attributed to out-of-plane bending stresses and corresponding out-of-plane web deflections, denoted by the new term 'plate breathing'. In-plane membrane stresses were also found to have a role in fatigue crack initiation, as had been previously concluded by Mueller & Yen (1967). A nonlinear finite element analysis was conducted by Davies & Roberts (1996) to determine the range of stresses in areas of potential crack initiation, and the results compared favorably to the test results by Davies et al. (1994).

Crocetti (2003) noted that most of the previous research concerning the investigation of plate breathing did not realistically represent the actual conditions that steel highway bridge plate girders are exposed to. Some of the noted inaccuracies were that the range of fatigue loads applied to the test girders did not represent the actual range of load effects due to traffic and dead load. In reality, the range of traffic load is much more moderate than what was previously assumed. Additionally, previous research assumed a predominance of shear loading instead of combined shear and bending. Actual steel bridge plate girders are commonly continuous over inner supports where transverse stiffener plates are utilized over the supports to prevent web local buckling. Maximum combinations of shear and bending are predominant in this vicinity. Furthermore, a large number of studies used small-scale girders instead of full-scale girders.

In an attempt to reduce these inaccuracies, fatigue loading tests were performed on four identical simply supported full-scale slender plate girders. A servo-controlled dynamic pulsating machine was used to produce concentrated fatigue loading upon the

57

top flange at mid-span. Double transverse stiffener plates were located on each girder directly below the concentrated loading, presumably to replicate the location of a continuous girder over an inner support. A single transverse stiffener plate was located at a quarter-point along each girder, while double transverse stiffener plates were located at the ends of each girder directly above the supports. Transducer bars were used to measure out-of-plane displacements, while numerous pairs of strain gauges were placed on both sides of the web to measure membrane and out-of-plane stresses. All four girders were then tested until failure.

As with the test results from previous related research, it was found that the initiation and growth of fatigue cracks were due to a combination of tensile membrane and out-of-plane stresses in the vicinity of the fillet weld boundaries between the web and flange or stiffener plates. Importantly, it was found that membrane stresses were predominant for small loads, while the out-of-plane stresses were predominant for larger loads. Most of the observed fatigue cracks originated on the web plate at the base of the fillet weld throat in the vicinity of the neutral axis of the girder, and propagated vertically along the weld boundary. Cracks also formed in the web along the weld boundary with the top flange, and propagated horizontally along the weld. It was demonstrated that once the fatigue cracks reached a critical length, the web failed due to shear buckling, which in turn led to the subsequent failure of the girders. The tests also confirmed that the initiation of fatigue cracks in the web near the fillet welds was largely due to imperfections in the weld such as stop/start points, porosity, and incomplete fusion with the web. These imperfections likely produced high concentrations of combined membrane and out-of-plane stresses.

The previously described fatigue loading tests demonstrated that fatigue cracks tend to initiate along the fillet weld boundaries between the web plate and the flange or stiffener plates due to a combination of out-of-plane and in-plane stresses. Maeda & Okura (1983, 1984) classified these cracks into three types. Type 1 cracks initiate on the web plate at the toe of the fillet weld connecting the compression flange. Type 2 cracks initiate on the web plate at the toe of the fillet weld connecting the transverse stiffener plates. Type 3 cracks initiate on the web plate at the toe of the fillet weld connecting the tension flange. The conclusions by Goodpasture & Stallmeyer (1967), Hall & Stallmeyer (1964), Yen (1963), and Yen & Mueller (1966) would suggest that Type 1 cracks are primarily formed by out-of-plane bending stresses, while Type 2 and Type 3 cracks are formed by a combination of out-of-plane bending stresses and normal in-plane tensile stresses.

In contrast to the fatigue crack classifications described by Maeda & Okura (1983, 1984), a more detailed classification scheme was described by Roberts & Davies (2002) due to the availability of more test data. Types 1, 4, 5, and 6 initiate on the web plate at the fillet weld connecting the flange or transverse stiffener plates and propagate along the weld boundary. These crack types are formed due to combinations of in-plane and out-of-plane stresses and are generally in agreement with the characteristics of cracks observed in previous fatigue loading tests. Types 2 and 3 initiate on the web plate below the neutral axis at the fillet weld connecting the tension flange or transverse stiffener plates, and are formed due to primarily in-plane tensile membrane stresses. Type 2 cracks propagate vertically along the fillet weld connecting the web plate to transverse stiffener plates. Type 3 cracks propagate vertically through the web plate from the fillet weld

connecting the web to the tension flange. Fatigue cracks in the flange plates were not classified.

Many other studies have focused on the effects of fatigue loading on the strength of composite steel-concrete girders. Slutter & Fisher (1966) investigated the fatigue strength of shear connectors by performing a series of pushout tests on slab-beam specimens possessing different types of shear connectors. It was found that the applied stress range is the most important variable affecting the shear connector strength. An expression was developed for calculating the spacing between shear connectors while taking into account the stress range. More recently, Yen, Lin, & Lai (1997) conducted static and fatigue loading tests on a total of *44* composite beam specimens. Several local failure modes were observed including the crushing of concrete in the region around the shear connectors, and cracks formed in the slab.

4.2.3   Residual Strength and Stability of Cracked Plate-like Structures

The development of LEFM allowed for the analysis of alternative failure modes including brittle fracture and impending ductile failure (Griffith, 1921; Inglis, 1913; Irwin, 1957). Furthermore, the introduction of the Paris-Erdogan crack growth equation provided a novel approach for predicting the propagation of fatigue cracks (see Appendix H: Empirical Crack Growth Law) (Paris & Erdogan, 1963). Some studies have examined the validity of empirical crack growth laws in plate-like structures (Hertzberg & Nordberg, 1969; Miki, Murakosi, & Sakano, 1987) and beam-like structures (Fisher, 1970; Marek et al., 1970; Osman & Roberts, 1999).

Numerous studies have investigated the effects of through-thickness cracks on the strength and stability of plate-like structures loaded under tension, compression, and shear using analytical, numerical, and experimental methods (Alinia, Hosseinzadeh, & Habashi, 2007a, b, c; Brighenti, 2005a, b, 2009; Brighenti & Carpinteri, 2011; Guz & Dyshel, 2001, 2004; Khedmati, Edalat, & Javidruzi, 2009; Kumar & Paik, 2004; Paik, Kumar, & Lee, 2005; Seifi & Khoda-yari, 2011; Vafai & Estekanchi, 1999). The presence of a crack was generally concluded to reduce the tensile and shear capacity of a plate, with the predominant buckling failure mode attributed to tension buckling. Tension buckling occurs when portions of the plate adjacent to the crack experience buckling due to local compressive stresses induced by the presence of the crack. Conversely, the presence of a crack was found to actually increase the buckling strength of a plate loaded under compression (Brighenti, 2005a, b, 2009; Khedmati et al., 2009). Other potential failure modes of cracked plate-like structures such as yielding and alternative buckling modes have not been directly investigated. However, these other potential failure modes, as well as tension buckling, brittle fracture, and impending ductile failure, may be analyzed using plane elasticity (see Appendix D: Theory of Elasticity).

4.2.3.1 Research Works

The concept of stress intensity at a crack tip by Irwin (1957) and the development of an empirical crack growth law by Paris & Erdogan (1963) provided a new approach for analyzing the propagation of fatigue cracks. Numerous studies such as by Barsom (1973, 1976), Hertzberg & Nordberg (1969), and Miki et al. (1987) have investigated the use of empirical growth laws in steel specimens under constant-amplitude and variable-

amplitude stress fluctuations. The study by Hertzberg & Nordberg (1969) examined fatigue crack propagation in welded plate specimens made of A514 steel. The behavior of fatigue crack growth as influenced by stress intensity range and specimen thickness was investigated. Additionally, the behavior of crack growth across and along weldments was examined. Fatigue crack growth rate curves were recorded for each trial. It was found that the crack propagation was largely dependent upon the range of the stress intensity factor, and independent of specimen thickness for thicknesses of up to *1* in. Furthermore, the fatigue crack growth rate curves showed a mostly linear correlation between growth rate and stress intensity factor range during the specimen fatigue life.

These results confirmed that the Paris-Erdogan equation could be used to predict fatigue crack growth rates in thin plate-like elements made of steel. It was also found that the crack growth rates through the weldments and heat affected zones were significantly lower than the growth rates in the base metals, especially at low stress intensities. It was thought that the residual stresses served to decrease the stress intensity range and thus reduce the growth rate. The growth rates in weldments and heat affected zones were found to converge with the growth rates in base metals at higher stress intensities. Summaries of this study and many others at Lehigh University are provided by Tall (1971).

The tests by Miki et al. (1987) were conducted on compact tension specimens made of SM 58 steel. The specimens were subjected to constant-amplitude and variable-amplitude stress fluctuations. The variable-amplitude stress fluctuations were calibrated to simulate the effects of vehicular live load induced within simply supported steel girders. Residual tensile stresses were generated in each specimen by cutting away a

rectangular strip of the plate and welding it back to the primary specimen such that the weld was oriented perpendicular to the direction of crack growth. An electro-hydraulic servo fatigue testing machine was used to produce the stress fluctuations. Fatigue crack growth was determined by measuring the compliance of the specimen through the use of strain gauges attached to the back of the specimen on the opposite side of the edge crack. Crack growth was also measured using a traveling microscope.

It was found that the Paris-Erdogan equation is valid for constant-amplitude stress fluctuations when the stress intensity factor range exceeds the stress intensity factor range threshold. The fatigue crack growth rate in the vicinity of the threshold region was found to be best expressed by a modified form of the Paris-Erdogan equation originally suggested by Klesnil & Lukas (1972) given by

$$\frac{da}{dN} = C\left(\Delta K^m - \Delta K_{th}^m\right) \qquad (4.2.1)$$

For variable-amplitude stress fluctuations, the mean crack growth rate was obtained and plotted as a function of the corresponding equivalent stress intensity factor range given by

$$\Delta K_{eq} = \left(\frac{\sum \Delta K_i^m N_i}{\sum N_i}\right)^{\frac{1}{m}} \qquad (4.2.2)$$

The Paris-Erdogan equation was found to accurately describe the resulting fatigue crack growth rate, even in the vicinity of the stress intensity range threshold. Hence, it was shown that the mean fatigue crack growth due to variable-amplitude stress fluctuations may be predicted by utilizing the equivalent stress intensity factor range in the Paris-Erdogan equation.

The previously discussed fatigue loading tests on girders, such as by Davies et al. (1994) and Roberts et al. (1995), and on plate specimens such as by Hertzberg & Nordberg (1969) and Miki et al. (1987), had not examined the growth of fatigue cracks through the plate thickness in detail. Osman & Roberts (1999) investigated the propagation of a semi-elliptical surface crack through the thickness of a plate under various stress configurations. Stress intensity factors for a surface crack were derived for use in the Paris-Erdogan equation. It was found that the initial crack depth, aspect ratio, and plate thickness have the most influence in affecting the number of load cycles for a crack to penetrate a plate. It was noted that these parameters and the Paris-Erdogan equation material constants may be difficult to obtain in real structures.

Besides the analytical and experimental analysis of fatigue crack behavior, the influence of crack growth on the static strength of plate girders had been largely passed over up until these two developments. Conclusions by Goodpasture & Stallmeyer (1967) and Yen (1963) suggested that the presence of fatigue cracks does not immediately affect the static girder strength. However, the matter was not investigated in detail. Most of the previously discussed failure modes of plate girders and the literature pertaining to post-buckling girder strength would suggest that the presence of a through-thickness crack may indeed adversely affect the static carrying capacity of plate girders.

Analytical and experimental investigations related to this matter were initiated in the late 1960s and early 1970s. Many studies focused on the effects of through-thickness cracks and openings on the static strength of plate-like structures. Clearly, openings such as holes, slots, or copings are not the same as through-thickness cracks. Nonetheless,

these studies provide invaluable insight for how a through-thickness crack may affect the static carrying capacity of plate-like structures.

Vafai & Estekanchi (1999) performed numerical analyses on cracked plates and shells, and the computed stress distributions in the crack tip area were compared to the stress distributions obtained from LEFM. It was found that the numerical results and theoretical results were in good agreement, and that a refined finite element mesh is required in the crack tip area in order to obtain accurate stress distributions. Furthermore, the presence of a crack in a plate under tension was shown to increase the compressive stresses at the crack center, thus reducing the so-called tension buckling strength.

As pointed out by Brighenti (2009), tension buckling occurs due to transverse compression fields created by the presence of a flaw in a stressed plate. This type of buckling appears as complex wrinkling of the plate. Tension buckling of a plate specimen containing an edge crack was experimentally investigated by Guz & Dyshel (2001) considering clamped and pinned boundary conditions. An empirical expression for the critical tension buckling stress was developed, given by

$$\sigma_{cr} = kE\frac{h^2 b^4}{a_0^6} \tag{4.2.3}$$

where h is the plate thickness, b is the plate width, a is the crack length, and k is an empirical constant. It was found that a clamped plate has a higher buckling strength than a pinned plate, and that the fracture strength of a plate in tension is greater if the plate is unbuckled than if it is buckled.

Guz & Dyshel (2004) later investigated the use of a slightly different critical tension buckling stress, given by

$$P_{cr} = kE\frac{h^2}{a_0^2} \tag{4.2.4}$$

The validity of this expression was compared to experimental tests on various plate specimens possessing different dimensions, materials, and crack configurations. The expression provided reasonable predictions of the tension buckling stress if the empirical constant k was modified for each parameter. Tension buckling is further examined by Friedl, Rammerstorfer, & Fischer (2000) in an uncracked plate and by Shimizu (2007) in a numerical analysis of a stressed plate containing a hole.

In contrast to the previous analytical methods, Kumar & Paik (2004) derived the elastic buckling strength of a cracked plate under compression and shear by discretizing the plate into several plate elements. Hierarchical trigonometric functions satisfying the appropriate boundary conditions were used to derive displacement functions for each plate element. The local stiffness and geometric stiffness matrices of the plate elements were then assembled into global stiffness and geometric stiffness matrices and used to formulate the eigenvalue problem. The resulting buckling loads correlated very well with finite element results. It was found that the analytical and numerical results essentially converged after discretizing the plate into 64 elements.

Paik et al. (2005) later investigated the effects of fatigue cracks on the ultimate strength of a steel plate loaded under uniaxial tension and compression using experimental and numerical methods. An ultimate strength limit state was suggested where ultimate failure is assumed to occur when the stress intensity factor at the crack tip equals or exceeds the fracture toughness. A second ultimate strength limit state was also suggested where the cross-sectional area besides the area removed by the crack is assumed to carry all of the axial stress, with failure occurring upon section yielding. The

experimental and numerical tests were found to correlate well with each other, and clearly demonstrated that the ultimate strength of a plate may be degraded by the presence of a crack. Specifically, the tests confirmed the validity of the second aforementioned ultimate strength limit state for both axial tension and compression.

Brighenti (2005a, b) performed analytical and numerical studies concerning the effects of cracks on the buckling strength of plates under tension or compression. The strengths were recorded in terms of a buckling load multiplier, which is defined as the ratio of the actual applied buckling load and the buckling load of an uncracked plate in compression (Brighenti, 2005a). A theoretical proposal and buckling load multiplier for predicting the buckling strength of stressed plates in tension as effected by cracks was developed. Namely, the portions of the plate adjacent to the crack were modeled as being part of an embedded deep beam under uniform tension loading. The boundary conditions and external stresses on the deep beam were then used to formulate a stress function of the plate. Additionally, a Gauss-like displacement function was assumed for the cracked plate. The resulting buckling strength from the theoretical proposal compared favorably with numerical analyses. It was concluded that cracks always degrade the buckling capacity of plates in tension. Furthermore, the crack length and orientation have a significant role in degrading the tension buckling strength. For plates under axial compression, it was concluded that the effects of cracks are largely dependent upon the plate boundary conditions, and the effects of crack closure have minimal impact on the buckling capacity. It was found that the presence of a crack may either increase or decrease the buckling capacity of plates in compression.

Brighenti (2009) further examined the sensitivity of crack orientation on the failure modes of cracked stressed plates in tension and compression through a series of finite element analyses. The buckling, fracture, and plastic failure modes were considered. The buckling strengths were recorded in terms of buckling load multipliers. In terms of compression buckling, cracks oriented transversely to the loading generally tended to increase the buckling strength, while cracks oriented parallel to the loading tended to decrease the buckling strength. In terms of tension, it was found that cracked plates are more prone to tension buckling than fracture failure. Plastic failure becomes more likely if a crack is oriented parallel to the tension loading. A buckling-plastic collapse function was derived which governed whether buckling or plastic failure occurs.

Khedmati et al. (2009) numerically investigated the elastic buckling strength of cracked plate-like structures under compression while considering the plate aspect ratio and crack length, orientation, and location. Namely, edge cracks and central cracks were considered, and were found to have completely different influences on the buckling strength. The buckling strengths were recorded in terms of the buckling coefficient. Conclusions similar to those of Brighenti (2005a, 2005b, 2009) were found in that cracks perpendicular to the compression loading tend to increase the buckling strength and cracks parallel to the loading degrade the buckling strength.

Seifi & Khoda-yari (2011) experimentally and numerically investigated the effect of a central crack in a plate under compression while considering different combinations of plate aspect ratios and thicknesses, as well as crack lengths and orientations. In contrast to the conclusions by Brighenti (2005a, b, 2009) and Khedmati et al. (2009), it

was found that cracks perpendicular to the compression load serve to decrease the buckling strength of the plate.

Other studies such as those by Alinia et al. (2007a, 2007b, 2007c) and Brighenti & Carpinteri (2011) have focused on the effects of cracks and openings on the shear strength of plate-like structures. Alinia et al. (2007a) examined the effects of through-thickness vertical edge cracks and horizontal cracks on the buckling and post-buckling strength of plates under shear by way of finite element simulations as outlined by Alinia et al. (2007c). The presence of a vertical edge crack reduced the elastic shear buckling strength. The presence of a horizontal crack did not significantly affect the buckling strength if the crack was located near the center of the plate edge. However, the buckling strength was reduced if the horizontal crack began to interfere with the tension fields near the corners of the plate. The theory by Basler & Thurlimann (1960b) would suggest that tension field action was not yet predominant if the plate had not buckled.

The effects of through-thickness central cracks on the buckling and post-buckling strength of plates under shear were also investigated numerically by Alinia et al. (2007b). As may have been expected, the presence of the central crack served to degrade the stiffness and elastic shear buckling strength of the plate. Furthermore, the orientation of the crack was found to have an influence on the buckling strength as had been demonstrated by Brighenti (2005). Small crack sizes were found to have very little influence on the post-buckling plate strength, though this influence increased with crack size.

Brighenti & Carpinteri (2011) recently examined the effects of plate boundary conditions, crack length, and crack orientation on the buckling strength of plates under

69

shear through the use of finite element analyses. The fracture failure mode was also considered. As with previous related research, the buckling strength was expressed in terms of the buckling load multiplier. As may have been expected, the presence of cracks generally degraded the buckling strength. In a similar manner to the method by Brighenti (2009), a buckling-fracture collapse function was derived which governed whether buckling or fracture failure occurs. It was concluded that buckling tends to occur before fracture unless the fracture toughness of the concerned material is very low. This was a similar conclusion to that by Brighenti (2009) concerning cracked plates in tension.

4.2.4   Residual Strength and Stability of Cracked Beam-like Structures

Very few studies have investigated the effects of cracks on the strength and stability of plate girders and beam-like structures (Roberts, Fisher, Irwin, Boyer, Hausammann, Krishna, Morf, & Slockbower, 1977; Roberts, Osman, Skaloud, & Zornerova, 1996). These studies did not provide comprehensive expressions or a clear procedure for determining the bending moment and shear force capacities of plate girders possessing various crack configurations. Furthermore, the fatigue and fracture requirements of the AASHTO bridge design specifications consider only the stress range induced within plate girder elements, and the stress intensity and the reduction in stability of plate girder elements due to the presence of cracks are not directly taken into account (AASHTO, 2010).

An abundance of studies have focused upon the effects of openings on the strength and stability of these structures (Bedair, 2011; Cheng & Yura, 1986; Cooper & Roychowdhury, 1990; Hagen & Larsen, 2009; Hagen, Larsen, & Aalberg, 2009; Ito,

Fujiwara, & Okazaki, 1991; Narayanan & Der-Avanessian, 1985; Redwood & Demirdjian, 1998; Shanmugam, Lian, & Thevendran, 2002; Zaarour & Redwood). Openings such as holes, slots, and copings are clearly not the same as through-thickness cracks. Nonetheless, these studies provide invaluable insight for how a through-thickness crack may affect the carrying capacity of beam-like structures.

4.2.4.1 Research Works

Marek et al. (1970) investigated the behavior of a pre-existing crack in a small-scale plate girder subjected to fatigue loading. The test girder was previously subjected to fatigue loading in order to produce initial through-thickness fatigue cracks. Unwanted cracks were repaired so as to leave one three-ended test crack at mid-span. The initial state of the test crack was such that it extended from the base of the web plate through both sides of the flange plate and up through the web. A concentrated fatigue load ranging from *30* to *80* kips was applied at mid-span at a rate of *250* cycles per minute. Specifically, the load was applied to the top of the flange opposite the test crack so that the crack was in a region of tensile stresses. The strains in the vicinity of the crack were recorded along with the crack growth rate.

The crack was observed to slowly propagate towards the outside edges of the flange plate and up through the web plate. Measurements showed that the crack grew at a slightly faster rate in the flange than in the web. Furthermore, the crack growth rate was observed to increase with the length of the crack. Neglecting the presumed effects of residual stresses from the welds, the strains and corresponding stresses at the crack tips would have generally increased with the growth of the crack.

A growth rate curve of a crack in a steel plate specimen obtained by Hertzberg & Nordberg (1969) was compared with the growth rate curve of the crack in the flange of the test girder. The two curves demonstrated similar upward trends of growth rate with the length of the crack. The vertical displacement between the two curves was thought to be due to the differences in geometry between the plate specimen and the actual geometry of the test girder flange. Nevertheless, the tests suggested that fatigue crack growth rate curves obtained from plate specimens could be used to predict fatigue crack growth in actual plate girders with the use of correction factors. A theoretical study conducted by Smith, Marek, & Yen (1970) in parallel with the experimental test utilized a lumped parameter method to analyze the stress and strain distributions in the vicinity of the crack. A mathematical model of the test girder was developed using the same geometrical and material properties, crack configuration, and load setup as in the experiment. The stress and strain results from the mathematical model were largely in agreement with the experimental test.

Fisher (1970) later performed further fatigue loading tests on a total of 374 small-scale girders made of different steels with various arrangements of details. Of particular interest were the tests that were conducted on cover-plated girders and girders without cover plates. The cover plated girders exhibited fatigue crack initiation at the transverse welds along the ends of the cover plate, and along the longitudinal welds connecting the cover plate to the flange. The cracks at the cover plate ends propagated outward toward the flange tips and up through the web plate. For girders without cover plates, multiple fatigue cracks were observed to form at flaws in the fillet welds connecting the web plate to the tension flange and compression flange. For all cases, the stress range and

72

corresponding range of stress intensity factor were found to be the overwhelming variables in controlling the crack growth rates as had been previously shown by Hertzberg & Nordberg (1969). A Paris-Erdogan crack growth equation was developed which predicted crack growth in good agreement with the observed crack growth.

Very few studies have been conducted relating to the effects of cracks on the load capacity of plate girders or beam-like structures. Roberts et al. (1977) performed an extensive set of fatigue loading tests at Lehigh University on a total of *24* full-scale girders with various attachments. The purpose of the study was to investigate tolerable flaw sizes in the test girders. The test girders were fabricated from structural steels conforming to the 1975 AASHTO toughness specifications. The girders were fatigue loaded until fracture and the locations and sizes of fatigue cracks were recorded. As would be expected, the fatigue cracks generally formed along the weld boundaries. It was concluded that the smallest tolerable crack size was on the order of the flange thickness. Details containing cracks of this size were estimated to have already exhausted 80% of their fatigue life.

An investigation into the effects of crack growth on the static shear capacity of *17* transversely stiffened test girders was conducted by Roberts et al. (1996). A portion of the test girders were tested to failure under static loading, and exhibited behaviors that would be expected from the theory by Basler & Thurlimann (1960b). The girders tested under fatigue loading exhibited plate breathing and corresponding out-of-plane bending stresses, which formed fatigue cracks at the web panel boundaries. Additionally, tension field action was evident, suggesting that the web plate had already effectively buckled. This had been previously observed in tests by Goodpasture & Stallmeyer (1967). The

73

effect of fatigue cracks on the tension field action was analyzed and a modified expression for the ultimate shear capacity was derived which took into account the length of the crack and the depth of the web.

As for the influence of openings on the static strength of beam-like structures, Narayanan & Der-Avanessian (1985) demonstrated that the ultimate shear capacity of a plate girder with a rectangular hole in the web is derived from the elastic capacity of the web, the post-buckling tension field action, and the plastic capacity of the flanges. An approximate expression for the shear buckling stress was derived from a finite element analysis. Specifically, the buckling coefficient was modified with an adjustment factor which takes into account the width and height of the rectangular hole. Overall, an approximate expression for the ultimate shear capacity was formulated, and compared favorably to results from 10 experimental tests.

Cheng & Yura (1986) examined the effects of copings on web local buckling of plate girders and rolled beams using numerical and experimental methods. Again, the buckling coefficient was modified with an adjustment factor which considers the dimensions of the coped web and the cutout. The resulting capacity expressions conservatively predicted the bending moment and shear force capacities at the coped region.

Cooper & Roychowdhury (1990) later developed a modified tension field action shear strength expression for plate girders containing web openings. The modified expression was essentially based on the tension field theory by Basler & Thurlimann (1960b). It was noted that the tension field action shear strength reduces to zero when the depth of the web opening exceeds *15%* to *20%* of the web panel depth. It was also noted

that the modified tension field action shear strength expression used in conjunction with the modified beam action shear strength expression proposed by Narayanan & Der-Avanessian (1985) is much more accurate than the theory by Basler & Thurlimann (1960b) for plate girders containing web openings.

Ito et al. (1991) tested a series of plate girders containing U-shaped holes in the top of the web plate. Each girder was tested under a concentrated load and strain gauges were used to obtain the experimental stress distributions. In terms of elastic behavior, the bending and shear stress distributions throughout the sections with and without openings correlated very well with the stress distributions obtained from finite element analyses and beam theory taking into account the so-called Vierendeel action. Vierendeel action is the effect due to modified shear forces acting along the T-shaped cross-section where the U-shaped holes are present. Expressions for the modified shear forces were formulated which take into account the unmodified shear force, the moment of inertias of the T-shaped section and the upper flange section, and the top and bottom widths of the U-shaped hole. Modified bending moments may also be derived from the modified shear forces. The modified shear forces and bending moments may then be used in traditional beam theory to obtain the shear and bending stress distributions.

Around the same time, Zaarour & Redwood (1996) tested *14* castellated beams in a three-point loading scheme until failure. The out-of-plane web deflections and vertical beam displacements were measured in order to identify the governing failure mode. Several beams exhibited local buckling of the portion of web plate separating the openings (termed the web post). The presence of the openings adjacent to the web post produced local instability which led to a decrease in the buckling strength. Other possible

failure modes included flange local buckling and yielding. It was concluded that local buckling of the web post should be considered in design, especially when the web is expected to be deep. Finite element analysis results correlated very well to the tests and were deemed to be sufficient for design purposes.

Bedair (2011) noted that web openings in deep plate girders are oftentimes required to pass through utilities such as electrical conduits or pipelines to locations that would otherwise be inaccessible. A brief review was given of the AISC *Guideline 2* (2003) flexural capacity expression for deep plate girders with rectangular web openings, given by

$$\Phi M_n = \Phi M_p \left[1 - \frac{\alpha t_w \left(\frac{\alpha}{4} + e \right)}{Z} \right] \qquad (4.2.5)$$

where Φ is the resistance factor, M_p is the plastic moment, α is the depth of the opening, t_w is the web thickness, e is the eccentricity of the opening, and Z is the plastic section modulus. It was noted that an ideal design would be one in which the geometry and location of the opening are such that the stresses about the opening are minimized. Several shortfalls of the expression were noted, namely the absence of parameters such as the width of the opening and the radius of curvature of the corners. These two parameters, along with the depth and eccentricity of the opening, were thought to have a significant effect on the near-field and mid-field stress distributions. Finite element analyses were carried out to further investigate the effects of these parameters, and a series of recommendations and guidelines were set forth for design purposes to minimize the stresses in the vicinity of web openings.

4.3   Synopsis

The behavior of plate girders loaded under predominantly bending, shear, and combined bending and shear has been comprehensively established through both theory and experimental methods. Also, past research has thoroughly explained the origins and configurations of fatigue crack growth within plate girders. However, much of the previous research concerning the residual strength of cracked plate-like and beam-like structures, as well as the relevant theories and methods, have not been deployed in such a manner to develop capacity expressions and an associated design procedure directly suitable for structural engineers. The aforementioned objectives of this research to develop such capacity expressions and a procedure concerning the residual elastic strength of fatigue-cracked plate girders therefore appears to be justified in light of the related work performed on this subject as well as the omnipresence of structurally deficient bridge infrastructure.

5   Methodology

5.1   Overview

5.1.1   Outline of Research Procedure

The theoretical expressions for the elastic bending moment and shear force capacities of I-shaped transversely stiffened steel plate girders as affected by the presence of cracks were analyzed and formulated using the various aforementioned theories including beam theory, plane elasticity, classical plate theory, the Rayleigh-Ritz method, and LEFM. Specifically, the capacities associated with the general limit states of flange local yielding, elastic section yielding, elastic flange local buckling, elastic web local buckling, brittle fracture, and impending ductile failure were developed. In general, the capacity expressions were developed by determining the local capacities of the flange and web plates and coupling these local capacities to the global girder capacities. The capacity expressions were then validated with FE analyses using ABAQUS/CAE 6.11. Following validation, the decay expressions were formulated using the derived capacity expressions. After the capacity and decay expressions were consolidated, the proposed design procedure was developed. A flowchart of the research procedure is shown in Figure 5.1.1.

Formulate theoretical expressions for bending moment and shear force

M_{cr} V_{cr}

Failure modes considered:

Flange local yielding
Section yielding
Flange local buckling
Web local buckling
Brittle fracture
Impending ductile failure

} *Considering prescribed crack configurations*

Perform FE analyses with ABAQUS/CAE to validate capacity expressions

Formulate decay expressions

Develop proposed design procedure

Figure 5.1.1: Flowchart of the research procedure.

5.1.2   Elastic Limit State Exceedance Criteria

The normal stress and shear stress components describing the state of stress of a material element are in part dependent upon the orientation of the coordinate axis system (see Figure 5.1.2). A reference coordinate axis system is employed for the formulation of each capacity expression. The associated normal stress and shear stress components obtained using the reference axis system are compared to the various elastic failure criteria such as the yield strength and elastic buckling strength. In accordance with conventional design procedures, it is assumed that the satisfaction or failure of these stress components in meeting the elastic failure criteria constitute whether or not elastic failure will occur for all orientations of coordinate axes (Salmon et al., 2009, sec. 2.6).
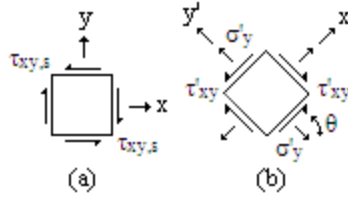
Figure 5.1.2: (a) Material element with normal stress and shear stress components, and (b) material element with transformed stress components under a rotated coordinate axis system.

5.1.3 Non-composite Configuration

The capacity expressions are formulated considering only non-composite plate girder configurations (see Figure 5.1.3). The I-shaped transversely stiffened steel plate girders are conservatively assumed to carry load independently of the concrete deck. The plate girder properties available to be modified include the flange and web plate dimensions, the transverse stiffener plate spacings, and the girder material properties.
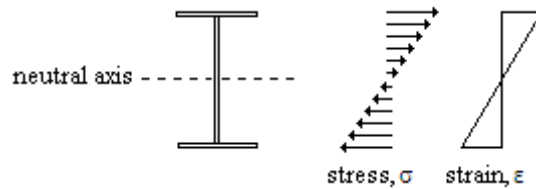
Figure 5.1.3: Non-composite girder section with corresponding stress and strain bending distributions.

5.1.4 Form of Capacity Expressions

The capacity expressions are of the following form:

$$M_{cr} = f\{\Gamma\} \tag{5.1.1}$$

$$V_{cr} = f\{\Gamma\} \tag{5.1.2}$$

where Γ represents the material properties, geometrical properties, and loading configuration of the girder, as well as the configuration and length of the associated crack. It is noted that the capacity expressions do not contain built-in resistance factors

and represent the nominal unfactored strength corresponding to the appropriate elastic limit state.

5.1.5 Investigated Fatigue Crack Configurations

5.1.5.1 Configurations Associated with Predominantly Bending

The investigated fatigue crack configurations are derived from various crack configurations observed in the literature (Crocetti, 2003; Davies, Roberts, Evans, & Bennett, 1994; Goodpasture & Stallmeyer, 1967; Hall & Stallmeyer, 1964; Kouba & Stallmeyer, 1959; Maeda & Okura, 1983, 1984; Marek, Perlman, Pense, & Tall, 1970; Roberts, Davies, & Bennett, 1995; Yen, 1963). The investigated crack configurations associated with girders loaded under predominantly bending include vertical edge-cracks extending from the tension flange through the web plate, cracks extending through one or both sides of the tension flange, and three-ended cracks extending through the web plate and both sides of the tension flange (see Figure 5.1.4).
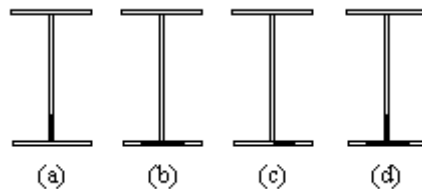
Figure 5.1.4: (a) Vertical edge-crack in web plate, (b) crack extended through both sides of tension flange, (c) crack extending through one side of tension flange, and (d) three-ended crack.

5.1.5.2 Configurations Associated with Predominantly Shear

In regions of a girder loaded under predominantly shear, a fatigue crack may continue to propagate under mixed-mode loading (Meguid, 1989, ch. 7; Sun & Jin, 2012, ch. 5). In the most general case, a fatigue crack may initiate in a corner of a web panel at

the junction of a flange and transverse stiffener plate (see Figure 5.1.5a) (Crocetti, 2003; Goodpasture & Stallmeyer, 1967; Hall & Stallmeyer, 1964; Kouba & Stallmeyer, 1959; Mueller & Yen, 1967; Yen, 1963; Yen & Mueller, 1966). Primarily opening-mode loading (Mode I) complemented by low values of sliding-mode loading (Mode II) may then cause the crack to propagate in a straight line diagonally through the web panel at an angle near to *45°* relative to the flange (see Figure 5.1.5b) (Paris & Erdogan, 1963; Sun & Jin, 2012, ch. 5).
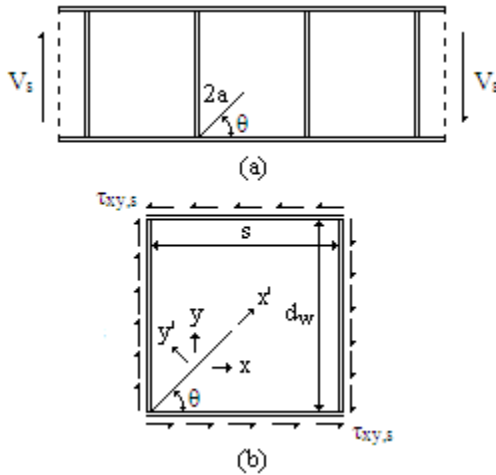
Figure 5.1.5: (a) Girder loaded under predominantly shear with diagonal fatigue crack originating at a corner of a web panel, (b) diagonal fatigue crack within the web panel displaying the *x-y* and *x'-y'* axis systems.

5.2   Theoretical Bending Moment Capacity Expressions

The continued growth of a fatigue crack associated with predominantly bending may adversely affect the bending strengths of the overall girder corresponding to the limit states of flange local yielding, flange local buckling, tension buckling, web local buckling, brittle fracture, and impending ductile failure (Minor & Woodward, 1996; Salmon et al., 2009, ch. 11; Sun & Jin, 2012, chs. 3, 6). It is assumed that the portions of

the plate girder that the bending moment capacity expressions are applicable to are loaded under predominantly bending (see Figure 5.2.1a). The plate girder itself is assumed to be an I-shaped transversely stiffened steel plate girder (see Figure 5.2.1b).
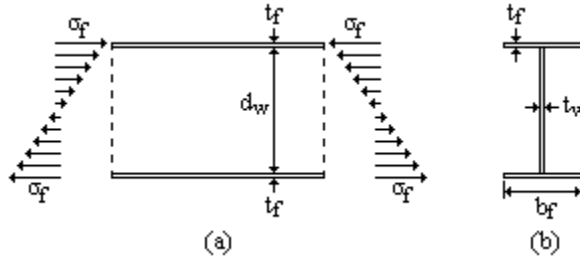
Figure 5.2.1: (a) Steel plate girder loaded under predominantly bending with (b) I-shaped cross-section.

5.2.1 Three-ended Crack

The three-ended crack configuration (see Figure 5.2.2) is assumed to be through-thickness and loaded primarily by Mode I loading. The three branches of the three-ended crack are assumed to propagate through the girder at approximately the same rate. In this way, the length, a, of each branch is always approximately equal to the other branch lengths.
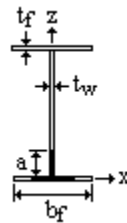
Figure 5.2.2: Three-ended crack configuration.

5.2.1.1 Tension Buckling in Tension Flange

The tensile capacity expression associated with tension buckling of the tension flange stem considering the presence of a three-ended through-thickness fatigue crack is derived using several assumptions. The flange stem is assumed to part of an I-shaped steel plate girder loaded under pure bending (see Figure 5.2.3a). The flange stem itself is assumed to be a rectangular, homogeneous, linear isotropic elastic, thin plate with plane stress conditions governing the stress field (see Figure 5.2.3b). The edge along the y-axis bordering the web plate is assumed to be clamped. Also, the flange stem is assumed to be loaded by far-field tensile stress, σ_f, equal in magnitude to the normal bending stress at the extreme outer fibers of the associated plate girder. Finally, the edge-crack of length a is assumed to be a single branch of a through-thickness three-ended fatigue crack extending through the web plate and out through the tension flanges in a direction perpendicular to the applied tensile stress.
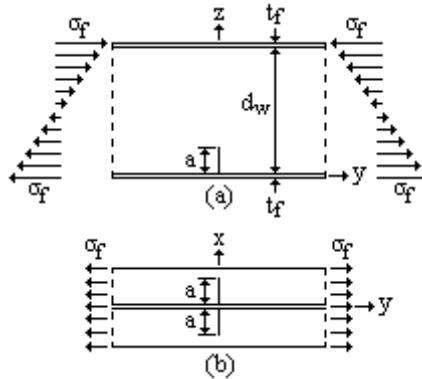
Figure 5.2.3: (a) I-shaped plate girder loaded under pure bending, (b) top view of tension flange stems loaded under far-field tensile stress σ_f.

The presence of the edge-crack in the loaded flange stem induces local transverse stresses, σ_x, in the vicinity of the crack. The compressive transverse stresses are theoretically capable of elastically buckling the portions of flange stem adjacent to the

edge-crack (see Figure 5.2.4a). The formulation of the tension buckling capacity requires at least an approximate expression describing the local transverse stress field. The non-symmetric nature and complicated boundary conditions of this configuration make difficult the calculation of the stress field. The configuration is therefore approximated by considering the edge-crack to be one half of a central crack within an infinite plate loaded by σ_f (see Figure 5.2.4b).
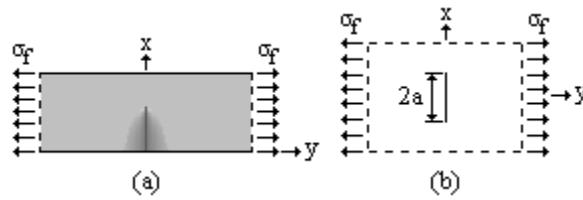
Figure 5.2.4: (a) Distribution of compressive transverse stresses σ_x adjacent to edge-crack and (b) infinite plate loaded by uniformly distributed far-field tensile stress σ_f.

The case in Figure 5.2.4b is more general and the complete two-dimensional stress field about the crack is readily derived by employing the Airy stress function, *F(x,y)* (see Appendix D: Theory of Elasticity). The Airy stress function must satisfy the applicable boundary conditions and the biharmonic equation, expressed by (D.2.5) and rewritten here for clarity as (Sadd, 2009, sec. 7.5)

$$\nabla^4 F = \frac{\partial^4 F}{\partial x^4} + 2\frac{\partial^4 F}{\partial x^2 \partial y^2} + \frac{\partial^4 F}{\partial y^4} = 0 \qquad (5.2.1)$$

which identically satisfies the equilibrium and compatibility requirements. The stress field is then given by

$$\sigma_x = \frac{\partial^2 F}{\partial y^2} \qquad \sigma_y = \frac{\partial^2 F}{\partial x^2} \qquad \tau_{xy} = -\frac{\partial^2 F}{\partial x \partial y} \qquad (5.2.2)$$

The Airy stress function for two-dimensional elastic bodies containing cracks may be expressed in terms of the real and imaginary parts of the Westergaard stress function, $Z(\zeta)$, in the form (Westergaard, 1939)

$$F = \operatorname{Re} \overline{\overline{Z}} + y \operatorname{Im} \overline{Z} \tag{5.2.3}$$

where

$$Z' = \frac{dZ}{d\zeta} \qquad Z = \frac{d\overline{Z}}{d\zeta} \qquad \overline{Z} = \frac{d\overline{\overline{Z}}}{d\zeta} \tag{5.2.4}$$

and ζ is the complex variable $\zeta = x + iy$ (see Appendix G: Linear Elastic Fracture Mechanics). Substitution of (5.2.3) into (5.2.2) results in the stress field about a crack given by

$$\begin{aligned}
\sigma_x &= \operatorname{Re} Z - y \operatorname{Im} Z' \\
\sigma_y &= \operatorname{Re} Z + y \operatorname{Im} Z' \\
\tau_{xy} &= -y \operatorname{Re} Z'
\end{aligned} \tag{5.2.5}$$

The stress field for the case in Figure 5.2.4b is calculated by superimposing the stress fields of two distinct configurations (Sun & Jin, 2012, sec. 3.5). The first configuration consists of the infinite plate without a crack subjected to far-field tensile stress equal in magnitude to σ_f (see Figure 5.2.5a). The second configuration consists of the central crack within the infinite plate loaded by internal crack face stresses equal in magnitude to σ_f (see Figure 5.2.5b). The transverse stress field for the first configuration is zero, and thus the complete transverse stress field is derived in its entirety from the second configuration.
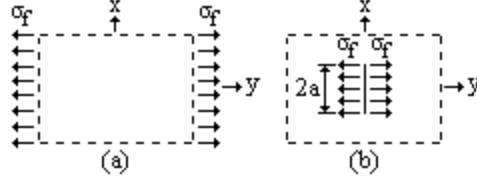
Figure 5.2.5: (a) Infinite plate loaded by uniformly distributed far-field tensile stress σ_f and (b) infinite plate with central crack loaded by internal crack face stress σ_f.

The Westergaard stress function for the second configuration (see Figure 5.2.3b) is given by (Sedov, 1972, sec. 13.2.8)

$$Z = \sigma_f \left(\frac{\zeta}{\sqrt{\zeta^2 - a^2}} - 1 \right) \tag{5.2.6}$$

Substituting (5.2.6) into (5.2.5)$_1$ and setting $x = 0$ results in the transverse stress distribution along the positive y-axis of the central crack shown in Figure 5.2.4b, expressed as

$$\sigma_x(0, y) = \sigma_f \left[-\frac{y^3}{\left(y^2 + a^2\right)^{3/2}} + \frac{2y}{\sqrt{y^2 + a^2}} - 1 \right] \tag{5.2.7}$$

It follows that the transverse stress distribution along the negative y-axis is the mirror of (5.2.7). Equation (5.2.7) represents an approximation of the transverse stress distribution along the clamped edge of the flange stem adjacent to the edge-crack on the y-axis. Close inspection of (5.2.7) reveals that the maximum compressive stress is equal to $-\sigma_f$ and occurs at the base of the crack when $y = 0$.

The magnitude of σ_f corresponding to elastic buckling of the portions of flange stem adjacent to the edge-crack is approximated by employing the Rayleigh-Ritz method (see Appendix E: Principle of Stationary Potential Energy). The buckled portions of flange stem are each assumed to be an embedded rectangular plate (see Figure 5.2.6a). Each plate has clamped support conditions along the three embedded edges and is

87

unrestrained along the edge formed by the edge-crack (see Figure 5.2.6b). These assumptions are substantiated by the buckled shapes of centrally cracked plates loaded under tension obtained in analyses by Brighenti (2005a, b, 2009) and Paik et al. (2005), and the buckled shape of a cracked plate girder web panel loaded under bending as observed by Minor & Woodward (1996).

The distribution of the compressive transverse stresses adjacent to the edge-crack (see Figure 5.2.4a) is approximated by loading the clamped edges of each embedded plate along the y-axis with the previously determined transverse stress distribution given by (5.2.7) (see Figure 5.2.6a). The length, b, of each plate is equal to the extent of (5.2.7) in compression, and is determined by equating (5.2.7) to zero and solving for y, resulting in

$$b \approx 0.786a \qquad\qquad (5.2.8)$$

It is evident that the length is entirely dependent upon the width, a, of the plate, which is equal to the edge-crack length (see Figure 5.2.6b).
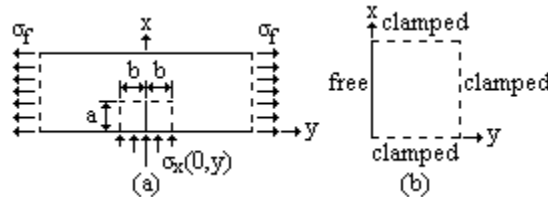
Figure 5.2.6: (a) Position of loaded embedded plates adjacent to the edge-crack and (b) geometrical boundary conditions of the embedded plate along the positive y-axis.

The buckled shape of each embedded plate is assumed to take on a form described by a displacement function, *w(x,y)*. The displacement function must satisfy the aforementioned geometrical boundary conditions indicated in Figure 5.2.6b and are explicitly expressed for the plate along the positive y-axis as

$$w(0, y) = 0 \qquad w(a, y) = 0 \qquad w(x, b) = 0$$

$$\frac{dw(0, y)}{dx} = 0 \qquad \frac{dw(a, y)}{dx} = 0 \qquad \frac{dw(x, b)}{dy} = 0$$

(5.2.9)

A displacement function of the following form satisfies these boundary conditions

$$w(x, y) = A(y - b)^2 \sin^2 \frac{\pi x}{a}$$

(5.2.10)

where A is an arbitrary variable controlling the amplitude of the displacement function.

The transverse stress distribution applied upon each embedded plate and the corresponding displacement function are both coupled to the total potential energy, Π, of the plate by (E.1.2) and expanded as (Vinson, 1974, ch. 6)

$$\Pi = \int_V W dV - \int_S T_i u_i dS = \frac{D}{2} \int_0^b \int_0^a \left\{ \left(\frac{\partial^2 w}{\partial x^2} + \frac{\partial^2 w}{\partial y^2} \right)^2 - 2(1-v)\left[\left(\frac{\partial^2 w}{\partial x^2} \right)\left(\frac{\partial^2 w}{\partial y^2} \right) - \left(\frac{\partial^2 w}{\partial x \partial y} \right)^2 \right] \right\} dxdy + \frac{1}{2} \int_0^b \int_0^a \sigma_x(0, y)\left(\frac{\partial w}{\partial x} \right)^2 dxdy$$

(5.2.11)

where D is the flexural rigidity of the plate given by (F.2.10) and rewritten here for clarity as (Barker & Puckett, 1997, p. 297)

$$D = \frac{Et_f^3}{12(1-v^2)}$$

(5.2.12)

The constant E is the modulus of elasticity, v is Poisson's ratio, and t_f is the flange plate thickness.

In accordance with the Rayleigh-Ritz method, the variation of total potential energy of each embedded plate with respect to A is set to zero as expressed by (E.1.3) and rewritten here for clarity:

$$\frac{\delta \Pi}{\delta A} = 0$$

(5.2.13)

Given that the transverse stress distribution applied upon each plate is directly dependent upon σ_f, the value of σ_f enabling this equilibrium of energy is solved for, which corresponds to elastic buckling of the portions of flange stem adjacent to the edge-crack (embedded plates). Substituting (5.2.7), (5.2.8), (5.2.10), and (5.2.12) into (5.2.11) results in an extended expression for the total potential energy of the embedded plate along the positive y-axis. Introducing the result into (5.2.13) requires that $\delta(A^2) = 2A\,\delta A$, allowing for A to be canceled from the expression (Vinson, 1974, ch. 6). Solving for σ_f and dividing the result by t_f gives

$$\sigma_{cr} = 3.58 \frac{E t_f^2 (v-2)}{a^2 (v^2-1)} \leq \sigma_Y \tag{5.2.14}$$

where σ_Y is the yield strength of the flange steel. Equation (5.2.14) represents the critical value of σ_f associated with elastic buckling of the portions of flange stem adjacent to the edge-crack (embedded plates). The corresponding elastic bending moment capacity of the associated plate girder is expressed as

$$M_{cr} = \sigma_{cr} S \tag{5.2.15}$$

where S is the elastic section modulus of the uncracked plate girder section with respect to the strong axis of bending.

5.2.1.2 Brittle Fracture

The presence of the edge-crack in the loaded flange stem may alternatively lead to the brittle fracture limit state. The edge-crack is again considered to be one half of a central crack within an infinite plate loaded by σ_f (see Figure 5.2.4b). From LEFM, the

Mode I stress intensity factor at the crack tip is given by (G.2.2), and written for clarity as (Sun & Jin, 2012, sec. 3.4)

$$K_I = \sigma_f \sqrt{\pi a} \qquad (5.2.16)$$

A stress intensity correction factor is typically employed to account for the finite dimensions of a cracked structure (see Appendix G: Linear Elastic Fracture Mechanics) (Sun & Jin, 2012, sec. 3.6). The length of the edge-crack is presumed to remain small in comparison to the flange stem prior to elastic failure, and thus the correction factor is deemed to be negligible.

The critical value of σ_f corresponding to brittle fracture is simply determined by solving (5.2.16) for σ_f and conservatively substituting the plane strain fracture toughness, K_{Ic}, of the flange steel for K_I giving

$$\sigma_{cr} = \frac{K_{Ic}}{\sqrt{\pi a}} \le \sigma_Y \qquad (5.2.17)$$

The corresponding elastic bending moment capacity of the associated plate girder is expressed as

$$M_{cr} = \sigma_{cr} S \qquad (5.2.18)$$

5.2.1.3 Impending Ductile Failure

The plastic region at the crack tip induced by σ_f must remain small in order for the stress intensity factor to remain valid (Meguid, 1989, ch. 6). The growth of the plastic region beyond a critical size invalidates the fracture toughness characterization of the flange steel and the impending ductile failure must be described using EPFM. A new

flange stem limit state may be defined by prescribing a critical plastic region size approximating the transition from LEFM to EPFM (see Figure 5.2.7).
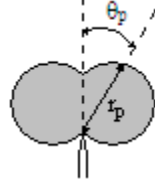
Figure 5.2.7: Plane stress plastic region at the crack tip.

The plastic region radius, r_p, measured from the crack tip is determined by employing the Mises yield criterion for plane stress, expressed by (Meguid, 1989, sec. 5.4)

$$\sigma_Y^2 = \sigma_1^2 + \sigma_2^2 - \sigma_1 \sigma_2 \qquad (5.2.19)$$

where σ_1 and σ_2 are the principal in-plane stresses expressed as (Beer et al., 2006, sec. 7.3)

$$\sigma_{1,2} = \frac{\sigma_x + \sigma_y}{2} \pm \sqrt{\left(\frac{\sigma_x - \sigma_y}{2}\right)^2 + \tau_{xy}^2} \qquad (5.2.20)$$

Also, the two-dimensional stress field in the local vicinity of the crack tip is expressed in terms of the stress intensity factor as (Sun & Jin, 2012, sec. 3.4)

$$\sigma_x = \frac{K_I}{\sqrt{2\pi r}} \cos\frac{\theta}{2}\left(1 - \sin\frac{\theta}{2}\sin\frac{3\theta}{2}\right)$$

$$\sigma_y = \frac{K_I}{\sqrt{2\pi r}} \cos\frac{\theta}{2}\left(1 + \sin\frac{\theta}{2}\sin\frac{3\theta}{2}\right) \qquad (5.2.21)$$

$$\tau_{xy} = \frac{K_I}{\sqrt{2\pi r}} \sin\frac{\theta}{2}\cos\frac{\theta}{2}\cos\frac{3\theta}{2}$$

where polar coordinates are used in place of the original rectangular coordinates. The variable r is the radius measured from the crack tip and θ is the angle of r with respect to the longitudinal axis of the crack.

Substituting (5.2.16), (5.2.20), and (5.2.21) into (5.2.19), setting $\theta = 0$, and solving for σ_f results in

$$\sigma_{cr} = \frac{\sigma_Y \sqrt{2ar_{p,cr}}}{a} \leq \sigma_Y \tag{5.2.22}$$

where $r_{p,cr}$ is a prescribed critical plastic region radius measured from the crack tip at $\theta = 0$. The corresponding elastic bending moment capacity of the associated plate girder is expressed as

$$M_{cr} = \sigma_{cr} S \tag{5.2.23}$$

5.2.2   Vertical Edge-crack in Web Plate

The vertical edge-crack in the web plate is assumed to be through-thickness and loaded primarily by Mode I loading (see Figure 5.2.8). The crack of length $2a$ is assumed to initiate along the boundary between the web plate and tension flange plate and propagate vertically through the web plate.
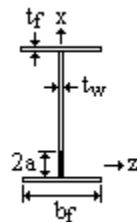
Figure 5.2.8: Vertical edge-crack configuration.

93

5.2.2.1 Yielding of Compression Flange

The bending moment capacity expression associated with yielding of the compression flange considering a vertical crack in the web plate is next derived. As with the three-ended crack, the I-shaped steel plate girder is assumed to be loaded under pure bending (see Figure 5.2.9). The presence of a vertical through-thickness edge-crack in the tension region of the web plate induces a local disturbance in the normal bending stress distribution. Specifically, the crack serves to locally shift the neutral axis of the plate girder towards the compression flange, which may give rise to premature yielding of the compression flange.
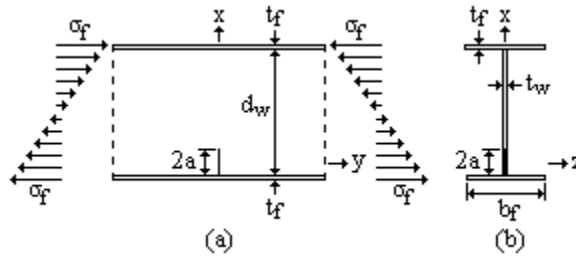
Figure 5.2.9: (a) I-shaped plate girder loaded under pure bending and (b) cross-section through edge-crack.

The normal bending stress distribution in uncracked sections of a plate girder is described by beam theory, in which the distribution takes on a linear form as shown in Figure 5.2.10a (Beer et al., 2006, ch. 4). The stress designated by σ_f is the bending stress at the extreme fibers of the plate girder. Using the coordinate system designated in Figure 5.2.9, the linear bending stress distribution in any uncracked section is expressed as

$$\sigma_y = -\frac{2\sigma_w}{d_w}(x+a)+\sigma_w \qquad (5.2.24)$$

where σ_w is the bending stress at the extreme fibers of the web plate, d_w is the depth of the web plate, and a is one half the crack length.
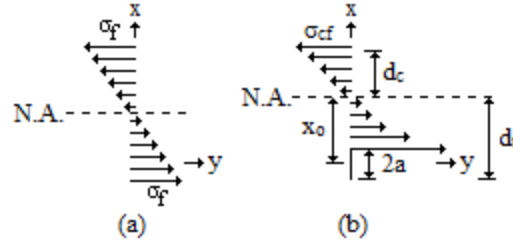
Figure 5.2.10: (a) Normal bending stress distribution, σ_y, in uncracked section of a plate girder, and (b) normal bending stress distribution, $\sigma_y(x,0)$, in cracked section.

Given that plate girders are constructed of relatively thin plates, plane stress conditions are assumed to govern the stress field within the plates. The local disturbance in the web plate stress field induced by the edge-crack is approximately determined with the use of the Airy stress function, $F(x,y)$ (see Appendix D: Theory of Elasticity). The two-dimensional stress field for any elastic body may be expressed in terms of the Airy stress function as (Sadd, 2009, sec. 7.5)

$$\sigma_x = \frac{\partial^2 F}{\partial y^2} \qquad \sigma_y = \frac{\partial^2 F}{\partial x^2} \qquad \tau_{xy} = -\frac{\partial^2 F}{\partial x \partial y} \tag{5.2.25}$$

where the Airy stress function satisfies the biharmonic equation given by (Sadd, 2009, sec. 7.5)

$$\nabla^4 F = \frac{\partial^4 F}{\partial x^4} + 2\frac{\partial^4 F}{\partial x^2 \partial y^2} + \frac{\partial^4 F}{\partial y^4} = 0 \tag{5.2.26}$$

hence satisfying the equilibrium and compatibility requirements. The presence of a crack within an elastic body requires an expanded definition of the stress field and is achieved by expressing the Airy stress function in terms of the Westergaard stress function, $Z(\zeta)$, as (Westergaard, 1939)

$$F = \operatorname{Re}\overline{\overline{Z}} + y\operatorname{Im}\overline{Z} \tag{5.2.27}$$

where

$$Z' = \frac{dZ}{d\zeta} \qquad \overline{Z} = \frac{d\overline{\overline{Z}}}{d\zeta} \qquad \overline{\overline{Z}} = \frac{d\overline{\overline{\overline{Z}}}}{d\zeta} \tag{5.2.28}$$

and ζ is the complex variable $\zeta = x + iy$ (see Appendix G: Linear Elastic Fracture Mechanics). The substitution of (5.2.27) into (5.2.25) results in the stress field about a crack becoming

$$\begin{aligned}
\sigma_x &= \operatorname{Re} Z - y \operatorname{Im} Z' \\
\sigma_y &= \operatorname{Re} Z + y \operatorname{Im} Z' \\
\tau_{xy} &= -y \operatorname{Re} Z'
\end{aligned} \tag{5.2.29}$$

The normal bending stress distribution, $\sigma_y(x,0)$, along the x-axis (see Figure 5.2.10b) is approximated by assuming that the vertical crack resides within an infinite plate loaded by far-field stresses, σ_y, distributed identically to the uncracked bending stress distribution (see Figure 5.2.10a) as expressed by (5.2.24). The peaks of the far-field stress distributions are equal to σ_f and are slightly offset from the y-axis in order to align with the actual triangular bending stress distribution within the plate girder (see Figure 5.2.11a). The stress field around the crack for this configuration is obtained by superimposing the stress fields for two distinct cases (Sun & Jin, 2012, sec. 3.5). The first case consists of the infinite plate and far-field stresses without the crack. The second case consists of the crack within the infinite plate loaded by internal crack face stresses distributed identically to the uncracked bending stress distribution as expressed by (5.2.24). As a further simplification, the linearly varying crack face stresses are approximated as being uniformly distributed with a magnitude σ_w' taken as the average of the crack face stresses (see Figure 5.2.11b). This average stress is obtained by substituting $x = 0$ into (5.2.24), resulting in

$$\sigma_w^{'} = -\frac{2\sigma_w a}{d_w} + \sigma_w \tag{5.2.30}$$
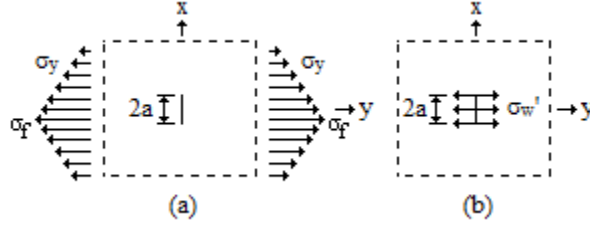
Figure 5.2.11: (a) Infinite plate with central crack loaded by far-field stresses and (b) central crack within an infinite plate loaded by uniform crack face stresses.

Superimposing the uncracked bending stress distribution for the first case as given by (5.2.24) with the stress distribution for the second case as given by (5.2.29)₂ and setting $y = 0$ results in

$$\sigma_y(x,0) = \operatorname{Re} Z + \sigma_y \tag{5.2.31}$$

The Westergaard stress function for the second case (see Figure 5.2.11b) is given by (Sedov, 1972, sec. 13.2.8)

$$Z = \sigma_w^{'}\left(\frac{\xi}{\sqrt{\xi^2 - a^2}} - 1\right) \tag{5.2.32}$$

Substituting (5.2.24), (5.2.30), and (5.2.32) into (5.2.31) results in the final expression for the normal bending stress distribution along the x-axis:

$$\sigma_y(x,0) = \left(-\frac{2\sigma_w a}{d_w} + \sigma_w\right)\left(\frac{x}{\sqrt{x^2 - a^2}} - 1\right) - \frac{2\sigma_w}{d_w}(x+a) + \sigma \tag{5.2.33}$$

The local shift of the neutral axis along the x-axis (see Figure 5.2.10b) is determined by equating (5.2.33) to zero and solving for x, resulting in:

$$x_o = \frac{1}{2}\sqrt{8a^2 - 4ad_w + d_w^2} \tag{5.2.34}$$

97

The depth of the web plate along the x-axis under tension, d_t, therefore becomes:

$$d_t = x_o + a = \frac{1}{2}\sqrt{8a^2 - 4ad_w + d_w^2} + a \qquad (5.2.35)$$

Also, the depth of the web plate along the x-axis under compression, d_c, becomes:

$$d_c = d_w - d_t = d_w - a - \frac{1}{2}\sqrt{8a^2 - 4ad_w + d_w^2} \qquad (5.2.36)$$

The localized shift of the neutral axis towards the compression flange serves to increase the bending stresses in the compression flange along the x-axis, which may lead to local yielding. In uncracked sections of a plate girder, the bending stresses at the extreme fibers of the compression flange, σ_f, and web plate, σ_w, are related by similar triangles in the form,

$$\frac{\sigma_f}{d_w/2 + t_f} = \frac{\sigma_w}{d_w/2} \qquad (5.2.37)$$

where t_f is the compression flange plate thickness. Solving (5.2.37) for σ_w gives,

$$\sigma_w = \frac{\sigma_f d_w}{d_w + 2t_f} \qquad (5.2.38)$$

The local increase of bending stresses in the compression flange is first calculated by equating the compressive force in the uncracked section of the web plate with the compressive force in the cracked section of the web plate, expressed as

$$\frac{\sigma_w d_w t_w}{4} = \frac{\sigma_{cw} d_c t_w}{2} \qquad (5.2.39)$$

where t_w is the web plate thickness, and σ_{cw} is the increased bending stress at the extreme fibers of the web plate along the x-axis. Solving for σ_{cw} results in:

$$\sigma_{cw} = \frac{\sigma_w d_w}{2d_c} \qquad (5.2.40)$$

Assuming a linear distribution of compressive bending stresses above the shifted neutral axis along the x-axis, the increased bending stresses at the extreme fibers of the compression flange, σ_{cf}, is calculated by employing similar triangles, in the form

$$\frac{\sigma_{cf}}{d_c + t_f} = \frac{\sigma_{cw}}{d_c} \tag{5.2.41}$$

Solving (5.2.41) for σ_{cf} results in:

$$\sigma_{cf} = \frac{\sigma_{cw}\left(d_c + t_f\right)}{d_c} \tag{5.2.42}$$

Substituting (5.2.36) and (5.2.38) into (5.2.40), and introducing the result into (5.2.42) results in:

$$\sigma_{cf} = \frac{\sigma_f}{\beta_{cf}} \tag{5.2.43}$$

where the factor β_{cf} is defined as

$$\beta_{cf} = \frac{\left(d_w + 2t_f\right)\left(2d_w - 2a - \sqrt{8a^2 - 4ad_w + d_w^2}\right)^2}{d_w^2\left(2t_f + 2d_w - 2a - \sqrt{8a^2 - 4ad_w + d_w^2}\right)} \tag{5.2.44}$$

Solving (5.2.43) for σ_f and setting σ_{cf} equal to the yield strength, σ_Y, of the girder steel results in:

$$\sigma_{cr} = \beta_{cf}\sigma_Y \leq \sigma_Y \tag{5.2.45}$$

Equation (5.2.45) represents the critical bending stress at the extreme fibers of the compression flange in uncracked sections of a plate girder corresponding to yielding of the extreme fibers of the compression flange in the cracked section along the x-axis. The corresponding elastic bending moment capacity of the associated plate girder is expressed as

$$M_{cr} = \sigma_{cr} S \tag{5.2.46}$$

5.2.2.2 Local Buckling of Compression Flange

The local increase in bending stresses within the compression flange may alternatively lead to elastic local buckling of the compression flange stems. The critical bending stress at the extreme fibers of the compression flange in uncracked sections of a plate girder corresponding to elastic buckling of a flange stem in the cracked section along the x-axis is determined using (5.2.43) and (5.2.44). Equating σ_{cf} in (5.2.43) to the classical elastic plate buckling strength results in (Salmon et al., 2009, sec. 6.14)

$$\sigma_{cf} = \sigma_{cr} = k \frac{D\pi^2}{t_f (b_f/2)^2} = \frac{\sigma_f}{\beta_{cf}} \tag{5.2.47}$$

where the factor k is dependent upon the geometrical properties and support conditions of the flange stem, and b_f is the compression flange width (see Appendix F: Classical Plate Theory). The constant D is the plate rigidity given by (Salmon et al., 2009, sec. 6.14)

$$D = \frac{E t_f^3}{12(1-v^2)} \tag{5.2.48}$$

where E is the modulus of elasticity and v is Poisson's ratio. Substituting (5.2.48) into (5.2.47) and solving for σ_f results in:

$$\sigma_{cr} = \beta_{cf} \sigma_{cr} = \beta_{cf} k \frac{\pi^2 E}{12(1-v^2)(b_f/2t_f)^2} \leq \sigma_Y \tag{5.2.49}$$

One side of a flange stem is unrestrained while the side bordering the web plate is assumed to be simply supported or fully clamped. Assuming the restrained side to be fully clamped requires that $k = 4$ (Salmon et al., 2009, sec. 6.15). The corresponding elastic bending moment capacity of the associated plate girder is expressed as

100

$$M_{cr} = \sigma_{cr} S \tag{5.2.50}$$

5.2.2.3 Web Local Buckling

The local increase in bending stresses within the compression region of the web plate (see Figure 5.2.10b) influences the elastic web local buckling strength of a plate girder. This strength is estimated by first calculating the critical bending stress at the extreme fibers of the web plate, σ_{cw}, along the x-axis. A predefined region of the cracked web plate is assumed to locally buckle, and the Rayleigh-Ritz method is employed to estimate σ_{cw} (see Appendix E: Principle of Stationary Potential Energy).

The predefined buckled region is presumed to be a square embedded plate of width d_c (see Figure 5.2.12a). This assumption is judged to be reasonable in light of the buckled shapes of cracked plates loaded under tension obtained by Brighenti (2005a, b, 2009). The central axis of the embedded plate is aligned with the crack along the x-axis. In accordance with the Rayleigh-Ritz method, the embedded plate is assumed to buckle in a form described by an out-of-plane displacement function, $w(x,y)$. The boundaries of the embedded plate are fully clamped, of which the boundary conditions are expressed as follows:

$$
\begin{aligned}
& w(x_o, y) = 0 && w(x_o + d_c, y) = 0 \\
& w(x, -d_c/2) = 0 && w(x, d_c/2) = 0 \\
& \frac{w(x_o, y)}{dx} = 0 && \frac{w(x_o + d_c, y)}{dx} = 0 \\
& \frac{w(x, -d_c/2)}{dy} = 0 && \frac{w(x, d_c/2)}{dy} = 0
\end{aligned}
\tag{5.2.51}
$$

A displacement function of the following form satisfies the boundary conditions expressed by (5.2.51):

$$w(x, y) = A\left(\cos\frac{2\pi y}{d_c}\cos\frac{2\pi(x-x_o)}{d_c} - \cos\frac{2\pi y}{d_c} + \cos\frac{2\pi(x-x_o)}{d_c} - 1\right) \tag{5.2.52}$$

where A is an arbitrary variable subject to variation. The actual compressive stress distribution in the region above the crack is approximated by loading the vertical sides of the embedded plate with the linear compressive bending stress distribution along the x-axis, $\sigma_y^c(x,0)$, as shown in Figure 5.2.12b, and given by:

$$\sigma_y^c(x,0) = \frac{\sigma_{cw}}{d_c}(x_o - x) \tag{5.2.53}$$
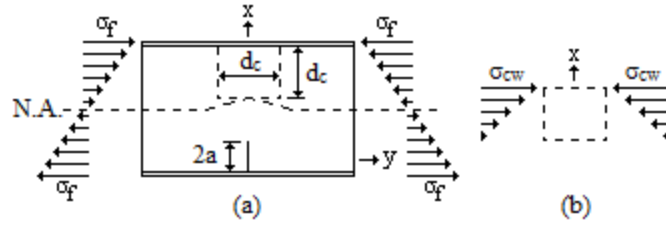
Figure 5.2.12: (a) Location of embedded plate within the web plate, and (b) the assumed external load distribution.

The total potential energy, Π, of the loaded embedded plate is expressed as (Vinson, 1974, sec. 6.1)

$$\Pi = \int_V W dV - \int_S T_i u_i dS = \frac{D}{2}\int_{-d_c/2}^{d_c/2}\int_{x_o}^{x_o+d_c}\left\{\left(\frac{\partial^2 w}{\partial x^2} + \frac{\partial^2 w}{\partial y^2}\right)^2\right.$$

$$\left. - 2(1-\nu)\left[\left(\frac{\partial^2 w}{\partial x^2}\right)\left(\frac{\partial^2 w}{\partial y^2}\right) - \left(\frac{\partial^2 w}{\partial x \partial y}\right)^2\right]\right\}dxdy \tag{5.2.54}$$

$$+ \frac{1}{2}\int_{-d_c/2}^{d_c/2}\int_{x_o}^{x_o+d_c}\left[\sigma_y^c(x,0) - \frac{d_c}{2}\right]\left(\frac{\partial w}{\partial x}\right)^2 dxdy$$

where W is the strain-energy density function, V is the volume of the plate, T_i are the applied surface tractions, u_i are the corresponding displacements, and S is the surface over which the tractions are applied. The y-intercept of (5.2.53) is shifted by a magnitude of $-d_c / 2$ such that (5.2.53) is applied upon the vertical side of the embedded plate at $y = -d_c / 2$. The change in total potential energy, $\delta\Pi$, with respect to A is then equated to zero, as expressed by (E.1.3). Solving for σ_{cw} and dividing the result by t_w gives:

$$\sigma_{cw} = \frac{64 D\pi^2 - 3d_c^3}{3 t_w d_c^2} \tag{5.2.55}$$

The substitution of (5.2.36) and (5.2.38) into (5.2.40) results in:

$$\sigma_{cw} = \frac{\sigma_f}{\beta_{cw}} \tag{5.2.56}$$

where the factor β_{cw} is defined as

$$\beta_{cw} = \frac{\left(d_w + 2t_f\right)\left(2d_w - 2a - \sqrt{8a^2 - 4ad_w + d_w^2}\right)}{d_w^2} \tag{5.2.57}$$

Introducing (5.2.55) into (5.2.56) and solving for σ_f results in

$$\sigma_{cr} = \beta_{cw} \frac{\left(64 D\pi^2 - 3d_c^3\right)}{3 t_w d_c^2} \leq \sigma_Y \tag{5.2.58}$$

where t_w is used in place of t_f in the plate rigidity. The corresponding elastic bending moment capacity of the associated plate girder is expressed as

$$M_{cr} = \sigma_{cr} S \tag{5.2.59}$$

5.2.2.4 Tension Buckling in Web Plate

The presence of the vertical crack in the loaded web plate induces transverse compressive stresses, σ_x, adjacent to the crack which may cause local buckling (see

Figure 5.2.13). The exact compressive stress distribution is difficult to obtain due to the non-symmetric configuration and complicated boundary conditions of the crack. As an alternative, the transverse stress distribution is approximated by considering the vertical crack to be a central crack located within an infinite plate loaded by linearly varying far-field tensile stress distributions (see Figure 5.2.14). The maximum magnitudes of the far-field stress distributions are equal to the bending stress within the extreme fibers of the tension flange, σ_f. The apex of each far-field stress distribution occurs at a location slightly offset from the y-axis in order to align with the actual triangular bending stress distribution in the plate girder.
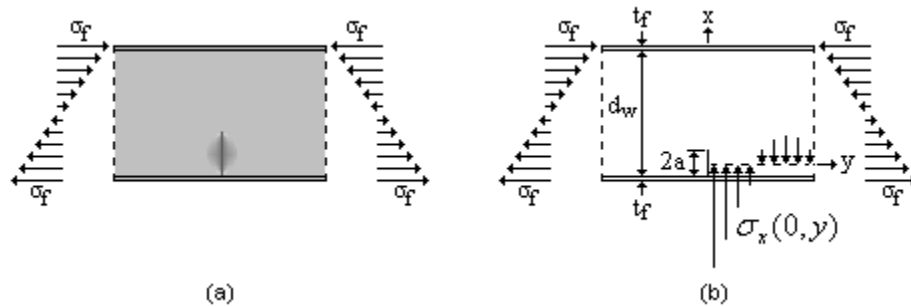
Figure 5.2.13: Web plate showing (a) transverse compressive stresses adjacent to edge-crack, and (b) distribution of transverse stresses along the positive y-axis adjacent to the edge-crack.
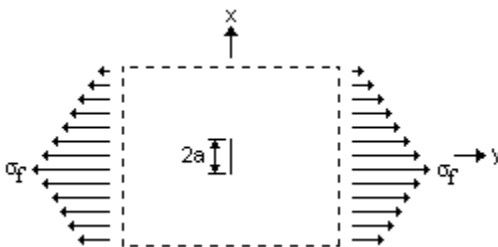
Figure 5.2.14: Central crack within an infinite plate subjected to linearly varying far-field tensile stress distributions.

The case in Figure 5.2.14 is more general and the stress field around the central crack can be readily approximated by employing the principle of superposition (Sun & Jin, 2012, sec. 3.5). This stress field is obtained by superimposing the stress field for the case in Figure 5.2.14 without a crack with the stress field for the case of a central crack within an infinite plate subjected to linearly varying crack face tensile stresses, $\sigma_y(x_o)$ (see Figure 5.2.15a). These tensile stresses are described by the function

$$\sigma_y(x_o) = \pm \sigma_f \left(\frac{2x_o}{d_w} + \frac{2a}{d_w} - 1 \right) \tag{5.2.60}$$

where x_o is the distance along the x-axis measured from the origin of the coordinate system, and d_w is the depth of the web plate. The variation of the crack face tensile stresses is identical to the stress variation of the case in Figure 5.2.14. The maximum tensile stress occurs at $x_o = -a$, and is equal to σ_f.
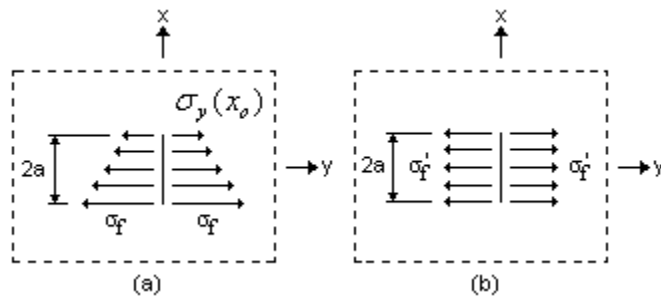
Figure 5.2.15: Central crack within an infinite plate subjected to (a) linearly varying and (b) uniform crack face tensile stresses.

The superimposed stress field of the case in Figure 5.2.14 without a crack has no effect on the transverse stress distribution around the central crack, and the stress field is sought for the case in Figure 5.2.15a. This case is greatly simplified by recognizing from (5.2.60) that, for small crack lengths and large web plate depths, σ_f is nearly equal to the crack face tensile stresses at the crack end given by $\sigma_y(a)$. The distribution of crack face

tensile stresses is therefore approximated as uniform tensile stress, σ_f' (see Figure 5.2.15b). The magnitude of σ_f' is taken as the average of σ_f and $\sigma_y(a)$, expressed by:

$$\sigma_f' = \pm \sigma_f \left(\frac{2a}{d_w} - 1 \right) \tag{5.2.61}$$

The two-dimensional stress field of the case in Figure 5.2.15b is obtained by employing the Airy stress function, $F(x,y)$ (see Appendix D: Theory of Elasticity). The Airy stress function must satisfy any given boundary conditions and the biharmonic equation given by (Sadd, 2009, sec. 7.5)

$$\nabla^4 F = \frac{\partial^4 F}{\partial x^4} + 2 \frac{\partial^4 F}{\partial x^2 \partial y^2} + \frac{\partial^4 F}{\partial y^4} = 0 \tag{5.2.62}$$

which identically satisfies the equilibrium and compatibility equations. The stress field is expressed as (Sadd, 2009, sec. 7.5)

$$\sigma_x = \frac{\partial^2 F}{\partial y^2} \qquad \sigma_y = \frac{\partial^2 F}{\partial x^2} \qquad \tau_{xy} = -\frac{\partial^2 F}{\partial x \partial y} \tag{5.2.63}$$

For elastic bodies containing cracks, the Airy stress function may be expressed in terms of the Westergaard stress function, $Z(\zeta)$, as (Westergaard, 1939)

$$F = \operatorname{Re} \overline{\overline{Z}} + y \operatorname{Im} \overline{Z} \tag{5.2.64}$$

where,

$$Z' = \frac{dZ}{d\zeta} \qquad \overline{Z} = \frac{d\overline{\overline{Z}}}{d\zeta} \qquad \overline{\overline{Z}} = \frac{d\overline{\overline{\overline{Z}}}}{d\zeta} \tag{5.2.65}$$

and ζ is the complex variable $\zeta = x + iy$ (see Appendix G: Linear Elastic Fracture Mechanics). Substitution of (5.2.64) into (5.2.63) results in the stress field around the crack:

$$\sigma_x = \operatorname{Re} Z - y \operatorname{Im} Z'$$
$$\sigma_y = \operatorname{Re} Z + y \operatorname{Im} Z' \qquad (5.2.66)$$
$$\tau_{xy} = -y \operatorname{Re} Z'$$

The Westergaard stress function for the case in Figure 5.2.15b is expressed as (Sedov, 1972, sec. 13.2.8)

$$Z = \frac{\sigma_f'}{\pi\sqrt{\zeta^2 - a^2}} \int_{-a}^{a} \frac{\sqrt{a^2 - x_o^2}}{\zeta - x_o} \, dx_o \qquad (5.2.67)$$

Evaluating the integral results in:

$$Z = \sigma_f' \left(\frac{\xi}{\sqrt{\xi^2 - a^2}} - 1 \right) \qquad (5.2.68)$$

Substituting (5.2.61) and (5.2.68) into (5.2.66)$_1$, and setting $x = 0$ results in the following expression for the two-dimensional transverse stress distribution along the positive y-axis of the central crack shown in Figure 5.2.14:

$$\sigma_x(0, y) = \sigma_f \left(\frac{2a}{d_w} - 1 \right) \left[\frac{y^3}{\left(y^2 + a^2\right)^{\frac{3}{2}}} - \frac{2y}{\sqrt{y^2 + a^2}} + 1 \right] \qquad (5.2.69)$$

Alternatively, setting $x = \pm a$ results in the transverse stress distribution at the crack ends, given by:

$$\sigma_x(\pm a, y) = -\sigma_f \left(\frac{2a}{d_w} - 1 \right) \left\{ \operatorname{Re} \left[\frac{a + iy}{\sqrt{(a + iy)^2 - a^2}} - 1 \right] \right.$$
$$\left. - y \operatorname{Im} \left[\frac{1}{\sqrt{(a + iy)^2 - a^2}} - \frac{(a + iy)^2}{\left((a + iy)^2 - a^2\right)^{\frac{3}{2}}} \right] \right\} \qquad (5.2.70)$$

Based on the prior assumption considering the edge-crack to be a central crack within an infinite plate, (5.2.69) approximately describes the transverse stress distribution at the middle of the crack on the positive y-axis, and (5.2.70) approximately describes the

transverse stress distribution along the clamped edge of the web plate and at the far end of the crack (see Figure 5.2.16).
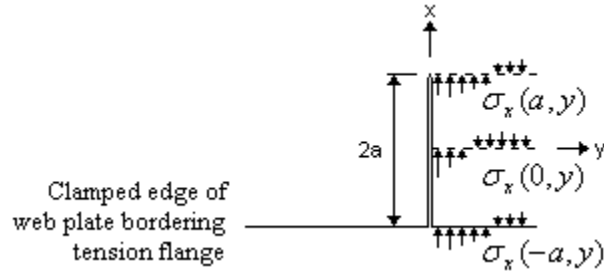
Figure 5.2.16: Transverse stress distributions at the middle and ends of edge-crack.

The transverse stress distributions given by (5.2.69) and (5.2.70) are used to calculate the local buckling strength of the portion of web plate adjacent to the crack by employing the Rayleigh-Ritz method (see Appendix E: Principle of Stationary Potential Energy). This portion of plate is assumed to be a rectangular embedded plate (see Figure 5.2.17a) with clamped support conditions along three edges and a free edge formed by the crack (see Figure 5.2.17b). These assumptions are substantiated by the buckled shapes of centrally cracked plates loaded under tension (Brighenti, 2005a, b, 2009; Paik et al., 2005), and the buckled shape of a cracked plate girder web panel loaded under bending (Minor & Woodward, 1996).

Figure 5.2.17: (a) Location of embedded plate adjacent to edge-crack with (b) exact and (c) approximate transverse stress distributions.

The compressive stress distribution in the region directly adjacent to the crack is approximated by loading the clamped edge of the embedded plate bordering the tension flange with a transverse compressive stress distribution, $\sigma_x'(-a, y)$, taken as the average of (5.2.69) and (5.2.70), expressed as

$$\sigma_x'(-a, y) = \frac{\sigma_x(0, y) + \sigma_x(a, y)}{2} \tag{5.2.71}$$

Substituting (5.2.69) and (5.2.70) into (5.2.71) results in a lengthy expression for the transverse stress distribution (see Figure 5.2.17b). Examination of (5.2.71) reveals that the stress distribution is triangular in shape and may be simplified as a linear distribution, $\sigma_x''(-a, y)$ (see Figure 5.2.17c). The slope of $\sigma_x''(-a, y)$ is taken as one half of (5.2.61) divided by the width, b, of the embedded plate, and the x-intercept is taken as one half of (5.2.61). The value of b is assumed to be equal to the extent of $\sigma_x'(-a, y)$ in compression, and is determined by setting (5.2.71) equal to zero and solving for y, resulting in

109

$$b \cong 1.16a \tag{5.2.72}$$

Accordingly, the simplified transverse stress distribution becomes

$$\sigma_x''(-a, y) = \frac{\sigma_f}{2}\left(\frac{2a}{d_w} - 1\right)\left(1 - \frac{y}{b}\right) \tag{5.2.73}$$

In accordance with the Rayleigh-Ritz method, the buckled shape of the embedded plate is assumed to take on a form described by an out-of-plane displacement function, $w(x,y)$. The displacement function satisfies the geometric boundary conditions indicated in Figure 5.2.17b and includes an arbitrary variable, A. The change in total potential energy, Π, with respect to A is set to zero and the stress distribution given by (5.2.73) enabling this equilibrium is solved for. The total potential energy of the embedded plate is given by (Vinson, 1974, sec. 6.1)

$$\begin{aligned}
\Pi = \int_V W dV - \int_S T_i u_i dS = \frac{D}{2} \int_0^b \int_{-a}^a & \left\{ \left(\frac{\partial^2 w}{\partial x^2} + \frac{\partial^2 w}{\partial y^2}\right)^2 \right. \\
& \left. - 2(1-\upsilon)\left[\left(\frac{\partial^2 w}{\partial x^2}\right)\left(\frac{\partial^2 w}{\partial y^2}\right) - \left(\frac{\partial^2 w}{\partial x \partial y}\right)^2\right]\right\} dxdy \\
& + \frac{1}{2} \int_0^b \int_{-a}^a \sigma_x''(-a, y)\left(\frac{\partial w}{\partial x}\right)^2 dxdy
\end{aligned} \tag{5.2.74}$$

where W is the strain-energy density function, V is the volume of the plate, T_i are the applied surface tractions, u_i are the corresponding displacements, and S is the surface over which the tractions are applied. D is the plate rigidity given by

$$D = \frac{Et_w^3}{12(1-v^2)} \tag{5.2.75}$$

where E is the modulus of elasticity, v is Poisson's ratio, and t_w is the web plate thickness.

The geometric boundary conditions indicated in Figure 5.2.17b are explicitly expressed as:

$$w(-a, y) = 0 \qquad w(a, y) = 0 \qquad w(\pm x, b) = 0$$

$$\frac{dw(-a, y)}{dx} = 0 \qquad \frac{dw(a, y)}{dx} = 0 \qquad \frac{dw(\pm x, b)}{dy} = 0 \tag{5.2.76}$$

A simple displacement function of the following form satisfies these conditions:

$$w = A(y - b)^2 \cos^2\left(\frac{\pi x}{2a}\right) \tag{5.2.77}$$

Substituting (5.2.72), (5.2.73), and (5.2.77) into (5.2.74) results in an expanded expression for the total potential energy. Setting the change in total potential energy with respect to A to zero requires that

$$\frac{\delta \Pi}{\delta A} = 0 \tag{5.2.78}$$

From calculus of variations, $\delta(A^2) = 2A\ \delta A,$ which allows for A to be canceled from the expanded expression (Vinson, 1974, sec. 6.1). Finally, solving for σ_f and dividing the result by t_w results in:

$$\sigma_{cr} = 2.97 \frac{E t_w^2 d_w (1.56 - v)}{a^2 (d_w - 2a)(1 - v^2)} \leq \sigma_Y \tag{5.2.79}$$

where σ_Y is the yield strength of the web plate steel. Equation (5.2.79) represents an approximation of the critical far-field bending stress at the extreme fibers of the plate girder corresponding to local buckling of the portion of web plate adjacent to the crack (embedded plate). The corresponding elastic bending moment capacity of the associated plate girder is expressed as

$$M_{cr} = \sigma_{cr} S \tag{5.2.80}$$

5.2.2.5 Brittle Fracture

The presence of the vertical edge-crack in the web plate may alternatively lead to brittle fracture originating from the crack tip bordering the tension flange (see Figure 5.2.9). In this case, the vertical edge-crack is loaded by the triangular tensile stress distribution induced by pure bending. In a manner similar to the tension buckling formulation, the edge-crack may be approximated as a central crack located within an infinite plate loaded by linearly varying far-field tensile stress distributions with peaks equal in magnitude to σ_f (see Figure 5.2.18).
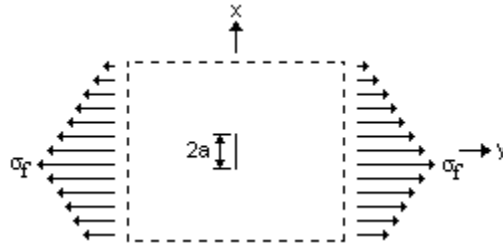
Figure 5.2.18: Central crack within an infinite plate subjected to linearly varying far-field tensile stress distributions.

It is observed that the total magnitude of the triangular tensile stress distribution is equal to one half of the total magnitude of a uniformly distributed far-field tensile stress, σ_f, acting over the same distance. Hence, the stress intensity factor, previously defined by (5.2.16), is effectively reduced by one half, resulting in:

$$K_I = \frac{1}{2}\sigma_f \sqrt{\pi a} \qquad\qquad (5.2.81)$$

As with the three-ended crack configuration, the vertical crack is presumed to remain small in comparison to the web plate prior to the occurrence of an elastic limit state. In a manner similar to the brittle fracture limit state of the three-ended crack configuration,

the critical value of σ_f corresponding to brittle fracture is determined by solving (5.2.81) for σ_f and conservatively substituting K_{Ic} of the web plate steel for K_I, resulting in:

$$\sigma_{cr} = \frac{2K_{Ic}}{\sqrt{\pi a}} \leq \sigma_Y \qquad (5.2.82)$$

The corresponding elastic bending moment capacity of the associated plate girder is expressed as

$$M_{cr} = \sigma_{cr} S \qquad (5.2.83)$$

5.2.2.6 Impending Ductile Failure

As with the three-ended crack configuration, the plastic region at the crack tip induced by the triangular bending stress distribution must remain small in order for the stress intensity factor to remain valid. A new limit state may be defined by prescribing a critical plastic zone size approximating the transition from LEFM to EPFM (see Figure 5.2.7). The plastic zone radius, r_p, measured from the crack tip is determined by employing the Mises yield criterion for plane stress, expressed by (5.2.19) (Meguid, 1989, sec. 5.4). Also, the two-dimensional stress field in the local vicinity of the crack tip is expressed in terms of the stress intensity factor by (5.2.21), and the principal in-plane stresses, σ_1 and σ_2, are expressed by (5.2.20) (Beer et al., 2006, sec. 7.3; Sun & Jin, 2012, sec. 3.4). Substituting (5.2.20), (5.2.21), and (5.2.81) into (5.2.19), setting $\theta = 0$, and solving for σ_f results in:

$$\sigma_{cr} = \frac{2\sigma_Y \sqrt{2ar_{p,cr}}}{a} \leq \sigma_Y \qquad (5.2.84)$$

where $r_{p,cr}$ is a prescribed critical plastic zone radius measured from the crack tip at $\theta = 0$ (see Figure 5.2.7). The corresponding elastic bending moment capacity of the associated plate girder is expressed as

$$M_{cr} = \sigma_{cr} S \tag{5.2.85}$$

5.2.3   Crack Extending Through One or Both Sides of Tension Flange

A fatigue crack extending through one or both sides of the tension flange is assumed to be through-thickness and loaded primarily by Mode I loading (see Figure 5.2.19a, b). Given the assumption that each crack branch propagates at approximately the same rate, the crack configuration extending through both sides of the tension flange is nominally symmetrical (see Figure 5.2.19a). Therefore, each crack branch of length *2a* is theoretically loaded by equivalent magnitudes of uniformly distributed far-field tensile stress. Furthermore, the absence of a vertical crack branch extending through the web plate serves to further isolate each crack branch in the tension flange. Each crack branch may then be analyzed as if the mirroring crack branch is nonexistent, such as in the configuration with the crack extending through one side of the tension flange (see Figure 5.2.19b). The two crack configurations shown in Figure 5.2.19 are thus nominally identical for the purpose of stress analyses, and may be analyzed using the configuration with the crack extending through one side of the tension flange (see Figure 5.2.19b).
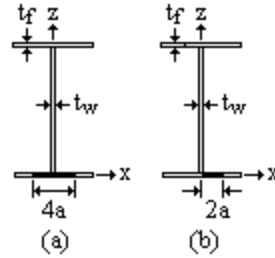
Figure 5.2.19: (a) Crack extended through both sides of tension flange and (b) crack extending through one side of tension flange.

5.2.3.1 Tension Buckling in Tension Flange

The tensile capacity expression associated with tension buckling of the tension flange stem considering the presence of a through-thickness fatigue crack extending through one side of the tension flange is derived using the same assumptions as was employed for the three-ended crack and the vertical edge-crack (i.e., the flange stem is assumed to be part of an I-shaped steel plate girder loaded under pure bending, and is assumed to be constructed of high-strength low-alloy steel). The edge of the tension flange bordering the web plate is assumed to be clamped. Also, the flange stem is assumed to be loaded by far-field tensile stress, σ_f, equal in magnitude to the normal bending stress at the extreme outer fibers of the associated plate girder (see Figure 5.2.20a). Finally, the edge-crack of length *2a* is assumed to extend through one side of the tension flange in a direction perpendicular to the applied tensile stress (see Figure 5.2.20b).
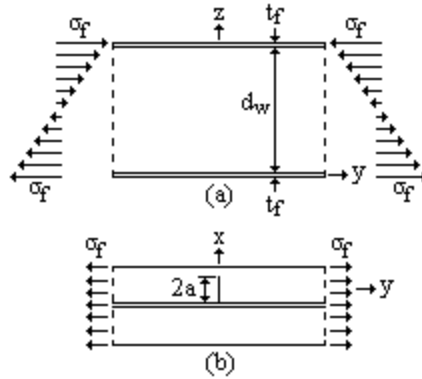
Figure 5.2.20: (a) I-shaped plate girder loaded under pure bending, (b) top view of tension flange stems loaded under far-field tensile stress σ_f.

The presence of the through-thickness edge-crack in the loaded tension flange induces transverse compressive stresses, σ_x, adjacent to the crack which may cause local buckling (see Figure 5.2.21a). The transverse stress distribution is approximated by considering the edge-crack to be a central crack located within an infinite plate loaded by uniformly distributed far-field tensile stress equal in magnitude to the normal bending stress at the extreme outer fibers of the associated plate girder (see Figure 5.2.21b).
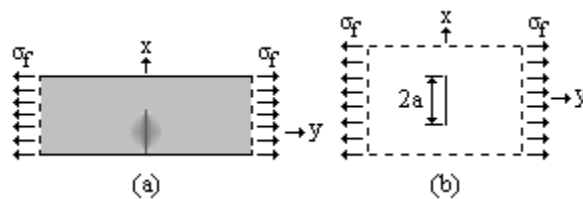
Figure 5.2.21: (a) Top view of tension flange with transverse compressive stresses adjacent to crack, and (b) infinite plate loaded by uniformly distributed far-field tensile stress σ_f.

The case in Figure 5.2.21b is more general and the stress field about the central crack is obtained by superimposing the stress field for the case in Figure 5.2.21b without a crack (see Figure 5.2.22a) with the stress field for the case of a central crack within an infinite plate subjected to uniform crack face tensile stresses, σ_f (see Figure 5.2.22b).

116
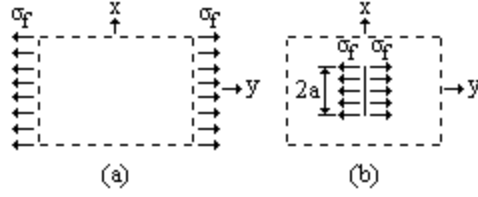
Figure 5.2.22: (a) Infinite plate loaded by uniformly distributed far-field tensile stress σ_f and (b) infinite plate with central crack loaded by internal crack face stress σ_f.

As with the three-ended crack configuration, the case in Figure 5.2.22a has no effect on the transverse stress distribution around the central crack, and the stress field is sought for the case in Figure 5.2.22b. The plane stress field expressed in terms of the Westergaard stress function was previously given by (G.1.3), and is rewritten for clarity as:

$$\begin{aligned}
\sigma_x &= \operatorname{Re} Z - y \operatorname{Im} Z' \\
\sigma_y &= \operatorname{Re} Z + y \operatorname{Im} Z' \\
\tau_{xy} &= -y \operatorname{Re} Z'
\end{aligned}$$

(5.2.86)

The Westergaard stress function for the case in Figure 5.2.22b is expressed as (Sedov, 1972, sec. 13.2.8)

$$Z = \sigma_f \left(\frac{\xi}{\sqrt{\xi^2 - a^2}} - 1 \right)$$

(5.2.87)

Substituting (5.2.87) into (5.2.86)₁ and setting $x = 0$ results in the following expression for the plane transverse stress distribution along the positive y-axis of the central crack shown in Figure 5.2.22b:

$$\sigma_x(0, y) = \sigma_f \left[-\frac{y^3}{\left(y^2 + a^2\right)^{\frac{3}{2}}} + \frac{2y}{\sqrt{y^2 + a^2}} - 1 \right]$$

(5.2.88)

Alternatively, setting $x = \pm a$ results in the plane transverse stress distribution at the crack ends given by

117

$$\sigma_x(\pm a, y) = \sigma_f \left\{ \text{Re}\left[\frac{a + iy}{\sqrt{(a+iy)^2 - a^2}} - 1 \right] \right.$$

$$\left. - y\,\text{Im}\left[\frac{1}{\sqrt{(a+iy)^2 - a^2}} - \frac{(a+iy)^2}{((a+iy)^2 - a^2)^{\frac{3}{2}}} \right] \right\} \tag{5.2.89}$$

Based on the prior assumption considering the edge-crack to be a central crack within an infinite plate, (5.2.88) approximately describes the transverse stress distribution at the middle of the crack on the positive y-axis, and (5.2.89) approximately describes the transverse stress distribution along the clamped edge of the tension flange stem and at the far ends of the crack (see Figure 5.2.23).
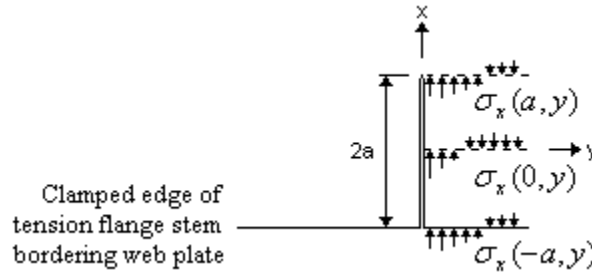
Figure 5.2.23: Transverse stress distributions at the middle and ends of edge-crack.

The transverse stress distributions given by (5.2.88) and (5.2.89) are used to calculate the local buckling stress of the portion of tension flange stem adjacent to the edge-crack by employing the Rayleigh-Ritz method (see Appendix E: Principle of Stationary Potential Energy). In a similar manner to the three-ended crack and vertical edge-crack tension buckling formulations, this portion of plate is assumed to be a rectangular embedded plate (see Figure 5.2.24a) with clamped support conditions along three edges and a free edge formed by the edge-crack (see Figure 5.2.24b) (Brighenti, 2005a, b, 2009; Minor & Woodward, 1996; Paik et al., 2005).
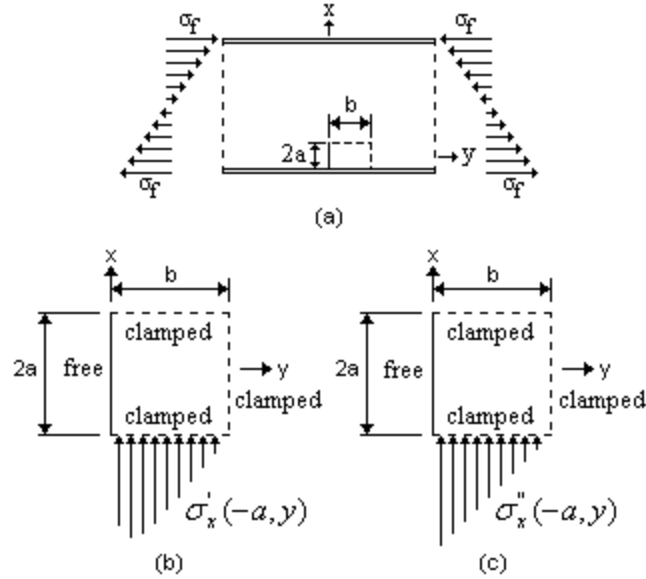
118
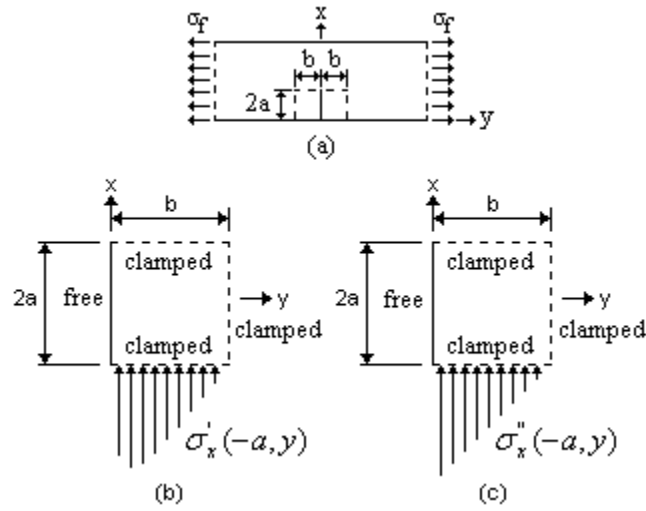
Figure 5.2.24: (a) Location of embedded plates adjacent to edge-crack with (b) exact and (c) approximate transverse stress distributions.

The compressive stress distribution adjacent to the crack is approximated by loading the clamped edge of the embedded plate bordering the web plate with a transverse compressive stress distribution, $\sigma_x'(-a, y)$, taken as the average of (5.2.88) and (5.2.89), expressed as:

$$\sigma_x'(-a, y) = \frac{\sigma_x(0, y) + \sigma_x(a, y)}{2} \tag{5.2.90}$$

Substituting (5.2.88) and (5.2.89) into (5.2.90) results in a lengthy expression for the transverse stress distribution (see Figure 5.2.24b). Examination of (5.2.90) reveals that the stress distribution is triangular in shape and can be simplified as a linear distribution, $\sigma_x''(-a, y)$ (see Figure 5.2.24c). The slope is taken as one half of σ_f divided by the width, b, of the embedded plate, and the x-intercept is taken as one half of σ_f. The value of b is assumed to be equal to the extent of $\sigma_x'(-a, y)$ in compression and is determined by setting (5.2.90) equal to zero and solving for y, resulting in:

$$b \cong 1.16a \tag{5.2.91}$$

Accordingly, the simplified transverse stress distribution becomes:

$$\sigma_x^{"}(-a, y) = \frac{\sigma_f(y - b)}{2b} \tag{5.2.92}$$

In accordance with the Rayleigh-Ritz method, the buckled shape of the embedded plate is assumed to take on a form described by an out-of-plane displacement function, $w(x,y)$. The displacement function satisfies the geometric boundary conditions indicated in Figure 5.2.24b and includes an arbitrary variable, A. The change in total potential energy, Π, with respect to A is set to zero and the stress distribution given by (5.2.92) enabling this equilibrium is solved for. The total potential energy of the embedded plate is given by (Vinson, 1974, sec. 6.1)

$$
\begin{aligned}
\Pi = \int_V W dV - \int_S T_i u_i dS &= \frac{D}{2} \int_0^b \int_{-a}^a \left\{ \left(\frac{\partial^2 w}{\partial x^2} + \frac{\partial^2 w}{\partial y^2} \right)^2 \right. \\
&\left. - 2(1-\upsilon) \left[\left(\frac{\partial^2 w}{\partial x^2} \right)\left(\frac{\partial^2 w}{\partial y^2} \right) - \left(\frac{\partial^2 w}{\partial x \partial y} \right)^2 \right] \right\} dxdy \\
&+ \frac{1}{2} \int_0^b \int_{-a}^a \sigma_x^{"}(-a, y)\left(\frac{\partial w}{\partial x} \right)^2 dxdy
\end{aligned}
\tag{5.2.93}
$$

where W is the strain-energy density function, V is the volume of the plate, T_i are the applied surface tractions, u_i are the corresponding displacements, and S is the surface over which the tractions are applied. The constant D is the plate rigidity given by

$$D = \frac{Et_f^3}{12(1-v^2)} \tag{5.2.94}$$

where E is the modulus of elasticity, v is Poisson's ratio, and t_f is the flange stem thickness.

The geometric boundary conditions indicated in Figure 5.2.24b are explicitly expressed as:

$$w(-a, y) = 0 \qquad w(a, y) = 0 \qquad w(\pm x, b) = 0$$

$$\frac{dw(-a, y)}{dx} = 0 \qquad \frac{dw(a, y)}{dx} = 0 \qquad \frac{dw(\pm x, b)}{dy} = 0 \tag{5.2.95}$$

A simple displacement function of the following form satisfies these conditions:

$$w = A(y-b)^2 \cos^2\left(\frac{\pi x}{2a}\right) \tag{5.2.96}$$

Substituting (5.2.91), (5.2.92), (5.2.94), and (5.2.96) into (5.2.93) results in an expanded expression for the total potential energy. Setting the change in total potential energy with respect to A to zero requires that:

$$\frac{\delta \Pi}{\delta A} = 0 \tag{5.2.97}$$

From calculus of variations, $\delta(A^2) = 2A\ \delta A$, which allows for A to be canceled from the expanded expression (Vinson, 1974, sec. 6.1). Solving for σ_f and dividing the result by t_f gives:

$$\sigma_{cr} = 2.97 \frac{Et_f^2(1.56-v)}{a^2(1-v^2)} \leq \sigma_Y \tag{5.2.98}$$

where σ_Y is the yield strength of the flange steel. Equation (5.2.98) represents an approximation of the critical far-field tensile stress at the extreme fiber of the plate girder corresponding to local buckling of the portion of flange stem adjacent to the edge-crack. The corresponding elastic bending moment capacity of the associated plate girder is expressed as

$$M_{cr} = \sigma_{cr} S \tag{5.2.99}$$

5.2.3.2 Brittle Fracture

The presence of a fatigue crack extending through one or both sides of the tension flange may alternatively lead to brittle fracture. In a manner similar to the brittle fracture limit state of the three-ended crack and vertical edge-crack, the horizontal edge-crack is again conservatively assumed to be a central crack loaded by a uniform distribution of far-field tensile stress, σ_f, equal in magnitude to the normal bending stress at the extreme fibers of the associated plate girder. In this case, the far-field tensile stress is in fact uniformly distributed and the unmodified stress intensity factor, K_I, is given by (5.2.16). The brittle fracture capacity is then expressed as:

$$\sigma_{cr} = \frac{K_{Ic}}{\sqrt{\pi a}} \leq \sigma_Y \tag{5.2.100}$$

The corresponding elastic bending moment capacity of the associated plate girder is expressed as

$$M_{cr} = \sigma_{cr} S \tag{5.2.101}$$

5.2.3.3 Impending Ductile Failure

As with the impending ductile failure limit state of the three-ended crack and vertical edge-crack, the plastic region at the crack tip induced by σ_f must remain small in order for the stress intensity factor to remain valid. In a procedure similar to the formulation of the three-ended crack and vertical edge-crack impending ductile failure capacities, the critical magnitude of σ_f corresponding to the transition from LEFM to EPFM is determined by employing the Mises yield criterion (5.2.19) and the two-dimensional stress field in the local vicinity of the crack tip expressed in terms of the stress intensity

factor (5.2.21) (Meguid, 1989, sec. 5.4; Sun & Jin, 2012, sec. 3.4). Substituting (5.2.20), (5.2.21), and (5.2.81) into (5.2.19), setting $\theta = 0$, and solving for σ_f results in:

$$\sigma_{cr} = \frac{\sigma_Y \sqrt{2ar_{p,cr}}}{a} \leq \sigma_Y \qquad (5.2.102)$$

where $r_{p,cr}$ is a prescribed critical plastic region radius measured from the crack tip at $\theta = 0$ (see Figure 5.2.7). The corresponding elastic bending moment capacity of the associated plate girder is expressed as

$$M_{cr} = \sigma_{cr} S \qquad (5.2.103)$$

5.3   Theoretical Shear Force Capacity Expressions

The continued growth of a diagonal fatigue crack may adversely affect the shear strength of a web panel, and concurrently the overall girder, corresponding to the limit states of shear yielding and local buckling. Furthermore, the presence of the crack introduces two additional limit states including brittle fracture and impending ductile failure (Sun & Jin, 2012, chs. 3, 5). Overall, the growth of a diagonal fatigue crack may bring about the premature occurrence of elastic limit states in a girder (Bowman, 2004; Chajes et al., 2005; Kirke & Al-Jamel, 2004, sec. 2.3.3; Lichtenstein, 1990; Minor & Woodward, 1996; Wardhana & Hadipriono, 2003; Zhou & Biegalski, 2010).

Several assumptions are made with regard to the formulation of the shear capacity expressions. It is assumed that the portions of the plate girder that the expressions are applicable to are loaded under predominantly shear (see Figure 5.3.1b). As with the formulation of the bending moment capacity expressions, the plate girder itself is assumed to be an I-shaped transversely stiffened steel plate girder (see Figure 5.3.1a).

The individual plates of the girder are assumed to be constructed of high-strength low-alloy structural steel. As such, the steel is implied to be homogeneous and behave as a linear isotropic elastic material (Sadd, 2009, sec. 4.1). Also, the plates are assumed to be sufficiently thin enough for plane stress conditions to predominate. The web panel itself is assumed to have a depth, d_w, and a width, s, designating the spacing between the stiffener plates (see Figure 5.3.1b, c).
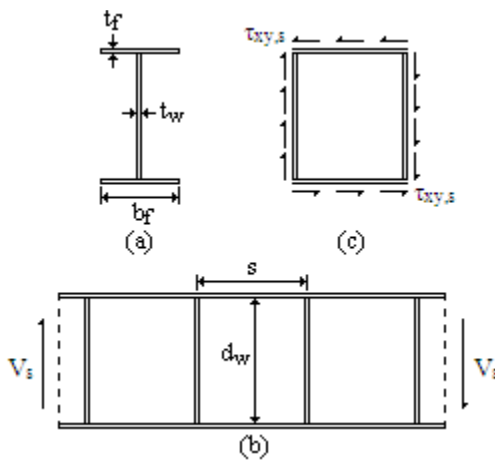
Figure 5.3.1: (a) I-shaped steel plate girder cross-section, (b) girder loaded under predominantly shear and subdivided into individual web panels by transverse stiffener plates, (c) web panel loaded under pure shear.

5.3.1   Diagonal Crack in Web Panel

The diagonal fatigue crack of length *2a* is assumed to be through-thickness and loaded primarily by Mode I loading with minimal influence from Mode II loading. As such, the crack is assumed to propagate in a comparatively straight line from a corner of the web panel at an angle $\theta \approx 45°$ relative to the flange (see Figure 5.3.2) (Sun & Jin, 2012, ch. 5). Two coordinate axis systems are stipulated; the *x'-y'* axis system is orthogonal with the diagonal crack, and the *x-y* axis system is orthogonal with the web panel.
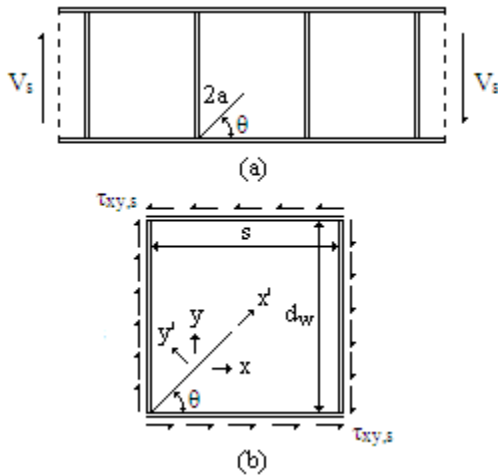
Figure 5.3.2: (a) Girder loaded under predominantly shear with diagonal fatigue crack originating at a corner of a web panel, (b) diagonal fatigue crack within the web panel displaying the *x-y* and *x'-y'* axis systems.

5.3.1.1 Web Local Buckling

A web panel located in a region of a girder loaded under predominantly shear is itself effectively loaded under pure shear (Salmon et al., 2009, sec. 11.7). This configuration is manifested in the form of uniform shear stress, $\tau_{xy,s}$, acting along the perimeter of the web panel (see Figure 5.3.2b). The perimeter shear stress is directly linked to and approximately equal to the internal shear stress within the web panel. Also, $\tau_{xy,s}$ is directly coupled to the external shear force, V_s, acting at that particular region of the girder (see Figure 5.3.2a). The distribution of internal shear stress along the depth of the web is nearly uniform, and thus $\tau_{xy,s}$ may be approximated as the magnitude of V_s divided by the gross cross-sectional area of the web, expressed as (Barker & Puckett, 1997, p. 818)

$$\tau_{xy,s} = \frac{V_s}{A_w} = \frac{V_s}{d_w t_w}$$

(5.3.1)

where A_w is the gross cross-sectional area of the web and t_w is the thickness of the web. The importance of $\tau_{xy,s}$ lies in its direct link to the internal shear stress, which itself has a direct influence upon the elastic buckling strength of the web panel (Vinson, 1974, sec. 6.1).

The presence of a diagonal crack originating at a corner of a web panel (see Figure 5.3.2b) may serve to influence the magnitude and distribution of the internal shear stress, thus affecting the buckling strength of the web panel. This process may be elucidated in two steps. First, the internal shear stress field, $\tau_{xy,c}$, within the cracked web panel is developed based upon $\tau_{xy,s}$ (see Figure 5.3.3a). Second, $\tau_{xy,c}$ influences the buckling strength of the web panel (see Figure 5.3.3b). It can thus be foreseen that the formulation of an expression for the elastic shear force capacity of a cracked web panel associated with the limit state of web local buckling requires an expression for $\tau_{xy,c}$.
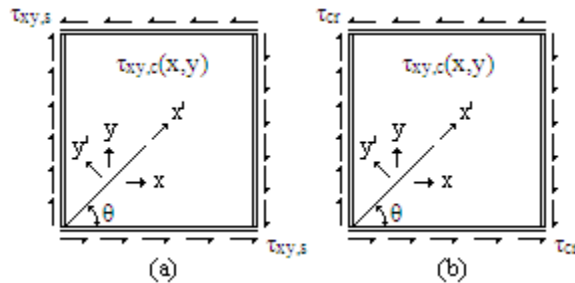
Figure 5.3.3: (a) Internal shear stress influenced by perimeter shear stress, (b) critical magnitude of perimeter shear stress corresponding to web buckling as influenced by internal shear stress.

The internal shear stress field, $\tau_{xy,c}$, within a cracked web panel may be approximately determined using elasticity theory (see Appendix D: Theory of Elasticity). The geometrical boundary conditions associated with the actual configuration of a diagonal crack originating at a corner of the web panel are inexorably complex, and a closed-form solution is difficult to obtain (see Figure 5.3.3a) (Sadd, 2009, ch. 7).

However, two observations are made regarding the geometrical boundary conditions of the crack and web panel. First, both ends of the crack are effectively restrained from opening. Second, the perimeter of the web panel formed by the flanges and stiffener plates is much more rigid than the web. As a consequence, the diagonal crack may be approximated as lying within the web plate and bounded by an outside margin of additional web plate representing the rigidity of the flanges and stiffener plates, thus resolving the original three-dimensional configuration into a two-dimensional configuration (see Figure 5.3.4a). A further approximation may then be made in assuming that the previous configuration is nearly equivalent to a diagonal crack lying within an infinite plate. The problem is thus reduced to that of determining the shear stress field around a central crack inclined at an angle $\theta \approx 45°$ and loaded by far-field shear stress equal in magnitude to $\tau_{xy,s}$ (see Figure 5.3.4b).
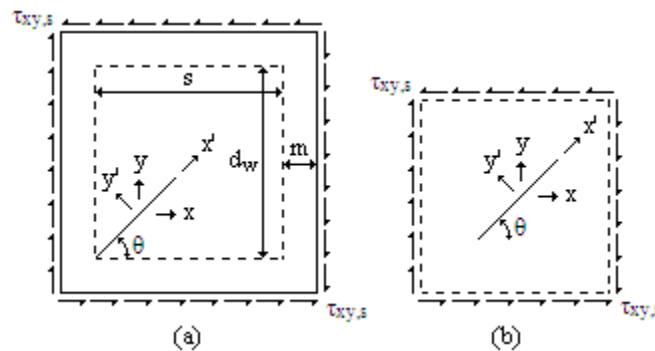
Figure 5.3.4: (a) Two-dimensional web panel configuration, (b) infinite plate web panel configuration.

The shear stress field around the inclined central crack (see Figure 5.3.4b) is determined by superimposing the stress fields of three distinct cases (Sun & Jin, 2012, sec. 3.5). The first case consists of an infinite plate without the crack loaded by far-field shear stress equal in magnitude to $\tau_{xy,s}$ (see Figure 5.3.5a). The second case consists of an

infinite plate with the inclined central crack loaded by crack-face normal stress, σ'_y (see Figure 5.3.5b). The third case consists of an infinite plate with the inclined central crack loaded by crack-face shear stress, τ'_{xy} (see Figure 5.3.5c). The magnitudes of σ'_y and τ'_{xy} are obtained from the state of stress of an element within the first case that has been transformed to the x'-y' axis system from the x-y axis system.
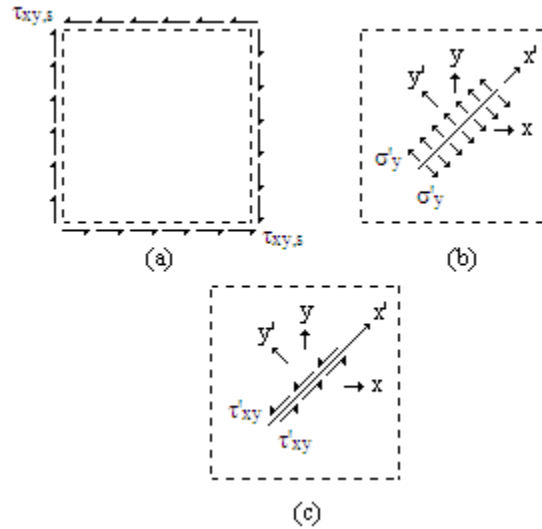
Figure 5.3.5: (a) Case 1: infinite plate without crack loaded by far-field shear stress, (b) Case 2: infinite plate with diagonal crack loaded by crack-face normal stress, (c) Case 3: infinite plate with diagonal crack loaded by crack-face shear stress.

Considering the first case with respect to the x-y axis system, an infinitesimal element at any location within the infinite plate is under a state of pure shear equal in magnitude to $\tau_{xy,s}$ (see Figure 5.3.6a). Rotation of the element by an angle θ to the x'-y' axis system results in the transformed normal and shear stresses σ'_y and τ'_{xy} (see Figure 5.3.6b) given by (Beer et al., 2006, ch. 7):

$$\sigma'_y = \tau_{xy,s} \sin(2\theta) \tag{5.3.2}$$

$$\tau'_{xy} = \tau_{xy,s} \cos(2\theta) \tag{5.3.3}$$
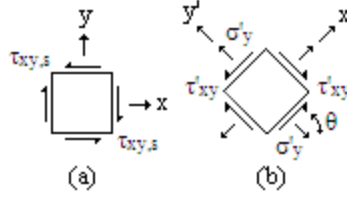
Figure 5.3.6: (a) Infinitesimal element under a state of pure shear, (b) rotated element with transformed normal and shear stresses.

These normal and shear stresses are assumed to act upon the crack-faces of the second and third cases, respectively (see Figure 5.3.5b, c). The stress field for each of these two cases is next determined.

In accordance with elasticity theory, the plane stress field is expressed in terms of the Airy stress function, $F(x,y)$, as (Sadd, 2009, ch. 7)

$$\sigma_x = \frac{\partial^2 F}{\partial y^2} \qquad \sigma_y = \frac{\partial^2 F}{\partial x^2} \qquad \tau_{xy} = -\frac{\partial^2 F}{\partial x \partial y} \tag{5.3.4}$$

The Airy stress function must satisfy the applicable boundary conditions and the governing biharmonic equation of plane elasticity given by (Sadd, 2009, ch. 7)

$$\nabla^4 F = \frac{\partial^4 F}{\partial x^4} + 2\frac{\partial^4 F}{\partial x^2 \partial y^2} + \frac{\partial^4 F}{\partial y^4} = 0 \tag{5.3.5}$$

such that the equilibrium equations and Beltrami-Michell compatibility equations are identically satisfied (see Appendix D: Theory of Elasticity). The presence of a crack introduces local disturbances in the stress field which complicates the determination of a suitable stress function. The stress field around a crack may then be determined using a subset of the complex potential method called the Westergaard function method (see Appendix G: Linear Elastic Fracture Mechanics) (Westergaard, 1939). In this method, the Airy stress function is expressed in terms of the Westergaard function, $Z(\zeta)$, for Mode I loading as (Sun & Jin, 2012, ch. 3)

$$F_I = \mathrm{Re}\,\overline{\overline{Z}}_I + y\,\mathrm{Im}\,\overline{Z}_I \tag{5.3.6}$$

and for Mode II loading as (Sun & Jin, 2012, ch. 3)

$$F_{II} = \mathrm{Re}\,\overline{\overline{Z}}_I + y\,\mathrm{Im}\,\overline{Z}_I - y\,\mathrm{Re}\,\overline{Z}_{II} \tag{5.3.7}$$

where

$$Z' = \frac{dZ}{d\zeta} \qquad \overline{Z} = \frac{d\overline{Z}}{d\zeta} \qquad \overline{\overline{Z}} = \frac{d\overline{\overline{Z}}}{d\zeta} \tag{5.3.8}$$

The terms Z_I and Z_{II} are the Westergaard functions for Mode I and Mode II loading, respectively. Also, ζ is the complex variable $\zeta = x + iy$.

The stress fields for the second and third cases are determined by employing the Westergaard stress functions associated with crack-face normal stress and crack-face shear stress, respectively, given by (Sedov, 1972, sec. 13.2.8)

$$Z_I = \sigma'_y \left(\frac{\xi}{\sqrt{\xi^2 - a^2}} - 1 \right) \tag{5.3.9}$$

$$Z_{II} = \tau'_{xy} \left(\frac{\xi}{\sqrt{\xi^2 - a^2}} - 1 \right) \tag{5.3.10}$$

It is noted that these stress functions are given with respect to the *x'-y'* axis system. Substituting (5.3.6) into (5.3.4) results in the complete stress field for the second case relative to the *x'-y'* axis system, given by (Sun & Jin, 2012, ch. 3)

$$\sigma'_{x,c2}(x', y') = \mathrm{Re}\,Z_I - y'\,\mathrm{Im}\,Z'_I$$

$$\sigma'_{y,c2}(x', y') = \mathrm{Re}\,Z_I + y'\,\mathrm{Im}\,Z'_I \tag{5.3.11}$$

$$\tau'_{xy,c2}(x', y') = -y'\,\mathrm{Re}\,Z'_I$$

In a similar manner, substituting (5.3.7) into (5.3.4) results in the complete stress field for the third case relative to the x'-y' axis system, given by (Sun & Jin, 2012, ch. 3)

$$\sigma'_{x,c3}(x', y') = 2\,\mathrm{Im}\,Z_{II} + y'\,\mathrm{Re}\,Z'_{II}$$

$$\sigma'_{y,c3}(x', y') = -y'\,\mathrm{Re}\,Z'_{II} \tag{5.3.12}$$

$$\tau'_{xy,c3}(x', y') = \mathrm{Re}\,Z_{II} - y'\,\mathrm{Im}\,Z'_{II}$$

The summation of (5.3.11) and (5.3.12) results in the superimposed stress field obtained from the second and third cases, given by

$$\sigma'_{x,c}(x', y') = \sigma'_{x,c2} + \sigma'_{x,c3}$$

$$\sigma'_{y,c}(x', y') = \sigma'_{y,c2} + \sigma'_{y,c3} \tag{5.3.13}$$

$$\tau'_{xy,c}(x', y') = \tau'_{xy,c2} + \tau'_{xy,c3}$$

The superimposed shear stress field, $\tau_{xy,ca}$, obtained from the second and third cases is transformed to the x-y axis system from the x'-y' axis system by substituting (5.3.13) into the following transformation expression (Beer et al., 2006, ch. 7):

$$\tau_{xy,ca}(x, y) = -\frac{\sigma'_{x,c} + \sigma'_{y,c}}{2}\sin(-2\theta) + \tau'_{xy,c}\cos(-2\theta) \tag{5.3.14}$$

where the coordinates of the x'-y' axis system are expressed in terms of the coordinates of the x-y axis system as

$$x' = y\sin\theta + x\cos\theta \tag{5.3.15}$$

$$y' = y\cos\theta - x\sin\theta \tag{5.3.16}$$

Finally, the complete shear stress field around the inclined central crack with respect to the x-y axis (see Figure 5.3.4b) is obtained by superimposing (5.3.14) with the shear stress field, $\tau_{xy,s}$, of the first case:

131

$$\tau_{xy,c}(x,\,y) = \tau_{xy,ca} + \tau_{xy,s} \tag{5.3.17}$$

The full expansion of (5.3.17) is quite lengthy and consists of real and imaginary terms. However, (5.3.17) is greatly simplified if $\theta \approx 45°$, thus reducing the expanded form of (5.3.17) to the following:

$$\tau_{xy,c}(x,\,y) = \sin(2\theta)\, y'\, \text{Im}\left[\frac{\tau_{xy,s}\sin(2\theta)a^2}{\left(2ix'\,y'+x'^2-y'^2-a^2\right)^{3/2}}\right] + \tau_{xy,s} \tag{5.3.18}$$

Resolving the imaginary term results in

$$\tau_{xy,c}(x,\,y) = \frac{\tau_{xy,s}\sin(2\theta)^2\, y'\, a^2\, \sqrt{2\sqrt{k_1}-k_2}\left(\sqrt{k_1}+k_2\right)}{k_1^{3/2}} + \tau_{xy,s} \tag{5.3.19}$$

where,

$$k_1 = 2x'^2\, y'^2 - 2x'^2\, a^2 + 2y'^2\, a^2 + x'^4 + y'^4 + a^4 \tag{5.3.20}$$

$$k_2 = 2x'^2 - 2y'^2 - 2a^2 \tag{5.3.21}$$

Equation (5.3.19) represents the complete shear stress field around the central crack inclined at $\theta \approx 45°$ and lying within the infinite plate loaded by the far-field shear stress $\tau_{xy,s}$ (see Figure 5.3.4b). In accordance with the aforementioned approximations, the shear stress field obtained from this configuration is approximately equivalent to the internal shear stress field obtained from the actual configuration of a cracked web panel with the diagonal crack originating at a corner of the web panel (see Figure 5.3.3a). Importantly, it is noted that (5.3.19) is in part a function of $\tau_{xy,s}$, and is therefore directly coupled to V_s by way of (5.3.1).

Close examination of (5.3.19) reveals that the distribution of $\tau_{xy,c}$ within a cracked web panel is quite complex. Magnitudes of shear stress much greater than $\tau_{xy,s}$ are especially prevalent in the local region around the crack. The distribution of $\tau_{xy,c}$ may be

132

approximated by subdividing the web panel into equal-sized rectangular elements. The total number of elements, N_e, are arranged such that the number of element rows, r_e, are equal to the number of element columns, c_e. Each element is designated by its row number, r, and column number, c, relative to the origin of the crack (see Figure 5.3.7a). Also, each element is loaded under pure shear designated by $\tau_{xy,e\text{-}rc}$. The magnitude of $\tau_{xy,e\text{-}rc}$ for each element is developed based upon $\tau_{xy,c}$. Specifically, the magnitude of $\tau_{xy,e\text{-}rc}$ for each element is the value of $\tau_{xy,c}$ at the central point of the element (see Figure 5.3.7b). It can be foreseen that a greater number of elements results in a higher degree of accuracy in describing the actual distribution of $\tau_{xy,c}$.
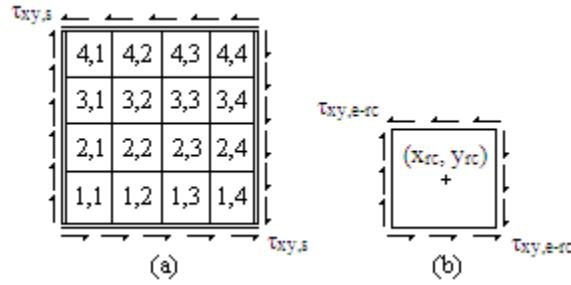
Figure 5.3.7: (a) Web panel subdivided into rectangular elements displaying row and column numbers, (b) individual panel element loaded under pure shear.

The magnitude of $\tau_{xy,e\text{-}rc}$ for any element is expressed in terms of $\tau_{xy,c}$ by setting x and y equal to the coordinates of the central point of the element, x_{rc} and y_{rc}, expressed as

$$x_{rc} = \frac{2sc - s - 2ar_e \cos\theta_o}{2r_e} \tag{5.3.22}$$

$$y_{rc} = \frac{2d_w r - d_w - 2ac_e \sin\theta_o}{2c_e} \tag{5.3.23}$$

where r_e and c_e are expressed in terms of N_e as

$$r_e = c_e = \sqrt{N_e} \tag{5.3.24}$$

133

and,

$$\theta_o = \theta \qquad (5.3.25)$$

Also, θ in (5.3.15), (5.3.16), and (5.3.19) is modified to take into account negative values of x:

$$\theta = \theta_o + \pi \left(\frac{|x_{rc}| - x_{rc}}{2x_{rc}} \right) \qquad (5.3.26)$$

Thus, the value of $\tau_{xy,e\text{-}rc}$ for any element is determined by substituting r, c, (5.3.24), and (5.3.25) into (5.3.22) and (5.3.23), and introducing the results into (5.3.19), implicitly expressed as

$$\tau_{xy,e\text{-}rc} = \tau_{xy,c}(x_{rc}, y_{rc}) \qquad (5.3.27)$$

It is observed that since $\tau_{xy,e\text{-}rc}$ is a function of $\tau_{xy,c}$, it is therefore also a function of $\tau_{xy,s}$. Altogether, the varying values of $\tau_{xy,e\text{-}rc}$ for each element represent an approximation of the internal shear stress distribution, $\tau_{xy,c}$, within the cracked web panel.

A closed-form solution for the elastic buckling strength of the cracked web panel is difficult to obtain using classical plate theory (see Appendix F: Classical Plate Theory) (Salmon et al., 2009, sec. 6.14; Vinson, 1974, ch. 5). This is primarily due to the non-uniform internal stress field caused by the presence of the crack, as well as the complex geometrical boundary conditions introduced by the crack. The Rayleigh-Ritz energy method employs the principle of stationary potential energy to approximate the buckling strength when complex boundary conditions are present (see Appendix E: Principle of Stationary Potential Energy) (Vinson, 1974, sec. 6.1). In this method, the buckled shape of the cracked web panel is assumed to take on a form described by an out-of-plane displacement function, $w(x'', y'')$, expressed in terms of the x''-y'' axis system with the

origin at the central point of the web panel (see Figure 5.3.8). The displacement function satisfies all or most of the geometrical boundary conditions and includes an arbitrary set of variables, A_i, which control the shape of the displacement function, in the form

$$w(x'', y'') = \sum_{i=1}^{n} A_i f_i(x'', y'') \tag{5.3.28}$$

where n is the number of degrees of freedom of the displacement function. The total potential energy, Π, of the panel is then formulated, expressed as (Vinson, 1974, sec. 6.1)

$$\Pi = \int_V U dV - \int_S T_i u_i dS \tag{5.3.29}$$

where U is the strain energy density function, V is the volume of the panel, T_i are the applied surface tractions, u_i are the displacements caused by the tractions, and S is the surface over which the tractions are applied. It is evident that the formulation of Π essentially couples $w(x'', y'')$ with the externally applied stress, $\tau_{xy,s}$ (see Figure 5.3.8). The variation of Π with respect to A_i is then set to zero, expressed by (F.1.3) and shown as (Vinson, 1974, sec. 6.1)

$$\frac{\delta \Pi}{\delta A_i} = 0 \tag{5.3.30}$$

It follows that the critical external stress, τ'_{cr}, enabling this equilibrium is an initial estimation of the buckling strength of the cracked web panel.
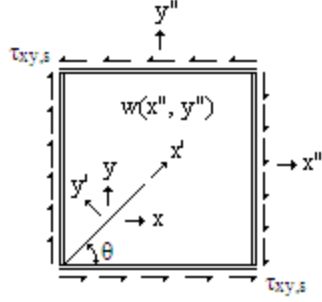
Figure 5.3.8: Cracked web panel with externally applied perimeter shear stress and corresponding out-of-plane displacement function.

The initial magnitude of τ'_{cr} may be further developed by employing the web panel elements and the previously derived approximate internal shear stress distribution, $\tau_{xy,e\text{-}rc}$. Specifically, the overall initial cracked web panel buckling strength is assumed to be uniformly distributed among each of the web panel elements. The strength of each element is further assumed to be degraded by the ratio of $\tau_{xy,s}$ to $\tau_{xy,e\text{-}rc}$. In this way, the buckling strength of each element, $\tau_{cr,e\text{-}rc}$, is equal to the product of the ratio of $\tau_{xy,s}$ to $\tau_{xy,e\text{-}rc}$ and the initial cracked web panel buckling strength, divided by the total number of elements, expressed as

$$\tau_{cr,e-rc} = \frac{\tau'_{cr}}{N_e}\left(\frac{\tau_{xy,s}}{\tau_{xy,e-rc}}\right) \tag{5.3.31}$$

Each element is thus assumed to buckle when $\tau_{xy,e\text{-}rc}$ equals or exceeds $\tau_{cr,e\text{-}rc}$. The corresponding critical value of $\tau_{xy,s}$ for each element may then be determined. It follows that the final estimation of the buckling strength of the cracked web panel, τ_{cr}, is the sum of the critical values of $\tau_{xy,s}$.

An expression for $w(x'', y'')$ for the overall cracked web panel is first required for the formulation of Π and the determination of τ'_{cr}. The geometrical boundary conditions

136

concerning the edges of the web panel are conservatively assumed to be simply supported (Salmon et al., 2009, sec. 11.7):

$$w\left(\frac{s}{2}, y''\right) = 0 \qquad w\left(-\frac{s}{2}, y''\right) = 0$$

$$w\left(x'', \frac{d_w}{2}\right) = 0 \qquad w\left(x'', -\frac{d_w}{2}\right) = 0$$

(5.3.32)

The approximation is made that $w(x'', y'')$ for the cracked web panel is nearly identical to $w(x'', y'')$ for an uncracked web panel. The geometrical boundary conditions concerning the diagonal crack are therefore neglected, and $w(x'', y'')$ is formulated based only upon the boundary conditions given by (5.3.32). In essence, the approximation is made that the initial buckling strength of the cracked web panel is dependent only upon the external shear stress, with $w(x'', y'')$ remaining identical to $w(x'', y'')$ for the uncracked web panel. A unilateral displacement function of the following form satisfies the boundary conditions given by (5.3.32):

$$w(x'', y'') = A\cos\left(\frac{\pi x}{s}\right)\cos\left(\frac{\pi y}{d_w}\right)$$

(5.3.33)

The formulation of Π is developed by substituting (5.3.33) and $\tau_{xy,s}$ into (5.3.29), implicitly expressed as (Vinson, 1974, sec. 6.1)

$$\Pi = \frac{D}{2}\int_{-\frac{d_w}{2}}^{\frac{d_w}{2}}\int_{-\frac{s}{2}}^{\frac{s}{2}}U_e dx''dy'' + \tau_{xy,s}\int_{-\frac{d_w}{2}}^{\frac{d_w}{2}}\int_{-\frac{s}{2}}^{\frac{s}{2}}W_e dx''dy''$$

(5.3.34)

where,

$$U_e = \left(\frac{\partial^2 w}{\partial x''^2} + \frac{\partial^2 w}{\partial y''^2}\right)^2 - 2(1-v)\left[\left(\frac{\partial^2 w}{\partial x''^2}\right)\left(\frac{\partial^2 w}{\partial y''^2}\right) - \left(\frac{\partial^2 w}{\partial x''\partial y''}\right)^2\right]$$

(5.3.35)

137

and,

$$W_e = \left(\frac{\partial w}{\partial x''}\right)\left(\frac{\partial w}{\partial y''}\right) \tag{5.3.36}$$

Also, the term D is the web panel rigidity given by (Salmon et al., 2009, sec. 6.14)

$$D = \frac{Et_w^3}{12(1-v^2)} \tag{5.3.37}$$

where E is the modulus of elasticity and v is Poisson's ratio. The initial cracked web panel buckling strength is then determined by introducing (5.3.34) into (5.3.30), solving for $\tau_{xy,s}$, and dividing the result by t_w, giving

$$\tau'_{cr} = \frac{D}{2t_w}\frac{\int\limits_{-\frac{d_w}{2}}^{\frac{d_w}{2}}\int\limits_{-\frac{s}{2}}^{\frac{s}{2}} U_e dx'' dy''}{\int\limits_{-\frac{d_w}{2}}^{\frac{d_w}{2}}\int\limits_{-\frac{s}{2}}^{\frac{s}{2}} W_e dx'' dy''} \tag{5.3.38}$$

where the arbitrary term A in (5.3.33) vanishes in accordance with calculus of variations (Vinson, 1974, sec. 6.1).

The initial cracked web panel buckling strength is further refined by determining the buckling strengths of the web panel elements and summing the associated critical values of $\tau_{xy,s}$. The external stress applied to each element is the previously derived pure shear stress $\tau_{xy,e\text{-}rc}$ given by (5.3.27) (see Figure 5.3.7b). Equation (5.3.27) may be rewritten to be explicitly expressed in terms of $\tau_{xy,s}$ as

$$\tau_{xy,e-rc} = \tau_{xy,s}(C_{rc}+1) \tag{5.3.39}$$

138

where C_{rc} is a constant directly derived from (5.3.19) and partially dependent upon r, c, x_{rc}, and y_{rc} of a given element, expressed as

$$C_{rc} = \frac{\sin(2\theta)^2 \, y' a^2 \sqrt{2\sqrt{k_1} - k_2}\,(\sqrt{k_1} + k_2)}{k_1^{3/2}} \tag{5.3.40}$$

The critical value of $\tau_{xy,s}$ corresponding to buckling of each element is determined by setting $\tau_{xy,e-rc} = \tau_{cr,e-rc}$, introducing (5.3.38) and (5.3.39) into (5.3.31), and solving for $\tau_{xy,s}$, giving

$$\tau_{cr,e-rc} = \frac{D}{2N_e t_w (C_{rc} + 1)^2} \frac{\displaystyle\int_{-\frac{d_w}{2}}^{\frac{d_w}{2}} \int_{-\frac{s}{2}}^{\frac{s}{2}} U_e \, dx'' \, dy''}{\displaystyle\int_{-\frac{d_w}{2}}^{\frac{d_w}{2}} \int_{-\frac{s}{2}}^{\frac{s}{2}} W_e \, dx'' \, dy''} \tag{5.3.41}$$

Finally, the approximate buckling strength of the cracked web panel is determined by taking the sum of $\tau_{cr,e-rc}$ for all of the elements, expressed as

$$\tau_{cr} = \sum_{r=1}^{\sqrt{N_e}} \sum_{c=1}^{\sqrt{N_e}} \tau_{cr,e-rc} \leq \tau_Y \tag{5.3.42}$$

The term τ_Y is the shear yield strength of the web panel steel given by (Salmon et al., 2009, sec. 2.6)

$$\tau_Y = \frac{\sigma_Y}{\sqrt{3}} \tag{5.3.43}$$

where σ_Y is the yield strength of the web panel steel. Setting $\tau_{cr} = \tau_{xy,s}$, substituting (5.3.42) into (5.3.1), and solving for V_s results in the shear force capacity of a cracked web panel corresponding to the limit state of web local buckling:

139

$$V_{cr} = \tau_{cr} d_w t_w \tag{5.3.44}$$

5.3.1.2 Shear Yielding

The growth of the diagonal fatigue crack originating at a corner of the web panel reduces the gross cross-sectional area of the panel (see Figure 5.3.9). From (5.3.1) it can be deduced that the reduction in gross cross-sectional area serves to decrease the shear force capacity corresponding to shear yielding. The reduced web panel depth, d_{wc}, above the crack tip is given by

$$d_{wc} = d_w - 2a\sin\theta \tag{5.3.45}$$

Substituting (5.3.45) for d_w, and τ_Y for $\tau_{xy,s}$ in (5.3.1), and solving for V_s results in

$$V_{cr} = \tau_Y t_w \left(d_w - 2a\sin\theta\right) \tag{5.3.46}$$

The internal shear stress along d_{wc} achieves shear yielding first at the crack tip and last at the perimeter of the web panel. The critical value of $\tau_{xy,s}$ corresponding to V_{cr} thus occurs when $\tau_{xy,s}$ equals the shear yield strength of the web panel steel, given by

$$\tau_{cr} = \tau_Y \tag{5.3.47}$$

Setting $\tau_{cr} = \tau_{xy,s}$, substituting (5.3.47) into (5.3.1), and solving for V_s results in the shear force capacity of a cracked web panel corresponding to the limit state of shear yielding:

$$V_{cr} = \tau_{cr} d_w t_w \tag{5.3.48}$$
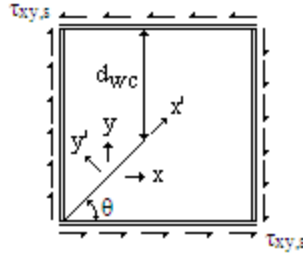
Figure 5.3.9: Cracked web panel with reduced web panel depth.

5.3.1.3 Brittle Fracture

The propagation of the diagonal fatigue crack originating at a corner of the web panel (see Figure 5.3.2b) is accompanied by a corresponding increase in the stress intensity factor, K, at the crack tip. This increase in K introduces two additional limit states including brittle fracture and impending ductile failure. Brittle fracture is characterized by the sudden rupture of the web panel and occurs when the fatigue crack grows to a critical length and K equals the critical stress intensity factor, K_c, of the web panel steel (Meguid, 1989, ch. 3; Sun & Jin, 2012, chs. 2, 3). Alternatively, impending ductile failure is characterized by the growth of the plastic region around the crack tip to a critical size and occurs when the crack length and K each equal a critical magnitude (Meguid, 1989, chs. 5, 6).

In accordance with linear elastic fracture mechanics (LEFM), the theoretical form of K is given by (Sun & Jin, 2012, sec. 3.4)

$$K = \sigma_o \sqrt{\pi a} \tag{5.3.49}$$

where σ_o is the far-field Mode I or II stress acting upon the crack. As previously mentioned, the diagonal crack shown in Figure 5.3.2b is loaded primarily by Mode I loading with minimal influence from Mode II loading when $\theta \approx 45°$. Employing the

principle of superposition, the total stress intensity factor, K_T, is the sum of the stress intensity factors derived from the Mode I and II loading, expressed by (Sun & Jin, 2012, sec. 3.5)

$$K_T = K_I + K_{II} \qquad (5.3.50)$$

where K_I and K_{II} are the stress intensity factors associated with Mode I and II loading, respectively. The magnitudes of K_I and K_{II} for the diagonal crack may be approximated by assuming once again that the actual configuration of the diagonally cracked web panel (see Figure 5.3.2b) is nearly equivalent to the configuration of a diagonal crack inclined at an angle $\theta \approx 45°$ and lying within an infinite plate loaded by far-field shear stress equal in magnitude to $\tau_{xy,s}$ (see Figure 5.3.4b).

The Mode I and II stress intensity factors are derived from the state of stress of an element in the previously described configuration (see Figure 5.3.4b) that has been transformed to the *x'-y'* axis system from the *x-y* axis system (see Figure 5.3.6). The normal stress, σ'_y, and shear stress, τ'_{xy}, of the transformed element are expressed by (5.3.2) and (5.3.3), respectively. The magnitudes of σ'_y and τ'_{xy} represent the far-field normal and shear stresses, respectively, acting upon the diagonal crack. Substituting (5.3.2) and (5.3.3) into (5.3.49) results in expressions for K_I and K_{II}, shown as

$$K_I = \tau_{xy,s} \sin(2\theta)\sqrt{\pi a} \qquad (5.3.51)$$

$$K_{II} = \tau_{xy,s} \cos(2\theta)\sqrt{\pi a} \qquad (5.3.52)$$

Under plane strain conditions, Mode I brittle fracture occurs when K_I exceeds the Mode I fracture toughness, K_{Ic}, of the web panel steel (Meguid, 1989, chs. 3, 4). Similarly, Mode II brittle fracture occurs when K_{II} exceeds the Mode II fracture toughness, K_{IIc}, of the web panel steel (Meguid, 1989, chs. 3, 4).

Given that the crack is concurrently subjected to Mode I and II loading, certain critical combinations of K_I and K_{II} may produce mixed-mode fracture. The interaction between K_I and K_{II} with respect to K_{Ic} and K_{IIc} may be described by a simple elliptical model, expressed as (Sun & Jin, 2012, sec. 5.1)

$$\left(\frac{K_I}{K_{Ic}}\right)^2 + \left(\frac{K_{II}}{K_{IIc}}\right)^2 = 1 \tag{5.3.53}$$

Stress intensity correction factors may be used to modify K_I and K_{II} in (5.3.53) to account for the finite dimensions of the web panel (Shukla, 2005, ch. 3). However, the length of the diagonal crack is expected to remain small in comparison to the web panel prior to an elastic limit state being attained, and thus the correction factor is neglected. The perimeter shear stress capacity of the cracked web panel corresponding to the limit state of brittle fracture is determined by introducing (5.3.51) and (5.3.52) into (5.3.53) and solving for $\tau_{xy,s}$:

$$\tau_{cr} = \frac{K_{Ic} K_{IIc}}{\sqrt{\pi a}\sqrt{K_{IIc}^2 \sin(2\theta)^2 - K_{Ic}^2 \sin(2\theta)^2 + K_{Ic}^2}} \leq \tau_Y \tag{5.3.54}$$

It is noted that the use of K_{Ic} and K_{IIc} in (5.3.54) is conservative since plane stress conditions are presumed to predominate throughout the web panel, and the actual critical stress intensity factors are greater than K_{Ic} and K_{IIc} (Shukla, 2005, ch. 4). Setting $\tau_{cr} = \tau_{xy,s}$, substituting (5.3.54) into (5.3.1), and solving for V_s results in the shear force capacity of a cracked web panel corresponding to the limit state of brittle fracture:

$$V_{cr} = \tau_{cr} d_w t_w \tag{5.3.55}$$

5.3.1.4 Impending Ductile Failure

The plastic region around the crack tip as induced by the Mode I and II loading must remain small in order for K_I and K_{II} to remain valid (Meguid, 1989, chs. 5, 6). The growth of the plastic region beyond a critical size renders the fracture toughness characterization of the web panel steel inapplicable. EPFM must then be employed to describe the impending ductile failure. A new limit state may be postulated corresponding to a critical plastic region size indicating the approximate transition to a ductile failure mode (i.e., the transition from LEFM to EPFM).

The size of the plastic region around the crack tip as induced by the mixed-mode loading may be determined by superimposing the plastic regions obtained from the Mode I and II loadings. Specifically, the two plastic radii along the longitudinal direction of the crack as obtained from the Mode I and II loadings may be determined and superimposed to obtain the mixed-mode plastic radius (see Figure 5.3.10). The critical magnitude of $\tau_{xy,s}$ associated with a critical mixed-mode plastic radius indicating impending ductile failure may then be solved for.
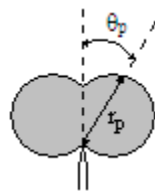
Figure 5.3.10: Plastic region around the crack tip.

The near-tip stress field is expressed in terms of K_I as (Sun & Jin, 2012, ch. 3),

$$\sigma_x = \frac{K_I}{\sqrt{2\pi r}} \cos \frac{\theta_p}{2} \left(1 - \sin \frac{\theta_p}{2} \sin \frac{3\theta_p}{2} \right)$$

$$\sigma_y = \frac{K_I}{\sqrt{2\pi r}} \cos \frac{\theta_p}{2} \left(1 + \sin \frac{\theta_p}{2} \sin \frac{3\theta_p}{2} \right) \tag{5.3.56}$$

$$\tau_{xy} = \frac{K_I}{\sqrt{2\pi r}} \sin \frac{\theta_p}{2} \cos \frac{\theta_p}{2} \cos \frac{3\theta_p}{2}$$

Similarly, the near-tip stress field is expressed in terms of K_{II} as (Sun & Jin, 2012, ch. 3),

$$\sigma_x = -\frac{K_{II}}{\sqrt{2\pi r}} \sin \frac{\theta_p}{2} \left(2 + \cos \frac{\theta_p}{2} \cos \frac{3\theta_p}{2} \right)$$

$$\sigma_y = \frac{K_{II}}{\sqrt{2\pi r}} \sin \frac{\theta_p}{2} \cos \frac{\theta_p}{2} \cos \frac{3\theta_p}{2} \tag{5.3.57}$$

$$\tau_{xy} = \frac{K_{II}}{\sqrt{2\pi r}} \cos \frac{\theta_p}{2} \left(1 - \sin \frac{\theta_p}{2} \sin \frac{3\theta_p}{2} \right)$$

It is noted that the near-tip stress fields are formulated in terms of polar coordinates with the origin at the crack tip. The variable r is the radius and θ_p is the angle of r with respect to the longitudinal direction of the crack (see Figure 5.3.10). The mixed-mode radius of the plastic region, r_p, is determined by employing the Mises yield criterion for plane stress, expressed as (Meguid, 1989, sec. 5.4)

$$\sigma_Y^2 = \sigma_1^2 + \sigma_2^2 - \sigma_1 \sigma_2 \tag{5.3.58}$$

where σ_1 and σ_2 are the principal stresses given by (Beer et al., 2006, sec. 7.3)

$$\sigma_{1,2} = \frac{\sigma_x + \sigma_y}{2} \pm \sqrt{\left(\frac{\sigma_x - \sigma_y}{2} \right)^2 + \tau_{xy}^2} \tag{5.3.59}$$

Substituting (5.3.56) and (5.3.57) into (5.3.59), introducing the results into (5.3.58), setting $\theta_p = 0°$, and solving for r results in the plastic radii along the longitudinal direction of the crack associated with Mode I and II loadings:

$$r_{p,I} = \frac{K_I^2}{2\pi\sigma_Y^2} \tag{5.3.60}$$

$$r_{p,II} = \frac{3K_{II}^2}{2\pi\sigma_Y^2} \tag{5.3.61}$$

The superposition of $r_{p,I}$ and $r_{p,II}$ requires that r_p is the greater value of (5.3.60) or (5.3.61). Given that the diagonal fatigue crack is inclined at an angle $\theta \approx 45°$, the Mode I loading predominates and the contribution of $r_{p,II}$ is superseded such that $r_p = r_{p,I}$. Substituting (5.3.51) into (5.3.60) and solving for $\tau_{xy,s}$ results in

$$\tau_{cr} = \frac{\sigma_Y\sqrt{2ar_{p,cr}}}{a\sin(2\theta)} \leq \tau_Y \tag{5.3.62}$$

where $r_{p,cr}$ is a predefined critical plastic radius along the longitudinal direction of the crack corresponding to the transition from LEFM to EPFM. Setting $\tau_{cr} = \tau_{xy,s}$, substituting (5.3.54) into (5.3.1), and solving for V_s results in the shear force capacity of a cracked web panel corresponding to the limit state of brittle fracture:

$$V_{cr} = \tau_{cr}d_wt_w \tag{5.3.63}$$

5.4   Validation of Capacity Expressions Using FE Analyses

5.4.1   Overview of FE Analyses

The derived flange plate capacity expressions, $\sigma_{cr} = f\{\Gamma\}$, are summarized in Table 5.4.1 for the fatigue crack configurations associated with predominantly bending.

Similarly, the derived web panel capacity expressions, $\tau_{cr} = f\{\Gamma\}$, are summarized in Table 5.4.2 for the fatigue crack configuration associated with predominantly shear. These formulations were numerically validated using the general FE software ABAQUS/CAE 6.11.

Table 5.4.1. Flange stem capacity expressions (associated with bending moment).

Crack configuration	Limit state	Capacity expression
Three-ended crack	Tension buckling in flange	$\sigma_{cr} = 3.58 \dfrac{Et_f^2(v-2)}{a^2(v^2-1)} \leq \sigma_Y$
	Brittle fracture	$\sigma_{cr} = \dfrac{K_{Ic}}{\sqrt{\pi a}} \leq \sigma_Y$
	Impending ductile failure	$\sigma_{cr} = \dfrac{\sigma_Y\sqrt{2ar_{p,cr}}}{a} \leq \sigma_Y$
Vertical edge-crack	Yielding of compression flange	$\sigma_{cr} = \beta_{cf}\sigma_Y \leq \sigma_Y$
	Local buckling of compression flange	$\sigma_{cr} = \beta_{cf}k\dfrac{\pi^2 E}{12(1-v^2)(b_f/2t_f)^2} \leq \sigma_Y$
	Web local buckling	$\sigma_{cr} = \beta_{cw}\dfrac{(64D\pi^2 - 3d_c^3)}{3t_w d_c^2} \leq \sigma_Y$
	Tension buckling In web	$\sigma_{cr} = 2.97 \dfrac{Et_w^2 d_w(1.56-v)}{a^2(d_w-2a)(1-v^2)} \leq \sigma_Y$
	Brittle fracture	$\sigma_{cr} = \dfrac{2K_{Ic}}{\sqrt{\pi a}} \leq \sigma_Y$
	Impending ductile failure	$\sigma_{cr} = \dfrac{2\sigma_Y\sqrt{2ar_{p,cr}}}{a} \leq \sigma_Y$
Horizontal crack extending through one or both sides of tension flange	Tension buckling in flange	$\sigma_{cr} = 2.97 \dfrac{Et_f^2(1.56-v)}{a^2(1-v^2)} \leq \sigma_Y$
	Brittle fracture	$\sigma_{cr} = \dfrac{K_{Ic}}{\sqrt{\pi a}} \leq \sigma_Y$
	Impending ductile failure	$\sigma_{cr} = \dfrac{\sigma_Y\sqrt{2ar_{p,cr}}}{a} \leq \sigma_Y$

Table 5.4.2. Web panel capacity expressions (associated with shear force).

Crack configuration	Limit state	Capacity expression
Diagonal crack in web panel	Web local buckling	$\tau_{cr} = \sum\limits_{r=1}^{\sqrt{N_e}} \sum\limits_{c=1}^{\sqrt{N_e}} \tau_{cr,e-rc} \leq \tau_Y$
	Shear yielding	$\tau_{cr} = \tau_Y$
	Brittle fracture	$\tau_{cr} = \dfrac{K_{Ic} K_{IIc}}{\sqrt{\pi a}\sqrt{K_{IIc}^2 \sin(2\theta)^2 - K_{Ic}^2 \sin(2\theta)^2 + K_{Ic}^2}} \leq \tau_Y$
	Impending ductile failure	$\tau_{cr} = \dfrac{\sigma_Y \sqrt{2 a r_{p,cr}}}{a \sin(2\theta)} \leq \tau_Y$

5.4.1.1 FE Analyses for Bending Moment Capacity Expressions

The general FE software ABAQUS/CAE 6.11 was used to model a series of full-scale trial plate girders (PG-1 through PG-4) for the purpose of numerically validating the capacity expressions associated with predominantly bending (see Table 5.4.1). Each trial girder was modeled with a length, $L = 5\ m$, and configured as a horizontal cantilever (see Figure 5.4.1a). The web plate depth was set to $d_w = 127\ cm$ and the flange plate width set to $b_f = 35\ cm$ (see Figure 5.4.1b). Each girder was assigned a varying flange plate thickness ranging from 0.3 to 2.4 cm (see Table 5.4.3). The web plate thickness, t_w, was set to half the flange plate thickness. The section dimensions of PG-1 and PG-2 are purely theoretical for the function of investigating a wide range of failure modes. Conversely, the section dimensions of PG-3 and PG-4 are comparable to realistic plate girders (Blodgett, 1966; Salmon et al., 2009, ch. 11)

Each through-thickness fatigue crack configuration was modeled at the mid-spans of each series of trial girders (PG-1 through PG-4) (see Figure 5.4.1a, c). Each crack configuration, in turn, was modeled with varying incremental branch lengths. The trial

girders were modeled with the general properties of high-strength low-alloy steel (see Table 5.4.4). General values of the Paris-Erdogan equation material constants were taken as *C = 3.6 x 10^{-10}* and *m = 3.0* (Bowman, 2002; Shukla, 2005, ch. 5).
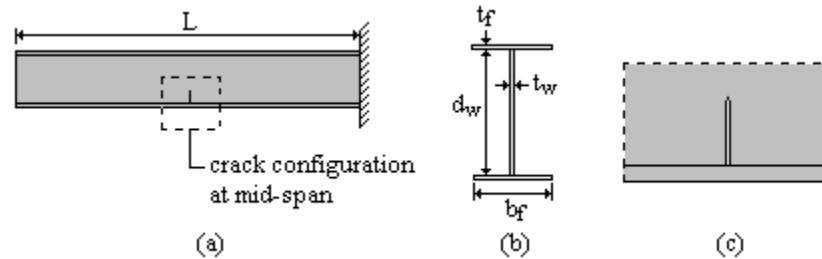
Figure 5.4.1: (a) Cantilever configuration of trial plate girders with (b) cross-section dimensions and (c) crack configuration at mid-span.

Table 5.4.3. Trial plate girder geometric properties.

Plate girder (PG)	Flange thickness, t_f (cm)	Web thickness, t_w (cm)	Web depth, d_w (cm)	Flange width, b_f (cm)
PG-1	0.30	0.15	127	35
PG-2	0.60	0.30	127	35
PG-3	1.20	0.60	127	35
PG-4	2.40	1.20	127	35

Table 5.4.4. Trial web panel material properties.

Modulus of elasticity, E (GPa)	Poisson's ratio, ν	Yield strength, σ_Y (MPa)	Mode I fracture toughness, K_{Ic} (MPa·m$^{1/2}$)
200[a]	0.3[a]	345[a]	98[b]

a. General properties of high-strength low-alloy structural steel (Salmon et al., 2009, ch. 2).
b. Representative fracture toughness of high-strength alloy steel (Meguid, 1989, ch. 5).

The trial girders were meshed using 10-node quadratic tetrahedron solid elements seeded at *5 – 15* cm (global or part seeds) (see Appendix I: FEA Models). The fixed end of each girder was modeled by configuring the entire face of one end with encastre support conditions. Each crack configuration was modeled as *0.1* cm wide rectangular extrusions with triangular notches at the crack tips (see Figure 5.4.1c). For tests involving

149

brittle fracture and impending ductile failure, a circular partition was modeled around the crack tip of interest and meshed with 20-node quadratic brick elements seeded at *0.025 – 0.250* cm (local seeds).

Full-scale trial flange stems and web plates corresponding to PG-1 through PG-4 were used to indirectly validate the capacity expressions associated with tension buckling. Numerical buckling analyses of the girders may result in alternative local and global buckling modes overriding the intended mode of tension buckling. Therefore, distinct flange stem and web plate models were employed for the purpose of concentrating the buckling analyses to that of buckling of the portions of the associated plate adjacent to the crack (embedded plates). Furthermore, the out-of-plane translation of each associated plate was restrained except for the areas of the embedded plates, essentially reducing the analysis to that of buckling of the embedded plates (as in an isolated system). The flange stems and web plates were modeled using 4-node shell elements seeded at *0.25 – 1.00* cm. The rotational and out-of-plane translations of the longitudinal edge bordering the web plate or flange plate were constrained. The area of each embedded plate was defined by modeling partitions along the perimeter of each plate. The associated crack configurations were modeled by assigning a seam to a single-line partition.

For each series of trial girders (PG-1 through PG-4), and associated flange stems, web plates, and crack configurations, an external bending moment, M_o, was applied to the free end of the girder, depending upon which capacity expression was being validated (see Figures 5.4.2 and 5.4.3). The external bending moment was modeled by loading the face on the free end with a linear stress distribution with the top half in compression and

the bottom half in tension. The bending moment and shear force capacities of the girders, flange stems, and web plates were then numerically calculated (see Section 3.3.2) and compared to the values obtained from the corresponding theoretical capacity expressions (see Table 5.4.1).
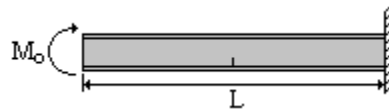
Figure 5.4.2: Trial plate girder loaded with external bending moment.
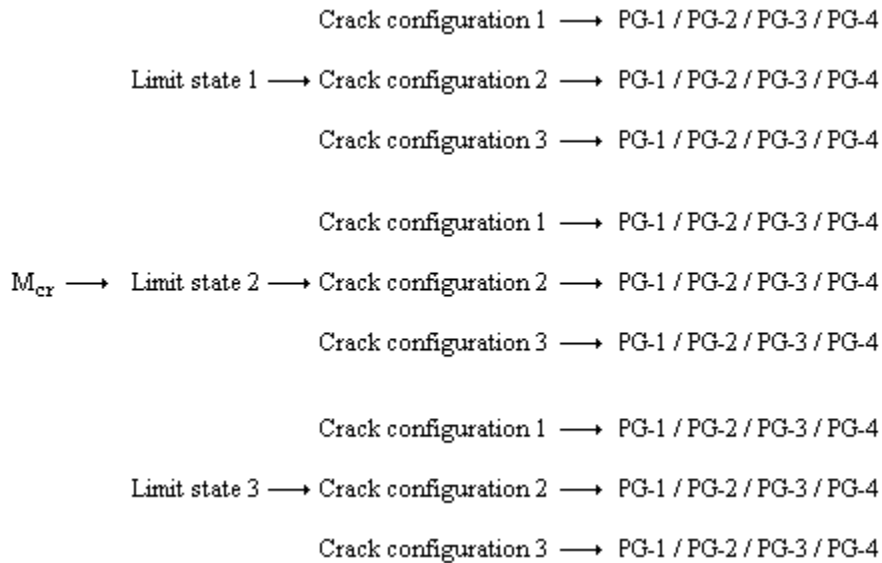
Figure 5.4.3: General outline of the FEA validation procedure for the bending moment capacity expressions: Each limit state was evaluated for various fatigue crack configurations. Each crack configuration was evaluated with a series of trial plate girders (PG-1 through PG-4).

5.4.1.2 FE Analyses for Shear Force Capacity Expressions

A total of four trial web panels were modeled with ABAQUS 6.11 and employed to validate the capacity expressions associated with predominantly shear (see Table 5.4.2). The widths and depths for all four trial panels were set as constant with $s = 102$

cm and $d_w = 127$ *cm*, respectively. Each panel was modeled with a different web panel thickness, t_w, ranging from *0.15 cm* to *1.20 cm*. A through-thickness diagonal crack was modeled in each panel with $\theta = 45°$. The length of the crack, *2a*, in each panel was set to range from *10 cm* to *70 cm*. in *10 cm* increments. Also, the panels were modeled with the material properties of high-strength low-alloy structural steel. The geometrical and material properties of the trial web panels are listed in Tables 5.4.5 and 5.4.6, respectively.

Table 5.4.5. Trial web panel geometrical properties.

Trial web panel	Thickness, t_w (cm)
WP-A	0.15
WP-B	0.30
WP-C	0.60
WP-D	1.20

Table 5.4.6. Trial web panel material properties.

Modulus of elasticity, E (GPa)	Poisson's ratio, ν	Yield strength, σ_Y (MPa)	Mode I fracture toughness, K_{Ic} (MPa·m$^{1/2}$)	Mode II fracture toughness, K_{IIc} (MPa·m$^{1/2}$)
200[a]	0.3[a]	345[a]	98[b]	74[c]

a. General properties of high-strength low-alloy structural steel (Salmon et al., 2009, ch. 2).
b. Representative fracture toughness of high-strength alloy steel (Meguid, 1989, ch. 5).
c. Assuming $K_{IIc} \approx 0.75K_{Ic}$ (Sun & Jin, 2012, ch. 5).

The trial web panels with $t_w = 0.15$ *cm* and $t_w = 0.30$ *cm* (*WP-A* and *WP-B*) were purely theoretical for the purpose of investigating a broader range of potential elastic limit states. The panels were meshed using 4-node shell elements seeded at *0.50* cm (see Appendix I: FEA Models). The mesh was seeded at *0.05* cm near the crack tips. Also, the crack in each panel was modeled by assigning a seam to a single-line partition.

For stress analyses, the increased rigidity along each panel perimeter caused by the flanges and stiffener plates was accounted for by modeling an outside margin of additional web plate, resolving the actual three-dimensional panel configuration into a

two-dimensional configuration (see Figure 5.4.4a). The width of the outside margin, m, was approximated by setting the gross cross-sectional area of the margin equal to the gross cross-sectional area of the flange plate and solving for m, resulting in

$$m = \frac{b_f t_f}{t_w} \tag{5.4.1}$$

where b_f is the flange width and t_f is the flange thickness. The flange thickness was assumed to be twice the web panel thickness such that $t_f = 2t_w$, thus transforming (5.4.1) into $m = 2b_f$. Furthermore, the flange width was assumed to be constant with $b_f = 35\ cm$. For buckling analyses, the outside margin of additional web plate was removed (see Figure 5.4.4b). The crack was slightly shifted away from the corner of the web panel to allow the crack to behave as a central crack while remaining near to its original position relative to the panel perimeter.

The perimeter of each panel was set to have simply supported boundary conditions restraining out-of-plane and in-plane movement while allowing side-to-side movement (see Figure 5.4.4a, b). Each trial web panel was then loaded under pure shear by applying shell edge loads along the perimeter of the panel margin (see Figure 5.4.4a, b). The resulting capacities associated with shear yielding of the web, web local buckling, brittle fracture, and impending ductile failure were then numerically calculated for each trial web panel (see Figure 5.4.3) and compared to the capacities obtained from the theoretical capacity expressions (see Table 5.4.2).
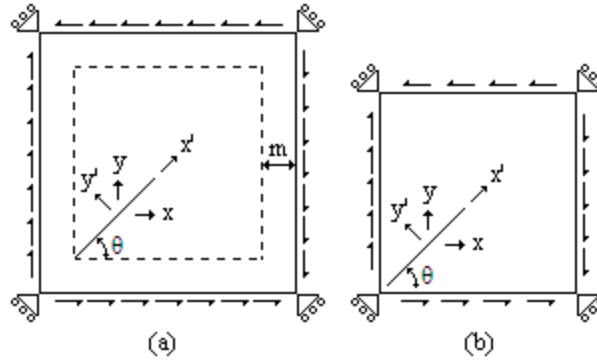
Figure 5.4.4: (a) Trial web panel configuration for stress analyses, (b) trial panel configuration for buckling analyses.

5.4.2 FE Validation of Bending Moment Capacity Expressions

5.4.2.1 Three-ended Crack

PG-1 through PG-4 and the associated three-ended crack configurations (see Table 5.4.7) were first employed to validate the expression for the transverse stress distribution given by (5.2.7) along the positive y-axis (see Figure 5.2.4). The external bending moment was set to $M_o = 500 \, kN·m$ and the transverse stress distributions were numerically calculated for each trial girder and associated three-ended crack configuration. The plots of the distributions as obtained from (5.2.7) and the FE analyses are shown in Figure 5.4.5 for PG-1 and PG-4. It can be seen that the analytical and numerical results display a close correlation.

Table 5.4.7. Trial plate girder geometric properties.

Plate girder (PG)	Flange thickness (cm)	Crack length (cm)	Plate girder (PG)	Flange thickness (cm)	Crack length (cm)
PG-1a	0.3	2.0	PG-3a	1.2	2.0
PG-1b	0.3	4.0	PG-3b	1.2	4.0
PG-1c	0.3	8.0	PG-3c	1.2	8.0
PG-1d	0.3	12	PG-3d	1.2	12
PG-2a	0.6	2.0	PG-4a	2.4	2.0
PG-2b	0.6	4.0	PG-4b	2.4	4.0
PG-2c	0.6	8.0	PG-4c	2.4	8.0
PG-2d	0.6	12	PG-4d	2.4	12

PG-1

0 1 2 3 4 5 6 7 8 9 10

0
-50
-100
-150
-200
-250
-300

$\sigma_x(0,y)$ (MPa)

Distance from base of crack, y (cm)

PG-4

0 1 2 3 4 5 6 7 8 9 10

0
-10
-20
-30
-40
-50

Distance from base of crack, y (cm)

—— Eq.: a = 2 cm   – – – Eq.: a = 4 cm
– · – · Eq.: a = 8 cm   – · · – Eq.: a = 12 cm
– – – – FE: a = 2 cm   ········ FE: a = 4 cm
············ FE: a = 8 cm   – · · – FE: a = 12 cm
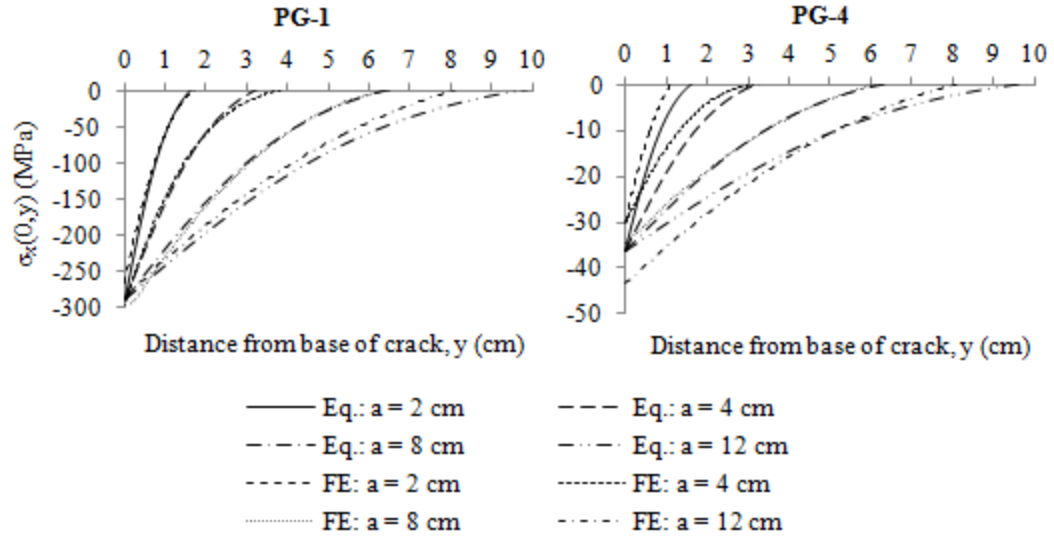
Figure 5.4.5: Analytical and numerical compressive transverse stress distributions along the positive y-axis as obtained from PG-1 and PG-4.

Provided the accuracy of (5.2.7), the trial flange stems were next used to indirectly validate the capacity expression for tension buckling in the flange given by (5.2.14). Each trial flange stem was loaded along the edges of the embedded plates bordering the web plate with a unit stress distribution in the form of (5.2.7) (see Figure 5.2.6a). The scaled magnitude of the unit stress distribution associated with first mode buckling was then numerically calculated. Given that (5.2.7) is directly coupled to σ_f, the critical value of σ_f corresponding to tension buckling was equal to the scaled value. The tension buckling capacities of each flange stem and associated three-ended crack configurations as calculated from (5.2.14) and the FE analyses are listed in Table 5.4.8.

155

Table 5.4.8. Tension buckling capacities.[a]

Plate girder (PG)	t_f/a ratio	Eq. (5.2.14) (GPa)	FE analysis (GPa)	Plate girder (PG)	t_f/a ratio	Eq. (5.2.14) (GPa)	FE analysis (GPa)
PG-1a	0.15	30.0	36.0	PG-3a	0.60	480	71.0
PG-1b	0.075	7.50	11.0	PG-3b	0.30	120	71.0
PG-1c	0.038	1.90	2.90	PG-3c	0.15	30.0	36.0
PG-1d	0.025	0.80	1.30	PG-3d	0.10	13.0	18.0
PG-2a	0.30	120	71.0	PG-4a	1.20	1900	71.0
PG-2b	0.15	30.0	36.0	PG-4b	0.60	480	71.0
PG-2c	0.075	7.50	11.0	PG-4c	0.30	120	71.0
PG-2d	0.05	3.30	5.00	PG-4d	0.20	54.0	53.0

a. Assuming $\sigma_Y = \infty$.

The resulting capacities are purely theoretical since the flange steel was provisionally assumed to have infinite yield strength (i.e. $\sigma_Y = \infty$) for the purpose of comparing a wide range of results. The correspondence between the analytical and numerical results is closest for lower t_f / a ratios (*0.025* to *0.20*). The correlation decays at higher t_f / a ratios (*0.30 to 1.20*). This decay of correspondence is irrelevant since tension buckling is unlikely to occur in configurations with higher t_f / a ratios or with thicker flange stems. Consequently, tension buckling is possible only in configurations with lower t_f / a ratios with thinner flange stems.

A comparison of the compressive transverse stress distributions adjacent to the edge-crack in the flange as obtained from PG-3 and the associated trial flange stem is shown in Figure 5.4.6 for *x = 1/3a ≈ 2.67 cm* and *x = 2/3a ≈ 5.33 cm* (see Figure 5.2.4). The reasonable correspondence between the two distributions validated the earlier assumption regarding loading the clamped edges of each embedded plate along the y-axis with (5.2.7) for the function of approximating the actual compressive stresses.
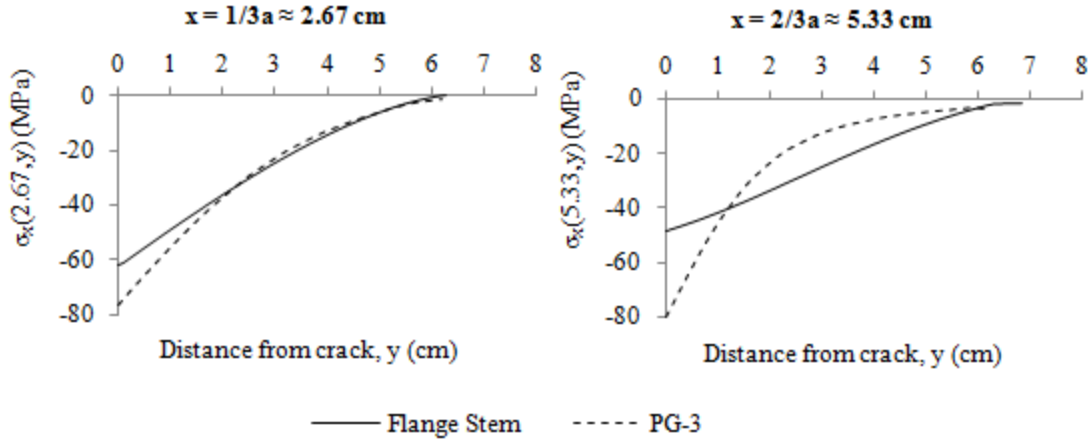
Figure 5.4.6: Numerical compressive transverse stress distributions along the positive y-axis as obtained from PG-3 and the corresponding trial flange stem ($M_o = 500$ kN·m, $\sigma_f = 72.3$ MPa, $t_f = 1.2$ cm, $a = 8$ cm).

PG-1 through PG-4 were next employed to validate the capacity expressions for brittle fracture and impending ductile failure in the flange given by (5.2.17) and (5.2.22), respectively. The external bending moment was set to $M_o = 6000$ kN·m and the load time period was increased to *10* with an increment size of *1*. History outputs were requested for the Mode I stress intensity factor. The bending stress at the extreme fibers of the trial girders corresponding to the stress intensity factor exceeding K_{Ic} was the flange stem tensile capacity associated with brittle fracture. Similarly, the bending stress at the extreme fibers of the trial girders corresponding to the plastic region radius at $\theta = 0$ exceeding $r_{p,cr} = t_f / 50$ was the flange stem tensile capacity associated with the approximate transition from LEFM to EPFM (Shukla, 2005, ch. 4). The tensile capacities of each flange stem and associated three-ended crack configurations as calculated from (5.2.17) and (5.2.22), and from the FE analyses, are shown in Tables 5.4.9 and 5.4.10.

157

Table 5.4.9. Brittle fracture capacities.[a]

Plate girder (PG)	Eq. (5.2.17) (MPa)	FE analysis (MPa)	Plate girder (PG)	Eq. (5.2.17) (MPa)	FE analysis (MPa)
PG-1a	390	380	PG-3a	390	460
PG-1b	280	260	PG-3b	280	290
PG-1c	200	180	PG-3c	200	190
PG-1d	160	120	PG-3d	160	130
PG-2a	390	620	PG-4a	390	450
PG-2b	280	430	PG-4b	280	390
PG-2c	200	270	PG-4c	200	200
PG-2d	160	120	PG-4d	160	130

a. Assuming $\sigma_Y = \infty$.

Table 5.4.10. Impending ductile failure capacities.

Plate girder (PG)	Eq. (5.2.22) (MPa)	FE analysis (MPa)	Plate girder (PG)	Eq. (5.2.22) (MPa)	FE analysis (MPa)
PG-1a	27.0	24.0	PG-3a	53.0	69.0
PG-1b	19.0	12.0	PG-3b	38.0	51.0
PG-1c	13.0	6.00	PG-3c	27.0	20.0
PG-1d	11.0	1.60	PG-3d	22.0	14.0
PG-2a	38.0	39.0	PG-4a	76.0	84.0
PG-2b	27.0	26.0	PG-4b	53.0	58.0
PG-2c	19.0	10.0	PG-4c	38.0	35.0
PG-2d	15.0	8.20	PG-4d	31.0	27.0

The results generally exhibit a closer correlation for shorter crack lengths. The finite width of each crack, the mesh fineness, and the absence of the stress intensity correction factor may negatively influence the correlation for longer crack lengths. This decay of correspondence is irrelevant since alternative elastic limit states are likely to occur at longer crack lengths. Also, the resulting residual strengths are purely theoretical since the flange steel was provisionally assumed to have infinite yield strength, $\sigma_Y = \infty$, for the purpose of comparing a broader range of results.

5.4.2.2 Vertical Edge-crack in Web Plate

PG-1 through PG-4 and the associated vertical edge-crack configurations (see Table 5.4.11) were next employed to validate capacity expressions corresponding to the

limit states of flange local yielding, flange local buckling, and web local buckling given by (5.2.45), (5.2.49), and (5.2.58), respectively. The expression for the normal bending stress distribution between the edge-crack tip and the shifted neutral axis given by (5.2.33), and between the shifted neutral axis and the extreme fibers of the compression flange given by (5.2.53), were first validated by employing PG-1 through PG-4 and the associated vertical edge-crack configurations (see Figure 5.2.10b). The external bending moment was set to $M_o = 500\ kN{\cdot}m$ and the corresponding bending stress distribution above the vertical edge-crack was numerically calculated. The plots of bending stress distributions for each trial girder and associated vertical crack configurations as obtained from (5.2.33) and (5.2.53), as well as from the FEA, are shown in Figure 5.4.7.

Table 5.4.11. Trial plate girder geometric properties.

Plate girder (PG)	Web thickness, t_w (cm)	Crack length, $2a$ (cm)	Plate girder (PG)	Web thickness, t_w (cm)	Crack length, $2a$ (cm)
PG-1a	0.15	6.0	PG-3a	0.60	6.0
PG-1b	0.15	12	PG-3b	0.60	12
PG-1c	0.15	24	PG-3c	0.60	24
PG-1d	0.15	48	PG-3d	0.60	48
PG-2a	0.30	6.0	PG-4a	1.20	6.0
PG-2b	0.30	12	PG-4b	1.20	12
PG-2c	0.30	24	PG-4c	1.20	24
PG-2d	0.30	48	PG-4d	1.20	48
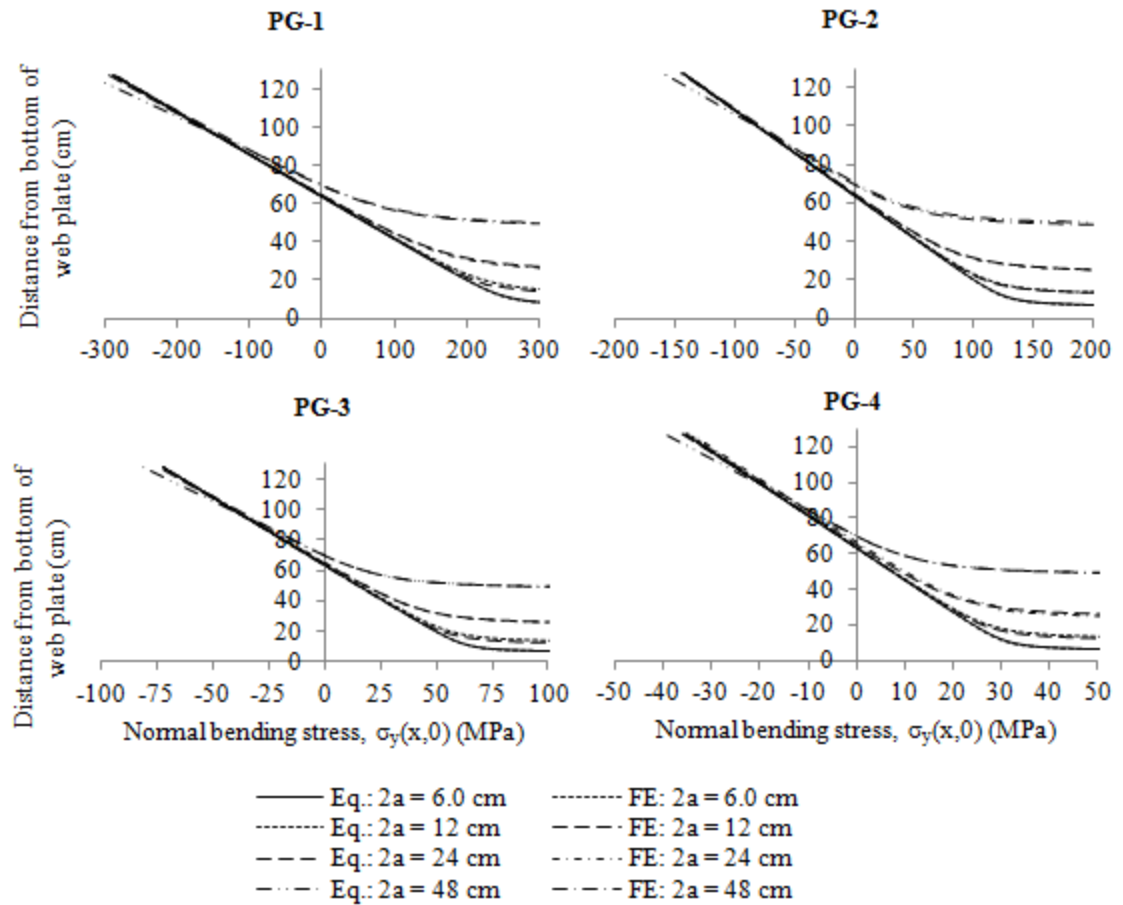
Figure 5.4.7: Analytical and numerical normal bending stress distributions along the x-axis above the edge-crack for each trial plate girder.

Given that the analytical bending stress distributions closely correlated to the numerical results, PG-1 through PG-4 were next employed to validate the expression for the residual bending moment strength corresponding to flange local yielding given by (5.2.46). This was achieved by increasing M_o to a magnitude exceeding the yield moment, M_y, and requesting stress history outputs of elements at the extreme outer fibers of the compression flange directly above the vertical crack. The critical bending moment at which the stresses in these elements exceeded the yield strength was then calculated. The residual bending moment strengths for each trial girder and associated vertical crack

160

configurations as calculated from (5.2.46), as well as from the FEA, are listed in Table 5.4.12.

Table 5.4.12. Analytical and numerical flange local yielding capacities.

Plate girder (PG)	Eq. (5.2.46) (kN·m)	FE analysis (kN·m)	Error (%)	Plate girder (PG)	Eq. (5.2.46) (kN·m)	FE analysis (kN·m)	Error (%)
PG-1a	597.9	598.6	-0.10	PG-3a	2384	2386	-0.08
PG-1b	595.6	598.6	-0.50	PG-3b	2374	2386	-0.50
PG-1c	585.5	596.6	-1.86	PG-3c	2334	2386	-2.18
PG-1d	534.9	595.7	-10.2	PG-3d	2129	2380	-10.5
PG-2a	1194	1196	-0.17	PG-4a	4749	4754	-0.10
PG-2b	1190	1196	-0.50	PG-4b	4730	4754	-0.50
PG-2c	1170	1193	-1.92	PG-4c	4647	4754	-2.25
PG-2d	1068	1192	-10.4	PG-4d	4233	4752	-10.9

It is observed that a close correlation exists between the analytically and numerically calculated flange local yielding strengths. In this case, the resulting capacities are always equal to or less than the yield moment, M_y. This is because (5.2.46) inherently outputs stress values equal to or less than the yield strength of the flange steel.

The numerical buckling simulations employed by the FE analyses are made difficult in part by global and local buckling modes overriding intended buckling modes. The expression for the bending moment capacity corresponding to flange local buckling given by (5.2.50) was indirectly validated by recognizing that the accuracy of (5.2.46) is directly dependent upon the accuracy of the stress at the extreme fibers of the compression flange, as well as the accuracy of the bending stress distribution given by (5.2.33) and (5.2.53). The close correlation between the analytical and numerical bending moment capacities associated with flange local yielding signified that the corresponding critical stresses at the extreme fibers of the compression flange also exhibited a close correlation. Furthermore, given that (5.2.33) and (5.2.53) were previously validated, it

was determined that (5.2.50) represents a reasonably accurate expression of the bending moment capacity associated with flange local buckling. This is because the flange local buckling strength given by (5.2.49) is in part dependent upon the classical plate theory buckling strength, which itself is derived for a plate loaded under uniaxial compression. In (5.2.49), the uniaxial compression is given by the stresses at the extreme fibers of the compression flange directly above the vertical crack in the web.

Full-scale trial web plates corresponding to PG-1 through PG-4 were next employed to indirectly validate the expression for the bending moment capacity corresponding to the web local buckling limit state given by (5.2.59). Only the web plates were modeled in order to avoid the aforementioned difficulties concerning numerical buckling simulations of an overall girder. Each web plate was configured to have fully clamped support conditions along the longitudinal edges bordering the flange plates. The web plates were modeled using 4-node shell elements. The associated edge-cracks were modeled by assigning a seam to a single-line partition. Furthermore, the out-of-plane translation of each web plate was restrained except for the region of the embedded plate, thus reducing the analysis to that of a fully clamped embedded plate (see Figure 5.2.12a).

The vertical sides of the embedded plate were then loaded with a unit compressive stress distribution in the form expressed by (5.2.53) (see Figure 5.2.12b). The first buckling mode stress corresponding to σ_{cw} was then computed and introduced into (5.2.56). The bending moment capacity was then calculated by solving (5.2.56) for σ_f and plugging the result into (5.2.59). The web local buckling capacities for each trial girder and associated vertical crack configuration as calculated from (5.2.59), as well as from the FE analyses, are listed in Table 5.4.13.

162

Table 5.4.13. Analytical and numerical web local buckling capacities.[a]

Plate girder (PG)	Eq. (5.2.59) (kN·m)	FE analysis (kN·m)	Error (%)	Plate girder (PG)	Eq. (5.2.59) (kN·m)	FE analysis (kN·m)	Error (%)
PG-1a	30.2	27.9	8.24	PG-3a	2422	1780	36.1
PG-1b	30.4	28.1	8.19	PG-3b	2431	1784	36.3
PG-1c	31.3	28.5	9.82	PG-3c	2473	1825	35.5
PG-1d	36.0	35.2	2.27	PG-3d	2708	1994	35.8
PG-2a	294.1	223.2	31.8	PG-4a	19711	14106	39.7
PG-2b	295.3	224.6	31.5	PG-4b	19786	14144	39.9
PG-2c	300.7	227.9	31.9	PG-4c	20126	14602	37.8
PG-2d	330.9	249.0	32.9	PG-4d	22021	15936	38.2

a. Assuming $\sigma_Y = \infty$

As with the tension buckling results for the three-ended crack, the capacities are purely theoretical since the flange steel was provisionally assumed to have infinite yield strength (i.e. $\sigma_Y = \infty$) for the purpose of comparing a wide range of results. The correlation is much more accurate for thinner web plates with lower t_w / a ratios. The correlation becomes less accurate for web plates possessing higher t_w / a ratios. However, the divergence in correlation at higher t_w / a ratios is determined to be tolerable because alternative elastic limit states are likely to govern thereafter.

Unlike the previously validated capacity expressions, the web local buckling capacity expression outputs higher values of critical stresses for longer crack lengths. This indicates that the web local buckling strength actually becomes greater with increasing crack length. The increase in buckling strength is explained by the nature of (5.2.58). As the vertical crack propagates up through the web plate towards the compression flange, the embedded plate situated just above the crack tip shrinks. The shrinking of the embedded plate therefore serves to increase its buckling strength and the corresponding residual bending moment strength.

PG-1 through PG-4 and the associated vertical crack configurations (see Table 5.4.14) were next used to indirectly validate the tension buckling capacity expression given by (5.2.79). To achieve this, PG-1 through PG-4 were first employed to confirm the accuracy of the transverse compressive stress distribution at the middle of the crack given by (5.2.69) along the positive y-axis (see Figure 5.2.13b). The external bending moment, M_o, was set such that the far-field tensile stress at the extreme fibers of the web was equal to *172.5* MPa. The transverse compressive stress distributions for the trial girders and the associated vertical crack configurations obtained using (5.2.69) and the FE analyses demonstrated a close correlation (see Figure 5.4.8).

Table 5.4.14. Trial plate girder geometric properties.

Plate girder (PG)	Web thickness, t_w (cm)	Crack length, 2a (cm)	Plate girder (PG)	Web thickness, t_w (cm)	Crack length, 2a (cm)
PG-1a	0.15	4.0	PG-3a	0.60	4.0
PG-1b	0.15	8.0	PG-3b	0.60	8.0
PG-1c	0.15	16	PG-3c	0.60	16
PG-1d	0.15	32	PG-3d	0.60	32
PG-2a	0.30	4.0	PG-4a	1.20	4.0
PG-2b	0.30	8.0	PG-4b	1.20	8.0
PG-2c	0.30	16	PG-4c	1.20	16
PG-2d	0.30	32	PG-4d	1.20	32

Figure 5.4.8: Transverse compressive stress distributions at middle of crack obtained analytically and numerically for each trial girder.

Having validated the transverse stress distribution given by (5.2.69), FE analyses were next employed to indirectly validate the critical far-field tensile stress in the flange associated with tension buckling adjacent to the vertical crack given by (5.2.79). Two measures were taken to obtain the first mode buckling stress due to the transverse compressive stresses adjacent to the vertical crack. First, only the web plates of PG-1 through PG-4 were modeled. Second, the out-of-plane translation of the web plate

besides that of the embedded plate was restrained (see Figure 5.2.17a). Also, 4-node shell elements were used to model the trial girder web plates.

For each trial web plate, the clamped edge along the positive y-axis adjacent to the vertical crack was loaded with a unit transverse compressive stress distribution in the form given by (5.2.73) (see Figure 5.2.17c). The scaled magnitude of the unit stress distribution associated with first mode buckling was then numerically calculated. Given that (5.2.73) is directly coupled to σ_f, the critical value of σ_f corresponding to tension buckling was equal to the scaled value. The resulting critical far-field tensile stresses obtained from (5.2.79) and the FE analyses are summarized in Table 5.4.15.

Table 5.4.15. Analytical and numerical tension buckling stresses.[a]

Plate girder (PG)	Eq. (5.2.79) (GPa)	FE analysis (GPa)	% Error	Plate girder (PG)	Eq. (5.2.79) (GPa)	FE analysis (GPa)	% Error
PG-1a	4.77	5.83	18.2	PG-3a	76.4	67.2	-13.7
PG-1b	1.23	1.57	21.7	PG-3b	19.7	22.0	10.5
PG-1c	0.33	0.43	23.3	PG-3c	5.28	6.61	20.1
PG-1d	0.10	0.10	0.00	PG-3d	1.55	1.52	-1.97
PG-2a	19.1	21.2	9.91	PG-4a	305	156	-95.5
PG-2b	4.93	6.04	18.4	PG-4b	79.0	69.6	-13.5
PG-2c	1.32	1.72	23.3	PG-4c	21.2	24.1	12.4
PG-2d	0.39	0.39	0.00	PG-4d	6.18	5.85	-5.64

a. Assuming $\sigma_Y = \infty$

The correlation between the critical tension buckling stress as obtained from (5.2.79) and the FE analyses is much closer for thin web plates possessing lower t_w / a ratios. The divergence of correlation for web plates possessing higher t_w / a ratios is tolerable because alternative elastic limit states are likely to govern thereafter. In general, it is observed that the critical tension buckling stress as obtained from (5.2.79) is mostly conservative.

The trial plate girders possessing the thinnest and thickest flanges and webs (PG-1 and PG-4, respectively) together with the associated vertical crack configurations (see Table 5.4.11) were finally employed to indirectly validate the capacity expressions corresponding to the limit states of brittle fracture and impending ductile failure given by (5.2.82) and (5.2.84), respectively. Specifically, the analytically calculated values of K_I expressed by (5.2.81) were validated, thus confirming the accuracy of the impending ductile failure and brittle fracture capacities. The external bending moment was set to M_o = *500 kN·m* and the load time period was set to 10 with an increment size of 1. History outputs were then requested for the Mode I stress intensity factor. The resulting numerically determined values of K_I and the corresponding analytically calculated values of K_I given by (5.2.81) are plotted in Figure 5.4.9 as functions of crack for PG-1 and PG-2.
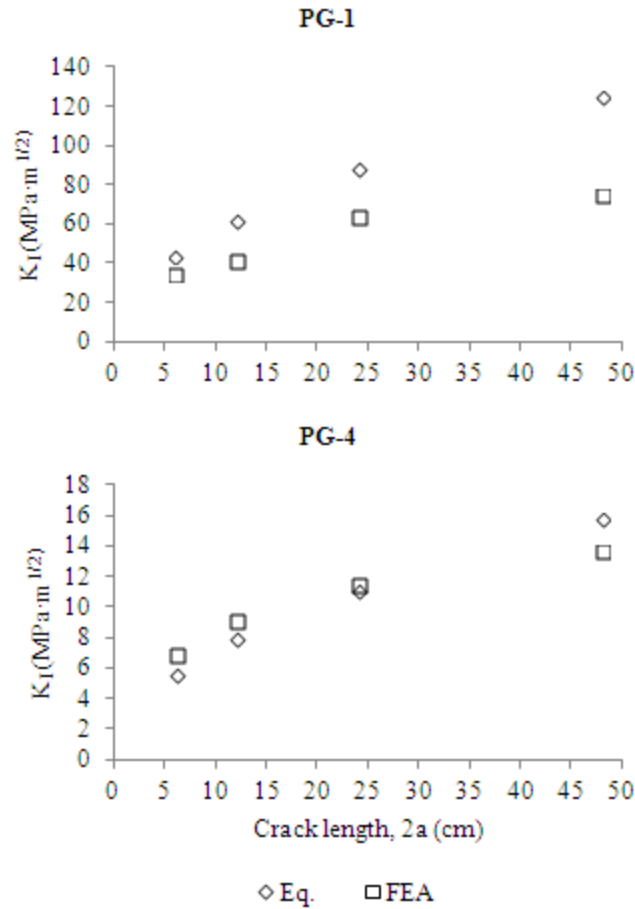
Figure 5.4.9: Values of K_I as obtained from (5.2.81) and FEA for PG-1 and PG-4.

The correlation between the numerical and analytical values of K_I degrades for PG-1 as the crack length increases. The correlation is strongest for shorter crack lengths, thus indirectly validating (5.2.82) and (5.2.84) for thinner girders. The discrepancy of the correlation for longer crack lengths is irrelevant because limit states such as brittle fracture, impending ductile failure, and tension buckling may begin to govern at longer crack lengths. In fact, the resulting values of K_I greater than K_{Ic} are purely theoretical since K_{Ic} was provisionally assumed to be infinite (i.e. $K_{Ic} = \infty$) for the purpose of comparing a wide range of results. The correlation between the numerical and analytical

168

values of K_I for PG-4 is in good agreement for all considered crack lengths, thus indirectly validating (5.2.82) and (5.2.84) for realistically sized girders.

5.4.2.3 Crack Extending Through One or Both Sides of Tension Flange

The trial plate girders possessing the thinnest and thickest flanges and webs (PG-1 and PG-4, respectively) were next used to validate the expression for the transverse stress distribution given by (5.2.88) along the positive y-axis for the horizontal crack configuration (see Figure 5.2.21). The external bending moment was set to $M_o = 500$ $kN·m$ and the transverse stress distributions were numerically calculated for each trial girder and associated horizontal crack configuration (see Table 5.4.16). The plots of the distributions as obtained from (5.2.88) and the FE analyses are shown in Figure 5.4.10 for PG-1 and PG-4. The analytical and numerical results display a closer correlation for PG-1. For PG-4, the analytical results conservatively predict slightly greater stress magnitudes than the FEA results.

Table 5.4.16. Trial plate girder geometric properties.

Plate girder (PG)	Flange thickness (cm)	Crack length (cm)	Plate girder (PG)	Flange thickness (cm)	Crack length (cm)
PG-1a	0.3	2.0	PG-4a	2.4	2.0
PG-1b	0.3	4.0	PG-4b	2.4	4.0
PG-1c	0.3	8.0	PG-4c	2.4	8.0
PG-1d	0.3	12	PG-4d	2.4	12
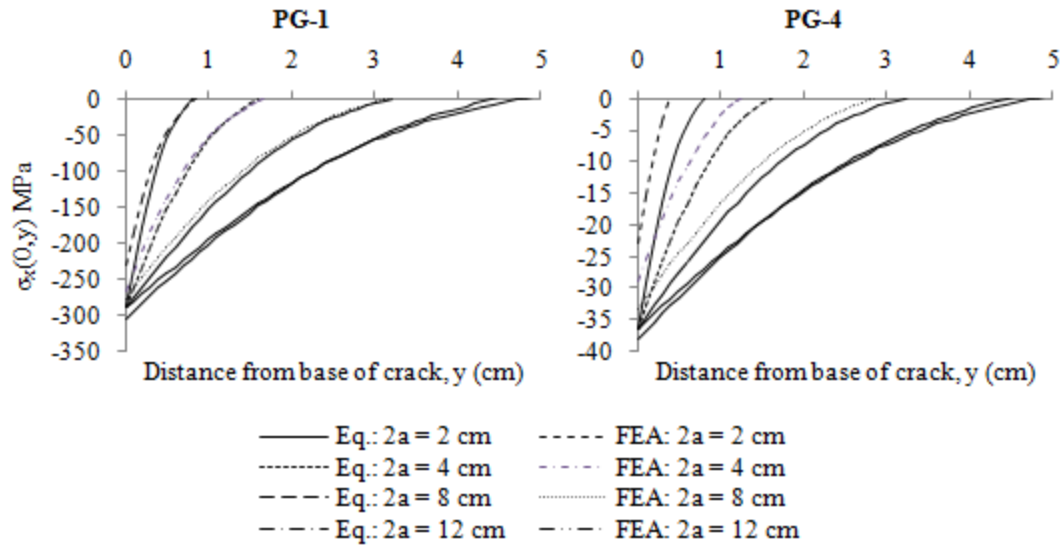
Figure 5.4.10: Analytical and numerical compressive transverse stress distributions along the positive y-axis as obtained from PG-1 and PG-4.

Having validated (5.2.88), the trial flange stems were next used to indirectly validate the tension buckling capacity given by (5.2.98) considering exceptionally thin flange plate thicknesses. The trial flange stem thicknesses are purely theoretical for the function of investigating a wide range of buckling capacities. It was found that realistic flange plate thicknesses are unlikely to experience tension buckling prior to the advent of alternative elastic limit states. As with the vertical crack configuration in the web, each flange stem was loaded along the edges of the embedded plates bordering the web plate with a unit stress distribution in the form of (5.2.92). The scaled magnitude of the unit stress distribution associated with first mode buckling was then numerically calculated. Given that (5.2.92) is directly coupled to σ_f, the critical value of σ_f corresponding to tension buckling was equal to the scaled value. The tension buckling capacities of each flange stem and associated horizontal crack configurations as calculated from (5.2.98) and the FE analyses are plotted in Figure 5.4.11.
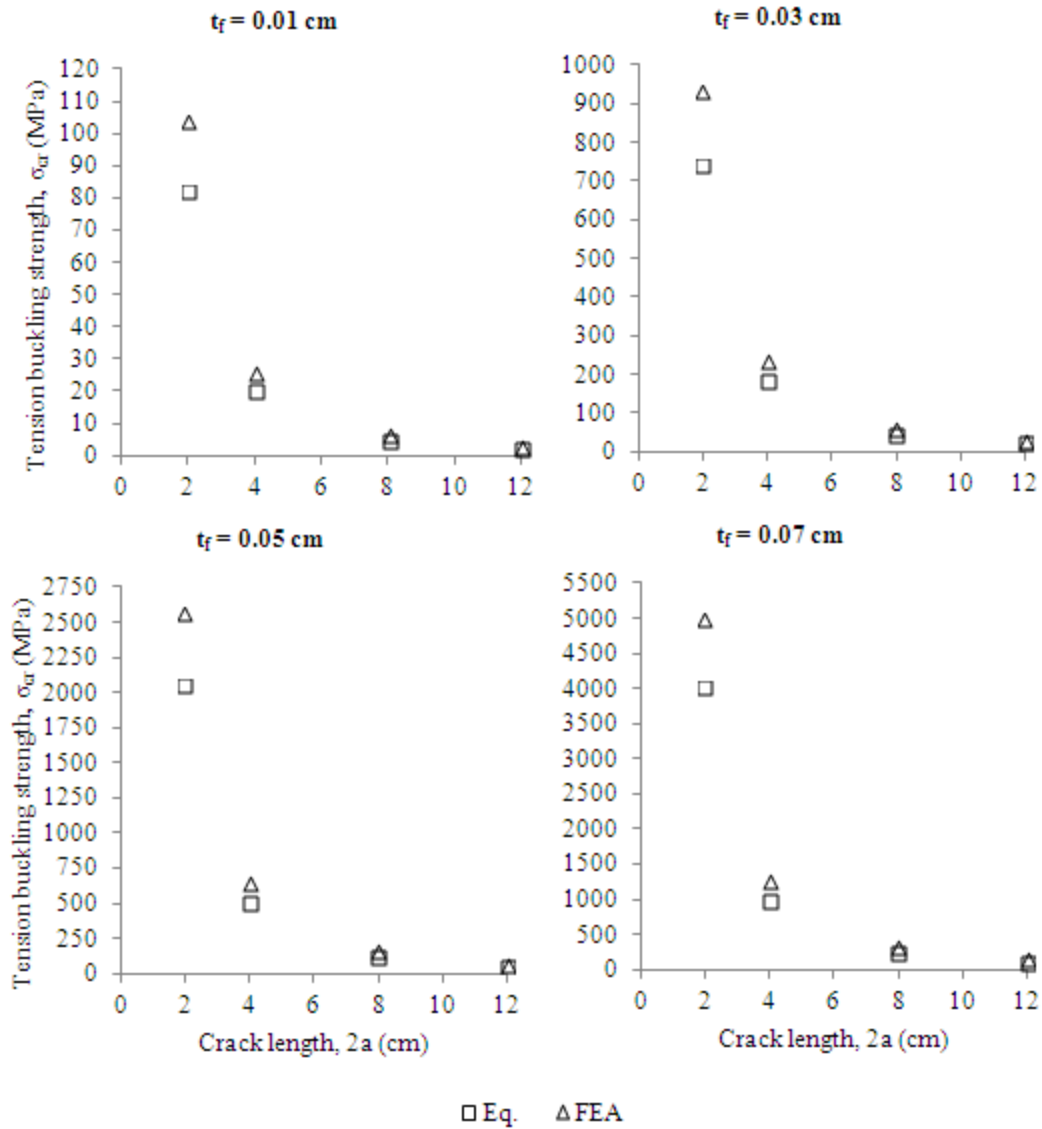
Figure 5.4.11: Analytical and numerical tension buckling capacities of trial flange stems considering exceptionally thin flange plate thicknesses.

The analytically and numerically determined capacities display a reasonable correlation. It is noted that the yield strength of the trial flange stems was assumed to be infinite (i.e. $\sigma_Y = \infty$) for the purpose of displaying the full extent of the tension buckling capacity correlations. The correlation between the analytical and numerical results is closest for thin flange stems possessing lower t_f / a ratios. The correlation decays for higher t_f / a ratios. In general, the correlation becomes less accurate for thicker flange

171

stems. As with the three-ended crack and vertical crack configurations, the divergence in correlation at higher t_f / a ratios is tolerable because alternative elastic limit states are likely to govern from then on.

The trial plate girders possessing the thinnest and thickest flanges and webs (PG-1 and PG-4, respectively) along with the associated horizontal crack configurations (see Table 5.4.16) were finally employed to indirectly validate the capacity expressions corresponding to the limit states of brittle fracture and impending ductile failure given by (5.2.100) and (5.2.102), respectively. The external bending moment was set to $M_o = 500$ $kN{\cdot}m$ and the load time period was set to 10 with an increment size of 1. History outputs were then requested for the Mode I stress intensity factor. The resulting numerically determined values of K_I and the corresponding analytically calculated values of K_I given by (5.2.16) are plotted in Figure 5.4.12 as functions of crack length for PG-1 and PG-4.
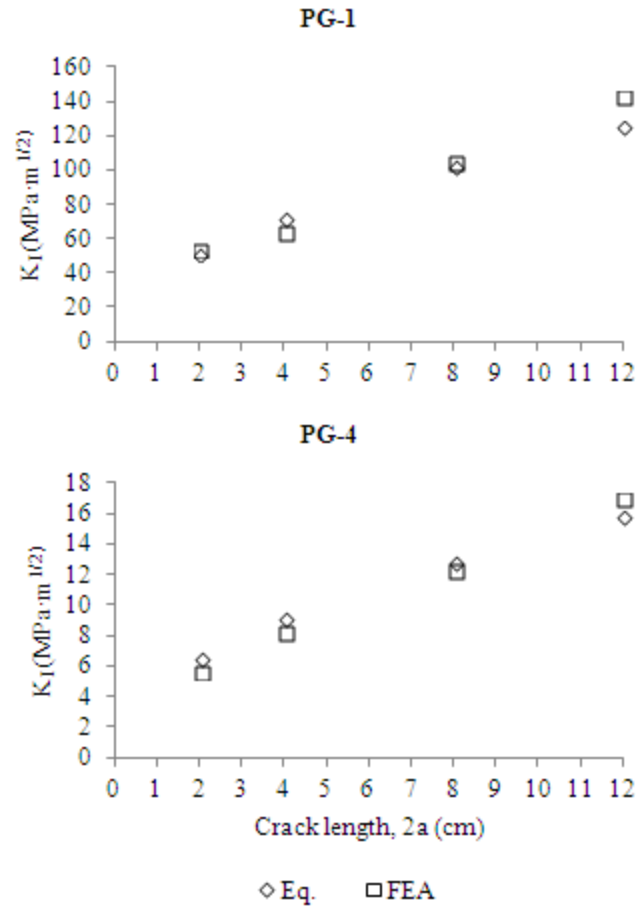
Figure 5.4.12: Values of K_I as obtained from (5.2.16) and FEA for PG-1 and PG-4.

The analytically and numerically determined values of K_I for PG-1 and PG-4 display a good correlation for all considered crack lengths. It is noted that the resulting values of K_I greater than K_{Ic} are purely theoretical since K_{Ic} was provisionally assumed to be infinite (i.e. $K_{Ic} = \infty$) for the purpose of comparing a wide range of results. In view of the fact that the brittle fracture and impending ductile failure capacity expressions are directly dependent upon the accuracy of K_I, the correlation indirectly validates (5.2.100) and (5.2.102).

5.4.3 FE Validation of Shear Force Capacity Expressions

5.4.3.1 Diagonal Crack in Web Panel

The trial web panel WP-C was first used to validate the expression for the internal shear stress distribution given by (5.3.19). The uniform perimeter shear stress was set to $\tau_{xy,s}$ = *150 MPa*, the crack angle set to θ = *45°*, and the crack length set to *2a* = *40 cm*. Plots of the internal shear stress distributions were analytically determined using (5.3.19) for two arbitrary horizontal paths designated by $\tau_{xy,c}$*(x, 25 cm)* and $\tau_{xy,c}$*(x, 40 cm)* (see Figure 5.4.12).
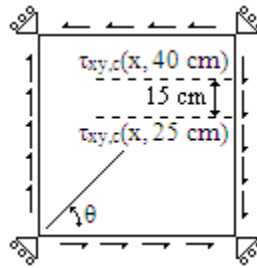
Figure 5.4.12: Locations of horizontal paths in *WP-C* for which the internal shear stress distributions were analytically and numerically obtained.

The analytically determined shear stress distributions were compared to numerically calculated distributions by creating two nodal paths within WP-C in the locations designated in Figure 5.4.12. The *X-Y* data for the in-plane shear stress was then requested for each of the nodal paths. The shear stress distributions as obtained from (5.3.19) and the FE analyses are plotted in Figure 5.4.13.

174
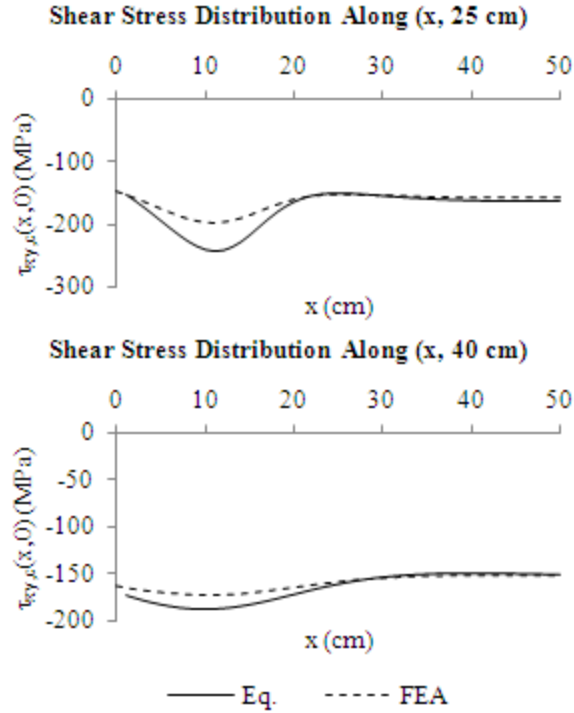
Figure 5.4.13: Plots of internal shear stress distributions within WP-C along the horizontal paths designated in Figure 5.4.12 as obtained from (5.3.19) and FEA. The shear yield strength is temporarily neglected for the purpose of displaying the full extent of the stress distributions.

The analytically and numerically determined shear stress distributions exhibit a closer correlation along $y = 40$ cm than along $y = 25$ cm. This suggests that (5.3.19) is more accurate in describing the mid-field and far-field shear stress distributions than in describing the near-field distributions. Nonetheless, (5.3.19) is conservative for both cases displayed in Figure 5.4.13.

All four trial web panels were next employed to directly validate the capacity expression for web local buckling given by (5.3.42). Each trial web panel was loaded with a unit uniform perimeter shear stress, $\tau_{xy,s} = 1$ MPa. A linear perturbation buckling analysis was then performed on each trial web panel considering different crack lengths ranging from 10 cm to 70 cm, in 10 cm increments. The resulting Mode I eigenvalues were finally divided by t_w to obtain the critical values of $\tau_{xy,s}$ associated with buckling.

175

The buckling capacities of the trial web panels as obtained from (5.3.42) with $N_e = 100$ and the FE analyses are plotted in Figure 5.4.14 as functions of crack length.
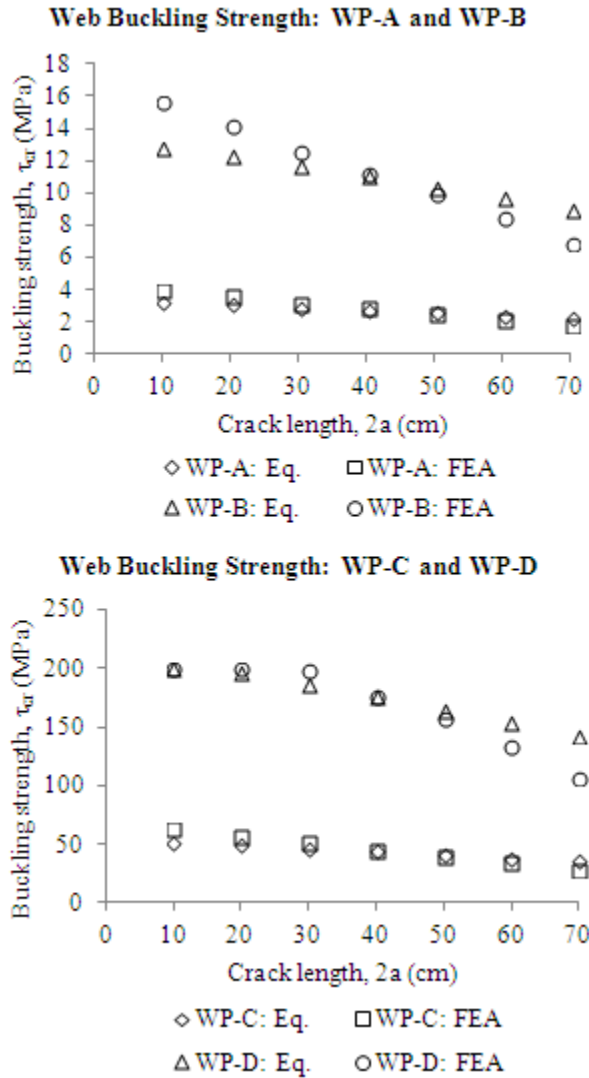
Figure 5.4.14: Web panel buckling capacities as calculated from (5.3.42) and FEA.

It is evident that the analytically and numerically determined web buckling strengths demonstrate a relatively close correlation for all crack lengths considered. Equation (5.3.42) is slightly more conservative for crack lengths up to *40 cm*. Conversely, the FE results are slightly more conservative for crack lengths beyond *40 cm*.

From (5.3.43) and Table 5.4.6, the shear yield strength is approximately $\tau_Y = 200\ MPa$. In general, web panel strengths exceeding the shear yield strength are governed by τ_Y. This is the case for the buckling strength of *WP-D* for shorter crack lengths, as demonstrated in Figure 5.4.14.

The shear force capacity of a cracked web panel corresponding to the limit state of shear yielding is given by (5.3.46). Upon the advent of shear yielding, the perimeter shear stress attains the shear yield strength. Given that the trial web panels are loaded under pure shear by default, FE analyses were unnecessary to validate (5.3.47).

The trial web panels were next employed to indirectly validate the capacity expressions associated with brittle fracture and impending ductile failure given by (5.3.54) and (5.3.62), respectively. Specifically, the trial web panels were used to confirm the accuracy of K_I and the web panel brittle fracture strength corresponding to Mode I crack loading. Given that $\theta = 45°$, K_{II} remains negligible and the brittle fracture strength corresponding to Mode II crack loading approaches $\tau_{cr} = \infty$. FE analyses were thus unnecessary to validate K_{II} and the Mode II fracture strength. The Mode I fracture strength is analytically determined by solving (5.3.51) for $\tau_{xy,s}$ and setting $K_I = K_{Ic}$, resulting in

$$\tau_{cr} = \frac{K_{Ic}}{\sin(2\theta)\sqrt{\pi a}} \qquad (5.4.2)$$

Since (5.3.54) and (5.3.62) are directly dependent upon the accuracy of K_I, K_{II}, and the Mode I and II web panel brittle fracture strengths, the validation of (5.4.2) serves to indirectly validate (5.3.54) and (5.3.62).

The web panel brittle fracture strength was first numerically calculated for each trial web panel considering Mode I crack loading. This was performed by setting the shell

edge load to a ramp load configuration. The magnitude of the shell edge load was set to an arbitrary value such that K_I exceeded K_{Ic}. The total load time period was set to 10 and the load time incrementation set to 1. The stress intensity factor was obtained by assigning a history output request for K_I at the crack front for each load time increment. Load scales were then obtained by dividing the load time increments at which K_I equaled K_{Ic} by the total load time period. Lastly, the load scales were multiplied by the final magnitude of the shell edge load to obtain the critical magnitudes of perimeter shear stress. The Mode I brittle fracture capacities of the trial web panels as obtained from (5.4.2) and the FE analyses are plotted in Figure 5.4.15 as functions of crack length.
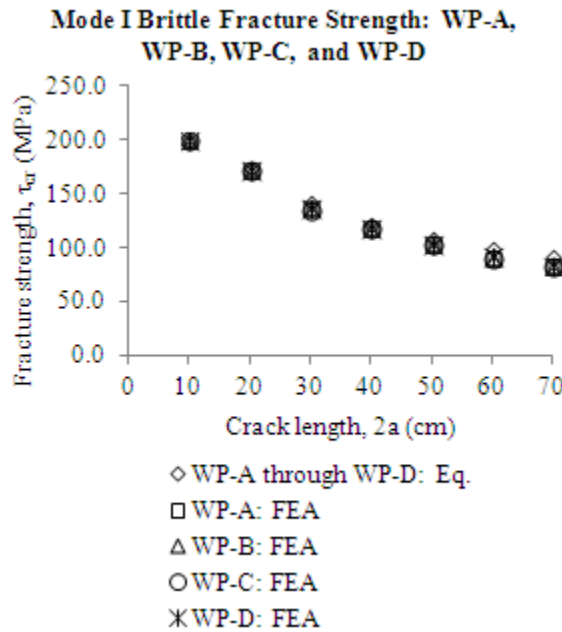
Figure 5.4.15: Web panel brittle fracture strengths as calculated from (5.4.2) and FEA.

It can be seen that the FE results correlate very well with the analytical results for all considered crack lengths. The accuracy of K_I and (5.4.2) is thus confirmed, thereby providing indirect validation of (5.3.54) and (5.3.62).

178

5.5   Incremental Decay of Capacity Expressions

5.5.1   Paris-Erdogan Empirical Crack Growth Equation

The formulated bending moment and shear force capacity expressions (see Tables 5.4.1 and 5.4.2) are inherently functions of crack length, and may be denoted by $M_{cr}\{a\}$ and $V_{cr}\{a\}$, respectively. Close inspection of these expressions reveal that the capacity decreases with increasing crack length. Given that the far-field cyclic stress induced by the fluctuating bending moments and shear forces serves to extend the crack length with each load cycle, it can be expected that the corresponding capacity may fall below the required capacity when the crack exceeds a critical length, a_{cr}. The fluctuating bending moments and shear forces may be described by constant-amplitude trigonometric load functions (see Figure 5.5.1).
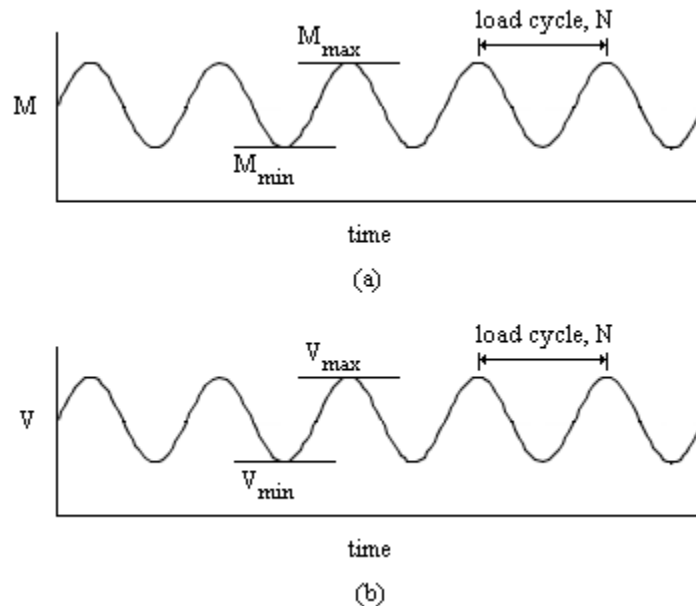
Figure 5.5.1: Constant-amplitude trigonometric load functions for (a) bending moment and (b) shear force.

The incremental crack extension, da, per load cycle, dN, may be described by the Paris-Erdogan crack growth equation given by (Paris & Erdogan, 1963)

$$\frac{da}{dN} = C(\Delta K_I)^m$$

(5.5.1)

where C and m are material constants, and ΔK_I is the range of the stress intensity factor expressed as

$$\Delta K_I = \Delta \sigma_f \sqrt{\pi a}$$

(5.5.2)

The variable $\Delta \sigma_f$ is the range of the far-field stress defined as

$$\Delta \sigma_f = \sigma_{f-max} - \sigma_{f-min}$$

(5.5.3)

where $\sigma_{f\text{-}max}$ and $\sigma_{f\text{-}min}$ are the maximum and minimum values of the far-field cyclic stress, respectively, applied upon the web or flange (see Appendix H: Empirical Crack Growth Law).

5.5.2 Incremental Decay of Capacity Expressions

The incremental decay of bending moment capacity, dM_{cr}, and shear force capacity, dV_{cr}, per load cycle is simply found by subtracting the capacity corresponding to a given load cycle from the capacity corresponding to the previous load cycle. Since the load cycle is related to the change in crack length by (5.5.1), the decay in bending moment capacity is expressed as

$$\frac{dM_{cr}}{dN} = M_{cr}\{a\} - M_{cr}\{a + C\Delta K_I^m\}$$

(5.5.4)

Similarly, the decay in shear force capacity is expressed as

$$\frac{dV_{cr}}{dN} = V_{cr}\{a\} - V_{cr}\{a + C\Delta K_I^m\}$$

(5.5.5)

Equations (5.5.4) and (5.5.5) represent the slopes of the capacities of a fatigue-cracked plate girder plotted as functions of load cycle, N.

Solving (5.5.1) for dN and integrating from an initial crack length, a_i, to a final crack length, a_f, results in an expression for the number of load cycles, ΔN, required for the crack to grow across this difference in length. The expression is written as

$$\Delta N = \int_{a_i}^{a_f} \frac{1}{C \Delta K_I^m} \, da \qquad (5.5.6)$$

Substituting (5.5.2) and (5.5.3) into (5.5.6) and resolving the integral results in:

$$\Delta N = \frac{2}{C(m-2)} \left[\frac{a_i}{\left(\Delta \sigma_f \sqrt{\pi a_i}\right)^m} - \frac{a_f}{\left(\Delta \sigma_f \sqrt{\pi a_f}\right)^m} \right] \qquad (5.5.7)$$

Assuming that the fatigue crack has already propagated through the flange or web plate thickness, the crack length constants are taken as $a_i \approx 0$ and $a_f = a$. Using (5.5.7), the capacity expressions may be indirectly plotted as functions of N. It can be expected that the capacity may fall below the required capacity after a critical number of load cycles, N_{cr}, corresponding to a_{cr}. Based upon the presumption that $a_i \approx 0$, N_{cr} is the extended fatigue life of the plate girder neglecting the load cycles required to propagate the crack through the flange or web plate thickness (Osman & Roberts, 1999).

6 Results and Discussion

6.1 Overview

6.1.1 Capacity Expressions as Functions of Crack Length

The formulated bending moment and shear force capacity expressions, $M_{cr} = f\{\Gamma\}$ and $V_{cr} = f\{\Gamma\}$, and the corresponding flange plate and web panel capacity expressions, $\sigma_{cr} = f\{\Gamma\}$ and $\tau_{cr} = f\{\Gamma\}$, were plotted as functions of crack length for the associated trial plate girders, flange stems, and web panels. In general, the capacities decrease with increasing crack length. The governing capacity, M_{cr}, V_{cr}, σ_{cr}, or τ_{cr}, may fall below the required capacity, M_r, V_r, τ_{cr} or σ_r, when a critical crack length, a_{cr}, is achieved. The formulated flange stem and web panel capacity expressions are summarized in Tables 6.1.1 and 6.1.2, respectively. The flange stem capacity expressions, $\sigma_{cr} = f\{\Gamma\}$, are associated with the bending moment capacity of a fatigue-cracked girder:

$$M_{cr} = \sigma_{cr} S \tag{6.1.1}$$

Similarly, the web panel capacity expressions, $\tau_{cr} = f\{\Gamma\}$, are associated with the shear force capacity of a fatigue-cracked girder:

$$V_{cr} = \tau_{cr} d_w t_w \tag{6.1.2}$$

Table 6.1.1. Flange stem capacity expressions (associated with bending moment).

Crack configuration	Limit state	Capacity expression
Three-ended crack	Tension buckling in flange	$\sigma_{cr} = 3.58 \dfrac{Et_f^2(v-2)}{a^2(v^2-1)} \leq \sigma_Y$
	Brittle fracture	$\sigma_{cr} = \dfrac{K_{Ic}}{\sqrt{\pi a}} \leq \sigma_Y$
	Impending ductile failure	$\sigma_{cr} = \dfrac{\sigma_Y\sqrt{2ar_{p,cr}}}{a} \leq \sigma_Y$
Vertical edge-crack	Yielding of compression flange	$\sigma_{cr} = \beta_{cf}\sigma_Y \leq \sigma_Y$
	Local buckling of compression flange	$\sigma_{cr} = \beta_{cf} k \dfrac{\pi^2 E}{12(1-v^2)(b_f/2t_f)^2} \leq \sigma_Y$
	Web local buckling	$\sigma_{cr} = \beta_{cw} \dfrac{(64D\pi^2 - 3d_c^3)}{3t_w d_c^2} \leq \sigma_Y$
	Tension buckling In web	$\sigma_{cr} = 2.97 \dfrac{Et_w^2 d_w(1.56-v)}{a^2(d_w-2a)(1-v^2)} \leq \sigma_Y$
	Brittle fracture	$\sigma_{cr} = \dfrac{2K_{Ic}}{\sqrt{\pi a}} \leq \sigma_Y$
	Impending ductile failure	$\sigma_{cr} = \dfrac{2\sigma_Y\sqrt{2ar_{p,cr}}}{a} \leq \sigma_Y$
Horizontal crack extending through one or both sides of tension flange	Tension buckling in flange	$\sigma_{cr} = 2.97 \dfrac{Et_f^2(1.56-v)}{a^2(1-v^2)} \leq \sigma_Y$
	Brittle fracture	$\sigma_{cr} = \dfrac{K_{Ic}}{\sqrt{\pi a}} \leq \sigma_Y$
	Impending ductile failure	$\sigma_{cr} = \dfrac{\sigma_Y\sqrt{2ar_{p,cr}}}{a} \leq \sigma_Y$

Table 6.1.2. Web panel capacity expressions (associated with shear force).

Crack configuration	Limit state	Capacity expression
Diagonal crack in web panel	Web local buckling	$\tau_{cr} = \displaystyle\sum_{r=1}^{\sqrt{N_e}} \sum_{c=1}^{\sqrt{N_e}} \tau_{cr,e-rc} \le \tau_Y$
	Shear yielding	$\tau_{cr} = \tau_Y$
	Brittle fracture	$\tau_{cr} = \dfrac{K_{Ic} K_{IIc}}{\sqrt{\pi a}\sqrt{K_{IIc}^2 \sin(2\theta)^2 - K_{Ic}^2 \sin(2\theta)^2 + K_{Ic}^2}} \le \tau_Y$
	Impending ductile failure	$\tau_{cr} = \dfrac{\sigma_Y \sqrt{2 a r_{p,cr}}}{a \sin(2\theta)} \le \tau_Y$

6.1.1.1 Three-ended Crack

The formulated flange stem capacity expressions given by (5.2.14), (5.2.17), and (5.2.22) corresponding to the limit states of tension buckling, brittle fracture, and impending ductile failure, respectively, were plotted as functions of crack branch length, a, for the trial flange stems and associated plate girders (see Figure 5.2.2) considering a wider range of flange plate thicknesses with $b_f = 35$ cm (see Figure 6.1.1). The critical plastic region radius, $r_{p,cr}$, measured from the crack tip at $\theta = 0$ was taken as $r_{p,cr} = t_f / 50$ (Shukla, 2005, ch. 4). It can be seen that the governing limit states and associated capacities are predominantly attributed to impending ductile failure, thus invalidating the brittle fracture limit state. The general trends of the plots indicate that the governing limit state transitions to brittle fracture at much thicker flange plate thicknesses. It is noted that the impending ductile failure limit state is restricted to the region near the crack tip. As a consequence, alternative limit states may not be immediately influenced by the presence of the plastic region at the crack tip unless the plastic region becomes extremely large. Therefore, alternative limit states such as tension buckling may remain valid despite the

occurrence of the impending ductile failure limit state. Nevertheless, tension buckling was concluded to be an unlikely limit state for realistic plate girders unless the flange stem thickness is exceptionally thin and the crack branch length is relatively long (lower t_f / a ratios with thinner flange stems).
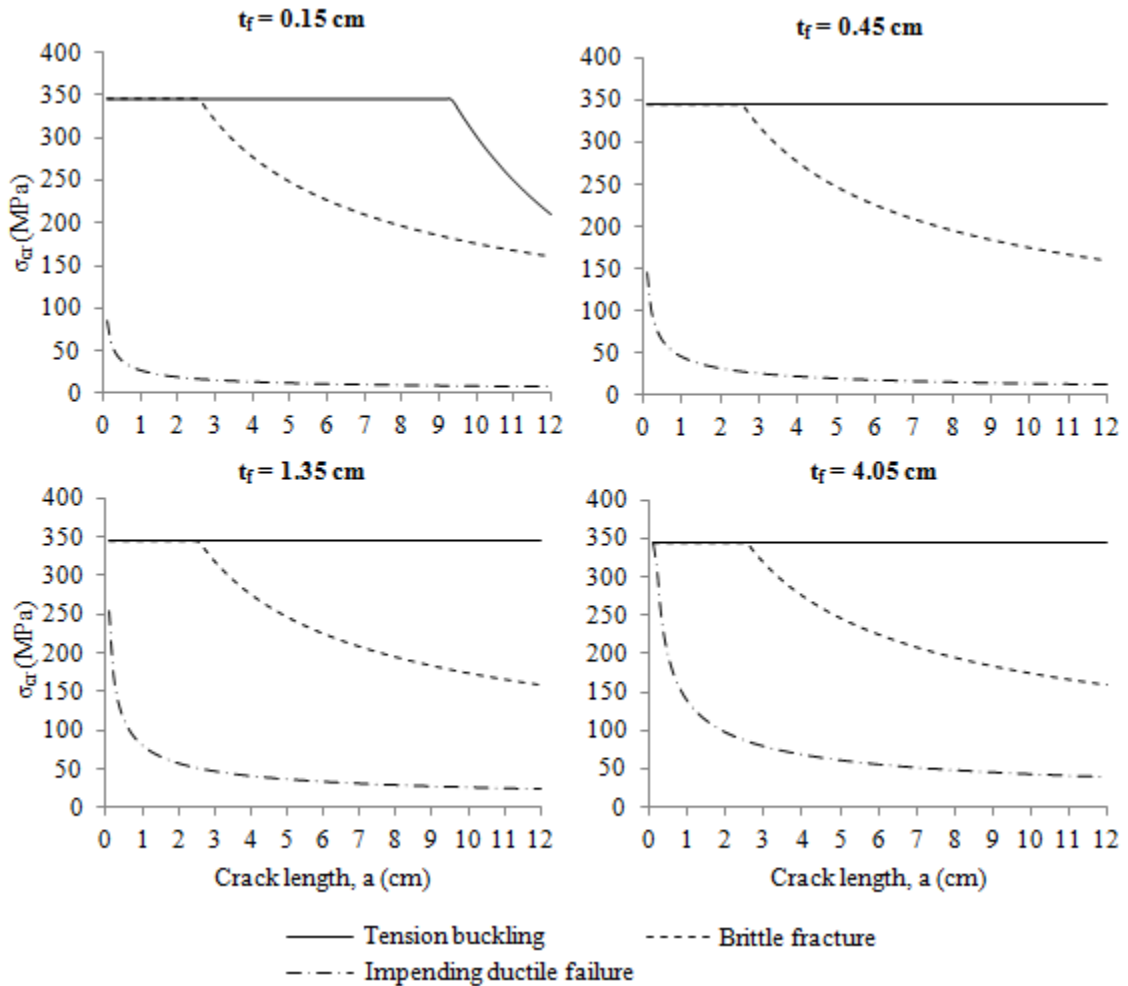
Figure 6.1.1: Trial flange stem capacities plotted as functions of crack branch length. The horizontal portions of the plots indicate the yield strength of the flange steel.

6.1.1.2 Vertical Edge-crack in Web Plate

The formulated bending moment capacity expressions given by (5.2.46), (5.2.50), (5.2.59), (5.2.80), (5.2.83), and (5.2.85) corresponding to the limit states of flange local

yielding, flange local buckling, web local buckling, tension buckling, brittle fracture, and impending ductile failure, respectively, were plotted as functions of vertical edge-crack length, *2a*, (see Figure 5.2.8) for each trial plate girder (see Figure 6.1.2). The critical plastic region radius, $r_{p,cr}$, measured from the crack tip at $\theta = 0$ was taken as $r_{p,cr} = t_w / 50$ (Shukla, 2005, ch. 4). Impending ductile failure is the governing limit state for all of the trial girders, thus invalidating the brittle fracture limit state. If the impending ductile failure limit state is neglected, the tension buckling limit state governs for all of the trial girders. Furthermore, if the tension buckling limit state is neglected, web local buckling is the governing limit state for PG-1 and PG-2. This is reflective of the extremely thin web plate thicknesses of PG-1 and PG-2. It can be seen that the web local buckling capacity gradually increases with increasing crack length. This phenomenon was previously observed by Brighenti (2005a, b, 2009) and Khedmati et al. (2009) in numerical tests of centrally cracked plates loaded under compression. The increase in buckling strength despite the local increase in bending stresses is in part explained by the shrinking of the embedded plate as the vertical crack length increases.

Neglecting the impending ductile failure, brittle fracture, and tension buckling limit states, flange local yielding is the governing limit state for the realistic trial plate girders (PG-3 and PG-4). It is observed that the vertical crack must grow to a length in the order of *20 - 25 cm* before the flange local yielding capacity begins to significantly decrease. For instance, a crack length of *2a = 5 cm* results in a negligible decrease in capacity relative to M_y, while a crack length of *2a = 40 cm* results in a decrease of *7%*. Several criteria must then be met in order for premature flange local yielding failure to occur in this particular type of cracked section (vertical edge-crack in web plate). First,

the crack length must be within or exceed the range of *20 - 25 cm*. Second, the required

elastic bending moment capacity, M_r, must be just below the provided capacity, M_{cr}.

Third, the impending ductile failure, brittle fracture, and tension buckling limit states are

neglected.

PG-3

PG-4

Crack length, 2a (cm)

——— Flange local yielding ----- Flange local buckling ----·---- Web local buckling

-------- Tension buckling ——— Impending ductile failure —--— Brittle fracture

Figure 6.1.2: Trial plate girder bending moment capacities plotted as functions of edge-crack length. The horizontal segments of the plots indicate the yield moment capacities. The tension buckling, brittle fracture, and impending ductile failure capacities are shown in separate plots for clarity.

6.1.1.3 Crack Extending Through One or Both Sides of Tension Flange

The formulated flange stem capacity expressions given by (5.2.98), (5.2.100), and (5.2.102) corresponding to the limit states of tension buckling, brittle fracture, and impending ductile failure, respectively, were plotted as functions of crack length, *2a*, for the trial flange stems and associated plate girders (see Figure 5.2.19) considering a wider

188

range of flange plate thicknesses with $b_f = 35\ cm$ (see Figure 6.1.3). The critical plastic region radius, $r_{p,cr}$, measured from the crack tip at $\theta = 0$ was taken as $r_{p,cr} = t_f\ /\ 50$ (Shukla, 2005, ch. 4). As with the three-ended crack and vertical edge-crack configurations, impending ductile failure is the governing limit state for all of the trial girders. If the impending ductile failure and brittle fracture limit states are neglected, the flange stem tensile capacities are overwhelmingly governed by the yield strength, $\sigma_Y = 345\ MPa$, of the flange steel. Hence, the bending moment capacities of the trial girders are mostly governed by the yield moment capacities, M_y. The only exception is when $t_f = 0.10\ cm$, where the tension buckling limit state governs when the crack length exceeds $2a = 10\ cm$. As with the three-ended crack configuration, tension buckling is nevertheless concluded to be an unlikely governing limit state for realistic plate girders unless the flange stem thickness is exceptionally thin and the edge-crack is relatively long (lower $t_f\ /\ a$ ratios with thinner flange stems).
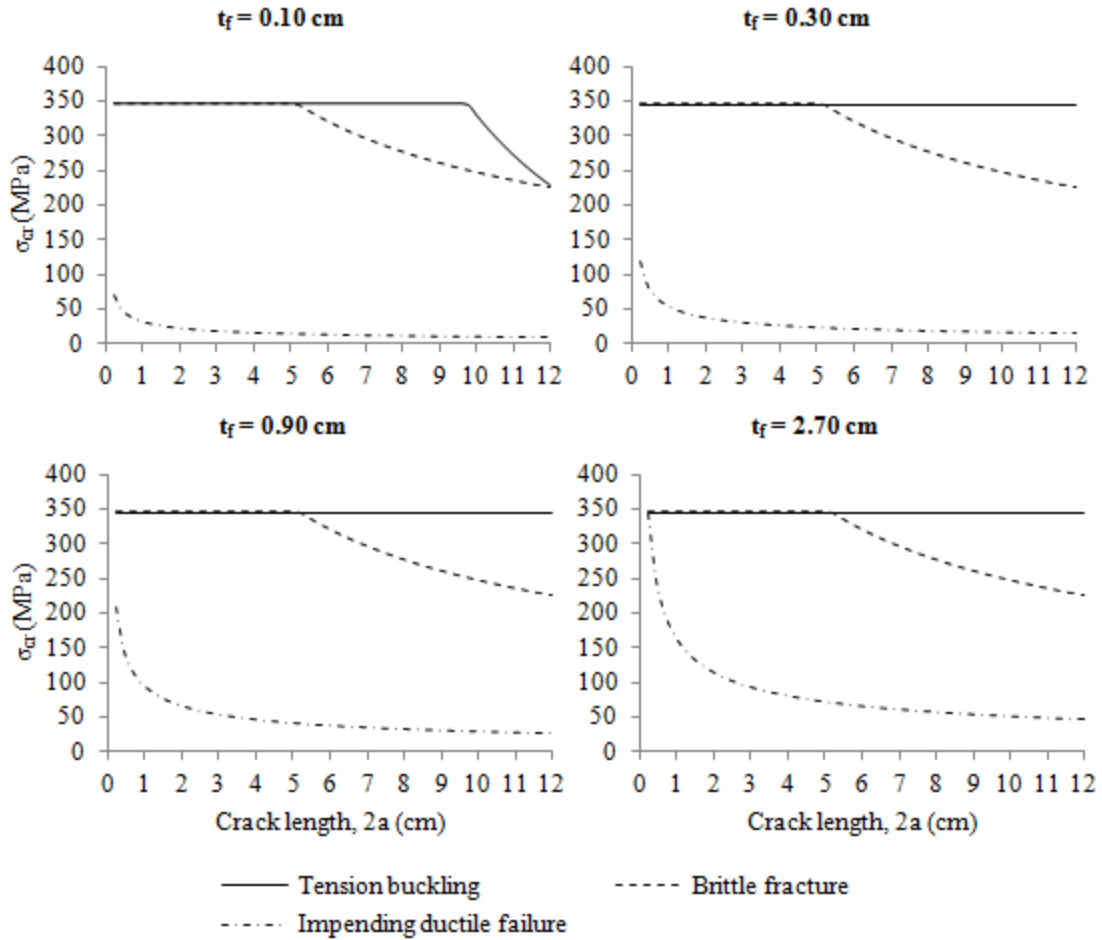
Figure 6.1.3: Trial flange stem tensile capacities plotted as functions of edge-crack length. The horizontal portions of the plots indicate the yield strength of the flange steel.

6.1.1.4 Diagonal Crack in Web Panel

The formulated perimeter shear strength expressions given by (5.3.42), (5.3.47), (5.3.54), and (5.3.62) corresponding to the limit states of web panel buckling, shear yielding, brittle fracture, and impending ductile failure, respectively, were plotted as functions of diagonal crack length, *2a*, for each trial web panel (see Figure 5.3.2). The web panel strengths associated with brittle fracture and shear yielding are independent of t_w, and are plotted for all four trial web panels (WP-A through WP-D) in Figure 6.1.4 as functions of crack length with the crack assumed to propagate at $\theta \approx 45°$ relative to the

190

flange. Conversely, the web panel strengths associated with buckling and impending ductile failure are dependent upon t_w, and are plotted for each trial web panel in Figure 6.1.5 as functions of crack length with $N_e = 100$, $r_{p,cr} = t_w / 50$, and $\theta \approx 45°$ (Shukla, 2005, ch. 4).

The limit states of brittle fracture and shear yielding do not govern the perimeter shear strength of any of the trial web panels. Web buckling governs the capacity of WP-A for all considered crack lengths. Also, web buckling governs the capacity of WP-B for crack lengths up to $2a \approx 19\ cm$, with impending ductile failure governing thereafter. Similarly, web buckling governs the capacity of WP-C for crack lengths up to $2a \approx 3\ cm$, with impending ductile failure governing thereafter. Impending ductile failure governs the capacity of WP-D for all considered crack lengths.

It is noted that although impending ductile failure is a limit state in itself and signifies the invalidation of the brittle fracture limit state, the shear yielding and web buckling limit states may remain valid. With this in mind, it is observed that the web buckling capacities of the trial panels are significantly degraded with increased crack length. The trial web panel buckling strengths are degraded by as much as *30%* when the crack length reaches *70 cm*.

Figure 6.1.4: Web panel brittle fracture and shear yielding capacities for WP-A through WP-D.

WP-A: Web Buckling and Impending Ductile Failure Capacities

WP-B: Web Buckling and Impending Ductile Failure Capacities

WP-C: Web Buckling and Impending Ductile Failure Capacities

WP-D: Web Buckling and Impending Ductile Failure Capacities

Crack length, 2a (cm)

Crack length, 2a (cm)

– – – Web buckling   ····· Impending ductile failure
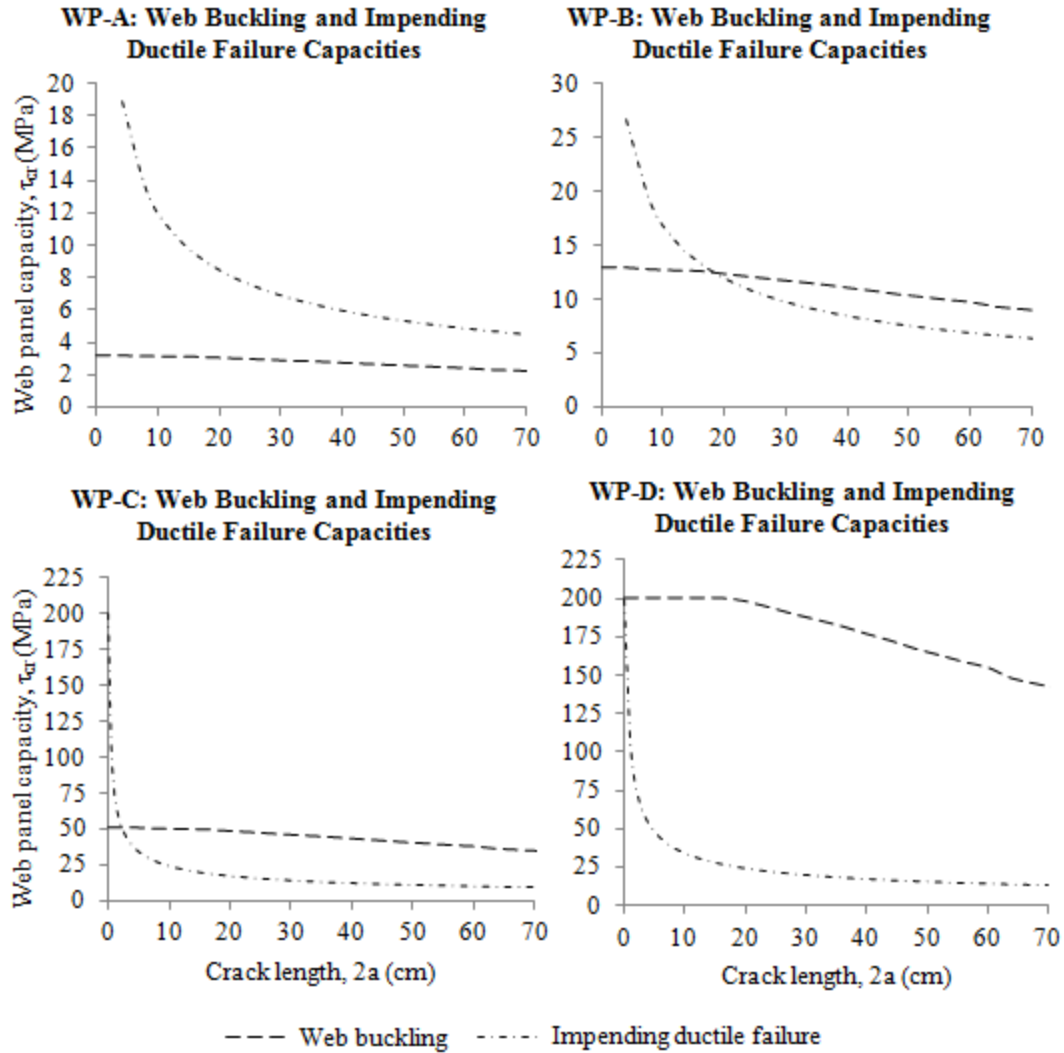
Figure 6.1.5: Web panel buckling and impending ductile failure capacities for WP-A through WP-D.

6.1.2 Capacity Expressions as Functions of Load Cycle

The formulated bending moment and shear force capacity expressions, $M_{cr} = f(\Gamma)$ and $V_{cr} = f(\Gamma)$, and the corresponding flange plate and web panel capacity expressions, $\sigma_{cr} = f(\Gamma)$ and $\tau_{cr} = f(\Gamma)$ (see Tables 6.1.1 and 6.1.2), were next plotted as functions of load cycle for the associated trial plate girders, flange stems, and web panels. The Paris-Erdogan equation material constants were taken as $C = 3.6 \times 10^{-10}$ and $m = 3.0$ (Bowman, 2002; Shukla, 2005, ch. 5). Also, the trial girders, flange stems, and web panels were

193

assumed to be loaded by constant-amplitude trigonometric load functions (see Figure 6.1.6).
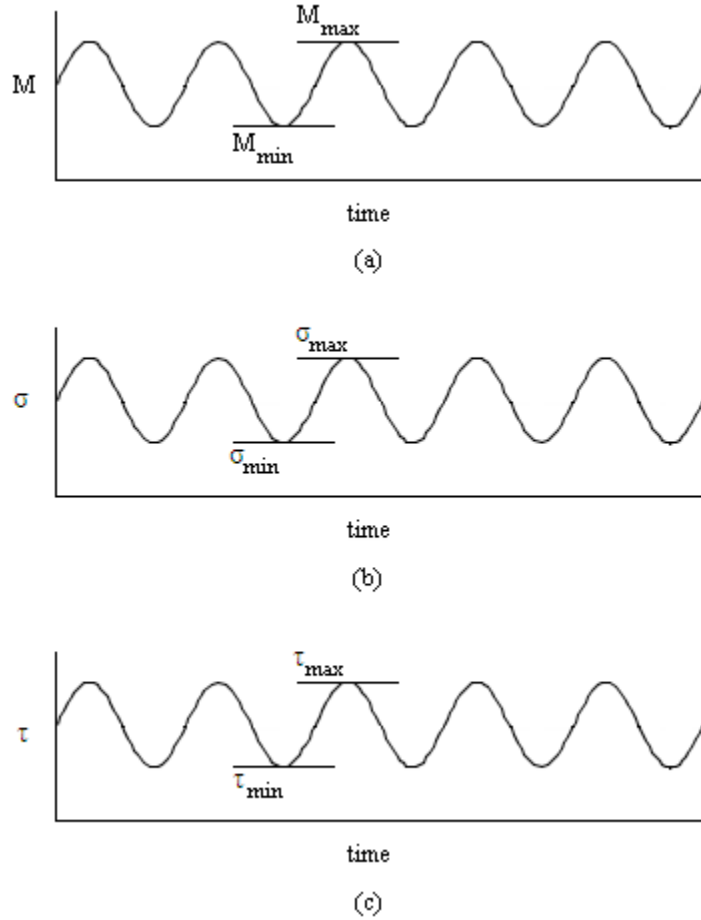
Figure 6.1.6: Constant-amplitude trigonometric load functions for (a) bending moment, (b) flange tensile stress, and (c) web panel perimeter shear stress.

The capacity expressions are not inherently functions of load cycle, but may be indirectly plotted as such by employing (5.5.7), rewritten here for clarity:

$$\Delta N = \frac{2}{C(m-2)} \left[\frac{a_i}{\left(\Delta \sigma_f \sqrt{\pi a_i} \right)^m} - \frac{a_f}{\left(\Delta \sigma_f \sqrt{\pi a_f} \right)^m} \right] \qquad (6.1.1)$$

For each limit state, the number of load cycles, ΔN, required to propagate a given fatigue crack from a_i to a_f were first determined using (6.1.1) considering the range in far-field

194

stress, $\Delta\sigma_f$. The capacity was then plotted as a function of the corresponding load cycles considering the branch length, a_f.

In general, the capacities decrease with increasing load cycle. The governing capacity, M_{cr}, V_{cr}, σ_{cr}, or τ_{cr}, may fall below the required capacity, M_r, V_r, τ_{cr} or σ_r, when a critical load cycle, N_{cr}, is achieved. It is noted that N_{cr} occurs when a_{cr} is achieved. If $a_i \approx 0$, N_{cr} is the approximate extended fatigue life of the plate girder neglecting the load cycles required to propagate the crack through the flange or web plate thickness (Osman & Roberts, 1999). The initial crack length was taken as $a_i = 0.1$ cm for all of the trial girders, flange stems, and web panels.

6.1.2.1 Three-ended Crack

The flange stem capacity expressions given by (5.2.14), (5.2.17), and (5.2.22) were plotted as functions of load cycle for the trial plate girders considering a wider range of flange plate thicknesses with $b_f = 35$ cm (see Figure 6.1.7). The constant-amplitude trigonometric load function was arbitrarily assumed to induce a maximum bending moment of $M_{max} = 180$ kN·m and a minimum bending moment of $M_{min} = 50$ kN·m. The governing limit states and associated capacities are identical to when the capacities were plotted as functions of crack length (see Figure 6.1.1).

$t_f = 0.15$ cm

$t_f = 0.45$ cm

$t_f = 1.35$ cm

$t_f = 4.05$ cm

——— Tension buckling   - - - - - Brittle fracture

— · — · · Impending ductile failure
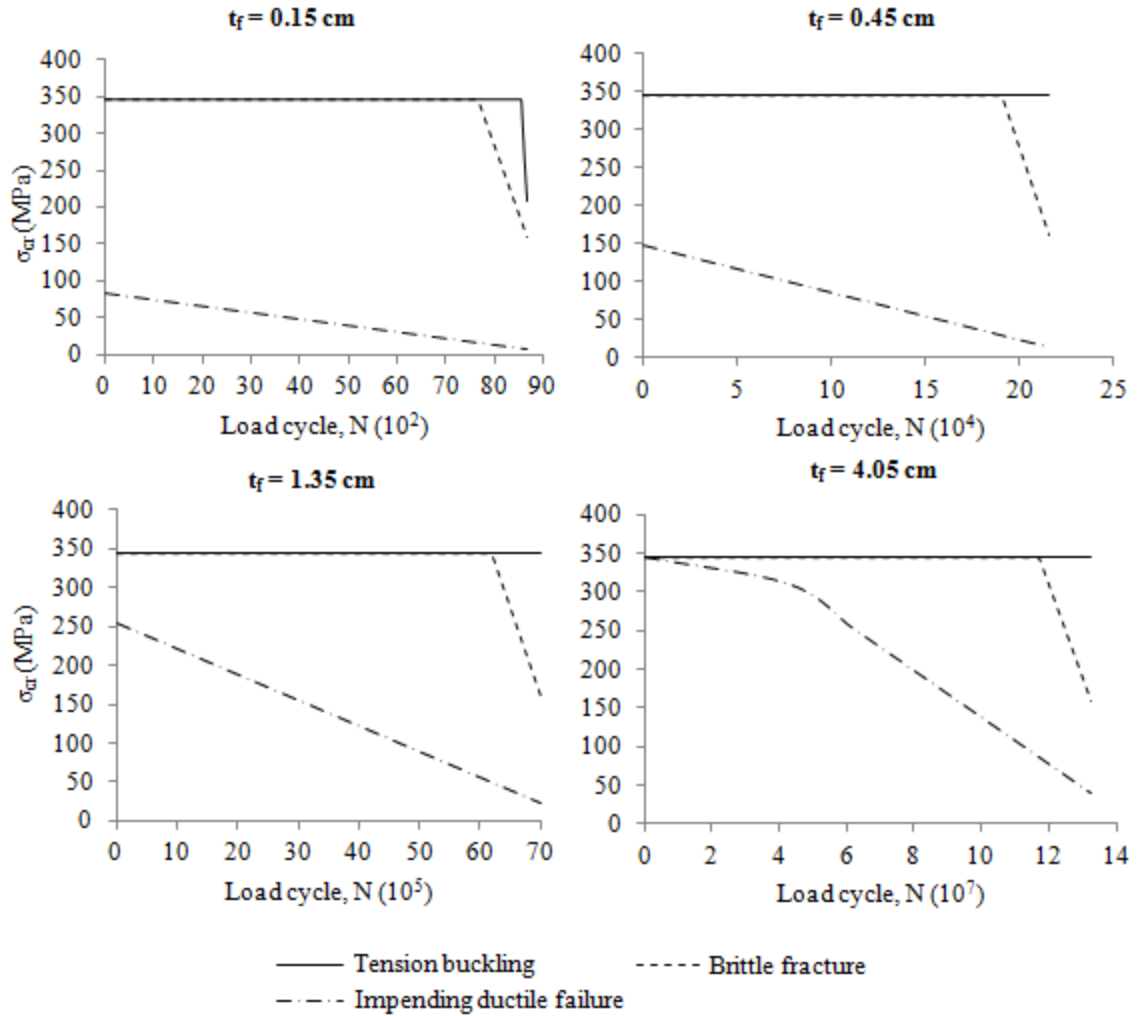
Figure 6.1.7: Trial flange stem tensile capacities plotted as functions of load cycle with $M_{max} = 180$ kN·m and $M_{min} = 50$ kN·m.

6.1.2.2 Vertical Edge-crack in Web Plate

The bending moment capacity expressions given by (5.2.46), (5.2.50), (5.2.59), (5.2.80), (5.2.83), and (5.2.85) were plotted as functions of load cycle for the trial plate girders (see Figure 6.1.8). The load function was arbitrarily assumed to induce a maximum bending moment of $M_{max} = 500$ kN·m and a minimum bending moment of $M_{min} = 200$ kN·m. The tension buckling, brittle fracture, and impending ductile failure capacities are shown in separate plots for clarity. As with the three-ended crack

196

configuration, the governing limit states and associated capacities are identical to when

the capacities were plotted as functions of crack length (see Figure 6.1.2).
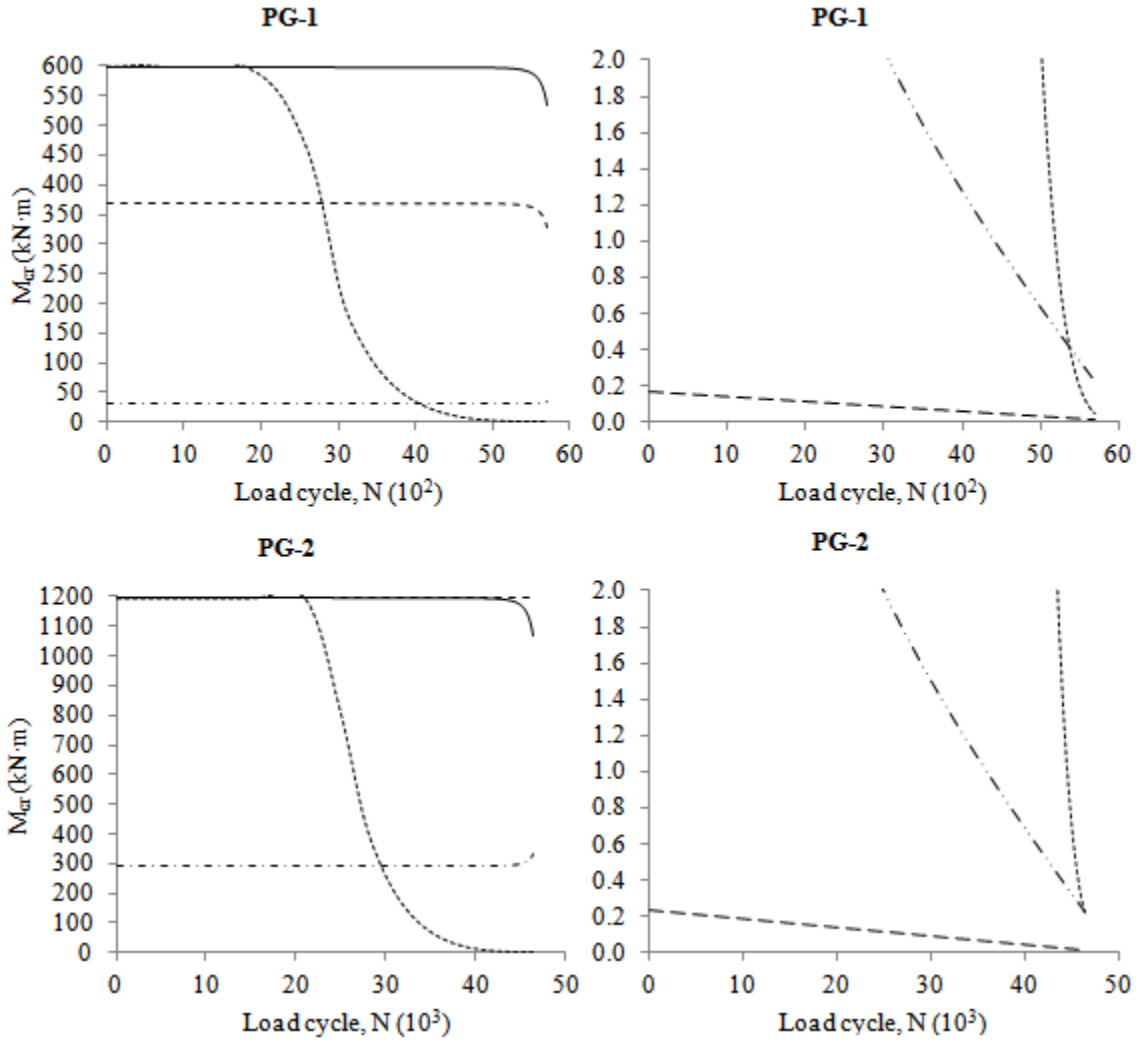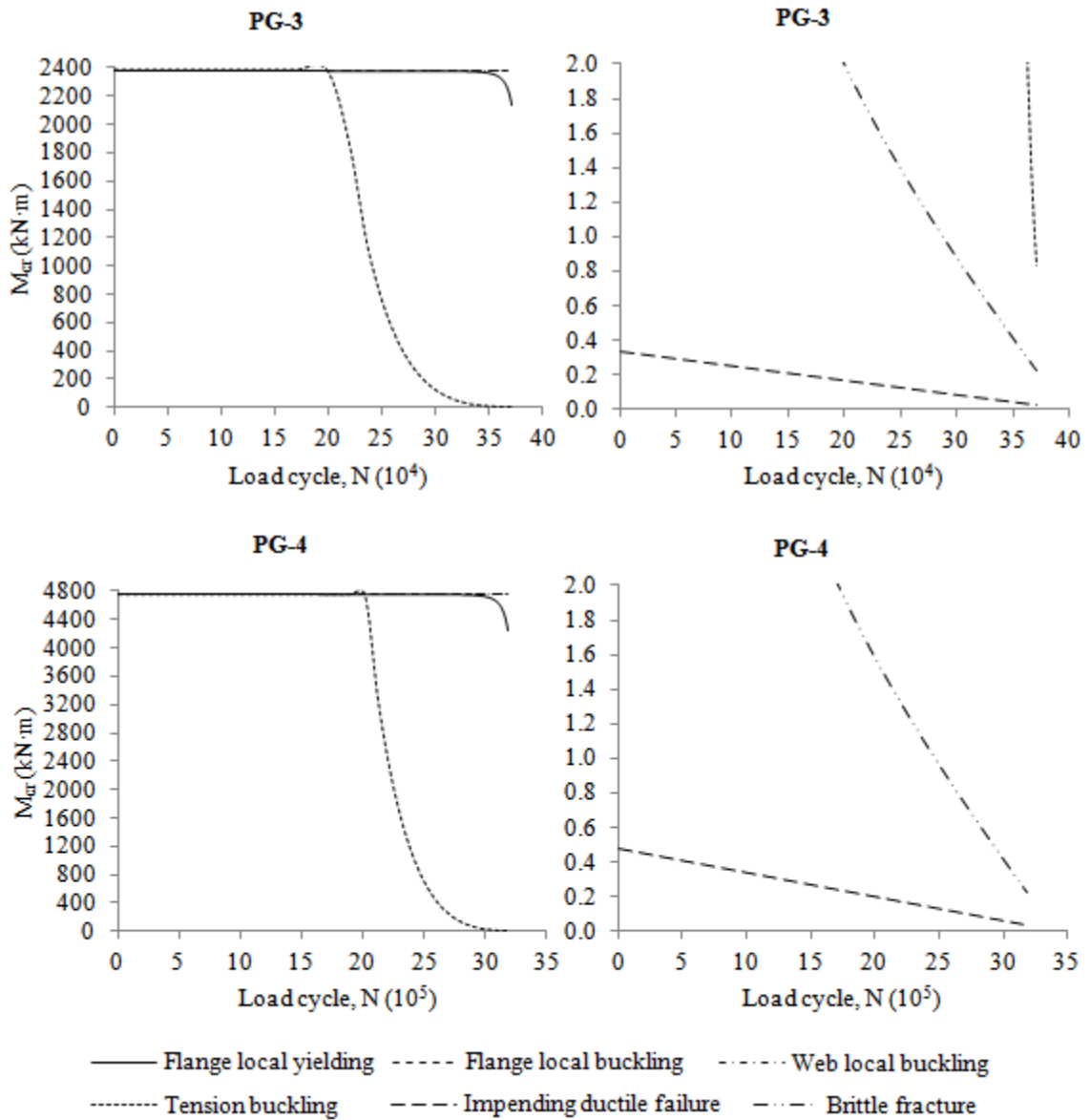
Figure 6.1.8: Trial plate girder bending moment capacities plotted as functions of load cycle.

6.1.2.3 Crack Extending Through One or Both Sides of Tension Flange

The flange stem capacity expressions given by (5.2.98), (5.2.100), and (5.2.102) were plotted as functions of crack length for the trial plate girders considering a wider range of flange plate thicknesses with $b_f = 35$ cm (see Figure 6.1.9). The applied load

function was assumed to induce a maximum bending moment of $M_{max} = 180\ kN{\cdot}m$ and a minimum bending moment of $M_{min} = 50\ kN{\cdot}m$.
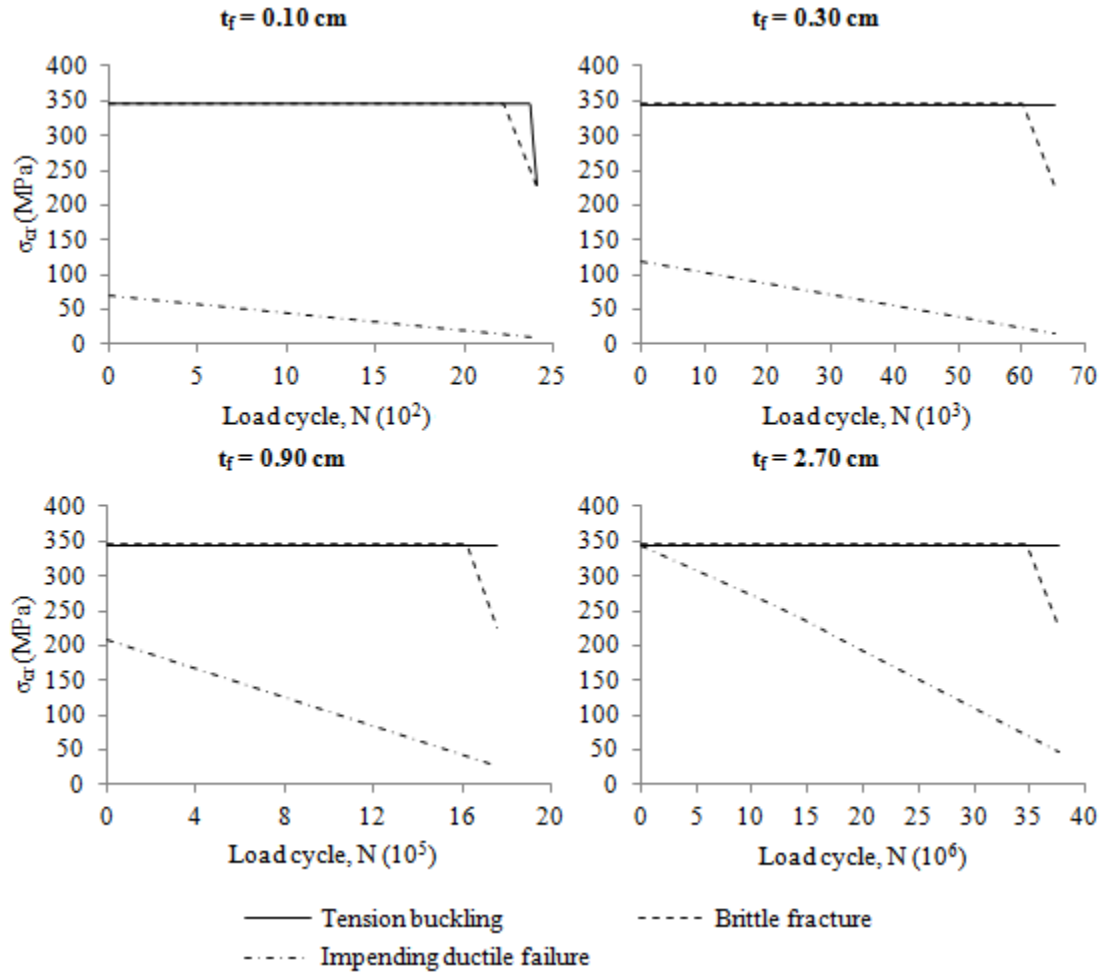
Figure 6.1.9: Trial flange stem tensile capacities plotted as functions of load cycle.

6.1.2.4 Diagonal Crack in Web Panel

The web panel strengths associated with brittle fracture and shear yielding given by (5.3.54) and (5.3.47), respectively, are independent of t_w, and are plotted for all four trial web panels (WP-A through WP-D) in Figure 6.1.10 as functions of load cycle with the crack assumed to propagate at $\theta \approx 45°$ relative to the flange. Conversely, the web

panel strengths associated with buckling and impending ductile failure given by (5.3.42) and (5.3.62), respectively, are dependent upon t_w, and are plotted for each trial web panel in Figure 6.1.11 as functions of load cycle with $N_e = 100$, $r_{p,cr} = t_w / 50$, and $\theta \approx 45°$ (Shukla, 2005, ch. 4). The applied load function was assumed to induce a maximum shear force of $V_{max} = 600\ kN$ and a minimum shear force of $V_{min} = 500\ kN$.
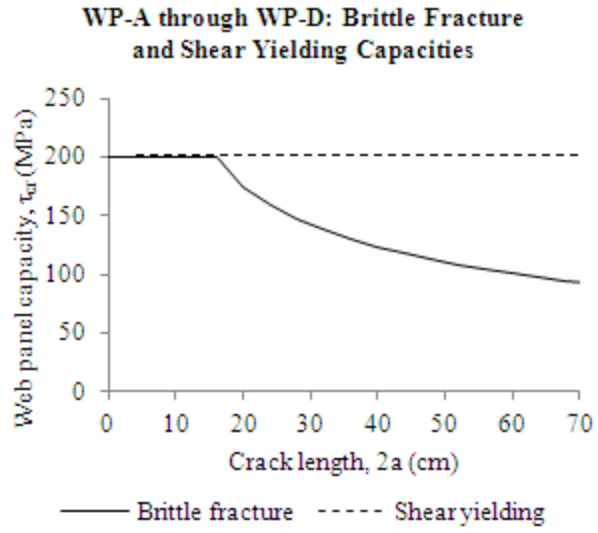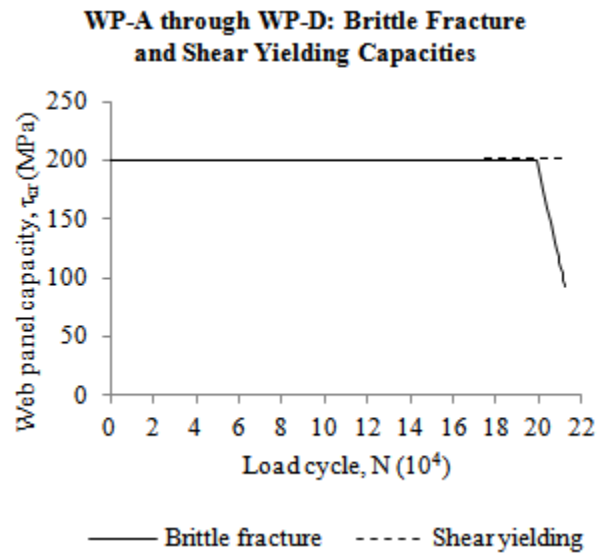

Figure 6.1.10: Web panel brittle fracture and shear yielding capacities for WP-A through WP-D.
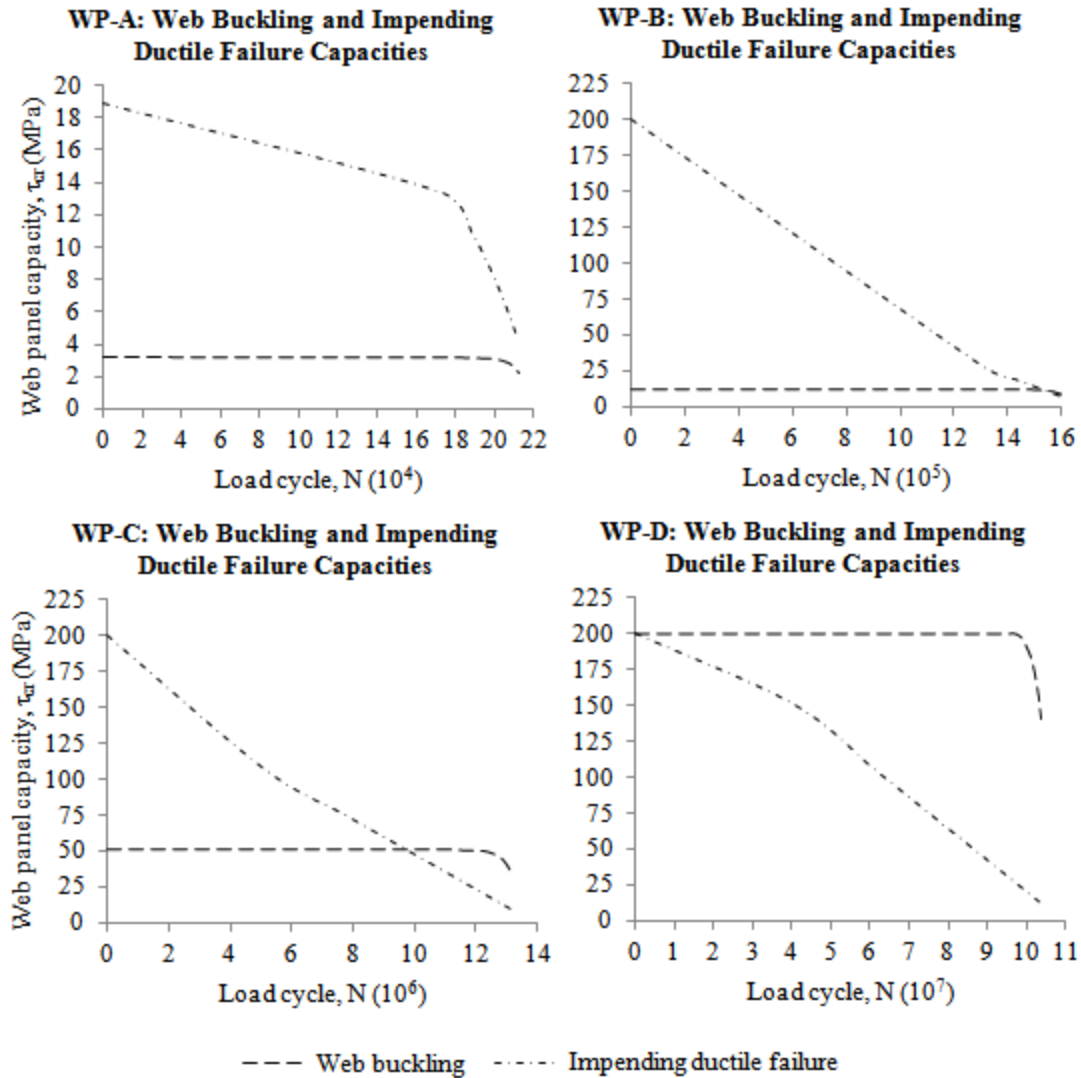
Figure 6.1.11: Web panel buckling and impending ductile failure capacities for WP-A through WP-D.

6.2   Proposed Design Procedure

6.2.1   Summary

A procedure for designing or otherwise modifying the elastic capacities and fatigue lives of plate girders for prescribed through-thickness fatigue crack configurations is finally outlined. As was previously mentioned, it may be useful for structural engineers to be able to design or otherwise modify the elastic capacities and fatigue lives of steel

highway bridge plate girders for presumed through-thickness fatigue crack configurations so that the premature occurrence of elastic limit states may be averted in between bridge inspection periods. It is not uncommon for design engineers to perform additional checks on a structural design even though the design satisfies the code-based requirements. Although the formulated capacity expressions (see Tables 6.1.1 and 6.1.2) pertain only to elastic limit states, and are not required by the AASHTO *LRFD Bridge Design Specifications* (2010), the expressions may be useful for engineers to perform conservative and brief checks on I-shaped transversely stiffened plate girders.

The proposed design procedure is described and demonstrated by conducting an initial design of an I-shaped plate girder that is part of a theoretical highway bridge using the *LRFD Bridge Design Specifications* (AASHTO, 2010) (see Appendix A: AASHTO LRFD Bridge Design Specifications). The formulated capacity and decay expressions are then employed to check the governing capacity and fatigue life of the initial girder design for prescribed through-thickness fatigue crack configurations and fatigue lives, respectively. Various limit states may be neglected or invalidated such as the impending ductile failure and brittle fracture limit states. The initial girder design is then modified by adjusting the flange thicknesses, web thickness, flange width, and web depth in order to satisfy the capacity and decay expression requirements.

6.2.2 Initial Code-based Plate Girder Design

6.2.2.1 Assumptions

The initial design of the I-shaped plate girder is performed with the following assumptions regarding a theoretical highway bridge:

1. U.S. customary units are employed for compatibility with the AASHTO *LRFD Bridge Design Specifications* (2010).

2. The bridge is a short-span slab-girder steel highway bridge.

3. The bridge has two design lanes and is part of a rural portion of the IHS.

4. The ADTT is approximately 2,000.

5. The bridge is single-span and is simply-supported.

6. The bridge is conservatively analyzed as having a non-composite configuration.

7. The superstructure is supported by four girders spaced at $s = 5$ ft. on-center.

8. The span length is $l = 85$ ft.

9. The plate girder considered is an interior girder.

10. The tension and compression flanges are identical at any location along the length of the girder.

A profile view and cross-section view of the theoretical highway bridge are shown in Figures 6.2.1 and 6.2.2, respectively. Also, the geometrical properties, material properties, and applied loads of the bridge are listed in Tables 6.2.1, 6.2.2, and 6.2.3, respectively.
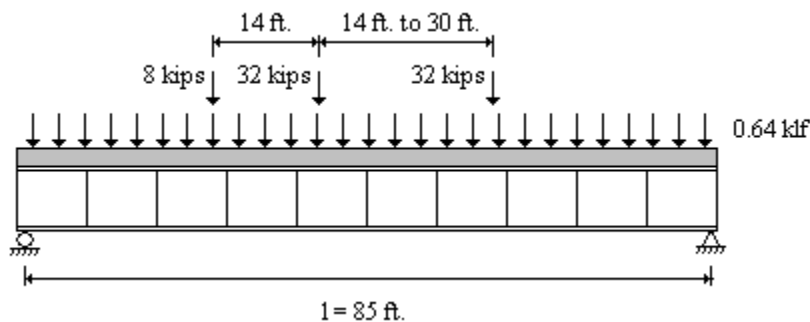
Figure 6.2.1: Profile view of highway bridge superstructure showing lane load and HL-93 design truck.
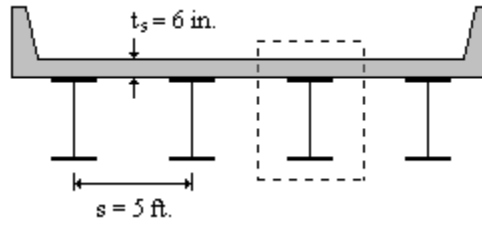
Figure 6.2.2: Cross-section of highway bridge superstructure indicating the girder being considered.

Table 6.2.1. Material properties of theoretical highway bridge.

Property	Value
Modulus of elasticity of steel, E_s	29,000 ksi
Yield strength of steel, F_y	50 ksi
Mode I fracture toughness of steel, K_{Ic}	180 ksi (in.)^2
Paris-Erdogan constant, C	3.6 x 10^{-10}
Paris-Erdogan constant, m	3.0
Poisson's ratio of steel	0.3
Unit weight of steel, γ_s	490 pcf
28-day concrete compressive strength, f'_c	5,000 psi
Unit weight of reinforced concrete, γ_c	150 pcf
Modulus of elasticity of concrete[1], E_c	4,290 ksi

1. For concrete with f'_c = 5000 psi and γ_c = 150 pcf
(ACI, 2005, sec. 8.5)

Table 6.2.2. Geometrical properties of theoretical highway bridge.

Property	Value
Span length, l	85 ft.
Girder spacing, s	5 ft.
Slab thickness[1], t_s	6 in.

1. Includes ½ in. wearing surface.

Table 6.2.3. Loads applied upon theoretical highway bridge.

Load	Value
Future wearing surface, p_{ws}	20 psf
Forms, p_f	15 psf
Miscellaneous, p_m	2 psf
Barriers[1], w_b	150 plf

1. Approximate load per linear foot upon each girder.

The tension and compression flange plates are initially selected to be *16" x 1"* plates. The web plate is initially selected to be a *50" x 3/8"* plate (see Figure. 6.2.3). Hence, $b_f = 16$ in., $t_f = 1.0$ in., $d_w = 50$ in., and $t_w = 0.375$ in.
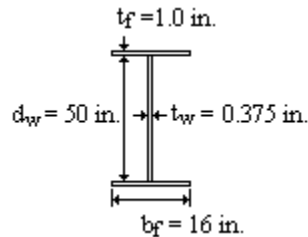
Figure 6.2.3: Initial cross-sectional dimensions of the girder being designed.

6.2.2.2 Live Load

The required live load bending moment, *LL*, is first calculated. An influence line is employed to calculate the total critical live load bending moment due to the HL-93 design truck or design tandem, and the design lane load. The total critical live load bending moment is then distributed to the interior girder being designed using a distribution factor determined in accordance with the girder line method as specified in Section 4.6.2.2.2 of the *LRFD Specifications* (2010). The maximum bending moment in the simply-supported span occurs at mid-span. Therefore, an influence line is developed for the bending moment at *l/2* as shown in Figure 6.2.4. The maximum magnitude of the influence line is given by:

$$\frac{l}{4} = \frac{85\,ft.}{4} = 21.25\,ft.$$

(6.2.1)
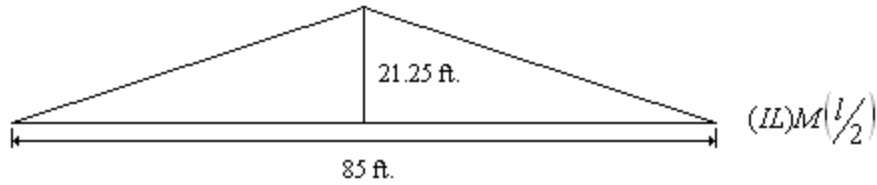
Figure 6.2.4: Influence line for the mid-span bending moment of the simply-supported girder.

The HL-93 design truck is first situated along the influence line in the position shown in Figure 6.2.5a to induce a critical live load bending moment, $M_{LL,dt}$. The critical live load bending moment is then calculated from the influence line using similar triangles, as follows:

$$M_{LL,dt} = (8k)(14.25\,ft) + (32k)(21.25\,ft) + (32k)(14.25\,ft) = 1250k * ft \qquad (6.2.2)$$

Next, the design tandem is situated along the influence line in the position shown in Figure 6.2.5b to induce a critical live load bending moment, $M_{LL,t}$, and is calculated as follows:

$$M_{LL,t} = (25k)(21.25\,ft) + (25k)(19.25\,ft) = 1012.5k * ft \qquad (6.2.3)$$

Finally, the design lane load is specified to act along the entire length of the girder as shown in Figure 6.2.5c to induce the critical design lane load bending moment, $M_{LL,dl}$, and is calculated as follows:

$$M_{LL,dl} = \frac{1}{2}\left(0.64\frac{k}{ft}\right)(85\,ft)(21.25\,ft) = 578k * ft \qquad (6.2.4)$$

206
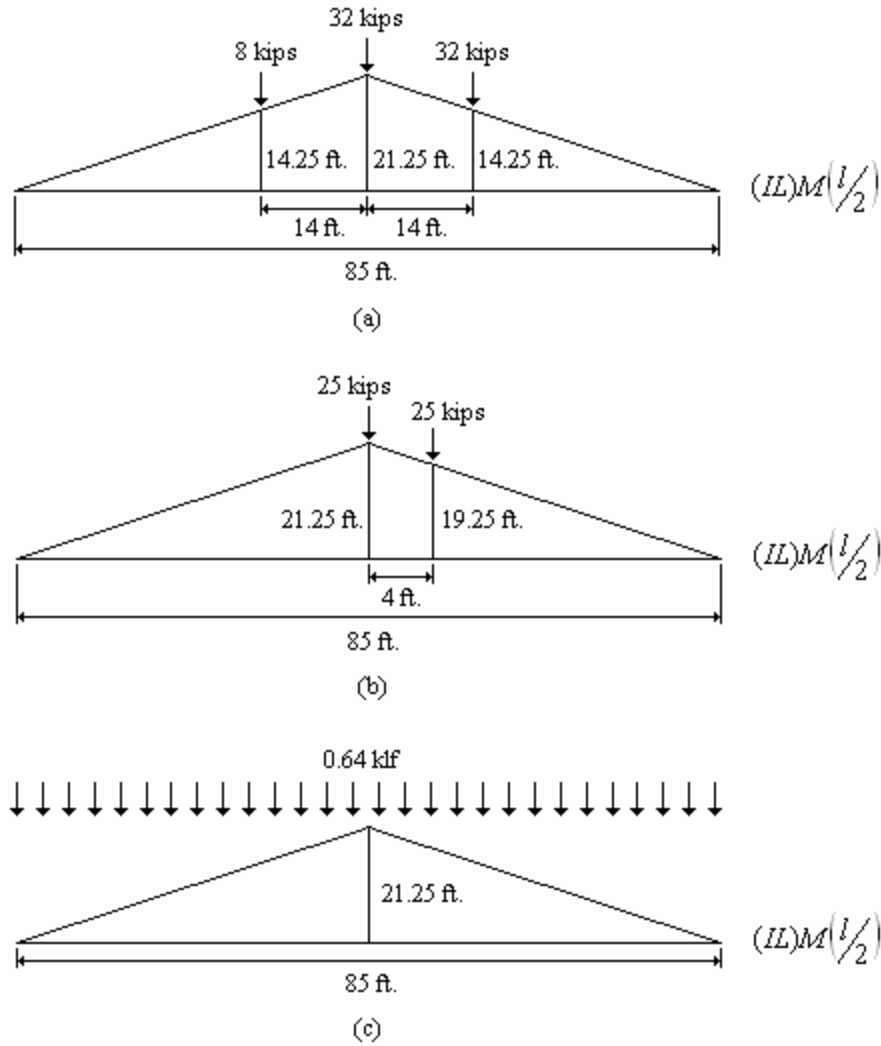
Figure 6.2.5: Influence line for the mid-span bending moment of the simply-supported girder with (a) HL-93 design truck, (b) design tandem, and (c) design lane load.

The critical live load bending moment due to the HL-93 design truck, $M_{LL,dt} = 1250\ k\cdot ft$, is greater than the live load bending moment due to the design tandem, $M_{LL,t} = 1012.5$ $k\cdot ft$. Therefore, the HL-93 design truck governs and is combined with the design lane load to obtain the total critical live load bending moment, M_{LL}:

$$M_{LL} = M_{LL,dt} + M_{LL,dl} = 1250k * ft + 578k * ft = 1828k * ft \qquad (6.2.5)$$

The total critical live load bending moment is next multiplied by a distribution factor, g, to distribute M_{LL} to the interior girder being designed. In accordance with the

207

girder line method, g for an interior girder that is part of a slab-girder configuration with two or more design lanes is specified as (AASHTO, 2010, sec. 4.6.2.2.2):

$$g = 0.075 + \left(\frac{s}{9.5}\right)^{0.6} \left(\frac{s}{l}\right)^{0.2} \left(\frac{K_g}{12.0lt_s^3}\right)^{0.1} \tag{6.2.6}$$

The term K_g is the longitudinal stiffness parameter, specified as

$$K_g = n\left(I + A_g e_g^2\right) \tag{6.2.7}$$

where A_g is the gross area of the steel girder, expressed as:

$$A_g = 2(1.0in)(16in) + (0.375in)(50in) = 50.75in^2 \tag{6.2.8}$$

The term n in (6.2.7) is defined as:

$$n = \frac{E_s}{E_c} = \frac{29000ksi}{4290ksi} = 6.76 \tag{6.2.9}$$

Also, I is the moment of inertia of the girder and is calculated from the initial girder cross-sectional dimensions of $b_f = 16$ in., $t_f = 1.0$ in., $d_w = 50$ in., and $t_w = 0.375$ in., resulting in $I = 24,717$ in^4. Finally, e_g is the distance between the centers of gravity of the girder and the concrete deck, expressed as:

$$e_g = \frac{d_w}{2} + t_f + \frac{t_s}{2} = \frac{50}{2}in + 1.0in + \frac{6}{2}in = 29in \tag{6.2.10}$$

Substituting (6.2.8), (6.2.9), (6.2.10), and $I = 11,530$ in^4 into (6.2.7) results in:

$$K_g = 6.76\left[24717in^4 + (50.75in^2)(29in)^2\right] = 455609in^4 \tag{6.2.11}$$

Finally, substituting (6.2.11) into (6.2.6) results in:

$$g = 0.075 + \left(\frac{5ft}{9.5}\right)^{0.6} \left(\frac{5ft}{85ft}\right)^{0.2} \left[\frac{455609in^4}{12.0(85ft)(6in)^3}\right]^{0.1} = 0.49 \tag{6.2.12}$$

The final live load bending moment upon the internal girder being designed is then expressed as:

$$LL = M_{LL}g = (1828k * ft)(0.49) = 895.7k * ft \qquad (6.2.13)$$

A dynamic load allowance, *IM*, is also applied to the final live load bending moment. For components of the superstructure besides the deck joints, the final live load bending moment is increased by *33%* (AASHTO, 2010, p. 3-30):

$$IM = 0.33LL = 0.33(895.7k * ft) = 295.6k * ft \qquad (6.2.14)$$

6.2.2.3 Dead Load

The required dead load bending moments are next calculated by considering the self-weight of the steel girder, the concrete deck, and additional load including forms, miscellaneous load, barriers, and future wearing surface. The weight per linear foot of the girder, concrete deck, forms, miscellaneous items, and barriers are designated as w_{DC}. The weight per linear foot of the future wearing surface is designated as w_{DW}.

The weight of the girder, $w_{DC,g}$, per linear foot is calculated with the following formula:

$$
\begin{aligned}
w_{DC,g} = A_g \gamma_s &= \left[2\left(\frac{16}{12} ft\right)\left(\frac{1}{12} ft\right) + \left(\frac{50}{12} ft\right)\left(\frac{0.375}{12} ft\right) \right]\left(490 \frac{lb}{ft^3} \right) \\
&= 173 \frac{lb}{ft} = 0.173 \frac{k}{ft}
\end{aligned}
\qquad (6.2.15)
$$

where γ_s is the unit weight of steel as listed in Table 6.2.1.

The weight of the concrete deck, $w_{DC,d}$, per linear foot is determined with the following formula:

$$w_{DC,d} = t_s s \gamma_c = \left(\frac{6}{12} ft\right)(5 ft)\left(150 \frac{lb}{ft^3}\right) = 375 \frac{lb}{ft} = 0.375 \frac{k}{ft} \qquad (6.2.16)$$

where t_s is the slab thickness, s is the tributary width of the interior girder being designed, and γ_c is the unit weight of reinforced concrete as listed in Table 6.2.1. It is noted that the tributary width of the interior girder being designed is the girder spacing, s.

The combined weight of the forms, miscellaneous items, and barriers, $w_{DC,m}$, per linear foot is determined with the following formula:

$$\begin{aligned} w_{DC,m} &= p_f\left(s - b_f\right) + p_m s + w_b \\ &= \left(15 \frac{lb}{ft^2}\right)\left(5 ft - \frac{16}{12} ft\right) + \left(2 \frac{lb}{ft^2}\right)(5 ft) + 150 \frac{lb}{ft} = 215 \frac{lb}{ft} = 0.215 \frac{k}{ft} \end{aligned} \qquad (6.2.17)$$

where p_f is the load from the forms, p_m is the load from miscellaneous items, and w_b is the load from the barriers, as listed in Table 6.2.3. The total load per linear foot of the girder, concrete deck, forms, miscellaneous items, and barriers is then calculated as:

$$\begin{aligned} w_{DC} &= w_{DC,g} + w_{DC,d} + w_{DC,m} \\ &= 0.173 \frac{k}{ft} + 0.375 \frac{k}{ft} + 0.215 \frac{k}{ft} = 0.763 \frac{k}{ft} \end{aligned} \qquad (6.2.18)$$

The weight of future wearing surface, w_{DW}, per linear foot is determined with the following formula:

$$w_{DW} = p_{ws} s = \left(20 \frac{lb}{ft^2}\right)(5 ft) = 100 \frac{lb}{ft} = 0.100 \frac{k}{ft} \qquad (6.2.19)$$

where p_{ws} is the weight of future wearing surface as listed in Table 6.2.3.

The maximum bending moment in a uniformly loaded simply-supported span occurs at mid-span, and is given by:

$$M = \frac{wl^2}{8} \qquad (6.2.20)$$

where M is the bending moment at mid-span, w is the uniform load per unit length, and l is the span length. Substituting $w_{DC} = 0.735\ klf$ and $w_{DW} = 0.100\ klf$ into (6.2.3) with $l = 85$ ft. results in the final dead load bending moments, DC and DW:

$$DC = \frac{\left(0.763\frac{k}{ft}\right)(85\,ft)^2}{8} = 689.1k * ft \tag{6.2.21}$$

$$DW = \frac{\left(0.100\frac{k}{ft}\right)(85\,ft)^2}{8} = 90.3k * ft \tag{6.2.22}$$

6.2.2.4 Load Combinations

The final live load and dead load bending moments are next combined into the Strength I load combination, specified as:

$$\gamma_p DC + \gamma_p DW + 1.75LL + 1.75IM \tag{6.2.23}$$

where γ_p for DC is taken as 1.25 and γ_p for DW is taken as 1.50 (AASHTO, 2010, sec. 3.4.1). Substituting (6.2.13), (6.2.14), (6.2.21), and (6.2.22) into (6.2.23) results in the required factored bending moment, M_u, associated with Strength I for the girder being designed:

$$M_u = 1.25(689.1k * ft) + 1.50(90.3k * ft) + 1.75(895.7k * ft)$$
$$+ 1.75(295.6k * ft) = 3081.6k * ft \tag{6.2.24}$$

6.2.2.5 Design for Strength Limit State

The strength of the girder being designed must be sufficient to resist the effects from the load combination given by (6.2.24). This requirement is given by (A.4.1) and is rewritten here for clarity:

$$f_{bu} + \frac{1}{3}f_l \leq \phi_f F_{nc} \qquad (6.2.25)$$

where f_l is the bending stress due to lateral bending. The term f_{bu} is the bending stress in the compression flange due to M_u, taken as,

$$f_{bu} = \frac{M_u}{S} \qquad (6.2.26)$$

The elastic section modulus, S, is determined based upon the initial girder cross-sectional dimensions of $b_f = 16$ in., $t_f = 1.0$ in., $d_w = 50$ in., and $t_w = 0.375$ in., resulting in $S = 951$ in^3. Substituting (6.2.24) and $S = 951$ in^3 into (6.2.26) results in:

$$f_{bu} = \frac{(3081.6k * ft)(12)}{951 in^3} = 38.9 ksi \qquad (6.2.27)$$

For simplicity, f_l is taken as equal to zero.

The nominal flexural resistance of the compression flange, F_{nc}, is first determined for the local buckling limit state (see Appendix F: Classical Plate Theory). The slenderness ratio, λ_f, for the compression flange is first determined:

$$\lambda_f = \frac{b_{fc}}{2t_{fc}} = \frac{16 in}{2(1.0 in)} = 8.0 \qquad (6.2.28)$$

where b_{fc} is the compression flange width and t_{fc} is the compression flange thickness. The slenderness ratio, λ_{pf}, for a compact flange is next calculated:

$$\lambda_{pf} = 0.38\sqrt{\frac{E_s}{F_{yc}}} = 0.38\sqrt{\frac{29000 ksi}{50 ksi}} = 9.15 \qquad (6.2.29)$$

where F_{yc} is the yield strength of the compression flange steel. It can be seen that $\lambda_f = 8.0 < \lambda_{pf} = 9.15$, and thus the compression flange is compact (i.e. the flange will not buckle prior to yielding). The flexural resistance of the flange is then specified as

$$F_{nc} = R_b R_h F_{yc} \qquad (6.2.30)$$

The terms R_b and R_h are taken as equal *1.0*. Substituting R_b and R_h into (6.2.30) results in:

$$F_{nc} = (1.0)(1.0)(50ksi) = 50ksi \qquad (6.2.31)$$

The nominal flexural resistance of the compression flange is next determined for the lateral torsional buckling limit state (AASHTO, 2010, sec. 6.10.8.2.3). The unbraced length, L_b, of the girder being designed is assumed to be less than the limiting unbraced length, L_p, such that lateral torsional buckling is prevented and F_{nc} is equal to (6.2.31). The governing flexural resistance of the compression flange is thus F_{nc} = *50 ksi*.

Substituting f_l = *0*, (6.2.27), and (6.2.31) into (6.2.25) results in

$$f_{bu} = 38.9ksi < \phi_f F_{nc} = 50ksi \qquad (6.2.32)$$

where the resistance factor for flexure is taken as Φ=*1.00* (AASHTO, 2010, sec. 6.5.4.2). The strength requirement specified by (6.2.25) is therefore satisfied and the initial girder cross-sectional dimensions of b_f = *16* in., t_f = *1.0* in., d_w = *50* in., and t_w = *0.375* in. are adequate for the Strength I load combination.

6.2.3 Modification of Initial Design for Prescribed Crack Configurations

The initial girder cross-sectional dimensions are next modified by adjusting t_f, b_f, t_w, and d_w in order that the elastic bending moment capacity of the girder is sufficient for prescribed fatigue crack configurations and fatigue lives. This requirement is essentially a form of (A.2.2) and is expressed as

$$\sigma_r \leq \sigma_{cr} \qquad (6.2.33)$$

where σ_r is the required bending stress in the flanges due to M_u, as expressed by (6.2.26). Based upon the initial girder cross-sectional dimensions of b_f = *16* in., t_f = *1.0* in., d_w = *50* in., and t_w = *0.375* in., it was determined that:

$$\sigma_r = f_{bu} = 38.9 ksi \tag{6.2.34}$$

as expressed by (6.2.27). The term σ_{cr} in (6.2.33) is the governing flange stem capacity, $\sigma_{cr} = f(\Gamma)$, and is in part dependent upon the prescribed fatigue crack configurations.

The prescribed fatigue crack configurations include the three-ended crack, the vertical edge-crack in the web, and the horizontal crack in the tension flange (see Figure 6.2.6). The corresponding prescribed branch lengths, a_i, are listed in Table 6.2.4. Also, the prescribed fatigue life for each crack configuration is specified to be *70* days to provide ample time for the cracks to be detected and arrested. The number of load cycles induced within the girder being designed over a *70* day period is expressed in the form of (A.5.3), given as:

$$N = (70)n(ADTT)_{SL} \tag{6.2.35}$$

where *n* is the number of stress cycles per truck passage, and $(ADTT)_{SL}$ is the average daily truck traffic for a single lane. Given that the single-span simply-supported theoretical highway bridge has two design lanes with *ADTT = 2,000*, it is determined that *n = 1.0* and *(ADTT)_{SL} = 1,700*, resulting in a prescribed fatigue life of (AASHTO, 2010, secs. 3.6.1.4, 6.6.1.2.5):

$$N = (75)(1.0)(1700) = 127500 \tag{6.2.36}$$
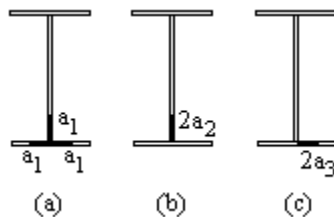
Figure 6.2.6: Prescribed fatigue crack configurations indicating branch lengths, a_i: (a) Three-ended crack, (b) vertical edge-crack in web, and (c) horizontal crack in the tension flange.

Table 6.2.4. Prescribed branch lengths.

Branch, a_i	Length (in)
a_1	6.0
$2a_2$	8.0
$2a_3$	6.0

6.2.3.1 Design for Prescribed Crack Length

The formulated flange stem capacity expressions listed in Table 6.1.1 are initially plotted as functions of crack branch length considering the material properties listed in Table 6.2.1. The plots are displayed for the three-ended crack, the vertical edge-crack in the web, and the horizontal crack in the tension flange in Figures 6.2.7, 6.2.8, and 6.2.9, respectively. Each plot indicates the required flange stress, $\sigma_r = 38.9\ ksi$, and the prescribed branch length, a_i.
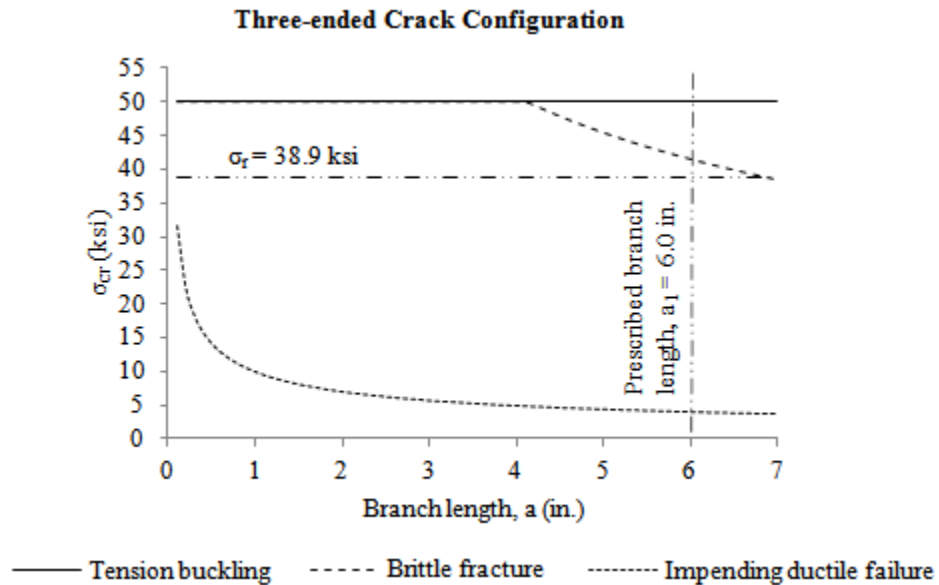
Figure 6.2.7: Capacities for three-ended crack configuration.

215
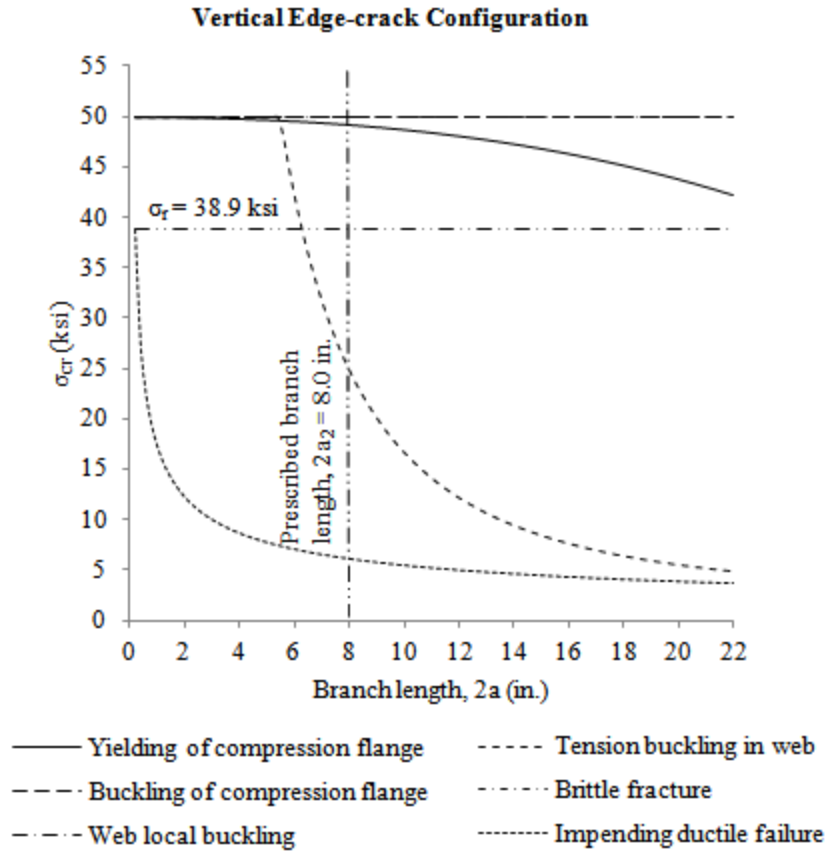
Figure 6.2.8: Capacities for vertical edge-crack configuration.
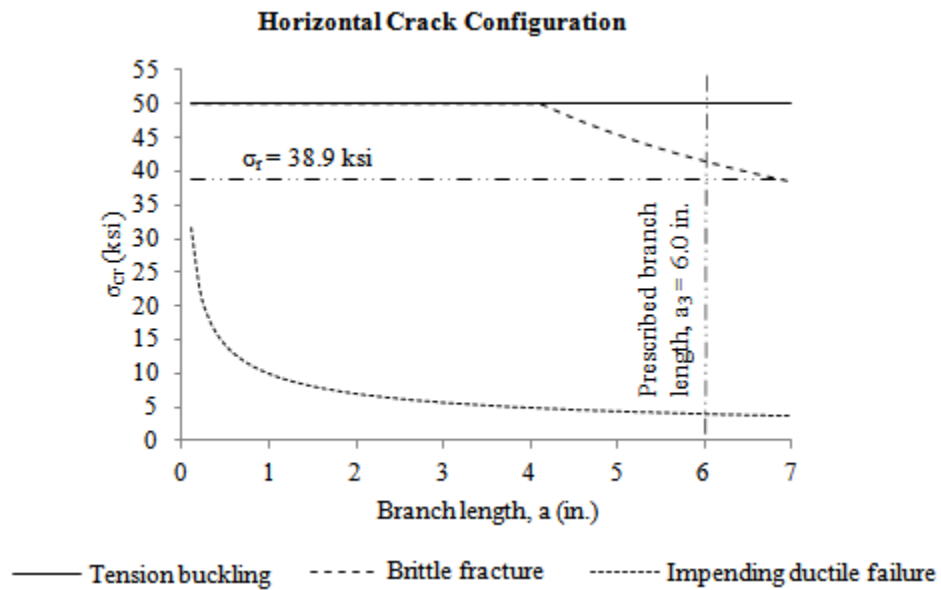
Figure 6.2.9: Capacities for horizontal crack configuration.

216

The impending ductile failure limit state is the governing limit state for all three crack configurations. Therefore, the brittle fracture limit state is invalidated for all three configurations. Assuming that the growth of the plastic region at the crack tip is largely localized, the impending ductile failure limit state may be neglected and employed only to indicate the invalidation of the brittle fracture limit state. The governing flange stem capacities considering the three-ended crack and horizontal crack configurations thus remain greater than $\sigma_r = 38.9\ ksi$ when the branch lengths achieve $a_1 = 6.0\ in.$ and $a_3 = 6.0\ in.$, respectively (see Figures 6.2.7 and 6.2.9). Therefore, the initial girder cross-sectional dimensions of $b_f = 16$ in., $t_f = 1.0$ in., $d_w = 50$ in., and $t_w = 0.375$ in. are sufficient for carrying the required load considering the three-ended crack and horizontal crack configurations.

The governing flange stem capacity considering the vertical edge-crack configuration falls below $\sigma_r = 38.9\ ksi$ before the branch length achieves $2a_2 = 8.0$ in. (neglecting the impending ductile failure and brittle fracture limit states) (see Figure 6.2.8). The governing elastic capacity is associated with tension buckling in the web. Therefore, the initial web plate thickness is slightly increased to $t_w = 0.50$ in. in order to satisfy (6.2.33). The increase in the web plate thickness results in a modified elastic section modulus of $S = 1001$ in^3 and a modified approximate required flange stress of $\sigma_r = 36.9\ ksi$. The modified capacities for the vertical edge-crack are displayed in Figure 6.2.10.

Vertical Edge-crack Configuration
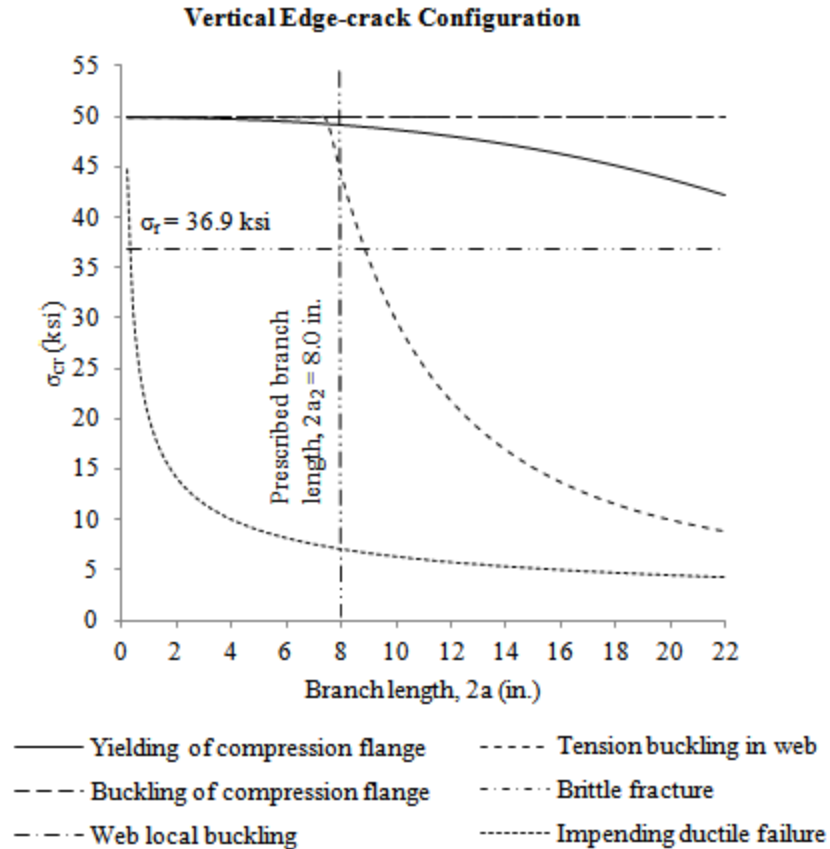
Figure 6.2.10. Modified capacities for vertical edge-crack configuration.

6.2.3.2 Design for Prescribed Fatigue Life

From (6.2.36), the prescribed fatigue life is $N = 127,500$ load cycles. The cyclic stresses within the flange plates induced by the fluctuating bending moments may be approximated by a constant-amplitude trigonometric load function (see Figure 6.2.11). The maximum flange stress is equivalent to the required flange stress, such that $\sigma_{max} = \sigma_r = 38.9\ ksi$. The minimum flange stress, σ_{min}, is induced by only the dead load effects. Considering only the dead load bending moments, DC and DW, in (6.2.24), the factored dead load moment becomes $M_{u,DL} = 996.8$ k*ft. Substituting $M_{u,DL} = 996.8$ k*ft and $S = 951$ in^3 into (9.2.26) results in:

218

$$\sigma_{min} = \frac{M_{u,DL}}{S} = \frac{(996.8k * ft)(12)}{951in^3} = 12.6ksi \qquad (6.2.37)$$

The stress range, defined by (5.5.3), is then calculated as:

$$\Delta\sigma = \sigma_{max} - \sigma_{min} = 38.9ksi - 12.6ksi = 26.3ksi \qquad (6.2.38)$$
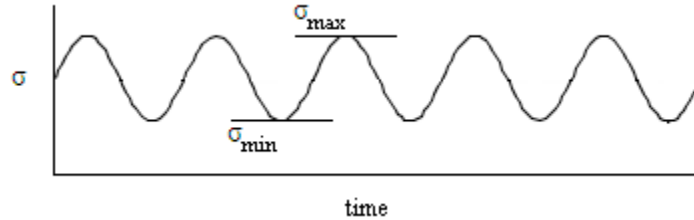
Figure 6.2.11: Constant-amplitude trigonometric load function for flange stress.

The formulated flange stem capacity expressions listed in Table 6.1.1 are plotted as functions of load cycle, N, considering the material properties listed in Table 6.2.1 and the stress range, $\Delta\sigma = 26.3$ ksi, given by (6.2.38). The plots are displayed for the three-ended crack, the vertical edge-crack in the web, and the horizontal crack in the tension flange in Figures 6.2.12, 6.2.13, and 6.2.14, respectively. Each plot indicates the required flange stress, $\sigma_r = 38.9$ ksi, and the prescribed fatigue life length, $N = 127,500$ load cycles.
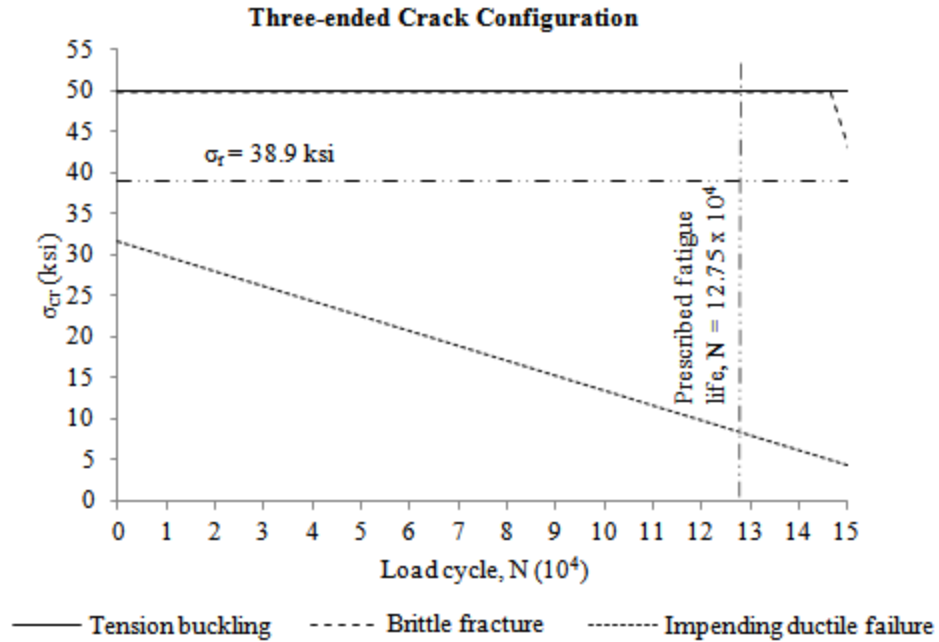
Figure 6.2.12: Capacities for three-ended crack configuration.
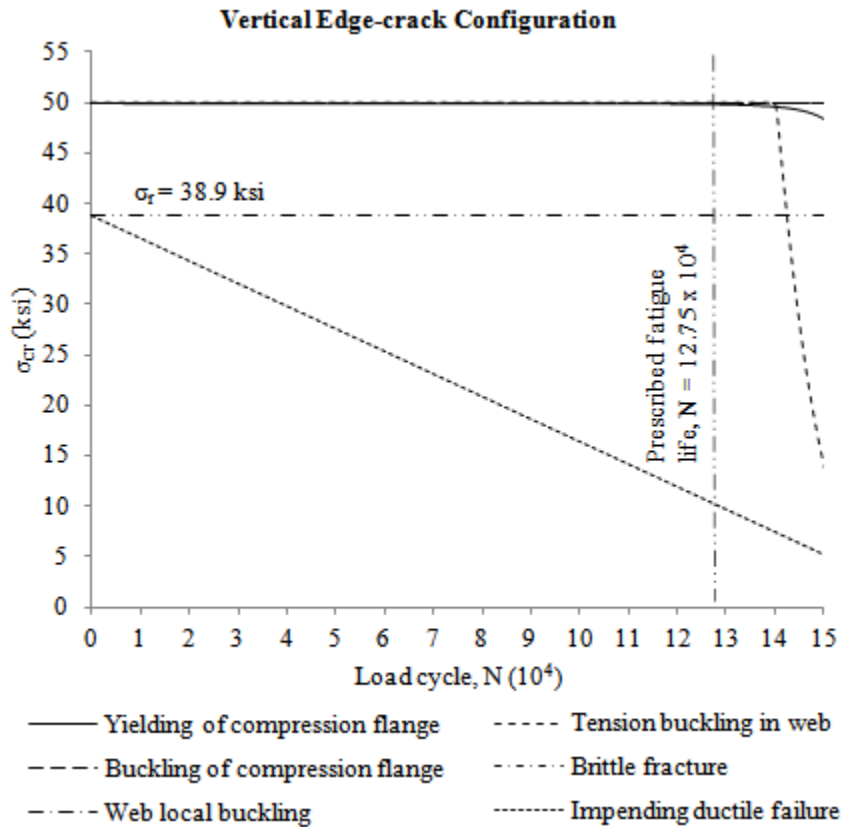
Figure 6.2.13: Capacities for vertical edge-crack configuration.
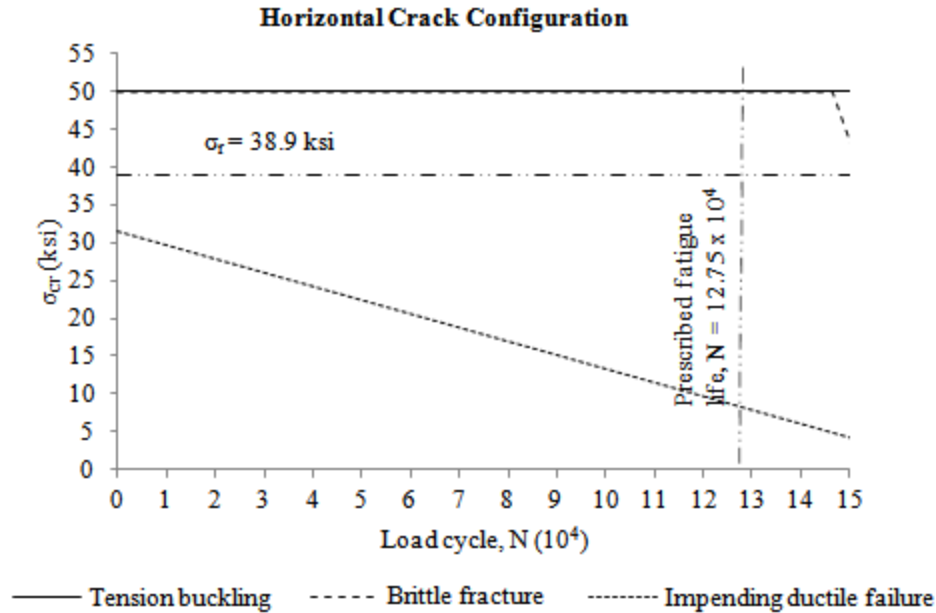
Figure 6.2.14: Capacities for horizontal crack configuration.

Neglecting the impending ductile failure limit state, the flange stem capacities for all three crack configurations remain above $\sigma_r = 38.9\ ksi$ before the prescribed fatigue life of $N = 127,500$ is achieved. The initial girder cross-sectional dimensions are sufficient for the prescribed fatigue life, and are inadequate for the prescribed crack lengths. The final girder cross-sectional dimensions are thus the modified dimensions given by $b_f = 16$ in., $t_f = 1.0$ in., $d_w = 50$ in., and $t_w = 0.50$ in.

6.2.4   Conclusions

In conclusion, an I-shaped plate girder was designed in accordance with the AASHTO *LRFD Bridge Design Specifications* (2010). The girder was assumed to be part of a theoretical highway bridge possessing the properties listed in Tables 6.2.1, 6.2.2, and 6.2.3. The formulated bending moment capacity expressions listed in Table 6.1.1 were employed to modify the initial girder cross-sectional dimensions considering prescribed

through-thickness fatigue crack configurations and a prescribed fatigue life. Specifically, the expressions were plotted as functions of fatigue crack length and load cycle. Each plot was then analyzed to ensure that the capacities remained greater than the required capacity at least until after the prescribed crack length or prescribed fatigue life was achieved.

It was determined that the initial web plate thickness of $t_w = 0.375$ in. was inadequate to satisfy the tension buckling limit state for the vertical edge-crack configuration with $2a_2 = 8.0$ in. The web plate thickness was therefore slightly increased to $t_w = 0.50$ in. in order to satisfy this requirement (see Figure 6.2.15). This increase results in a *33%* increase in the weight and gross area of the web plate.
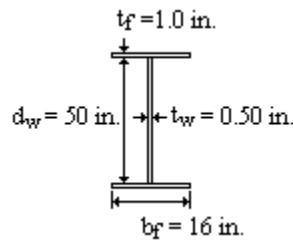
Figure 6.2.15: Initial cross-sectional dimensions of the girder being designed.

7   Conclusions

The objective of this research was to develop theoretical expressions for the bending moment and shear force elastic limit states of fatigue-cracked, I-shaped, transversely stiffened, steel plate girders. The formulation of the expressions, and their subsequent validation by way of FEA, served to contribute a set of preliminary design equations supported by theoretical and numerical bases, of which was concluded to be fundamentally absent from the literature (see Chapter 4). The formulated expressions demonstrated that various elastic limit states influence the overall strength of a girder at varying scales, and are dependent upon the geometric and material properties of the girder, as well as the fatigue crack configuration. Ultimately, it was demonstrated in Section 6.2 that the preliminary design equations may be useful for engineers to perform brief checks on plate girders for prescribed fatigue crack configurations and fatigue lives.

The series of preliminary design equations corresponded to various elastic limit states (yielding, elastic buckling, brittle fracture, and impending ductile failure) and considered various fatigue crack configurations observed in the literature (three-ended crack, vertical-edge crack in web, horizontal crack in tension flange, and diagonal crack). The formulation of the expressions employed various theories from solid mechanics including elasticity theory, linear elastic fracture mechanics, classical plate theory, and the principle of stationary potential energy. The expressions are inherently approximate owing to the fact that several approximations and simplifications were employed when deriving the expressions. In general, the use of these approximations and simplifications were necessary in order to reduce an otherwise complex configuration to a more general configuration, while maintaining a line of continuity to the actual arrangement. Each

223

approximation and simplification was therefore employed based upon a rational line of reasoning. A common approximation employed throughout this research was to assume that a fatigue crack configuration residing within the finite confines of a plate girder was approximately identical to a similar crack configuration residing within an infinite plate. This approximation was deemed to be appropriate because the scale of the fatigue crack was assumed to be relatively small when compared to the scale of the overall girder. Therefore, the actual local stress field around the crack in the girder would be essentially identical to the local stress field around the similar crack in the infinite plate. Moreover, it was presumed that one of the elastic limit states would be exceeded prior to the scale of the fatigue crack growing to such a size that the infinite plate approximation would be invalidated.

Another common approximation employed throughout this research was the combined use of the concept of an embedded plate and the Rayleigh-Ritz method to determine the tension buckling strength of cracked regions of a plate girder. The concept of the embedded plate was employed to define the approximate local region of a girder adjacent to a through-thickness crack undergoing local buckling. The embedded plate was generally presumed to be rectangular in area, and the embedded edges were presumed to be fully clamped except for the edge formed by the crack (Brighenti, 2005a, b, 2009; Minor & Woodward, 1996; Paik et al., 2005). The use of an embedded plate greatly simplified the determination of the tension buckling strength by reducing the configuration to that of elastic buckling of an isolated plate. The actual transverse compressive stress distribution in the cracked region of a girder was then approximated by applying an external transverse compressive stress distribution upon the embedded

224

plate. The external stress distribution itself was obtained from the infinite plate approximation. Using the Rayleigh-Ritz method, the external stress was coupled to an assumed out-of-plane displacement function, which itself satisfied the support conditions of the embedded plate. The elastic buckling strength of the embedded plate was then determined and coupled to the corresponding critical bending moment strength of the girder. Although this research focused upon plate girders, the general procedure for determining the tension buckling strength of a cracked web plate or flange plate could have theoretically been employed with any thin, cracked, plate-like structure loaded under tension.

The FEA procedure served to provide direct and indirect numerical validation of the formulated expressions. The FEA validations directly demonstrated that the infinite plate approximation for determining the local stress field around a crack was overwhelmingly accurate. Additionally, the FEA validations directly demonstrated that the infinite plate approximation for determining the stress intensity factor and plastic region size at the crack tip was reasonably accurate for shorter crack branch lengths. These particular validations were direct in that the FEA procedure employed the full-size trial plate girder models. Conversely, the FEA validations indirectly demonstrated that the combined use of the concept of an embedded plate and the Rayleigh-Ritz method to determine the tension buckling strength was reasonably accurate. These particular validations were indirect in that the FEA procedure employed the trial web plate and flange plate models instead of the full-size trial plate girder models, and employed similar approximations used in the analytical derivation of the tension buckling expressions. The embedded plate approximation was used in the FEA validations by restraining the out-of-

plane movement of the trial web plates and flange plates except for the regions of the embedded plates. Also, the FEA validations made use of the external stress distribution, itself obtained from the infinite plate approximation, to load the embedded plate. However, the subsequent eigenvalue buckling analysis was performed numerically.

Overall, the FEA procedure provided verification that the output from the formulated capacity expressions is for the most part in good agreement with the numerical output. In general, the predicted capacities obtained from the formulated expressions were found to be slightly more conservative than the capacities obtained from FEA. In other words, the formulated expressions predicted lower values of residual girder strength than as predicted from FEA. In some cases, the formulated expressions demonstrated close correlation with FEA for shorter crack branch lengths before diverging at longer crack branch lengths, with the FEA results being more conservative. In these cases, the divergence between the analytical and FEA results was deemed to be tolerable because the divergence occurred at longer crack branch lengths, at which point alternative elastic limit states would begin to govern the residual girder strength. In other cases regarding buckling, the correlation between the formulated expressions and FEA was closest for lower plate thickness-to-crack length ratios with thinner plate thicknesses. The correlation then diverged at higher plate thickness-to-crack length ratios. Again, the divergence between the analytical and FEA results was deemed to be tolerable because alternative elastic limit states would begin to govern the residual girder strength at higher plate thickness-to-crack length ratios.

The plots of the preliminary design equations as functions of crack length and load cycle demonstrated that various elastic limit states influence the overall strength of a

226

girder, and are largely dependent upon the fatigue crack configuration. The impending ductile failure limit state was found to be the most common governing limit state. However, the impending ductile failure limit state is highly localized in that the formation of the plastic region around a crack tip remains relatively small when compared to the overall scale of a plate girder. Similarly, the tension buckling limit state is highly localized in that the scale of buckling of the region of plate adjacent to a through-thickness crack is relatively small when compared to web panel buckling or lateral-torsional buckling. Furthermore, it was shown that tension buckling is possible only in configurations with lower plate thickness-to-crack length ratios with thinner plate thicknesses. On the contrary, the flange local yielding limit state may lead to the formation of a plastic hinge in the flange, which may adversely influence the stability of an overall plate girder. Similarly, the flange and web local buckling limit states may lead directly to the instability of an overall girder (Basler & Thurlimann, 1960a). Taken as a whole, the various elastic limit states influence the overall strength of a fatigue-cracked plate girder at varying scales; certain limit states may be neglected in favor of more detrimental limit states.

The contributions from this research could be extended upon in several ways. The residual strength of alternative cracked beam-like structures such as hot-rolled T-beams, L-beams, and box girders could be investigated. Additional fatigue crack configurations could also be investigated. Empirical or theoretical correction factors accounting for the influence of residual stresses induced by welded boundaries could be developed. Finally, expressions could be formulated for the ultimate residual strength of fatigue-cracked

girders. These ultimate residual strength expressions could then be validated using both FEA and experimental procedures.

Appendix A: AASHTO LRFD Bridge Design Specifications

A.1 Background

The authority over highways in the U.S. rests primarily with the state governments rather than the federal government (Oglesby & Hicks, 1982, p. 11). As such, the development of standards for the design, construction, and maintenance of highway bridges was originally the responsibility of individual state highway departments. The emergence of the automobile and the consequent expansion of the national highway system in the early 20th century encouraged the need for a national highway bridge design standard (AASHTO, 2010). As a result, engineers from each state highway department collaborated to establish the American Association of State Highway Officials (AASHO) in 1914 as a non-governmental organization to set technical standards for the design of highway infrastructure (Oglesby & Hicks, 1982).

AASHO developed and published the first national bridge design standard in 1931 entitled *Standard Specifications for Highway Bridges and Incidental Structures* (henceforth referred to as the *Standard Specifications*) (AASHTO, 2010). Successive editions of this standard were published every four to six years and were updated to keep pace with the advancement of the theory and practice of bridge design along with the advent of new construction materials (Taly, 1998). All of the state highway departments adopted the *Standard Specifications* along with specific amendments which varied from state to state. As such, the *Standard Specifications* became the legal set of standards by which highway bridges were to be designed (Salmon et al., 2009, p. 20). AASHO's name was expanded in 1973 to the American Association of State Highway and Transportation Officials (AASHTO) to reflect the growing scope of the organization's responsibilities with respect to the development of transportation infrastructure standards (Oglesby &

Hicks, 1982, p. 28). Subsequent highway design standards developed by the organization were henceforth published under the name of AASHTO.

The early editions of the *Standard Specifications* employed the allowable stress design (ASD) philosophy, also known as the working stress design (WSD) philosophy (Taly, 1998). A key disadvantage of this philosophy is that the factor of safety used to compute the allowable stresses in a structural member or element is fixed and therefore does not take into account the variability of the nominal design strength or applied loads (Barker & Puckett, 1997, p. 99). Extensive research conducted in the 1960s and 1970s led to the development of an alternative design philosophy termed the load and resistance factored design (LRFD) philosophy, also known as the limit states design philosophy (Tonias, 1995). The LRFD philosophy essentially requires that the factored nominal resistance of a structural member or element be designed to withstand various factored load combinations. AASHTO first incorporated the LRFD philosophy into a new highway bridge design standard in 1994 called the *LRFD Bridge Design Specification*s (Taly, 1998). As of the present time (2013), individual state highway departments are in the process of transitioning from the ASD based *Standard Specifications* to the *LRFD Specification*s (Withiam, 2003; AASHTO, 2010).

The *LRFD Bridge Design Specifications* (2010) require that the structural members and elements of short-span steel highway bridges be able to sufficiently resist a variety of factored load combinations corresponding to different limit states. The load combinations consist of various types of factored loads such as dead loads, vehicular live loads, vehicular dynamic loads, wind loads, and earthquake loads (AASHTO, 2010, pp. 3-7, 3-8). The limit states represent defined boundaries of structural usefulness and

include service, strength, fatigue and fracture, and extreme event (AASHTO, 2010, pp. 3-8 – 3-11). The service limit state refers to the requirement of structural members and elements to satisfy certain serviceability restrictions, such as limiting excess deformations or vibrations, under specific load combinations (AASHTO, 2010, p. 3-10). The strength limit state is the requirement of structural members and elements to satisfy certain strength restrictions, such as preventing the level of induced stresses from exceeding the elastic or plastic limit, under specific load combinations (AASHTO, 2010, pp. 3-9, 3-9). The fatigue and fracture limit state refers to the requirement of structural members and elements to be able to limit crack growth and prevent fracture due to specific load combinations (AASHTO, 2010, p. 3-11). Finally, the extreme event limit state is the requirement of a bridge structure to sufficiently resist extreme event load combinations relating to earthquake loads, ice loads, and collision loads (AASHTO, 2010, p. 3-9). The factored load combinations are essentially an effort by the *LRFD Bridge Design Specifications* (2010) to encompass the complex loading spectrum that a bridge may experience over its lifetime.

A.2   LRFD Design Philosophy

Many researchers such as Cornell (1969), Ellingwood, Galambos, MacGregor, & Cornell (1980), Galambos (1981), Pugsley (1966), and Ravindra & Galambos (1978) carried out research which led to the development and codification of the LRFD philosophy. The research investigated and reinforced the concept that different types of loads contribute varying proportions to the overall load applied upon a structural member or element throughout its lifetime (Ellingwood et al., 1980; Galambos, 1981).

Additionally, it was shown that the capacity of a structural member or element to resist applied loads varies depending upon the type of strength being considered, its configuration, material properties, and inherent flaws (Ellingwood et al., 1980; Galambos, 1981; Taly, 1998, p. 100). It was found, however, that the variation of applied loads and corresponding variation of resistance of a structural member or element nonetheless exhibits statistical regularity (Ellingwood et al., 1980).

The underlying principle of the LRFD philosophy is that the factored nominal resistance of a structural member or element is designed to withstand a range of factored load combinations. This principle may be expressed as (Ellingwood et al., 1980)

Factored resistance ≥ Factored loads (A.2.1)

This statement may also be expressed by the following formula (Ellingwood et al., 1980)

$$\Phi R_n \geq \sum_1^i \gamma_i Q_{ni}$$ (A.2.2)

where Φ is the resistance factor or strength reduction factor, R_n is the nominal design strength of a structural member or element, γ_i is the load factor, and Q_{ni} is the load effect. The resistance factor serves to reduce the nominal design strength of the structural member or element. Conversely, the load factor serves to increase or otherwise modify the magnitude of a specific load effect. The summation indicates that several load effects and corresponding load factors may be combined to form a particular factored load combination (AASHTO, 2010). In this way, both the load effects and nominal design strength may be adjusted depending upon their statistical variation, with the purpose of ensuring a functionally sufficient and safe design (Galambos, 1981).

As previously mentioned, the level of uncertainty of load effects induced upon a structural member or element varies depending upon the type of loading being considered

(Ellingwood et al., 1980; Galambos, 1981). LRFD takes this into account by assigning specific load factors to each type of load effect such that the probability of the actual load effect exceeding the factored load effect is acceptably low. For instance, the uncertainty of dead load is less than that of live load (Galambos, 1981). As a result, LRFD assigns a load factor to dead load which magnifies its effect by a lesser percentage than does a load factor applied to live load.

In a similar manner, the accuracy of the nominal design strength of a structural member or element as predicted from theory varies depending upon several factors, one of which is the type of strength being considered (Galambos, 1981). As such, LRFD assigns a specific resistance factor to each type of design strength in order that the probability of the actual design strength being less than the factored design strength is acceptably low. For example, the nominal bending strength of a structural member or element is more accurately predicted from beam theory than is its nominal compression strength as predicted from column theory (Galambos, 1981). Therefore, LRFD assigns a resistance factor which reduces the bending strength by a lesser percentage than the resistance factor applied against the compression strength.

Research conducted by Ellingwood et al. (1980) sought to provide tangible probability based load and resistance factors for buildings and other structures. The research was conducted as part of the development of American National Standards Institute (ANSI) *Standard A58* entitled *Building Code Requirements for Minimum Design Loads in Buildings and Other Structures*. Recommended load combinations and load factors were derived for various types of loads including dead, occupancy live, snow, wind, and earthquake loads. Additionally, resistance factors were derived for various

234

building materials including structural steel, reinforced and prestressed concrete, masonry, and aluminum. The derivations were essentially a summary of design formats from the then current design codes and specifications such as the *National Building Code of Canada* (NBCC) and ACI *Standard 318*.

The LRFD philosophy has been adopted by numerous design codes and specifications throughout the U.S. Beginning in 1985, ANSI *Standard A58* was published as American Society of Civil Engineers (ASCE) *Standard 7* (Ellingwood, 2001). ASCE *Standard 7*, in turn, was later adopted by reference by various design standards such as the American Institute of Steel Construction (AISC) *Specification for Structural Steel Buildings* (2005), ACI *Standard 318* (2005), and the International Code Council (ICC) *International Building Code* (IBC) (Ellingwood, 2001). The load and resistance factors in the *LRFD Specifications* (2010) are based upon reliability indices that were calibrated from designs of numerous existing and hypothetical bridges (Taly, 1998, p. 98).

A.3   Load Cases and Load Combinations

The *LRFD Bridge Design Specifications* (2010) provides a codified procedure for determining the load cases, load factors, and load combinations used for designing the members and elements of bridge structures. The dead load and vehicular live load are the two primary load cases. Additional load cases include but are not limited to vehicular dynamic loads, wind loads, earthquake loads, water loads, ice loads, and earth pressure loads. The dead load includes the self-weight of the members and elements of the bridge structure as well as additional permanent loads such as utilities, earth cover, wearing surface, future overlays, and planned widening (AASHTO, 2010, p. 3-16).

In general, the vehicular live load is derived from a combination of a design truck or design tandem, and a design lane load (see Figure A.3.1) (AASHTO, 2010, p. 3-19). The design truck is designated as HL-93 and consists of one *8* kip front axle and two *32* kip rear axles. The *8* kip front axle is spaced *14* ft. from the first *32* kip rear axle. The two *32* kip rear axles may be spaced over a distance ranging from *14* ft. to *30* ft. in order to produce the most critical load effect (AASHTO, 2010, p. 3-23). Alternatively, the design tandem consists of two *25* kip axles spaced at *4* ft. (see Figure A.3.1b). The design lane load consists of *0.64* klf loaded along the longitudinal direction of the lane and uniformly distributed across a *10* ft. lane width. For strength design, influence lines are generally employed to determine the critical position of the HL-93 design truck and the design lane load over the span of the superstructure. The associated critical live load bending moment is then calculated using the girder line method as specified in Section 4.6.2.2.2 of the *LRFD Specifications* (2010). In this method, distribution factors are calculated and used to distribute the critical live load bending moment to a single internal or external girder. It is noted that the multiple presence factor is already taken into account when using the girder line method.
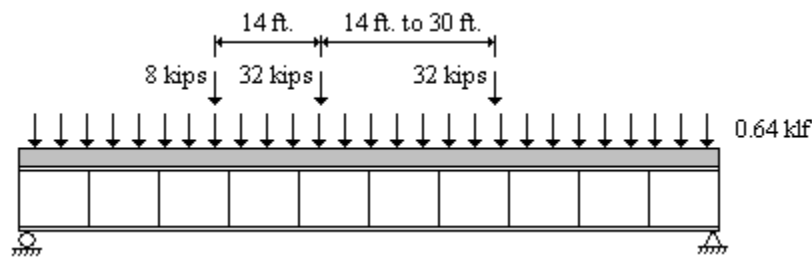
Figure A.3.1. Design lane load superimposed with the HL-93 design truck.

236

The effects of the various load cases are combined into several load combinations corresponding to specific limit states (AASHTO, 2010, sec. 3). The limit states related to strength are concerned with the elastic and ultimate strength of members and elements of bridge structures. The *LRFD Specifications* (2010) specifies a total of five load combinations associated with the strength limit state, termed Strength I through Strength V. As an example, a form of the Strength I load combination is given by

$$\gamma_p DC + \gamma_p DW + 1.75LL + 1.75IM + 1.75CE \tag{A.3.1}$$

where *DC* is the dead load of structural components and nonstructural attachments, *DW* is the dead load of wearing surfaces and utilities, *LL* is the vehicular live load, *IM* is the vehicular dynamic load allowance, and *CE* is the vehicular centrifugal force. Also, the term γ_p is a load factor for permanent loads and is specified by the *LRFD Specifications* (2010).

Alternatively, the load combinations related to fatigue and fracture limit states are termed Fatigue I and Fatigue II, and are concerned with infinite and finite fatigue life, respectively. The load combination corresponding to Fatigue I is given by

$$1.50LL + 1.50IM + 1.50CE \tag{A.3.2}$$

and the load combination corresponding to Fatigue II is given by

$$0.75LL + 0.75IM + 0.75CE \tag{A.3.3}$$

For the case of the Fatigue I and II load combinations (A.3.2 and A.3.3), the HL-93 design truck is specified to have a constant spacing of *30* ft. between the *32* kip axles. This specific configuration is referred to as the fatigue load (AASHTO, 2010, p. 3-28).

A.4   Strength Limit State

The flexural strength of composite I-shaped girder sections in negative flexure and non-composite I-shaped girder sections is specified by Section 6.10.8 of the *LRFD Specifications* (2010). In general, the load effects within the girder as obtained from the Strength I through Strength V load combinations must be equal to or less than the factored nominal strength of the girder. This requirement is essentially a form of (A.2.2) and is expressed as

$$f_{bu} + \frac{1}{3} f_l \leq \phi_f F_{nc} \tag{A.4.1}$$

where f_{bu} and f_l are the flange stresses, Φ is the resistance factor for flexure, and F_{nc} is the nominal flexural resistance of the flange. The flange stresses are calculated from the Strength I through Strength V load combinations. The nominal flexural resistance of the flange is then calculated for the limit states of local buckling and lateral torsional buckling as specified in Section 6.10.8.2 of the *LRFD Specifications* (2010). The local buckling strength of the flange is dependent upon whether the flange is compact, noncompact, or slender (see Appendix F: Classical Plate Theory). The lateral torsional buckling strength of the girder is dependent upon its unbraced length. It follows that the governing flange strength is the lower strength of the two limit states.

A.5   Fatigue and Fracture Limit State

The fatigue and fracture mechanism of a structural member or element is largely dependent upon cyclical load applications (Shukla, 2005, p. 153). In this sense, the magnitudes of load effects are alone not sufficient for a complete fatigue and fracture analysis (AASHTO, 2010, p. 3-28). The *LRFD Specifications* (2010) specifies a

simplified procedure for ensuring the safe design of structural members and elements for the fatigue and fracture limit state (sec. 6.6). In this procedure, the live load stress range induced within a structural member or element must be equal to or less than a specified stress range in order to prevent fatigue and fracture failure. This requirement is essentially a form of (A.2.2) and is expressed as

$$\gamma(\Delta f) \le (\Delta F)_n \tag{A.5.1}$$

where Δf is the live load stress range induced by the Fatigue I or Fatigue II load combinations, and γ represents the load factor associated with the fatigue load combinations. The term $(\Delta F)_n$ is a specified limiting stress range dependent upon the type of structural detail being analyzed (AASHTO, 2010, sec. 6.6.1.2.3).

For infinite fatigue life, $(\Delta F)_n$ is equivalent to a threshold stress range, $(\Delta F)_{TH}$, dependent upon the type of structural detail being analyzed. If the induced live load stress range corresponding to the Fatigue I load combination is less than $(\Delta F)_{TH}$, then the structural detail theoretically has an infinite fatigue life. For finite fatigue life, $(\Delta F)_n$ is defined as

$$\Delta(F)_{TH} = \left(\frac{A}{N}\right)^{\frac{1}{3}} \tag{A.5.2}$$

where A is a constant dependent upon the type of structural detail being analyzed. The term N is the number of stress cycles induced within the structural detail over a 75-year design life, defined as

$$N = (365)(75)n(ADTT)_{SL} \tag{A.5.3}$$

where n is the number of stress cycles per truck passage, and $(ADTT)_{SL}$ is the average daily truck traffic for a single lane. The $(ADTT)_{SL}$ is generally a percentage of the

average daily truck traffic (ADTT) traveling in one direction over the bridge (AASHTO, 2010, sec. 3.6.1.4). The ADTT is in turn a fraction of the average daily traffic (ADT) traveling in one direction over the bridge. If the induced live load stress range corresponding to the Fatigue II load combination is less than $(\Delta F)_{TH}$ as defined by (A.5.2), then the structural detail theoretically has a 75-year fatigue life.

Appendix B: Bridge Inspection and Evaluation

B.1   Overview

The state departments of transportation are required by the FHWA to periodically inspect and report the condition ratings, appraisal ratings, deficient statuses, and sufficiency ratings of all highway bridges in their respective states belonging to the NHS, state highway systems, and networks of local roads and streets (OLA, 2008, pp. 30-32). These inspections are carried out under the FHWA National Bridge Inspection Program (NBIP) (CRS, 2007, p. 8). Bridges excluded from inspection requirements are those that are federally or tribally owned, or that have spans of less than *20* ft. (CRS, 2007, p. 8).

A condition rating is a measure of the current condition of a structural member or element of a bridge relative to its original as-built condition (OLA, 2008, p. 30). Conversely, an appraisal rating is a measure of the current condition of a structural member or element of a bridge relative to the currently accepted design and construction standards (OLA, 2008, p. 30). The deficient status and sufficiency rating pertain to the eligibility of a bridge to receive HBP funds for its replacement or rehabilitation (CRS, 2007, p. 7). The state departments of transportation are generally required to inspect and report these ratings to the FHWA every *24* months (CRS, 2007, p. 8). The FHWA uses this data to maintain the condition criteria for bridges listed in the NBI.

The national standard for inspecting and reporting condition ratings, appraisal ratings, deficient statuses, and sufficiency ratings of highway bridges is the FHWA *Bridge Inspector's Reference Manual* (BIRM) (CRS, 2007, p. 8). The FHWA *National Bridge Inspection Standards* (NBIS) provides the basis for the BIRM (FHWA, 2009). The NBIS incorporates by reference the AASHTO specification entitled *Manual for Bridge Evaluation* (AASHTO, 2011). The *Manual for Bridge Evaluation*, in turn,

references the national standard for inspecting and reporting appraisal ratings of highway bridges entitled *Recording and Coding Guide for the Structure Inventory and Appraisal of the Nation's Bridges* (henceforth referred to as the *Recording and Coding Guide*) published by the FHWA (OLA, 2008, p. 30). Individual state departments of transportation base their bridge inspection regulations upon the BIRM (CRS, 2007, p. 8).

Condition ratings for bridges assessed in accordance with the BIRM range from *0* to *9*. A rating of *0* represents a failed bridge which is out of service and is irreparable, while a rating of *9* represents a bridge in excellent condition (USDOT, 2010, p. 3-11). Likewise, appraisal ratings for bridges assessed in accordance with the BIRM range from *0* to *9*. A rating of *0* represents a closed bridge and a rating of *9* represents a bridge condition exceeding desirable criteria (USDOT, 2010, p. 3-13).

The BIRM is also used by the state departments of transportation to classify a bridge as structurally deficient, functionally obsolete, or non-deficient. A bridge is classified as being structurally deficient if its members and elements are found to have been deteriorated or damaged to a certain degree as determined by the BIRM. A bridge classified as being structurally deficient does not necessarily signify that it is unsafe and may imminently collapse (USDOT, 2010, p. 3-10). However, it does indicate that the bridge may require extensive repairs.

A bridge is classified as being functionally obsolete if its functional capacity is unable to accommodate the current functional demand (USDOT, 2010, p. 3-10). In most cases, the functional capacity refers to the traffic capacity allowed by the geometry of the bridge deck while the functional demand refers to the current traffic demand (CRS, 2007, p. 2). However, functional capacity and functional demand may also refer to the

243

underclearance of a bridge and the current underclearance requirements, respectively (CRS, 2007, p. 2). It is important to note that structural deficiency takes priority over functional obsolescence (USDOT, 2010, p. 3-15). Bridges classified as structurally deficient, functionally obsolete, or both, are ultimately listed as being deficient (FHWA, 2011). Bridges not classified as structurally deficient, functionally obsolete, or both, are listed as non-deficient.

Appendix C: Structural Steel

C.1 Production

Structural steel is produced by combining iron ore with other raw materials including coke, limestone, and chemical additives. The raw materials are placed in a blast furnace and heated to a molten state during which they undergo a smelting process to separate the iron from the ore. The coke and limestone combines with the ore and various other impurities to form slag which collects on the top of the molten iron and is removed. Additionally, the coke serves to add carbon to the molten iron (Barker & Puckett, 1997, p. 703).

At this stage the molten iron has been separated from the ore and is transferred to an oxygen furnace. Scrap metal, additional alloying elements, and various fluxes are then added to the molten iron at which point the materials are reheated (Jackson, 1969, pp. 9-13). Oxygen is then blown through the molten iron to initiate a process of oxidation which, with the assistance of the fluxes, removes excess elements from the iron, namely silicon, carbon, and phosphorus (Jackson, 1969, pp. 2-5). The oxidation process essentially transforms the molten iron into liquid steel which is then formed into slabs, blooms, or billets through a continuous casting process (Barker & Puckett, 1997, pp. 703-705). The slabs, blooms, or billets are then hot-rolled to form various structural shapes such as wide flange sections or plates conforming to ASTM A709 or AASHTO M270 (Salmon et al., 2009, p. 12; AASHTO, 2010, p. 6-24).

C.2 Engineering Properties

Structural steel is classified based upon its material properties (yield strength, ultimate tensile strength, ductility, hardness, toughness, and corrosion resistance)

(Blodgett, 1966, p. 2.1-1; Barker & Puckett, 1997, p. 702). For the purpose of most structural applications, it is generally appropriate to assume that the material properties of structural steel are homogenous (Sadd, 2009, p. 80). Additionally, the stress-strain behavior of structural steel is nearly the same to that of an ideally linear elastic material in compression, tension, and shear for small deformations (Beer et al., 2006, p. 54; Sadd, 2009, p. 79). Furthermore, structural steel is isotropic, meaning that its stress-strain behavior is identical in all directions (Sadd, 2009, p. 80). Hence, structural steel behaves nearly the same to that of an ideally linear isotropic elastic material.

The yield strength refers to the maximum strength at which a material behaves elastically under load (Blodgett, 1966, p. 2.1-3; Salmon et al., 2009). The uniaxial yield strength, σ_Y, corresponds to a one-dimensional state of normal stress, and the shear yield strength, τ_Y, corresponds to a one-dimensional state of shear stress. The stress-strain curves of most structural steels are nominally linear up until the proportional limit, which is in the local vicinity of the yield point (Blodgett, 1966, p. 2.1-3). For most structural steels, the proportional limit and the yield point are generally assumed to be identical (Sadd, 2009, p. 78). The yield point may be further distinguished between an upper yield point and a lower yield point, although the lower yield point is considered to be the actual yield strength (Beer et al., 2006, p. 53). Since structural steel behaves nearly the same to that of an ideally linear isotropic elastic material, its uniaxial yield strength is theoretically identical in both tension and compression (Beer et al., 2006, p. 54). The uniaxial yield strength of most structural steels ranges from $\sigma_Y = 36$ to $\sigma_Y = 100\ ksi$ (Salmon et al., 2009, p. 36). The shear yield strength is generally some fraction of the uniaxial yield strength. Multiaxial states of stress are commonly induced within the

members and elements of a structure and thus a more general criterion is required to define yielding (Salmon et al., 2009, p. 44). The most commonly accepted criterion is the Mises yield criterion.

The linear portion of the stress-strain curve is referred to as the elastic region and indicates the range of strain and corresponding stress at which a deformed material will return to its original shape after it is unloaded (Beer et al., 2006, p. 57). In this region, the stress-strain relationship for both normal stress and shear stress obeys Hooke's law up until the proportional limit. For uniaxial normal stress and normal strain, Hooke's law is expressed as

$$\sigma = E\varepsilon \qquad\qquad\qquad\qquad (C.2.1)$$

It can be seen that the normal stress, σ, is directly proportional to the normal strain, ε. The slope of the uniaxial normal stress-strain curve in the elastic region is referred to as the modulus of elasticity, or Young's modulus, E. The modulus of elasticity for all grades of steel is approximately *29,000 ksi* (Salmon et al., 2009, p. 42).

The uniaxial normal stress-strain curve for structural steel can be obtained through tension testing of specimens. A standard test method for tension testing of metallic specimens is published by ASTM entitled *E8 - Standard Test Methods for Tension Testing of Metallic Materials*. It is noted that there are two types of stress-strain curves, namely the engineering stress-strain curve and the true stress-strain curve (Salmon et al., 2009, p. 42). Whereas the former uses stress and strain values based on the initial geometric properties of the specimen, the latter uses the instantaneous geometric properties. Phenomena observed during uniaxial tension testing of metallic specimens such as necking are indicative of the ductile nature of structural steel at normal

temperatures, and are further discussed by Jones (2009, sec. 2.2) and Salmon et al. (2009, sec. 2.4).

For one-dimensional shear stress and shear strain, Hooke's law is expressed as

$$\tau = G\gamma \tag{C.2.2}$$

As with the uniaxial normal stress-strain curve, the shear stress, τ, is directly proportional to the shear strain, γ, in the elastic region. The slope of the one-dimensional shear stress-strain curve in this zone is called the modulus of rigidity, or shear modulus, written as G or μ (Beer et al., 2006, p. 91). The modulus of elasticity and modulus of rigidity are referred to as elastic constants for linear isotropic elastic materials. Three other elastic constants include the bulk modulus, k, Poisson's ratio, v, and Lamé's constant, λ. Only two elastic constants are necessary for characterizing a material since all five elastic constants are interconnected through a series of relations. The elastic constants and their relations are further discussed by Sadd (2009, ch. 4).

The portion of the stress-strain curve beyond the elastic region is called the plastic region and indicates the range of strain and corresponding stress at which a material exhibits plastic, or ductile, behavior (Beer et al., 2006, p. 109). In this zone, a material retains permanent deformation after it is unloaded. Additionally, the linear stress-strain behavior is no longer valid in the plastic region. For structural steel specimens loaded under uniaxial tensile stress, increasing values of strain beyond the yield point results in an ideally constant value of stress, i.e. the yield strength, being induced in the specimen (Salmon et al., 2009, p. 42). In reality, the stress begins to increase again at even higher values of strain in a separate zone referred to as the strain hardening zone (Salmon et al., 2009, p. 42). Strain hardening continues until the induced stress attains a maximum value

referred to as the ultimate tensile strength. The induced stress then decreases until the specimen fractures. Brittle materials such as glass and cast iron exhibit very little deformation in tension beyond the elastic zone and prior to fracture (Jones, 2009, p. 62). Conversely, structural steel is a ductile material because it exhibits large deformations in the plastic and strain hardening zones prior to fracture. In some cases, however, structural steel may exhibit brittle properties in low-temperature environments or when loaded in a multiaxial state of tensile stress (Barker & Puckett, 1997, p. 717).

Material toughness is a measure of the amount of energy a material can absorb prior to fracture (Barker & Puckett, 1997, p. 702). The area beneath the uniaxial stress-strain curve represents the strain energy density, or resilience, of a material (Jones, 2009, p. 63). Brittle materials usually have a low toughness while ductile materials usually have a high toughness, though this is not always the case (Jones, 2009, pp. 62-64). A related material property called the fracture toughness is concerned with the ability of a material containing a crack to resist fracture.

Based upon the aforementioned material and engineering properties, structural steels commonly used for steel highway bridges may be separated into three general classes: carbon steels, high-strength low-alloy steels, and alloy steels (Taly, 1998, pp. 118-121). Carbon steels have a carbon content ranging between *0.15 - 0.29%* and demonstrate well-defined yield points. High-strength low-alloy steels also have well-defined yield points albeit typically have higher yield strengths than carbon steels ranging between *40 – 70 ksi*. Alloy steels usually have a carbon content of up to *0.20%* and have yield strengths ranging between *80 – 110 ksi* (Salmon et al., 2009, sec. 2.1).

Appendix D: Theory of Elasticity

D.1 Background

Mechanics of materials and the theory of elasticity may be used to analyze the internal behavior of steel plate girders in response to external or internal loads. These two theories have several differences, however. According to Ugural (1999), mechanics of materials "uses assumptions based on experimental evidence along with engineering experience to make a reasonable solution of the practical problem possible," while the theory of elasticity "concerns itself largely with more mathematical analysis of the 'exact' stress distribution on a loaded body" (p. 4). A mechanics of materials approach may be more practical for certain engineering applications because of its use of average stresses and simplified definitions of strain (Ugural, 1999, p. 4). A more rigorous approach using the theory of elasticity may be better suited for engineering problems requiring exact distributions of stress and strain. Despite being termed as an "exact" theory, the theory of elasticity nonetheless employs several approximate assumptions such as modeling solids as a continuum and the use of small deformation theory (Sadd, 2009, pp. 34-37). Furthermore, as its name suggests, the theory of elasticity is only valid for elastic analyses of solids.

A comprehensive history of the development of the general equations of elasticity has been presented by Love (1892), Timoshenko (1983), and Todhunter (1886, 1893). These equations were developed over a period of centuries and include the constitutive equations, the equilibrium equations, the compatibility equations, and the relations between strain and displacement. The earliest contributions to elasticity theory were made in the 17th and 18th centuries by such scientists and mathematicians as Hooke, Marriotte, Euler, and Coulomb, along with the Bernoulli family of Swiss mathematicians

(Love, 1892). Much of the foundational relations and formulations of elasticity were developed in the 19th century by such scientists and mathematicians as Navier, Young, Cauchy, Lamé, Lagrange, Poisson, and Saint-Venant (Todhunter, 1886). These relations and formulations were consolidated into a general theory of elasticity which can lead to exact solutions of stress, strain, and displacement fields in three-dimensional or two-dimensional solids.

As Love (1892) points out, the first major breakthrough leading to the general equations was the discovery of Hooke's law in 1660 which states that the strain of an elastic solid is directly proportional to the applied stress (pp. 2-3). Hence, Hooke's law, with further experimental development by Marriotte in 1680, came to be recognized as the constitutive equation relating stress and strain (Love, 1892, p. 3; Todhunter, 1886, p. 6). This relationship allowed Jacob, John, and Daniel Bernoulli, along with Euler and Coulomb, to develop their theories regarding elastic curves and the bending behavior of beams in the 18th century (Timoshenko, 1983, pp. 25-36, 49-50). The development of the modulus of elasticity by Young in 1807 had major implications for the theory of elasticity (Todhunter, 1886, p. 81-82). Whereas the ratio of applied stress and corresponding strain in Hooke's law was originally understood to be dependent upon the geometry of the solid of interest, the introduction of the modulus of elasticity allowed Hooke's law to be applicable to the material of the elastic solid itself and independent of its geometry (Askeland & Phulé, 2006, p. 198).

In subsequent decades, further relations and formulations regarding stress and strain were developed. The theories of stress and strain were initially formulated by Cauchy, Lamé, and Saint-Venant in the 1820s and 1830s (Love, 1892, pp. 6-7;

Todhunter, 1886, p. 835). Cauchy was the first to discover that the stresses and strains at any location within a solid body could be described in terms of three normal stresses and corresponding normal strains along with three shear stresses and corresponding shear strains (Love, 1892, p. 6; Todhunter, 1886, p. 320). Work by Saint-Venant in the 1830s further advanced the theories concerning shear stress and shear strain (Todhunter, 1886, pp. 836-837).

Work by Navier in the 1820s involved the development of a molecular hypothesis in which he described the small scale "intermolecular" behavior of solids under external or internal loads (Love, 1892, p. 8). Through this work he developed the equations of equilibrium in terms of the differential displacements which must hold true at any location within a solid body as well as at its surface (Love, 1892, p. 7; Todhunter, 1886, p. 133). In the late 1820s, Poisson, Cauchy, and Lamé developed the equilibrium equations in terms of stresses by following a slightly different method than Navier (Love, 1892, pp. 8-10; Todhunter, 1886, pp. 326, 546-547). Further work by Saint-Venant concerning strain and displacement led to the development of the conditions of compatibility in 1860, which ensure that a solution to a problem of elasticity results in a continuous displacement field (Sadd, 2009, p. 41; Todhunter, 1893, p. 74).

D.2 Formulation of the General Equations of Elasticity

It can be seen that the stress, strain, and displacement fields in a solid can be derived given a set of boundary conditions along with the constitutive equations, the equilibrium equations, the compatibility equations, and the strain-displacement relations. There are two general solution formulations which depend upon the order in which the

general equations of elasticity are solved for and whether the general equations are expressed in terms of stresses or displacements (Timoshenko & Goodier, 1951, ch. 2). In the stress formulation, the general equations are expressed in terms of stresses. The stress field, then, must satisfy the equilibrium equations and the Beltrami-Michell compatibility equations (Sadd, 2009, pp. 97-98). The strain and displacement fields can then be derived from the stress field through the use of the constitutive equations and the strain-displacement relations, respectively. The stress formulation is used when the boundary conditions are given as stresses (Sadd, 2009, p. 97). In the displacement formulation, the general equations are expressed in terms of displacements (Sadd, 2009, sec. 5.4). The displacement field must satisfy the Navier equilibrium equations and the Saint-Venant compatibility equations. The strain and stress fields can then be derived from the displacement field by using the strain-displacement relations and constitutive equations, respectively. The displacement formulation is used when the boundary conditions are given as displacements (Sadd, 2009, p. 98).

A fully three-dimensional elastic analysis of a structure may become extremely complex. A two-dimensional analysis is oftentimes sufficient to obtain approximate results (Sadd, 2009, p. 135). Two similar sets of general equations of elasticity are derived by reducing a three-dimensional analysis to an approximate two-dimensional analysis (Donnell, 1976, pp. 104-106; Flügge, 1962, ch. 37). In the plane strain formulation, no normal strain or shear strain is assumed to occur in the out-of-plane direction. In the plane stress formulation, no normal stress or shear stress is assumed to occur in the out-of-plane direction. The general equations for both the plane strain and

plane stress formulations may be expressed in terms of stresses or displacements for the stress formulation and displacement formulation, respectively (Sadd, 2009, pp. 135-140).

Barber (2010), Donnell (1976), Flügge (1962), Jones (2009), Love (1892), Meguid (1987), Timoshenko & Goodier (1951), and Sadd (2009) present derivations of the general equations of elasticity along with various applications. For a two-dimensional stress formulation with zero body forces, the equilibrium equations reduce to the stresses relating to in-plane directions within a solid. The equilibrium equations are identical for both plane strain and plane stress formulations and are expressed as (Barber, 2010, p. 26)

$$\frac{\partial \sigma_x}{\partial x} + \frac{\partial \tau_{xy}}{\partial y} = 0 \tag{D.2.1}$$

$$\frac{\partial \tau_{xy}}{\partial x} + \frac{\partial \sigma_y}{\partial y} = 0 \tag{D.2.2}$$

Likewise, the Beltrami-Michell compatibility equations, which are the Saint-Venant compatibility equations expressed in terms of stresses, reduce to one relation concerning the stresses relating to in-plane directions. For zero body forces, the Beltrami-Michell compatibility equation is identical for both the plane strain and plane stress formulations, expressed as (Meguid, 1989, p. 24)

$$\frac{\partial^2 \sigma_x}{\partial x^2} + \frac{\partial^2 \sigma_x}{\partial y^2} + \frac{\partial^2 \sigma_y}{\partial x^2} + \frac{\partial^2 \sigma_y}{\partial y^2} = \nabla^2 \left(\sigma_x + \sigma_y \right) = 0 \tag{D.2.3}$$

The two-dimensional stress field may be expressed in terms of the Airy stress function, $F(x,y)$. The Airy stress function is formulated such that the resulting stress field identically satisfies the equilibrium equations, the Beltrami-Michell compatibility equation, and applicable boundary conditions (Meguid, 1989, p. 23). The following form

of the two-dimensional stress field identically satisfies the equilibrium equations (Donnell, 1976, p. 111):

$$\sigma_x = \frac{\partial^2 F}{\partial y^2} \qquad \sigma_y = \frac{\partial^2 F}{\partial x^2} \qquad \tau_{xy} = -\frac{\partial^2 F}{\partial x \partial y} \tag{D.2.4}$$

Substituting (D.2.4) into (D.2.3) results the governing biharmonic equation of elasticity for both plane strain and plane stress formulations, expressed as (Sadd, 2009, sec. 7.5)

$$\nabla^4 F = \frac{\partial^4 F}{\partial x^4} + 2\frac{\partial^4 F}{\partial x^2 \partial y^2} + \frac{\partial^4 F}{\partial y^4} = 0 \tag{D.2.5}$$

The formulation of an Airy stress function that satisfies the governing biharmonic equation and applicable boundary conditions results in a stress field, given by (D.2.4), which identically satisfies equilibrium and compatibility. For plane strain, the out-of-plane shear stresses vanish, while the out-of-plane normal stress is expressed in terms of the in-plane normal stresses and Poisson's ratio, given by (Sadd, 2009, p. 136)

$$\sigma_z = \nu\left(\sigma_x + \sigma_y\right) \tag{D.2.6}$$

Conversely, for plane stress, the out-of-plane normal stress and shear stresses vanish.

The strain and displacement fields may be derived from the stress field by employing the constitutive and strain-displacement relations, respectively. For plane strain, the out-of-plane normal strain and shear strains are zero. The constitutive equations in terms of stresses for plane strain are given by (Sadd, 2009, p. 148)

$$\varepsilon_x = \frac{1+v}{E}\left[(1-v)\sigma_x - v\sigma_y\right]$$

$$\varepsilon_y = \frac{1+v}{E}\left[(1-v)\sigma_y - v\sigma_x\right] \qquad\qquad \text{(D.2.7)}$$

$$\varepsilon_{xy} = \frac{1+v}{E}\tau_{xy}$$

For plane stress, the out-of-plane shear strains are zero, while the out-of-plane normal strain is expressed in terms of the in-plane normal stresses, Poisson's ratio, and Young's modulus. Hence, the constitutive equations in terms of stresses for plane stress are given by (Sadd, 2009, p. 139)

$$\varepsilon_x = \frac{1}{E}\left(\sigma_x - v\sigma_y\right)$$

$$\varepsilon_y = \frac{1}{E}\left(\sigma_y - v\sigma_x\right)$$

$$\qquad\qquad \text{(D.2.8)}$$

$$\varepsilon_z = -\frac{v}{E}\left(\sigma_x + \sigma_y\right)$$

$$\varepsilon_{xy} = \frac{1+v}{E}\tau_{xy}$$

The strain-displacement relations for plane strain are expressed as

$$\varepsilon_x = \frac{\partial u}{\partial x} \qquad \varepsilon_y = \frac{\partial v}{\partial y} \qquad \varepsilon_{xy} = \frac{1}{2}\left(\frac{\partial u}{\partial y} + \frac{\partial v}{\partial x}\right) \qquad \text{(D.2.9)}$$

Also, the strain-displacement relations for plane stress are expressed as

$$\varepsilon_x = \frac{\partial u}{\partial x} \qquad \varepsilon_y = \frac{\partial v}{\partial y} \qquad \varepsilon_z = \frac{\partial w}{\partial z} \qquad \varepsilon_{xy} = \frac{1}{2}\left(\frac{\partial u}{\partial y} + \frac{\partial v}{\partial x}\right) \qquad \text{(D.2.10)}$$

D.3   Solution Methods

The inverse method or semi-inverse method may be used to determine an appropriate Airy stress function. A solution may be found in the form of polynomials, power functions, or Fourier methods (Donnell, 1976, sec. 3.3; Flügge, 1962, ch. 37; Sadd, 2009, secs. 8.1, 8.2). The Michell solution may be employed for problems formulated in polar coordinates such as in half space problems (Sadd, 2009, sec. 8.3). For torsion problems, the stress field is expressed with the Prandtl stress function (Sadd, 2009, sec. 9.3).

Appendix E: Principle of Stationary Potential Energy

E.1   Rayleigh-Ritz Energy Method

The stability of a plate girder is largely dependent upon the local buckling capacities of the individual plates from which a plate girder is fabricated. The determination of the elastic plate buckling strength using classical plate theory (see Appendix F: Classical Plate Theory) may be extremely difficult to obtain when the boundary conditions are complicated, such as when considering the effects of a crack (Ugural, 1999, ch. 3). The plate buckling strength may be approximately determined using the Rayleigh-Ritz energy method.

The Rayleigh-Ritz method employs the principle of stationary potential energy to approximate the buckling stress when complex boundary conditions are present (Vinson, 1974, ch. 6). In this method, the buckled shape of a plate is assumed to take on a form described by an assumed displacement function. The displacement function satisfies the geometric boundary conditions and includes an arbitrary set of variables, A_i, which control the shape of the displacement function (Vinson, 1974, ch. 6), in the form

$$w(x, y) = \sum_{i=1}^{n} A_i f_i(x, y) \tag{E.1.1}$$

where n is the number of degrees of freedom of the displacement function. The total potential energy, Π, of the plate is then expressed as (Vinson, 1974, ch. 6)

$$\Pi = \int_V W dV - \int_S T_i u_i dS \tag{E.1.2}$$

where W is the strain energy density function, V is the volume of the plate, T_i are the applied surface tractions, u_i are the displacements caused by the tractions, and S is the surface over which the tractions are applied.

The variation in total potential energy with respect to A_i is set to zero such that (Vinson, 1974, ch. 6)

$$\frac{\delta\Pi}{\delta A_i} = 0 \qquad\qquad (E.1.3)$$

It follows that the external stress enabling this equilibrium is the buckling stress. The compressive stress fields induced or influenced by a crack as determined by the Westergaard function method (see Appendix G: Linear Elastic Fracture Mechanics) may be approximated by an external stress. The Rayleigh-Ritz method may then be used to determine the critical value of the external stress associated with buckling.

Appendix F: Classical Plate Theory

F.1   Background

The internal behavior of thin plates in response to external load may be analyzed using a specific application of the broader theory of elasticity (see Appendix E: Theory of Elasticity), variously known as the classical small-deflection theory of thin plates, the Kirchhoff-Love theory of plates, or classical plate theory. Plates are defined as nominally two-dimensional flat structures having a small thickness compared to the other dimensions, and are capable of carrying and distributing loads in two directions to applicable external supports (Ventsel & Krauthammer, 2001, p. 1). Classical plate theory employs a series of simplifying assumptions which reduce a mathematically rigorous three-dimensional theory of plates to a two-dimensional formulation (Donnell, 1976, p. 160). It turns out that classical plate theory yields accurate results for plates with relatively small thicknesses and for small deflections (Ugural, 1999, p. 71-73). However, the solutions of classical plate theory become less accurate as the plate thickness increases, at which point the problem turns into a three-dimensional formulation (Timoshenko & Woinowsky-Krieger, 1959, p. 2).

Love (1892), Taly (1998), Timoshenko (1983), Todhunter (1886, 1893), and Ventsel & Krauthammer (2001) present histories of the development of classical plate theory. The historical developments concerning the theory of elasticity (see Appendix E: Theory of Elasticity) are inherently intertwined with the mathematical foundations of classical plate theory. Euler in 1766 first investigated and discussed the behavior of vibrating membranes (Todhunter, 1886, p. 55). His method was to model thin membranes as two series of simply supported elastic threads oriented perpendicular to each other such that they resembled a two-dimensional surface. In 1787, Chladni conducted

experiments concerning the vibrations of plates and observed the patterns produced by fine powder placed upon the vibrating plates (Todhunter, 1886, p. 411). James Bernoulli in 1788 unsuccessfully attempted to formulate a theoretical basis to explain the results obtained by Chladni (Todhunter, 1886, p. 73; Ventsel & Krauthammer, 2001, p. 4).

In 1813, Germain formulated a rather inaccurate governing equation of plates in terms of displacements, which was subsequently corrected by Lagrange (Ventsel & Krauthammer, 2001, p. 5). Cauchy, Poisson and Navier later derived the Germain-Lagrange governing equation of plates using the recently developed general equations of elasticity. In 1850, Kirchhoff set forth a series of simplifying assumptions which effectively allowed the forces and bending moments applied upon a thin plate to be expressed in terms of the displacement of the middle surface (Donnell, 1976, p. 160; Ventsel & Krauthammer, 2001, p. 5). Love (1888) extended upon Kirchhoff's plate theory with work pertaining to the vibration of thin plates now known as the aforesaid Kirchhoff-Love theory of plates or classical plate theory. Numerous other contributions to plate theory were later made by Timoshenko, G.H. Bryan, von Karman, and many others as outlined by Taly (1998, sec. 9.5.1) and Ventsel & Krauthammer (2001, sec. 1.2).

F.2 Formulation of the General Equations of Classical Plate Theory

Derivations of the general equations of classical plate theory along with various applications have been presented by Barker & Puckett (1997), Donnell (1976), Salmon et al. (2009), Taly (1998), Timoshenko & Woinowsky-Krieger (1959), and Ugural (1999). It can be seen that the stress, strain, and displacement fields of thin elastic plates can be

derived using the displacement formulation. That is, the strain and stress fields are derived from the displacement field through the use of the strain-displacement and constitutive equations expressed in terms of displacements. The displacement field is expressed with a displacement function in much the same way that the stress field is expressed with the Airy stress function in the stress formulation (Ugural, 1999, p. 74). The forces and bending moments applied upon a thin elastic plate can be related to the displacement of the middle surface by using the simplifying assumptions set forth by Kirchhoff (Donnell, 1976, p. 160). These assumptions are stated as (Timoshenko & Woinowsky-Krieger, 1959, p. 1)

1. There is no deformation in the middle plane of the plate. This plane remains neutral during bending.

2. Points of the plate lying initially on a normal-to-the-middle plane of the plate remain on the normal-to-the-middle surface of the plate after bending.

3. The normal stresses in the direction transverse to the plate can be disregarded.

These assumptions are collectively known as the Kirchhoff hypotheses and are valid for homogeneous, linear isotropic elastic, thin plates (Ugural, 1999, p. 72).

In accordance with the Kirchhoff hypotheses, the engineering strain-displacement relations reduce to (Ugural, 1999, p. 74)

$$\varepsilon_x = \frac{\partial u}{\partial x} \qquad\qquad \varepsilon_z = \frac{\partial w}{\partial z} = 0$$

$$\varepsilon_y = \frac{\partial v}{\partial y} \qquad\qquad \varepsilon_{xz} = \frac{\partial w}{\partial x} + \frac{\partial u}{\partial z} = 0 \qquad\qquad (F.2.1)$$

$$\varepsilon_{xy} = \frac{\partial u}{\partial y} + \frac{\partial v}{\partial x} \qquad\qquad \varepsilon_{yz} = \frac{\partial w}{\partial y} + \frac{\partial v}{\partial z} = 0$$

266

where the variables u, v, and w are the displacements of points on the middle plane of a thin elastic plate corresponding to the x, y, and z-directions. The normal strain and shear strains relating to the out-of-plane direction vanish in accordance with the second Kirchhoff hypothesis.

Integrating the shear strain-displacement relations relating to the out-of-plane direction and solving for u and v gives (Ugural, 1999, p. 74)

$$u = -z\frac{\partial w}{\partial x} + u_o(x, y) \tag{F.2.2}$$

$$v = -z\frac{\partial w}{\partial y} + v_o(x, y) \tag{F.2.3}$$

The values of u_o and v_o correspond to the rigid body displacement of the plate which, for thin plates, are based upon the displacement of the middle plane of the plate. However, the values of u_o and v_o vanish in accordance with the first Kirchhoff hypothesis. Substituting (F.2.2) and (F.2.3) into (F.2.1) relating to the in-plane directions results in the strains expressed in terms of the vertical displacement, $w(x,y)$, given by (Ugural, 1999, p. 74)

$$\varepsilon_x = -z\frac{\partial^2 w}{\partial x^2} \qquad \varepsilon_y = -z\frac{\partial^2 w}{\partial y^2} \qquad \varepsilon_{xy} = -2z\frac{\partial^2 w}{\partial x \partial y} \tag{F.2.4}$$

The middle plane of the plate undergoing flexure will take on a curved shape with varying values of vertical displacement throughout the plate. Likewise, the corresponding slope angles of the middle plane of the plate will also vary throughout the plate. The rate at which the slope angles vary along a given plane is called the curvature of the plate and is equal to the reciprocal of the radius of curvature. From (F.2.4), the curvatures of the middle plane of the plate can be expressed as (Ugural, 1999, p. 75)

$$\kappa_x = \frac{\partial}{\partial x}\left(\frac{\partial w}{\partial x}\right) \qquad \kappa_y = \frac{\partial}{\partial y}\left(\frac{\partial w}{\partial y}\right) \qquad \kappa_{xy} = \frac{\partial}{\partial x}\left(\frac{\partial w}{\partial y}\right) \qquad \text{(F.2.5)}$$

Substituting (F.2.5) into (F.2.4) results in the strain-curvature relations for thin elastic plates given by (Ugural, 1999, p. 75)

$$\varepsilon_x = -z\kappa_x \qquad \varepsilon_y = -z\kappa_y \qquad \varepsilon_{xy} = -2z\kappa_{xy} \qquad \text{(F.2.6)}$$

The stresses in the out-of-plane direction vanish in accordance with the third Kirchhoff hypothesis. Hence, the plate is in a state of plane stress (Donnell, 1976, p. 168). The constitutive equations for plane stress expressed in terms of strain are given by (Donnell, 1976, p. 106)

$$\sigma_x = \frac{E}{1-v^2}\left(\varepsilon_x + v\varepsilon_y\right)$$

$$\sigma_x = \frac{E}{1-v^2}\left(\varepsilon_y + v\varepsilon_x\right) \qquad \text{(F.2.7)}$$

$$\tau_{xy} = \frac{E}{2(1+v)}\varepsilon_{xy}$$

Substituting the strain-curvature relations given by (F.2.6) into (F.2.7) gives (Salmon et al., 2009, p. 285)

$$\sigma_x = -\frac{Ez}{1-v^2}\left(\frac{\partial^2 w}{\partial x^2} + v\frac{\partial^2 w}{\partial y^2}\right)$$

$$\sigma_y = -\frac{Ez}{1-v^2}\left(\frac{\partial^2 w}{\partial y^2} + v\frac{\partial^2 w}{\partial x^2}\right) \qquad \text{(F.2.8)}$$

$$\tau_{xy} = -\frac{Ez}{1+v}\frac{\partial^2 w}{\partial x \partial y}$$

The stress field varies throughout the thickness, t, of the plate, and may be integrated from $-t/2$ to $t/2$ to produce stress resultants in the form of bending moments given by (Ugural, 1999, p. 78)

$$M_x = \int_{-t/2}^{t/2} z\sigma_x dz = -D\left(\kappa_x + \nu\kappa_y\right)$$

$$M_y = \int_{-t/2}^{t/2} z\sigma_y dz = -D\left(\kappa_y + \nu\kappa_x\right) \tag{F.2.9}$$

$$M_{xy} = \int_{-t/2}^{t/2} z\tau_{xy} dz = -D(1-\nu)\kappa_{xy}$$

where the constant, D, is the flexural rigidity of the plate given by (Barker & Puckett, 1997, p. 297)

$$D = \frac{Et^3}{12\left(1-\nu^2\right)} \tag{F.2.10}$$

where E is the modulus of elasticity, ν is Poisson's ratio, and t is the plate thickness. It can be seen that the bending moments are expressed in terms of the modulus of elasticity, Poisson's ratio, the plate thickness, and the curvatures of the middle plane of the plate. The curvatures are themselves expressed in terms of the vertical displacement of the middle plane of the plate.

The bending moments, along with out-of-plane loading, p, and vertical shear forces, Q, must satisfy equilibrium along each axis of the plate. Summing the stress resultants in the x, y, and z-directions and removing like terms results in the following equilibrium equations (Salmon et al., 2009, p. 287)

$$\sum F_z = \frac{\partial Q_x}{\partial x} + \frac{\partial Q_y}{\partial y} + p = 0$$

$$\sum M_x = \frac{\partial M_{xy}}{\partial x} + \frac{\partial M_y}{\partial y} - Q_y = 0 \qquad \text{(F.2.11)}$$

$$\sum M_y = \frac{\partial M_{xy}}{\partial x} + \frac{\partial M_x}{\partial x} - Q_x = 0$$

Solving for Q_x and Q_y in (F.2.11)$_2$ and (F.2.11)$_3$ and substituting the results into (F.2.11)$_1$ gives the differential equation of equilibrium for thin elastic plates shown by (Ugural, 1999, p. 82)

$$\frac{\partial^2 M_x}{\partial x^2} + 2\frac{\partial^2 M_{xy}}{\partial x \partial y} + \frac{\partial^2 M_y}{\partial y^2} = -p \qquad \text{(F.2.12)}$$

Substituting (F.2.5) and (F.2.10) into (F.2.9), and substituting the results into (F.2.12) results in the governing differential equation of thin elastic plates for out-of-plane loading, expressed as (Taly, 1998, p. 938)

$$D\nabla^4 w = D\left(\frac{\partial^4 w}{\partial x^4} + 2\frac{\partial^4 w}{\partial x^2 \partial y^2} + \frac{\partial^4 w}{\partial y^4}\right) = p \qquad \text{(F.2.13)}$$

The general form of the governing differential equation takes into account all load cases, shown as (Chajes, 1974, sec. 6.2)

$$D\nabla^4 w = D\left(\frac{\partial^4 w}{\partial x^4} + 2\frac{\partial^4 w}{\partial x^2 \partial y^2} + \frac{\partial^4 w}{\partial y^4}\right) = N_x \frac{\partial^2 w}{\partial x^2} + N_y \frac{\partial^2 w}{\partial y^2} + 2N_{xy} \frac{\partial^2 w}{\partial x \partial y} \qquad \text{(F.2.14)}$$

where N_i are in-plane edge loads.

F.3   Solution Methods

The inverse method or semi-inverse method may be used to determine an appropriate displacement function. A solution may be found in the form of polynomials,

trigonometric functions, and Fourier methods (Donnell, 1976, secs. 4.4, 4.5; Timoshenko & Woinowsky-Krieger, 1959). Solutions to numerous plate problems are provided by Timoshenko (1936) and Timoshenko & Woinowsky-Krieger (1959). The displacement function must satisfy the governing differential equation of thin elastic plates given by (F.2.14) and applicable boundary conditions. The stress and strain fields may then be derived from the constitutive equations for plane stress given by (F.2.8) and the strain-curvature relations given by (F.2.6).

F.4   Application to Elastic Buckling

Buckling is directly related to the stability of a structure subjected to load. Stability, in turn, is the ability of a structure to maintain static equilibrium when subjected to load, where the applied load is generally compressive in nature. The load at which static equilibrium can no longer be maintained in the original structural configuration is called the critical load or buckling load. Hence, buckling is the loss of stability and stiffness, and may be accompanied by a drastic increase of deformations. Physically, the structure transforms into a buckled shape to maintain equilibrium. Mathematically, buckling implies the bifurcation of the equilibrium equations. Elastic buckling occurs when the stresses throughout a structure remain below the material yield strength. Conversely, inelastic buckling occurs when a portion of the stresses throughout a structure exceed the material yield strength.

The elastic buckling strength of a thin elastic plate may be determined by employing the semi-inverse method to formulate an appropriate displacement function satisfying (F.2.14) and applicable boundary conditions. The general form for the elastic

271

buckling strength is derived by considering a uniformly distributed compression load along the edge of a simply supported thin elastic plate (see Figure F.4.1), expressed as

$$P_X = F_{cr}t \tag{F.4.1}$$

where F_{cr} is the elastic buckling stress and t is the plate thickness. Satisfying equilibrium and solving for the out-of-plane loading due to plate bending gives (Salmon et al., 2009, p. 288)

$$p = -P_x \frac{\partial^2 w}{\partial x^2} \tag{F.4.2}$$

Substituting (F.4.2) into (F.2.13) results in

$$\frac{\partial^4 w}{\partial x^4} + 2\frac{\partial^4 w}{\partial x^2 \partial y^2} + \frac{\partial^4 w}{\partial y^4} = -\frac{P_x}{D}\frac{\partial^2 w}{\partial x^2} \tag{F.4.3}$$

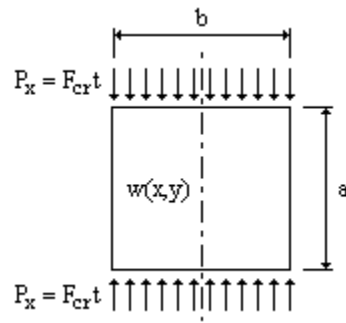Figure F.4.1: Simply supported thin elastic plate loaded by uniformly distributed uniaxial compression load, P_x.

It is assumed that the plate is simply supported along the edges parallel to the direction of load. Therefore, the boundary conditions are such that the out-of-plane plate displacements are zero along these edges, expressed as

$$w\left(x, -\frac{b}{2}\right) = 0 \tag{F.4.4}$$

272

$$w\left(x, \frac{b}{2}\right) = 0 \tag{F.4.5}$$

A displacement function of the following form satisfies (F.4.4) and (F.4.5) (Salmon et al., 2009, p. 289)

$$w = \left(\sin \frac{m\pi x}{a}\right)\left(C_1 \sinh \alpha y + C_2 \cosh \alpha y + C_3 \sin \beta y + C_4 \cos \beta y\right) \tag{F.4.6}$$

where m is the aspect ratio given by

$$m = \frac{a}{b} \tag{F.4.7}$$

and α is defined as

$$\alpha = \sqrt{\left(\frac{m\pi}{a}\right)^2 + \sqrt{\frac{P_x}{D}\left(\frac{m\pi}{a}\right)^2}} \tag{F.4.8}$$

and β is defined as

$$\beta = \sqrt{-\left(\frac{m\pi}{a}\right)^2 + \sqrt{\frac{P_x}{D}\left(\frac{m\pi}{a}\right)^2}} \tag{F.4.9}$$

Solving for the constants C_1, C_2, C_3, and C_4 using the boundary conditions given by (F.4.4) and (F.4.5), and isolating P_x results in (Salmon et al, 2009, p. 289)

$$P_x = \frac{D\pi^2}{b^2}\left(\frac{a}{mb} + \frac{mb}{a}\right)^2 \tag{F.4.10}$$

Substituting the flexural rigidity of the plate given by (F.2.10) into (F.4.10), plugging the result into (F.4.3), and solving for the elastic buckling stress results in (Salmon et al., 2009, p. 289)

$$F_{cr} = k\frac{\pi^2 E}{12(1-v^2)(b/t)^2} \tag{F.4.11}$$

where b is the plate width and k is a constant dependent upon the boundary conditions.

It is noted that (F.4.11) is general and therefore represents the elastic buckling stress of any thin elastic plate. For the present case of a plate loaded under uniform compression and with simple supports along the edges parallel to the load, k is given by (Taly, 1998, p. 944)

$$k = \left(\frac{a}{mb} + \frac{mb}{a} \right)^2$$

(F.4.12)

The width-to-thickness ratio, b/t, in (F.4.11) is called the slenderness ratio and is typically denoted by λ. Setting the elastic buckling stress given by (F.4.11) equal to or greater than the material yield strength, F_y, and solving for b/t results in (Taly, 1998, p. 948)

$$\lambda = \frac{b}{t} \leq \sqrt{\frac{k\pi^2 E}{12(1-v^2)F_y}}$$

(F.4.13)

Thin elastic plates with slenderness ratios satisfying the requirement expressed by (F.4.13) do not buckle elastically prior to yielding, and are classified as compact (Salmon et al., 2009, sec. 6.16.). Thin elastic plates that satisfy (F.4.13) and fail due to inelastic buckling are classified as noncompact. Finally, thin elastic plates that do not satisfy (F.4.13) may buckle elastically prior to yielding, and are classified as slender.

Appendix G: Linear Elastic Fracture Mechanics

G.1　Westergaard Function Method

The presence of a crack within a loaded plane elastic structure introduces local disturbances in the stress field which complicates the determination of a suitable stress function. The Kolosov-Muskhelishvili complex potential method employs stress functions expressed in terms of complex variables (Sun & Jin, 2012, sec. 3.2). A particular subset of the complex potential method is the Westergaard function method in which the Airy stress function is expressed in terms of the Westergaard stress function, $Z(\zeta)$, as (Westergaard, 1939)

$$F = \operatorname{Re} \overline{\overline{Z}} + y \operatorname{Im} \overline{Z} \tag{G.1.1}$$

for Mode I loading, where

$$Z' = \frac{dZ}{d\zeta} \qquad Z = \frac{d\overline{Z}}{d\zeta} \qquad \overline{Z} = \frac{d\overline{\overline{Z}}}{d\zeta} \tag{G.1.2}$$

and ζ is the complex variable $\zeta = x + iy$. In accordance with the Cauchy-Riemann differential equations, the substitution of (G.1.1) into the form of the two-dimensional stress field given by (D.2.4) results in the stress field about a crack for Mode I loading, given by (Westergaard, 1939)

$$\begin{aligned}
\sigma_x &= \operatorname{Re} Z - y \operatorname{Im} Z' \\
\sigma_y &= \operatorname{Re} Z + y \operatorname{Im} Z' \\
\tau_{xy} &= -y \operatorname{Re} Z'
\end{aligned} \tag{G.1.3}$$

In essence, the stress field about a crack is found by determining an appropriate Westergaard stress function, and the corresponding strain and displacement fields are calculated from the constitutive equations and strain-displacement relations, respectively. The determination of the stress field about a crack then allows for the elastic limit states of a fatigue-cracked plate girder to be analyzed. For the case of buckling limit states, the

stress field about a crack may be used to determine regions of a plate under compression, and the associated elastic buckling strength may be calculated using classical plate theory (see Appendix F: Classical Plate Theory) or energy methods (see Appendix E: Principle of Stationary Potential Energy).

G.2   Near-tip Solution

The limit states of brittle fracture and impending ductile failure may be analyzed by investigating the stress field near the tip of a crack (Irwin, 1957; Sun & Jin, 2012, sec. 3.4). For Mode I loading, the localized stress field is determined by employing a Westergaard stress function in the form (Meguid, 1989, sec. 4.3)

$$Z_I = \frac{K_I}{\sqrt{2\pi\zeta}} \tag{G.2.1}$$

where the coordinate axes have been shifted to the crack tip (Irwin, 1957; Sun & Jin, 2012, sec. 3.4). The term K_I controls the magnitude of stresses near the crack tip and is called the stress intensity factor (Meguid, 1989, ch. 4). The stress intensity factor is given by (Shukla, 2005, ch. 3)

$$K_I = f(g)\sigma_f\sqrt{\pi a} \tag{G.2.2}$$

where σ_f is the far-field opening mode stress and a is half the length of a central crack (see Figure G.2.1). The term $f(g)$ is a correction factor used to modify the theoretical stress intensity factor to account for the geometry of a crack as well as the finite geometry of a structure (Shukla, 2005, ch. 3; Sun & Jin, 2012, sec. 3.6). Theoretical stress intensity factors and correction factors for different loading configurations, structure geometries, and crack geometries have been given by Tada, Paris, & Irwin (2000).
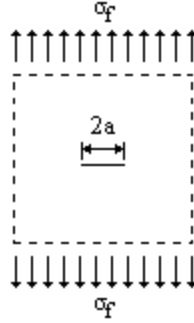
Figure G.2.1: Central crack of length 2a residing within an infinite plate subjected to far-field uniaxial tensile stress.

Whereas the energy release rate characterizes the potentiality of crack propagation in terms of energy at the crack tip, the stress intensity factor characterizes this in terms of stress at the crack tip. For plane stress, the stress intensity factor for Mode I loading is related to the energy release rate by (Shukla, 2005, ch. 2)

$$K_I = \sqrt{GE} \tag{G.2.3}$$

and for plane strain (Shukla, 2005, ch. 2)

$$K_I = \sqrt{\frac{GE}{1-\nu^2}} \tag{G.2.4}$$

Equations (G.2.3) and (G.2.4) imply that just as a crack will grow when the energy release rate equals or exceeds a critical value, brittle fracture will occur when K_I equals or exceeds a critical value, denoted by K_C, called the fracture toughness (Shukla, 2005, ch. 4; Sun & Jin, 2012, secs. 1.2, 2.3). The fracture toughness is dependent upon the material properties and thickness of a structure, and can only be experimentally determined (Shukla, 2005, p. 41). Experimental values of the stress intensity factor may be determined through such methods as the optical method of photoelasticity and the shadow method of caustics (Shukla, 2005, ch. 7).

For plate-like structures with thin to medium thicknesses, the fracture toughness is dependent upon the plate thickness (Rolf & Barsom, 1977, sec. 3.2). Loaded thin plate-like structures are under a state of plane stress, as assumed by the third Kirchhoff hypothesis (see Appendix F: Classical Plate Theory). Conversely, loaded plate-like structures with medium thicknesses are under a mixed-mode condition with the outside region under a state of plane stress and the inside region under a state of plane strain (Meguid, 1989, p. 187). For both of these conditions, the stress distribution around a crack is dependent upon the plate thickness. It follows that the corresponding fracture toughness is also dependent upon the plate thickness. At a certain critical thickness, loaded plate-like structures come predominantly under a state of plane strain and the fracture toughness becomes relatively constant and independent of the thickness (Askeland & Phulé, 2006, pp. 224-226). This constant value of fracture toughness is a unique material property called the plane strain fracture toughness denoted by K_{Ic} (Askeland & Phulé, 2006, pp. 224-226) (see Figure G.2.2).
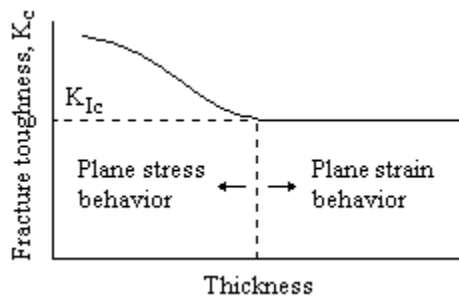

Figure G.2.2: Schematic of fracture toughness plotted as a function of plate thickness.

A standard test method for fracture toughness testing of metallics is specified in ASTM *E399 - Standard Test Method for Linear-Elastic Plane-Strain Fracture Toughness K_{Ic} of Metallic Materials*. The fracture toughness may also be indirectly calculated by

using the Charpy V-notch (CVN) test as specified in ASTM *E23 Standard Test Methods for Notched Bar Impact Testing of Metallic Materials* (Wright, 2002).

The fracture toughness characterization holds true as long as the plastic region at the crack tip remains small at fracture, as is the case for brittle materials (Meguid, 1989, ch. 6). Brittle materials have low fracture toughness and thus the plastic region always remains small up until fracture. Conversely, ductile materials have high fracture toughness and the plastic region may become quite large prior failure. The presence of a large plastic region invalidates the fracture toughness characterization for ductile materials, and the impending ductile failure must be described using elasto-plastic fracture mechanics (EPFM) (Meguid, 1989, ch. 6; Rolf & Barsom, 1977, ch. 16).

Appendix H: Empirical Crack Growth Law

H.1 Paris-Erdogan Empirical Crack Growth Equation

The vehicular live load effects induced within a plate girder may be idealized as constant-amplitude (see Figure H.1.1) or variable-amplitude trigonometric functions of time (Miki, Murakosi, & Sakano, 1987). For the case of a constant-amplitude stress function of time, the stress range is the difference between the maximum and minimum stresses, expressed as

$$\Delta\sigma = \sigma_{max} - \sigma_{min} \tag{H.1.1}$$

It follows that the stress intensity factor (see Appendix G: Linear Elastic Fracture Mechanics) of a crack in a girder also changes as a function of time. In general, the range of the Mode I stress intensity factor is the difference between the maximum and minimum magnitudes of K_I, expressed as

$$\Delta K_I = K_{I,max} - K_{I,min} \tag{H.1.2}$$
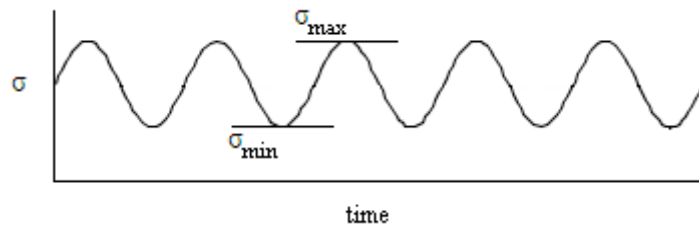
Figure H.1.1: Constant-amplitude trigonometric load function.

Preexisting cracks in a plate girder can slowly propagate under cyclic stresses even when the maximum stress intensity factor never exceeds the fracture toughness of the girder steel (Meguid, 1989, p. 243). The rate of crack growth can be described by the fatigue crack growth rate curve, which describes the rate of crack extension per stress cycle as a function of the logarithmic range of the stress intensity factor (see Figure

H.1.2). The fatigue crack growth rate curve may be divided into three distinct sub regions (Kohout, 1999). Region I represents the range of the stress intensity factor in which a crack initially forms at a threshold value, ΔK_{th}, and experiences very little initial growth. Region II represents the range of the stress intensity factor in which a crack experiences slow growth over the fatigue life of the girder. Region III is where the maximum stress intensity factor exceeds the fracture toughness resulting in brittle fracture.
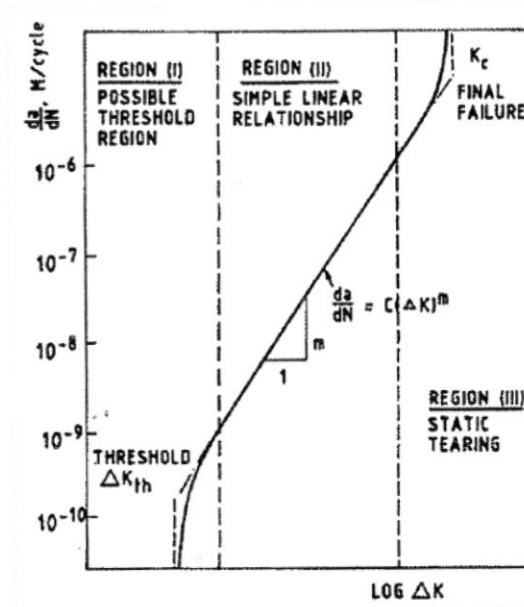
Figure H.1.2: Typical fatigue crack growth rate curve (Meguid, 1989, p. 248, fig. 7.4).

The portion of the fatigue crack growth rate curve in Region II may be described by an empirical growth relation given by Paris & Erdogan (1963)

$$\frac{da}{dN} = C(\Delta K_I)^m \qquad (H.1.3)$$

where C and m are experimentally determined material constants. Equation (H.1.3) is known as the Paris-Erdogan empirical crack growth equation. The crack growth rate is overwhelmingly dependent upon the range of the stress intensity factor. Other factors

may also influence the crack growth rate such as the mean stress and environmental factors as discussed by Frost (1962) and Wei (1970). However, these other factors are considered to be of secondary importance when the maximum stress intensity factor is much lower than the fracture toughness (Hertzberg & Nordberg, 1969).

Other empirical crack growth equations have been developed such as that given by Forman, Kearney, & Engle (1967)

$$\frac{da}{dN} = \frac{\lambda^m \Delta K^n}{K_c - \lambda \Delta K} \tag{H.1.4}$$

where,

$$\lambda = \frac{K_{max}}{\Delta K} \tag{H.1.5}$$

and K_{max} is the maximum stress intensity factor, K_c is the fracture toughness, and m and n are material constants.

Appendix I: FEA Models

I.1   Plate Girder Models

Herein are figures of the trial plate girder models (PG-1 through PG-4) described in Section 5.4.1.1:
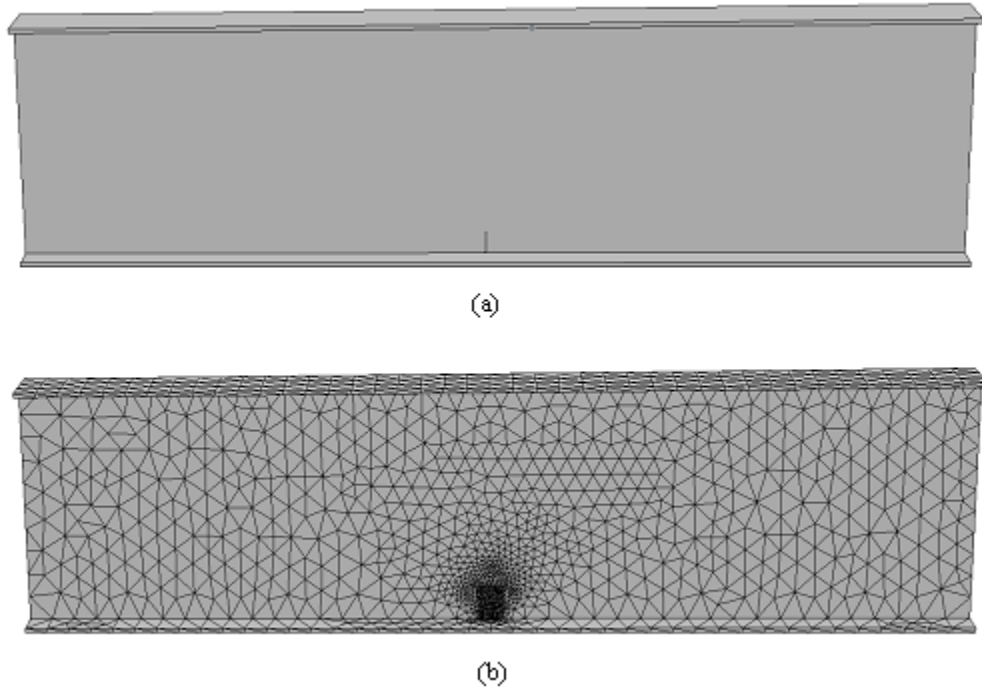
Figure I.1.1: Profile view of typical trial plate girder model with representative crack configuration located at mid-span (a) without mesh and (b) with mesh.

Figure I.1.2: Cross-section view of typical trial girder model.
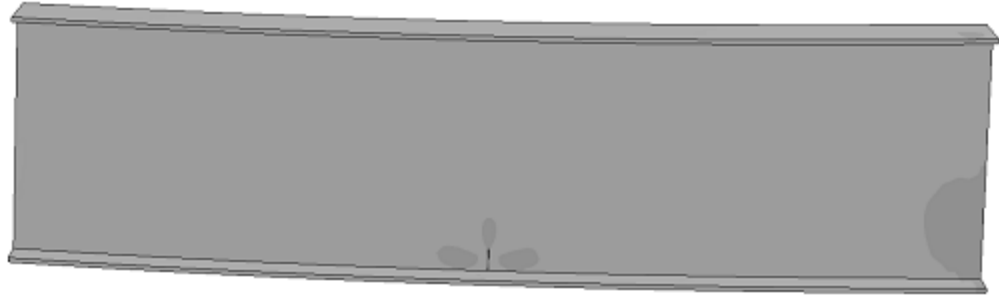
Figure I.1.3: Profile view of typical trial girder model configured as a cantilever loaded under pure bending with the deformation scale set to *100*.

(a)　　　　　　　　　　(b)
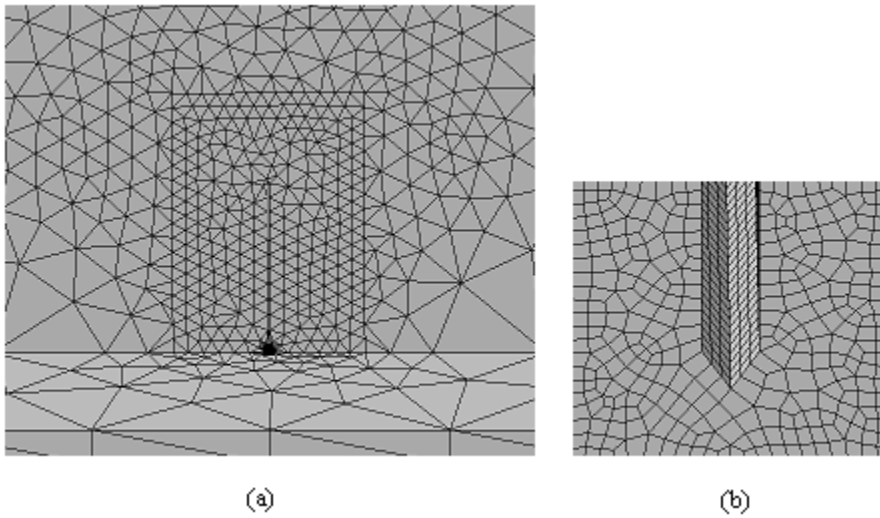
Figure I.1.4: (a) Refined mesh around a representative crack configuration with (b) the mesh at the crack tip.

I.2   Web Panel Models

Herein are figures of the trial web panel models (WP-A through WP-D) described in Section 5.4.1.2:
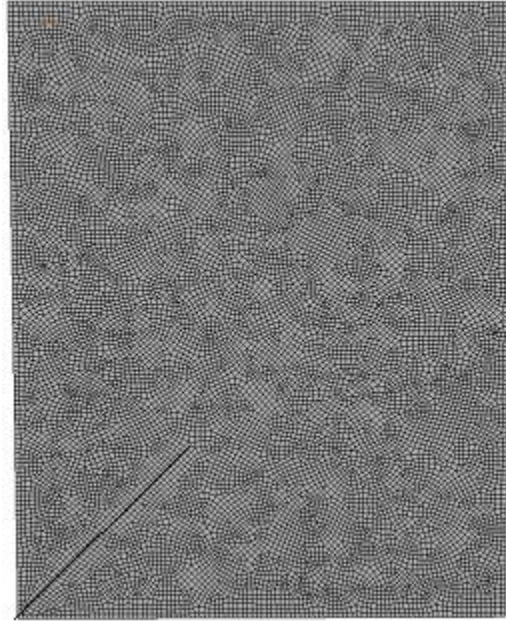
Figure I.2.1: Profile view of typical web panel model with representative diagonal crack configuration located at the bottom left corner.
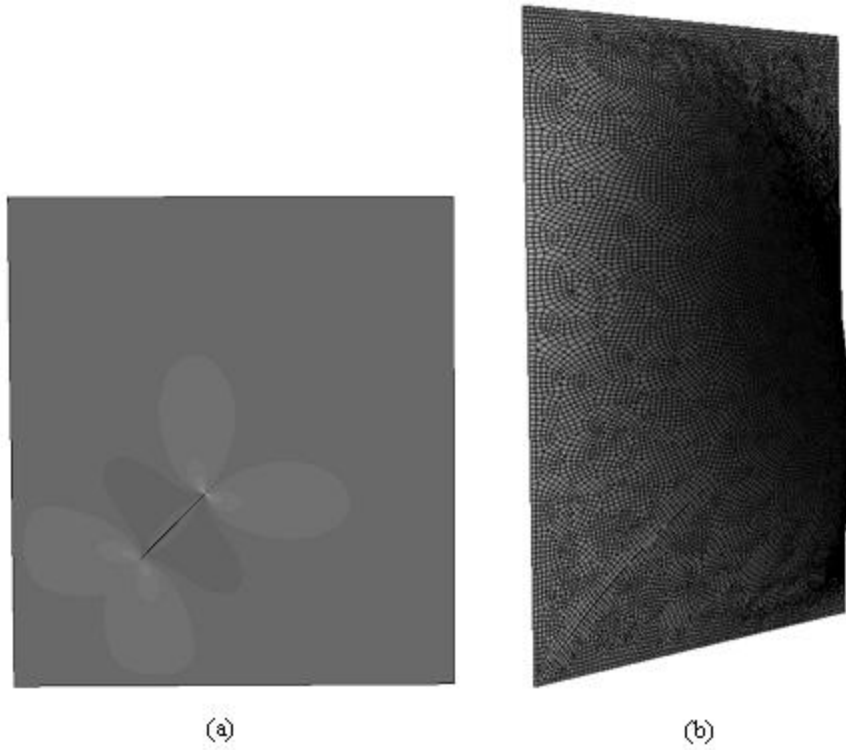
Figure I.2.2: Typical web panel model loaded under pure shear showing (a) the shear stress contours around the diagonal crack and (b) the first mode buckled shape with the deformation scale set to *25*.

Bibliography

AASHTO. (2010). *LRFD bridge design specifications* (5th ed.). Washington, DC: American Association of State Highway and Transportation Officials.

AASHTO. (2011). *The manual for bridge evaluation* (2nd ed.). Washington, DC: American Association of State Highway and Transportation Officials.

About Bridges. Beam bridge. *About Bridges*. Retrieved October 15, 2013, from https://sites.google.com/site/aboutbridges/home/4-beam-bridge

ACI. (2005). *Building code requirements for structural concrete (ACI 318-05) and commentary (ACI 318R-05)*. Farmington Hills, MI: American Concrete Institute.

AISC. (1969). *Specification for the design, fabrication and erection of structural steel for buildings*. New York, NY: American Institute of Steel Construction.

AISC. (2003). *Design of steel and composite beams with web openings: Guideline 2* (3rd ed.). D. Darwin (Ed.). Chicago, IL: American Institute of Steel Construction.

AISC. (2005). *Specification for structural steel buildings*. Chicago, IL: American Institute of Steel Construction.

Alinia, M.M., Hosseinzadeh, S.A.A., & Habashi, H.R. (2007a). Buckling and post-buckling strength of shear panels degraded by near border cracks. *Journal of Constructional Steel Research, 64*(12), 1483-1494.

Alinia, M.M., Hosseinzadeh, S.A.A., & Habashi, H.R. (2007b). Influence of central cracks on buckling and post-buckling behaviour of shear panels. *Thin-Walled Structures, 45*(4), 422-431.

Alinia, M.M., Hosseinzadeh, S.A.A., & Habashi, H.R. (2007c). Numerical modelling for buckling analysis of cracked shear panels. *Thin-Walled Structures, 45*(12), 1058-1067.

Anderson, T.L. (2005). *Fracture mechanics: Fundamentals and applications* (3rd ed.). Boca Raton, FL: CRC Press.

Askeland, D.R., & Phulé, P.P. (2006). *The science and engineering of materials.* Toronto, Canada: Nelson.

Barber, J.R. (2010). *Elasticity*. Springer: New York, NY.

Barker, R.M, & Puckett, J.A. (1997). *Design of highway bridges*. New York, NY: John Wiley & Sons.

Barsom, J.M. (1973). *Fatigue crack growth under variable-amplitude loading in ASTM A514-B steel* (ASTM STP 536). Philadelphia, PA: American Society for Testing and Materials.

Barsom, J.M. (1976). *Fatigue crack growth under variable-amplitude loading in various bridge steels* (ASTM STP 595). Philadelphia, PA: American Society for Testing and Materials.

Baskar, K., Shanmugam, N.E., & Thevendran, V. (2002). Finite-element analysis of steel-concrete composite plate girder. *Journal of Structural Engineering, 128*(9), 1158-1168.

Basler, K. (1961). *Plate girders under combined bending and shear* (Fritz Engineering Laboratory Report No. 251-21). Bethlehem, PA: Lehigh University.

Basler, K., Bung-Tseng, Y., Mueller, J.A., & Thurlimann, B. (1960a). *Web buckling tests on welded plate girders, overall introduction and part 1: The test girders* (Fritz Engineering Laboratory Report No. 251-11). Bethlehem, PA: Lehigh University.

Basler, K., Bung-Tseng, Y., Mueller, J.A., & Thurlimann, B. (1960b). *Web buckling tests on welded plate girders, part 2: Tests on plate girders subjected to bending* (Fritz Engineering Laboratory Report No. 251-12). Bethlehem, PA: Lehigh University.

Basler, K., Bung-Tseng, Y., Mueller, J.A., & Thurlimann, B. (1960c). *Web buckling tests on welded plate girders, part 3: Tests on plate girders subjected to shear* (Fritz Engineering Laboratory Report No. 251-13). Bethlehem, PA: Lehigh University.

Basler, K., Bung-Tseng, Y., Mueller, J.A., & Thurlimann, B. (1960d). *Web buckling tests on welded plate girders, part 4: Tests on plate girders subjected to combined bending and shear* (Fritz Engineering Laboratory Report No. 251-14). Bethlehem, PA: Lehigh University.

Basler, K., & Thurlimann, B. (1960a). *Strength of plate girders in bending* (Fritz Engineering Laboratory Report No. 251-19). Bethlehem, PA: Lehigh University.

Basler, K., & Thurlimann, B. (1960b). *Strength of plate girders in shear* (Fritz Engineering Laboratory Report No. 251-20). Bethlehem, PA: Lehigh University.

Bauchau, O.A., & Craig, J.I. (2009). *Structural analysis with applications to aerospace structures.* New York: Springer.

Bedair, O. (2011). Stress analyses of deep plate girders used at oil and gas facilities with rectangular web penetrations. *Practice Periodical on Structural Design and Construction, 16*(3), 112-120.

Beer, F.P., Johnston, E.R., & DeWolf, J.T. (2006). *Mechanics of materials*, 4th Edition. New York, NY: McGraw-Hill.

Blodgett, O.W. (1966). *Design of welded structures*. Cleveland, OH: The James F. Lincoln Arc Welding Foundation.

Bowman, M.D. (2002). *Fatigue behavior of beam diaphragm connections with intermittent fillet welds / Part II: Brittle fracture examination of the I-64 Blue River Bridge* (Report No. FHWA/IN/JTRP-2001/10-II). West Lafayette, IN: Purdue University.

Bowman, M.D. (2004). Brittle fracture of the blue river bridge. Proceedings from Structures Congress 2004: *Building on the Past, Securing the Future*. Nashville, TN: American Society of Civil Engineers.

Brendel, G. (1964). Strength of the compression slab of T-beams subject to simple bending. *ACI Journal, Proceedings, 61*, 57-76.

Brighenti, R. (2005a). Buckling of cracked thin-plates under tension or compression. *Thin-Walled Structures, 43*(2), 209-224.

Brighenti, R. (2005b). Numerical buckling analysis of compressed or tension cracked thin plates. *Engineering Structures, 27*(2), 265-276.

Brighenti, R. (2009). Buckling sensitivity analysis of cracked thin plates under membrane tension or compression loading. *Nuclear Engineering and Design, 239*(6), 965-980.

Brighenti, R., & Carpinteri, A. (2011). Buckling and fracture behaviour of cracked thin plates under shear loading. *Materials & Design, 32*(3), 1347-1355.

CALTRANS. (2008). *Local assistance program guidelines: Processing procedures for implementing federal and/or state funded local public transportation projects*. Sacramento, CA: State of California Department of Transportation.

Chajes, A. (1974). *Principles of structural stability*. Englewood Cliffs, NJ: Prentice-Hall, Inc.

Chajes, M., Mertz, D., Quiel, S., Roecker, H., & Milius, J. (2005). Steel girder fracture on Delaware's I-95 bridge over the Brandywine River. Proceedings from Structures Congress 2005: *Metropolis and Beyond*. New York, NY: American Society of Civil Engineers.

Chen, S.S., Aref, A.J., Ahn, I.-S., Chiewanichakorn, M., Carpenter, J.A., Nottis, A., & Kalpakidis, I. (2005). *Effective slab width for composite steel bridge members* (NCHRP Report No. 543). Washington, DC: Transportation Research Board.

Chen, W., & Duan, L. (Eds.). (1999). *Bridge engineering handbook*. Boca Raton, FL: CRC Press LLC.

Cheng, J., & Yura, J. (1986). Local web buckling of coped beams. *Journal of Structural Engineering, 112*(10), 2314-2331.

Cooper, P.B., & Roychowdhury, J. (1990). Shear strength of plate girders with web openings. *Journal of Structural Engineering, 116*(7), 2042-2048.

Cornell, C.A. (1969). A probability-based structural code. *ACI Journal , 66*(12).

Crocetti, R. (2003). Web breathing of full-scale slender I-girders subjected to combined action of bending and shear. *Journal of Constructional Steel Research, 59*(3), 271-290.

CRS. (2007). *Highway bridges: Conditions and the federal/state role* (Order Code RL34127). Washington, D.C.: Congressional Research Service.

D'Apice, M.A., & Cooper, P.B. (1965). *Static bending tests on longitudinally stiffened plate girders* (Fritz Engineering Laboratory Report No. 304-5). Bethlehem, PA: Lehigh University.

Davies, A.W., & Roberts, T.M. (1996). Numerical studies of fatigue induced by breathing of slender web plates. *Thin-Walled Structures, 25*(4), 319-333.

Davies, A.W., Roberts, T.M., Evans, H.R., & Bennett, R.J.H. (1994). Fatigue of slender web plates subjected to combined membrane and secondary bending stresses. *Journal of Constructional Steel Research, 30*(1), 85-101.

Devore, J., & Farnum, N. (2005). *Applied statistics for engineers and scientists*. Belmont, CA: Thomson Brooks/Cole.

Donnell, L.H. (1976). *Beams, plates, and shells.* New York, NY: McGraw-Hill.

Elgaaly, M. (2000). Post-buckling behavior of thin steel plates using computational models. *Advances in Engineering Software, 31*(8-9), 511-517.

Ellingwood. B.R. (2001). Probability-based load criteria for structural design. *A Century of Excellence in Measurements, Standards, and Technology: A Chronicle of Selected NBS/NIST Publications, 1901-2000* (Special Publication 958). Gaithersburg, MD: National Institute of Standards and Technology.

Ellingwood, B., Galambos, T.V., MacGregor, J.G., & Cornell, C.A. (1980). *Development of a probability based load criterion for American National Standard A58: Building code requirements for minimum design loads in buildings and other*

structures (NBS Special Publication 577). Washington, DC: US Department of Commerce, National Bureau of Standards.

FHWA. (1995). *Recording and coding guide for the structure inventory and appraisal of the nation's bridges* (Report No. FHWA-PD-96-001). Washington, D.C.: U.S. Department of Transportation.

FHWA. (2007). FHWA launches steel bridge testing program. *Focus*. Retrieved February 3, 2012, from http://www.fhwa.dot.gov/publications/focus/07sep/02.cfm

FHWA. (2009). National bridge inspection standards. *Federal Register, 74*(246), 68377-68379.

FHWA. (2011). National bridge inventory (NBI). *Federal Highway Administration*. Retrieved March 5, 2012, from http://www.fhwa.dot.gov/bridge/nbi.htm

FHWA. (2012a). Eisenhower interstate highway system home page. *Federal Highway Administration*. Retrieved March 3, 2012, from http://www.fhwa.dot.gov/interstate/homepage.cfm

FHWA. (2012b). The national network. *Federal Highway Administration*. Retrieved February 15, 2012, from http://ops.fhwa.dot.gov/freight/infrastructure/national_network.htm

Fisher, J.W. (1970). *Fatigue strength of welded A514 steel beams* (Fritz Engineering Laboratory Report No. 358-16). Bethlehem, PA: Lehigh University.

Flügge, W. (Ed.). (1962). *Handbook of engineering mechanics* (1st ed.). New York, NY: McGraw-Hill.

Forman, R.G., Kearney, V.E., & Engle, R.M. (1967). Numerical analysis of crack propagation in cyclic-loaded structures. *Journal of Basic Engineering, 89*(3), 459-464.

Friedl, N., Rammerstorfer, F.G., & Fischer, F.D. (2000). Buckling of stretched strips. *Computers & Structures, 78*(1-3), 185-190.

Frost, N.E. (1962). Effect of mean stress on the rate of growth of fatigue cracks in sheet materials. *Journal of Mechanical Engineering Science, 4*(1), 22-35.

Fujii, T. (1968). On an improved theory for Dr. Basler's theory. *Proceedings of the 8th Congress IABSE* (pp. 479-487). New York, NY: International Association for Bridge and Structural Engineering.

Galambos, T.V. (1981). Load and resistance factor design. *AISC Engineering Journal, 18*(3), 74-82.

Goodpasture, D.W., & Stallmeyer, J.E. (1967). *Fatigue behavior of welded thin web girders as influenced by web distortion and boundary rigidity* (Structural Research Series No. 328). Urbana, IL: University of Illinois.

Grant, J.A., Fisher, J.W., & Slutter, R.G. (1977). Composite beams with formed steel deck. *Engineering Journal, 14*(1), 24-43.

Griffith, A.A. (1921). The phenomena of rupture and flow in solids. *Philosophical Transactions of the Royal Society of London, 221*, 163-198.

Guz, A.N., & Dyshel, M.Sh. (2001). Fracture and buckling of thin panels with edge crack in tension. *Theoretical and Applied Fracture Mechanics, 36*(1), 57-60.

Guz, A.N., & Dyshel, M.Sh. (2004). Stability and residual strength of panels with straight and curved cracks. *Theoretical and Applied Fracture Mechanics, 31*(1-3), 95-101.

Hagen, N.C., & Larsen, P.K. (2009). Shear capacity of steel plate girders with large web openings part II: Design guidelines. *Journal of Constructional Steel Research, 65*(1), 151-158.

Hagen, N.C., Larsen, P.K., & Aalberg, A. (2009). Shear capacity of steel plate girders with large web openings, part I: Modeling and simulations. *Journal of Constructional Steel Research, 65*(1), 142-150.

Hall, L.R., & Stallmeyer, J.E. (1964). *Thin web girder fatigue behavior as influenced by boundary rigidity* (Structural Research Series No. 278). Urbana, IL: University of Illinois.

Hertzberg, R.W., & Nordberg, H. (1969). *Fatigue crack propagation in A514 steel* (Fritz Engineering Laboratory Report No. 358-7). Bethlehem, PA: Lehigh University.

Heins, C.P., & Fan, H.M. (1976). Effective composite beam width at ultimate load. *Journal of the Structural Division, 102*(11), 2163-2179.

Herzog, M.A.M. (1974). Ultimate static strength of plate girders from tests. *Journal of the Structural Division, 100*(5), 849-864.

Hibbeler, R.C. (2006). *Structural analysis* (6th ed.). Upper Saddle River, NJ: Pearson Prentice Hall.

Inglis, C.E. (1913). Stresses in a plate due to the presence of cracking and sharp corners. *Transactions of the Institute of Naval Architects, 54,* 219-241.

Irwin, G.R. (1957). Analysis of stresses and strains near the end of a crack transversing a plate. *Journal of Applied Mechanics, 24*, 361-364.

Ito, M., Fujiwara, K., & Okazaki, K. (1991). Ultimate strength of beams with U-shaped holes in top of web. *Journal of Structural Engineering, 117*(7), 1929-1945.

Jackson, A. (1969). *Oxygen steelmaking for steelmakers*. Great Britain: Adlard & Son Limited.

Jones, R.M. (2009). *Deformation theory of plasticity*. Blacksburg, VA: Bull Ridge Publishing.

Khedmati, M.R., Edalat, P., & Javidruzi, M. (2009). Sensitivity analysis of the elastic buckling of cracked plate elements under axial compression. *Thin-Walled Structures, 47*(5), 522-536.

Kirke, B., & Al-Jamel, I.H. (2004). *Steel structures design manual to AS 4100*. Author.

Klesnil, M., & Lukas, P. (1972). Influence of strength and stress history on growth and stabilisation of fatigue cracks. *Engineering Fracture Mechanics, 4*(1), 77-92.

Kohout, J. (1999). A new function describing fatigue crack growth curves. *International Journal of Fatigue, 21*, 813-821.

Kouba, N.G., & Stallmeyer, J.E. (1959). *The behavior of stiffened beams under repeated loads* (Structural Research Series No. 173). Urbana, IL: University of Illinois.

Kuhn, P. (1940). *Investigations on the incompletely developed plane-diagonal tension field* (NACA Report No. 697). Hampton, VA: National Advisory Committee for Aeronautics.

Kumar, Y.V.S., & Paik, J.K. (2004). Buckling analysis of cracked plates using hierarchical trigonometric functions. *Thin-Walled Structures, 42*(5), 687-700.

Lawn, B. (1993). *Fracture of brittle solids* (2nd ed.). E.A. Davis, & I.M. Ward (Eds.). Cambridge, UK: Cambridge University Press.

Liang, Q.Q., Uy, B., Bradford, M.A., & Ronagh, H.R. (2005). Strength analysis of steel-concrete composite beams in combined bending and shear. *Journal of Structural Engineering, 131*(10), 1593-1600.

Lichtenstein. (1990). *Special inspections of selected portions of The Providence Viaduct, Route I-95 from West Exchange Street to Promenade Street, Bridge No. 578* (Supplemental Report for Project No. 1213). Framingham, MA: A.G. Lichtenstein & Associates, Inc.

Love, A.E.H. (1892). *A treatise on the mathematical theory of elasticity.* Cambridge, UK: Cambridge University Press.

Love, A.E.H. (1888). <u>The small free vibrations and deformation of a thin elastic shell</u>. *Philosophical Transactions of the Royal Society of London, 179,* 491-546.

MacGregor, J.G., & Wight, J.K. (2005). *Reinforced concrete: Mechanics and design* (4th ed.). Upper Saddle River, NJ: Pearson Prentice Hall.

Maeda, Y., & Okura, I. (1983). <u>Influence of initial deflection of plate girder webs on fatigue crack initiation</u>. *Engineering Structures, 5*(1), 58-66.

Maeda, Y., & Okura, I. (1984). <u>Fatigue strength of plate girder in bending considering out-of-plane deformation of web</u>. *Structural Engineering/Earthquake Engineering, 1*(2), 149s-159s.

Marek, P., Perlman, M., Pense, A.W., & Tall, L. (1970). *Fatigue tests on a welded beam with pre-existing cracks* (Fritz Engineering Laboratory Report No. 358-4A). Bethlehem, PA: Lehigh University.

Massarelli, P.J., & Baber, T.T. (2001). *Fatigue reliability of steel highway bridge details* (Report No. 02-R4). Charlottesville, VA: Virginia Transportation Research Council.

Massonnet, C. (1948). *Voilement des plagues planes sollicitees dan leur plan* (C.E.C.M. Notes Techniques). Brussels, Belgium.

McGuire, W., Gallagher, R.H., & Ziemian, R.D. (2000). *Matrix structural analysis* (2nd ed.). New York, NY: John Wiley & Sons.

Meguid, S.A. (1989). *Engineering fracture mechanics*. New York, NY: Elsevier Science Publishing Co., Inc.

Mertz, D. (2012). *Steel bridge design handbook: Design for fatigue* (Report No. FHWA-IF-12-052 – Vol. 12). Pittsburgh, PA: HDR Engineering,, Inc.

Miki, C., Murakosi, J., & Sakano, M. (1987). <u>Fatigue crack growth in highway bridges</u>. *Structural Engineering/Earthquake Engineering, 4*(2), 371s-380s.

Minor, J., & Woodward, C. (1996). <u>Web buckle at I-40 bridge test</u>. *Journal of Bridge Engineering, 1*(1), 34-36.

Moore, R.L. (1942). *An investigation on the effectiveness of stiffeners on shear resistant plate girder webs* (Tech Memorandum No. 921). Hampton, VA: National Advisory Committee for Aeronautics.

MRC. (2013). Highway 17 steel river bridge construction progresses. *McCormick Rankin*. Retrieved April 8, 2012, from http://www.mrc.ca/mrc_news/highway-17-steel-river-bridge-construction-progresses/

Mueller, J.A., & Yen, B.T. (1967). *Girder web boundary stresses and fatigue* (Fritz Engineering Laboratory Report No. 327-2). Bethlehem, PA: Leigh University.

Narayanan, R., & Der-Avanessian, N. (1985). Design of slender webs having rectangular holes. *Journal of Structural Engineering, 111*(4), 777-787.

Nassif, H.H., & Salama, T. (2011). Effective flange width for composite steel beams. *The Journal of Engineering Research, 8*(1), 28-43.

Nowak, A.S. (1993). Live load model for highway bridges. *Structural Safety, 13*, 53-66.

Nowak, A.S., Nassif, H., & DeFrain, L. (1993). Effect of truck loads on bridges. *Journal of Transportation Engineering, 119*(6), 853-867.

Oglesby, C.H., & Hicks, R.G. (1982). *Highway engineering*. New York, NY: John Wiley & Sons.

Okura, I., & Maeda, Y. (1985). Analysis of deformation-induced fatigue of thin-walled plate girder in shear. *Structural Engineering/Earthquake Engineering, 2*(2), 377s-384s.

Okura, I., Yen, B.T., & Fisher, J.W. (1993). Fatigue of thin-walled plate girders. *Structural Engineering International, 3*(1), 39-44.

OLA. (2008). *Evaluation report: State highways and bridges*. Minnesota: Office of the Legislative Auditor.

Orowan, E. (1954). *Energy criteria of fracture* (Technical Report No. 3). Cambridge, MA: Massachusetts Institute of Technology.

Osman, M.H., & Roberts, T.M. (1999). Prediction of the fatigue life of slender web plates using fracture mechanics concepts. *Thin-Walled Structures, 35*(2), 81-100.

Paik, J.K., Kumar, Y.V.S., & Lee, J.M. (2005). Ultimate strength of cracked plate elements under axial compression or tension. *Thin-Walled Structures, 43*(2), 237-272.

Paris, P.C., & Erdogan, F. (1963). A critical analysis of crack propagation laws. *Journal of Basic Engineering, 85*(4), 528-534.

Pugsley, A. (1966). *The safety of structures*. London, UK: Edward Arnold Publishers.

Ravindra, M.K., & Galambos, T.V. (1978). Load and resistance factor design for steel. *ASCE Journal of the Structural Division, 104*(ST9), 1337-1353.

Redwood, R., & Demirdjian, S. (1998). Castellated beam web buckling in shear. *Journal of Structural Engineering, 124*(10), 1202-1207.

Roberts, R., Fisher, J.W., Irwin, G.R., Boyer, K.D., Hausammann, G.V., Krishna, V., Morf, R., & Slockbower, R.E. (1977). *Determination of tolerable flaw sizes in full size welded bridge details* (Fritz Engineering Laboratory Report No. 399-3). Bethlehem, PA: Lehigh University.

Roberts, T.M., & Davies, A.W. (2002). Fatigue induced by plate breathing. *Journal of Constructional Steel Research, 58*(12), 1495-1508.

Roberts, T.M., Davies, A.W., & Bennett, R.J.H. (1995). Fatigue shear strength of slender web plates. *Journal of Structural Engineering, 121*(10), 1396-1401.

Roberts, T.M., Osman, M.H., Skaloud, M., & Zornerova, M. (1996). Residual shear strength of fatigue cracked slender web panels. *Thin-Walled Structures, 24*(2), 157-172.

Rockey, K.C. (1956). The design of intermediate vertical stiffeners on web plates subjected to shear. *Aeronautical Quarterly, 12*, 275-296.

Rolfe, S.T., & Barsom, J.M. (1977). *Fracture and fatigue control in structures: Applications of fracture mechanics*. Englewood Cliffs, NJ: Prentice-Hall.

Ryan, T.W., Mann, J.E., Chill, Z.M., & Ott, B.T. (2012). *Bridge inspector's reference manual (BIRM)* (Report No. FHWA NHI 12-049). Moon Township, PA: Michael Baker, Jr., Inc.

Sadd, M.H. (2009). *Elasticity: Theory, applications, and numerics* (2nd ed.). Burlington, MA: Academic Press.

Salmon, C.G., Johnson, J.E., & Malhas, F.A. (2009). *Steel structures: Design and behavior* (5th ed.). Upper Saddle River, NJ: Pearson Prentice Hall.

Sedov, L.I. (1972). *A course in continuum mechanics*. J.R.M. Radok (trans.). Groningen, Netherlands: Wolters-Noordhoff Publishing.

Seifi, R., & Khoda-yari, N. (2011). Experimental and numerical studies on buckling of cracked thin-plates under full and partial compression edge loading. *Thin-Walled Structures, 49*(12), 1504-1516.

Shahabian, F., & Roberts, T.M. (1999). Buckling of slender web plates subjected to combinations of in-plane loading. *Journal of Constructional Steel Research, 51*(2), 99-121.

Shanmugam, N.E., Lian, V.T., & Thevendran, V. (2002). Finite element modelling of plate girders with web openings. *Thin-Walled Structures, 40*(5), 443-464.

Shimizu, S. (2007). Tension buckling of plate having a hole. *Thin-Walled Structures, 45*(10-11), 827-833.

Shukla, A. (2005). *Practical fracture mechanics in design* (2nd ed.). New York, NY: Marcel Dekker.

Sih, G.C., & Lee, Y.D. (1986). Tensile and compressive buckling of plates weakened by cracks. *Theoretical and Applied Fracture Mechanics, 6*(2), 129-138.

Sivakumar, B., Ghosn, M., & Moses, F. (2011). *Protocols for collecting and using traffic data in bridge design* (NCHRP Report No. 683). Washington, DC: Transportation Research Board.

Slater, R.E. (1996). The national highway system: A commitment to America's future. *Public Roads, 59*(4). Retrieved March 18, 2012, from http://www.fhwa.dot.gov/publications/publicroads/96spring/p96sp2.cfm

Slutter, R.G., & Dricoll, G.C. (1963). *The flexural strength of steel and concrete composite beams* (Fritz Engineering Laboratory Report No. 279-15A). Bethlehem, PA: Lehigh University.

Slutter, R.G., & Fisher, J.W. (1966). *Fatigue strength of shear connectors* (Fritz Engineering Laboratory Report No. 316-2). Bethlehem, PA: Lehigh University.

Smith, R.J., Marek, P., & Yen, B.T. (1970). *Redistribution of stress and strain in a plate with a crack* (Fritz Engineering Laboratory Report No. 358-8). Bethlehem, PA: Lehigh University.

Smith, S.T., Bradford, M.A., & Oehlers, D.J. (1999). Elastic buckling of unilaterally constrained rectangular plates in pure shear. *Engineering Structures, 21*(5), 443-453.

Sparkes, S.R. (1947). The behavior of webs of plate girders. *Welding Research, 10*(6).

Stockfish, J. (2011). One girder on Diefenbaker Bridge cracked. Retrieved May 3, 2012, from http://www.paherald.sk.ca/Local/News/2011-08-30/article-2735113/One-girder-on-Diefenbaker-Bridge-cracked/1

Sun, C.T., & Jin, Z.-H. (2012). *Fracture mechanics*. Waltham, MA: Academic Press.

Tada, H., Paris, P.C., & Irwin, G.R. (2000). *The stress analysis of cracks handbook* (3rd ed.). New York, NY: ASME Press.

Tall, L. (1971). *On cracks in welds and welded structures* (Fritz Engineering Laboratory Report No. 358-30). Bethlehem, PA: Lehigh University.

Taly, N. (1998). *Design of modern highway bridges*. New York, NY: McGraw-Hill.

Timoshenko, S. (1936). *Theory of elastic stability* (1st ed.). New York, NY: McGraw-Hill.

Timoshenko, S. (1983). *History of strength of materials.* Toronto, Canada: General Publishing Company. (Original work published 1953).

Timoshenko, S., & Goodier, J.N. (1951). *Theory of elasticity*. New York, NY: McGraw-Hill.

Timoshenko, S., & Woinowsky-Krieger, S. (1959). *Theory of plates and shells* (2nd ed.). New York, NY: McGraw-Hill.

Todhunter, I. (1886). *A history of the theory of elasticity and of the strength of materials: From Galilei to the present time* (Vol. 1). K. Pearson, (Ed.). Cambridge, UK: Cambridge University Press.

Todhunter, I. (1893). *A history of the theory of elasticity and of the strength of materials: From Galilei to the present time* (Vol. 2). K. Pearson, (Ed.). Cambridge, UK: Cambridge University Press.

Tonias, D.E. (1995). *Bridge engineering: Design, rehabilitation, and maintenance of modern highway bridges.* New York, NY: McGraw-Hill.

Ugural, A.C. (1999). *Stresses in plates and shells* (2nd ed.). New York, NY: McGraw-Hill.

USDOT. (2010). *2010 status of the nation's highways, bridges, and transit: Conditions & performance*. Washington, D.C.: U.S. Department of Transportation.

USDOT. (2011). *Freight facts and figures 2011*. Washington, D.C.: U.S. Department of Transportation.

Vafai, A., & Estekanchi, H.E. (1999). A parametric finite element study of cracked plates and shells. *Thin-Walled Structures, 33*(3), 211-229.

Ventsel, E., & Krauthammer, T. (2001). *Thin plates and shells: Theory, analysis, and applications*. New York, NY: Marcel Dekker.

Viest, I.M. (1974). <u>Composite steel concrete construction</u> (Report of the Subcommittee on the State-of-the-Art survey of the Task Committee on Composite Construction of the Committee on Metals of the Structural Division). *Journal of the Structural Division, 100*(ST5), 1085-1139.

Viest, I.M. (1960). <u>Review of research on composite steel-concrete construction</u>. *Journal of the Structural Division, 86*(ST6), 1-21.

Vinson, J.R. (1974). *Structural mechanics: The behavior of plates and shells*. New York, NY: John Wiley & Sons, Inc.

Wagner, H. (1931). *Flat sheet metal girder with very thin metal web* (Tech Memorandum Nos. 604-606). Hampton, VA: National Advisory Committee for Aeronautics.

Wardhana, K., & Hadipriono, F.C. (2003). <u>Analysis of recent bridge failures in the United States</u>. *Journal of Performance of Constructed Facilities, 17*(3), 144-150.

Wei, R.P. (1970). <u>Some aspects of environment-enhanced fatigue-crack growth</u>. *Engineering Fracture Mechanics, 1*(4), 633-651.

Wempner, G. (1981). *Mechanics of solids with applications to thin bodies. Alphen aan den Rijn, Netherlands:* Sijthoff & Noordhoff.

Westergaard, H.M. (1939). <u>Bearing pressures and cracks</u>. *Journal of Applied Mechanics, 6*(61), 49-53.

Withiam, J.L. (2003). *Implementation of the AASHTO LRFD Bridge Design Specifications for substructure design*. Paper presented at the International Workshop on Limit State Design in Geotechnical Engineering Practice, Massachusetts Institute of Technology, Cambridge, MA. NJ: World Scientific Publishing Co.

Wright, W.J. (2002). <u>Fracture toughness requirements for highway bridges: Past and future trends</u>. *Progress in Structural Engineering and Materials, 4*(1), 96-104.

Yen, B.T. (1963). *On the fatigue strength of welded plate girders* (Fritz Engineering Laboratory Report No. 303-1). Bethlehem, PA: Lehigh University.

Yen, B.T., & Basler, K. (1962). *Results of an investigation of plate girders* (Fritz Engineering Laboratory Report No. 251-25). Bethlehem, PA: Lehigh University.

Yen, B.T., & Mueller, J.A. (1966). *Fatigue tests of large-size welded plate girders* (Fritz Engineering Laboratory Report No. 303-10). Bethlehem, PA: Lehigh University.

Yen, J.Y.R., Lin, Y., & Lai, M.T. (1997). Composite beams subjected to static and fatigue loads. *Journal of Structural Engineering, 123*(6), 765-771.

Zaarour, W., & Redwood, R. (1996). Web buckling in thin webbed castellated beams. *Journal of Structural Engineering, 122*(8), 860-866.

Zhou, Y.E., & Biegalski, A.E. (2010). Investigation of large web fractures of welded steel plate girder bridge. *Journal of Bridge Engineering, 15*(4), 373-383.